DISSERTATION
Fakultät für Physik
Ludwig-Maximilians-Universität
München

MEASUREMENT OF THE TOP QUARK MASS WITH THE MATRIX ELEMENT METHOD IN THE SEMILEPTONIC DECAY CHANNEL AT D0

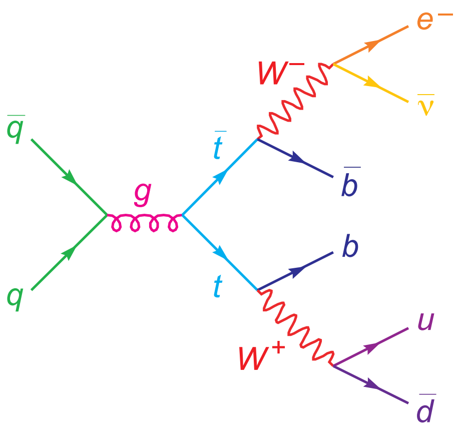

vorgelegt von

PETRA HAEFNER

geboren in
Münster i. Westf.

München, 31. Juli 2008

Erstgutachter: Prof. Dr. Otmar Biebel
Zweitgutachter: Prof. Dr. Christian Kiesling

mündliche Prüfung: 30. September 2008

”Miss alles, was sich messen lässt,
und mach alles messbar, was sich nicht messen lässt.”

Galileo Galilei
italienischer Physiker und Astronom
(1564 - 1642)

IN MEMORIAM,

Maria-Theresia Haefner
(1947-2008)

Zusammenfassung

Das Top-Quark spielt eine besondere Rolle im Standardmodell der Elementarteilchenphysik. Mit seiner enormen Masse von etwa 170 GeV ist es fast so schwer wie ein Goldatom und hat als einziges Quark eine Masse in der Nähe der elektroschwachen Skala. Die Massen des W-Bosons und des Top-Quarks erlauben gemeinsam Rückschlüsse auf die Masse des vorhergesagten Higgs-Bosons zu ziehen, das unter Umständen die Frage nach dem Ursprung der Masse selbst beleuchten kann.

Die Top Paarproduktion mit einem semileptonischen Zerfall $t\bar{t} \rightarrow W^{\pm}W^{\mp}b\bar{b} \rightarrow q\bar{q}l\nu b\bar{b}$ ist aufgrund des guten Verzweigungsverhältnisses und der relativ niedrigen Verunreinigung durch Untergrundereignisse verglichen mit anderen Zerfallskanälen der ”goldene Kanal” in der Bestimmung der Top-Masse. Die Messungen der Top-Masse, welche auf diesem Zerfall basieren und mit der Matrix-Element-Methode durchgeführt wurden, gehörten schon immer zu den besten Einzelmessungen weltweit. Im Jahr 2007 hat der Weltmittelwert der Top-Masse erstmals eine Genauigkeit von besser als 1% erreicht und wird nicht mehr durch die statistische Unsicherheit sondern durch systematische Unsicherheiten dominiert. Daher kommt der Verringerung der systematischen Unsicherheiten nun eine Schlüsselrolle bei der weiteren Verbesserung der Top-Massen Bestimmung zu.

In dieser Arbeit werden zwei neue Entwicklungen in der Behandlung von b-Jets vorgestellt. Die erste Verbesserung stellt eine Optimierung der Art und Weise dar, wie Informationen aus der b-Identifikation verwendet werden. Dadurch wird die Separation zwischen Signal- und Untergrundprozessen verbessert und die statistische Unsicherheit um ca. 16% verringert. Die zweite Verbesserung bestimmt Unterschiede in der Detektorantwort - und damit der Jet-Energieskala - zwischen leichten Jets und b-Jets. Damit zielt sie auf die Verringerung der Hauptquelle der systematischen Unsicherheit in den letzten Top-Massen Messungen ab.

Die Methode wurde mit Hilfe von Monte-Carlo-Ereignissen auf Generatorniveau validiert, mit vollsimulierten Ereignissen, die eine vollständige Detektorsimulation durchlaufen haben, kalibriert und schließlich auf echte Daten angewendet, die einer integrierten Luminosität von 1 fb^{-1} entsprechen. Mögliche Ursachen systematischer Unsicherheiten wurden untersucht. Die Top-Massen Messung ergibt:

$$m_t = (169.2 \pm 3.5\,(stat.) \pm 1.0\,(syst.))\ \text{GeV}\ .$$

Gleichzeitig wurden auch ein Skalierungsfaktor der Jet-Energieskala für leichte Jets und ein separater Skalierungsfaktor für b-Jets bestimmt. Sie wurden gemessen als 1.038 ± 0.023 beziehungsweise 1.056 ± 0.045. Dieses Ergebnis deutet darauf hin, dass die nominelle D0 Jet-Energieskala, die auf γ+Jets Ereignissen bestimmt wurde, die Energie sowohl von leichten Jets als auch von b-Jets in $t\bar{t}$-Zerfällen unterschätzt. Die verbesserte Analyse verringerte die größte systematische Unsicherheit, die Jet-Energieskala von b-Jets, von ca. 800 MeV auf etwa 150 MeV.

Abstract

The top quark plays a special role in the Standard Model of Particle Physics. With its enormous mass of about 170 GeV it is as heavy as a gold atom and is the only quark with a mass near the electroweak scale. Together with the W boson mass, the top quark mass allows indirect constraints on the mass of the hypothetical Higgs boson, which might hold the clue to the origin of mass.

Top pair production with a semileptonic decay $t\bar{t} \to W^{\pm}W^{\mp}b\bar{b} \to q\bar{q}l\nu b\bar{b}$ is the "golden channel" for mass measurements, due to a large branching fraction and a relatively low background contamination compared to other decay channels. Top mass measurements based on this decay, performed with the matrix element method, have always been among the single best measurements in the world. In 2007, the top mass world average broke the 1% level of precision. Its measurement is no longer dominated by statistical but instead by systematic uncertainties. The reduction of systematic uncertainties has therefore become a key issue for further progress.

This thesis introduces two new developments in the treatment of b jets. The first improvement is an optimization in the way b identification information is used. It leads to an enhanced separation between signal and background processes and reduces the statistical uncertainty by about 16%. The second improvement determines differences in the detector response and thus the energy scales of light jets and b jets. Thereby, it addresses the major source of systematic uncertainty in the latest top mass measurements.

The method was validated on Monte Carlo events at the generator level, calibrated with fully simulated events, including detector simulation, and applied to D0 Run II data corresponding to 1 fb^{-1} of integrated luminosity. Possible sources of systematic uncertainties were studied. The top mass is measured to be:

$$m_t = (169.2 \pm 3.5\,(stat.) \pm 1.0\,(syst.))\ \text{GeV}\ .$$

The simultaneous measurement of a scaling factor for the jet energy scale of light jets and a separate scaling factor for b jets yields 1.038 ± 0.023 and 1.056 ± 0.045, respectively. This result indicates that the nominal D0 jet energy scale derived from γ+jets events underestimates the energy of light jets and b jets in $t\bar{t}$ decays. The improved analysis was successful in reducing the major systematic uncertainty caused by the b jet energy scale from about 800 MeV to approximately 150 MeV.

Contents

1 Introduction **1**

1.1 How Was the Top Quark Discovered? 1

1.2 What Makes the Top Quark Special? 3

2 Experimental Setup **7**

2.1 The Tevatron Collider 7

2.2 The D0 Detector 8

2.2.1 Coordinate System 8

2.2.2 Tracking System 9

2.2.3 Calorimeter 11

2.2.4 Muon Spectrometer 13

2.2.5 Trigger Setup 14

3 Event Reconstruction **15**

3.1 Tracks 15

3.2 Primary Vertices 16

3.3 Electrons 16

3.4 Muons 17

3.5 Jets 18

3.5.1 Calorimeter Cells Selection 18

3.5.2 Calorimeter Cluster Building 19

3.5.3 Jet Reconstruction 19

3.5.4 Jet Identification 20

3.5.5 Jet Energy Scale 20

3.6 Identification of Bottom Quark Jets 21

3.7 Neutrinos 23

4 Top Quark Events **25**
4.1 Top Quark Production 25
4.2 Top Quark Decay 27
4.3 Top Mass Measurements 29

5 The Matrix Element Method **31**
5.1 Topological Likelihood 31
5.2 Transfer Functions 34
5.2.1 Jet Transfer Functions 36
5.2.2 Muon Transfer Functions 41
5.3 Topological Signal Likelihood 46
5.4 Topological Background Likelihood 52
5.5 Normalization 53
5.6 b Identification Probabilities 56
5.7 The Fitting Procedure 62

6 Top Mass Measurement **65**
6.1 Event Selection 65
6.2 Method Validation 67
6.2.1 Ensemble Testing Procedure 67
6.2.2 Overview of the Event Pools 69
6.2.3 Normalization 70
6.2.4 Pure Signal Studies 71
6.2.5 Studies Including Background 78
6.3 Method Calibration 91
6.3.1 Overview of Monte Carlo Samples 91
6.3.2 Signal Fraction Determination 93
6.3.3 Normalization 96
6.3.4 Calibration for the Data Measurement 98
6.4 Data Measurement 102
6.5 Systematic Uncertainties 107

6.5.1 Method . . . 107
6.5.2 Detector Modeling . . . 110
6.5.3 Physics Modeling . . . 113
6.5.4 Summary of Systematic Uncertainties . . . 114

7 Conclusions 117

8 Outlook 121

A Example Calculation for *b* Identification Probabilities 123

B Parton Level Studies Including Background 125

C `CAF` Package List 133

D Monte Carlo Request IDs 135

E Overview of Trigger Lists and Integrated Luminosities 137

F Input Variables for Topological Likelihood Fits 139

G Data to Monte Carlo Comparisons 143

H Additional Monte Carlo Studies 153

I Data Measurement requiring *b* tags 155

List of Figures 157

List of Tables 163

Bibliography 165

Chapter 1

Introduction

1.1 How Was the Top Quark Discovered?

On March 2nd, 1995 the discovery of the top quark was officially announced by the CDF and D0 collaborations at Fermilab, Chicago. The decade-long search for the last missing piece in the quark sector of the Standard Model had come to an end and the Standard Model depicted in Fig. 1.1 had tryly become *standard*.

In the 1950's and 60's hundreds of new particles called hadrons were discovered and a real zoo of "elementary" particles emerged. Gell-Mann and others were the first to classify these by postulating three new constituents of matter, the up (u), down (d) and strange (s) quarks together with their anti-particles (see, for example [1]). With the assumption that this new type of fundamental particle has spin 1/2 and a charge of either -1/3 or +2/3 (in units of the elementary charge), they could explain the whole observed hadron spectrum. Nevertheless, the question remained wether this was only a convenient abstraction for hadron classification or wether it offered a glimpse of a more fundamental theory of particle physics. After the discovery of the J/Ψ in 1974 at a mass of 3.1 GeV[1] [2, 3], the existence of a fourth quark, the charm (c), was deduced. It became obvious that a symmetry exists between quarks and leptons and that they can be grouped in pairs belonging to either of two generations. The (u, d) and the (ν_e, e) form the first generation of which all ordinary matter that we observe today is composed. The second generation is built of the (c, s) quarks and the (ν_μ, μ) leptons, which only existed right after the Big Bang at very high temperatures. The Standard Model, although not yet standard, was born. But the nice symmetry between quarks and leptons did not survive very long. In 1975 the tau (τ) lepton discovered at SLAC [4] ushered in a third generation of leptons. Soon after, in 1977, the discovery of the upsilon (Υ) hadron at around 10 GeV [5, 6] gave evidence for yet another quark, the bottom (b) quark. In order to rescue the Standard Model, the existence of two other particles was predicted, the top (t) quark as partner of the b quark and the tau neutrino (ν_τ) as partner of the τ lepton. The hunt for "the top" has begun.

First calculations, based on the mass ratios of the other two quark generations and the known hadron masses, predicted a heavy new hadron composed of $t\bar{t}$ at around 30 GeV. However, the

---

[1] Here, and in the rest of this document, so-called *natural units* ($\hbar = 1, c = 1$) are used.

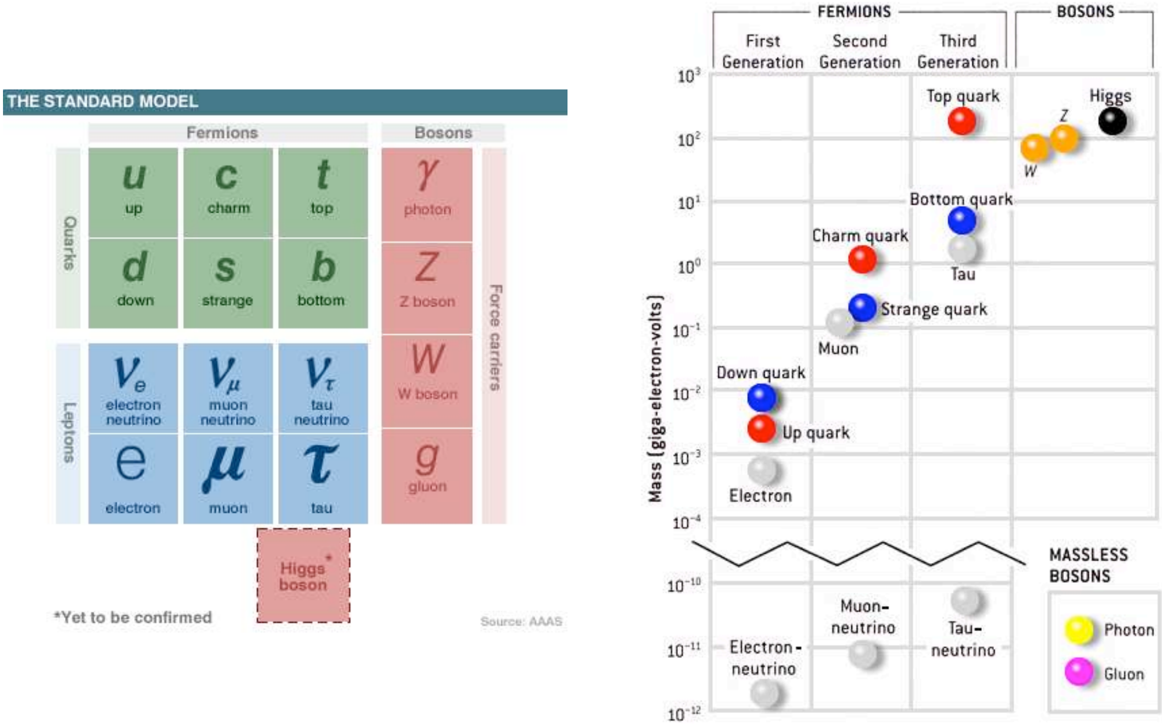

Figure 1.1: Overview of the content of the Standard Model of particle physics and the particle masses.

electron-positron colliders at SLAC and PETRA found no hint of such a thing. The baton was passed to the next generation of colliders. At CERN in the early 1980's a proton anti-proton collider at a much higher center-of-mass energy of up to 540 GeV started data taking. With this collider the important discoveries of the W [7, 8] and Z [9, 10] bosons were made. In the Standard Model, forces are transmitted by particles serving as force carriers. In the unified electroweak theory, the massless photon carries the electromagnetic force and the massive W and Z bosons mediate the weak force. In the same way, gluons transmit the strong force between quarks. This discovery was a great success for the Standard Model because it demonstrated that the W and Z masses had been correctly predicted. However, the top quark remained an elusive particle. By 1987, when the Tevatron proton anti-proton collider at Fermilab started operation, the mass limit of the top quark had been pushed to 41 GeV [11, 12], ruling out the first estimates of a $t\bar{t}$ hadron. The Tevatron collider with a center-of-mass energy of 1800 GeV could improve this limit to 91 GeV [13–16] in the beginning of the 1990's (cf. Fig. 1.2, direct searches). This was an important milestone as it excluded possible decays of the W boson into $t\bar{b}$. With such a high mass, it became clear that the top quark could only be produced in pairs of isolated quarks, each one almost allways decaying to a W and a b (see, for example [17]). In 1992, the newly formed D0 experiment at Fermilab entered the hunt. It was intended to provide an independent cross check of the CDF[2] results and had a complimentary experimental approach. Whereas the CDF detector emphasizes the ability to accurately track paths of single particles and measure their momenta, the D0 experiment relies on the energy measurement in an precisely segmented calorimeter.

---

[2] Collider Detector at Fermilab

With these two huge, complicated instruments with hundreds of thousand of electronic channels, and beam intensities improved by a factor of four by the Tevatron operation staff, the existence of the top quark was finally verified in 1995 after nearly two decades of intense searches. CDF found 49 events with a chance of 1 in a million that this could be a fluctuation of the background [18]. D0 observed 17 events with a 1 in 2 million chance that these were mimicked by background [19]. These first measurements indicated a top quark mass of 176 ± 13 GeV and 199 ± 30 GeV, respectively [18, 19]. This was in perfect agreement with the indirect prediction of 173^{+18}_{-20} GeV of the high precision electroweak fits made possible by the LEP experiments [20] (see Fig. 1.2). With such an enormous mass a single top quark is 40 times more massive than the second heaviest quark, the b; it weighs nearly 200 times more than a proton and has approximately the same mass as an entire gold atom.

1.2 What Makes the Top Quark Special?

The huge mass of the top quark suggests that it has a special role to play in answering the question of the origin of mass. The Higgs mechanism, proposed in 1964, suggests that particles acquire mass via the interaction with a postulated Higgs field. At high energies all fermions and bosons are massless, whereas at low energies the electroweak symmetry is broken and the particles become massive. However, the coupling to the predicted Higgs particle is unconstrained for fermions and is thus an adjustable parameter in the model. For the light electron, the interaction strength is only $3 \cdot 10^{-6}$, whereas for the heavy top quark it is almost unity. This means the top quark is the only fermion with

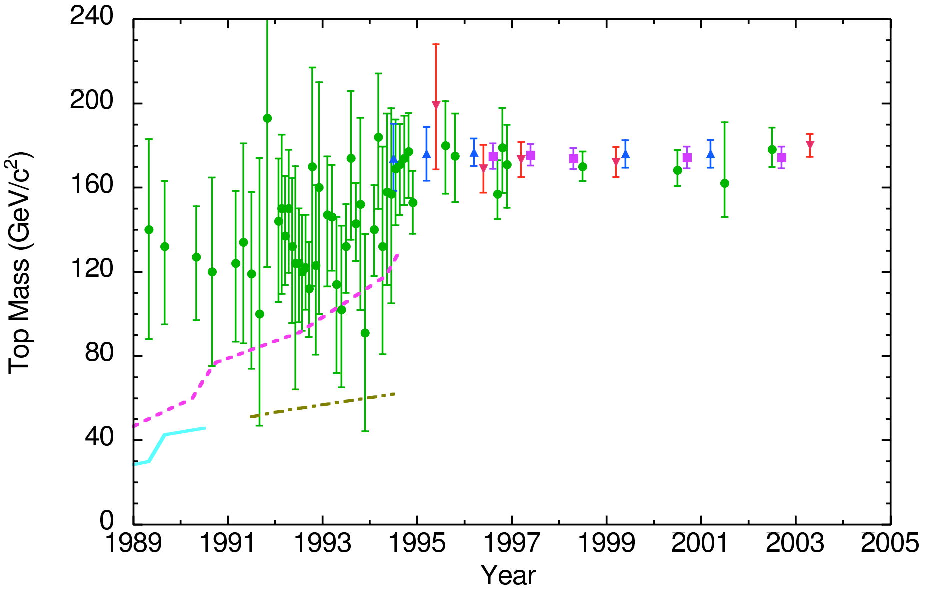

Figure 1.2: Evolution of the indirect prediction and direct measurement of the top quark mass with time [21]. (●) Indirect bounds on the top-quark mass from precision electroweak data. (■) World-average direct measurement of the top-quark mass; (▲) CDF and (▼) D0 measurements. Lower bounds from direct searches of $p\bar{p}$ (dashed) and e^+e^- (solid) colliders.

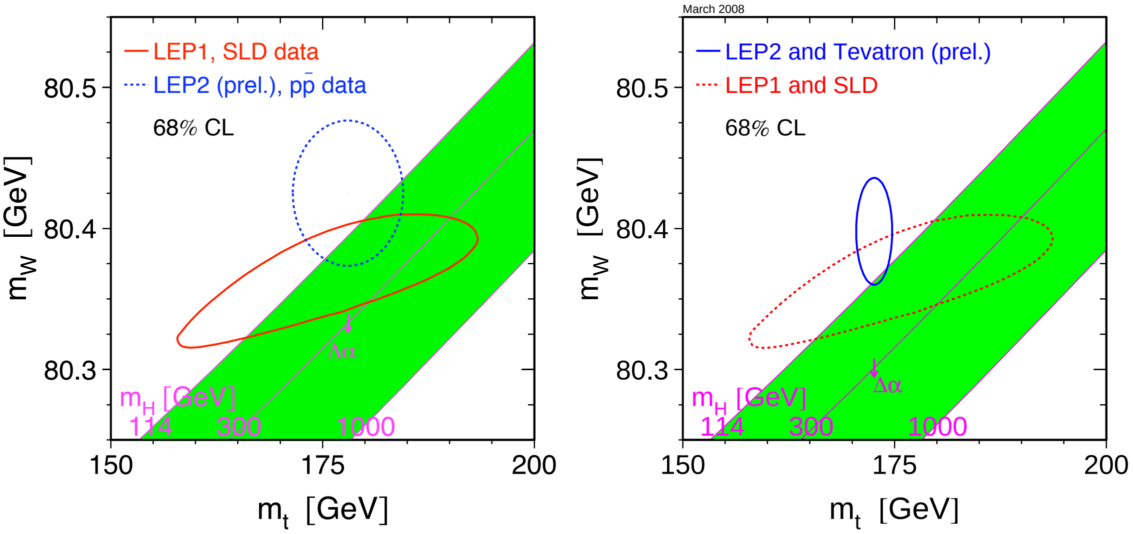

Figure 1.3: Contour curves of 68% probability in the (m_t, m_W) plane. The shaded band shows the Standard Model prediction based on the value for G_F for various values of the Higgs boson mass. See [22] for details. *Left*: Status as of April, 2005. *Right*: Status as of March, 2008.

a mass near the electroweak scale (cf. Fig. 1.1). It implies that the top quark is the most influential quark in studies of electroweak symmetry breaking. Precision measurements of the W boson mass and the top quark mass allow indirect constraints on the Higgs mass. This is the only way to infer the existence of the Higgs before direct observations are made. Due to the fact that precise measurements of the W mass are difficult to make in a hadron collider environment, the top mass is the best handle for improvement in the Higgs predictions. This statement is confirmed by the higher precision of the top mass measurements and the simultaneous improvement in the Higgs mass estimate during the course of this thesis (cf. Fig 1.3).

These improvements would be impossible without another unique property of the top quark. As explained above, due to the nature of the strong force bare quarks have never been observed. They hadronize rapidly and can only be detected as particle jets in high energy collisions. In contrast, the top quark has a tiny lifetime of $\approx 10^{-25}$ s, an order of magnitude smaller than the timescale for hadronization. Thus, it decays before hadronization can take place, giving us the unique opportunity to study a bare quark. Although we cannot detect it directly, the decay products of the top quark, the W and a b quark, carry information about its properties. Hence, it is possible to infer the mass of the top quark simply by measuring the four-vectors of its decay products and summing them up. Of course, this is much more complicated than it sounds because neither the W nor the b can be measured directly in the detector; instead only their decay products are visible. Nevertheless, it is a much more promising approach than infering masses from bound states of quarks in hadrons. Due to this unique decay in the quark sector, the top quark mass today is known to a higher precision than any other quark mass despite the fact that it is a little more than ten years ”old”. This makes the top quark a true high precision testing tool of the Standard model (and beyond).

One should not forget to mention, that it is due to the strong efforts of the CDF and D0 collaborations to improve their detectors and reconstruction, refine the measurements and develop new analysis methods, that such large progress has been made in these ten years of study. As a consequence, the top mass world average broke the ”magic” 1% level of precision about a year ago. Also, the precision is no longer limited by the statistics of the data set but by theoretical and experimental systematic uncertainties. Hence, the improvement of the mass estimate methods has become a key issue for further progress. This work will introduce two such improvements, aiming at the reduction of the systematic uncertainty due to b jets. The first one is an optimization in the way b identification information is used in top mass measurements. The second one addresses the difference in the detector response and thus the energy scales of light quarks and b quarks and thereby reduces the largest systematic uncertainty of the latest top mass measurements.

Chapter 2

Experimental Setup

The D0 experiment is located at the Tevatron proton-antiproton collider at Fermilab near Chicago. It is an omnipurpose detector designed to perform particle identification and precision measurements of individual particle momenta in $p\bar{p}$ collision final states. It consists of three major subsystems: the central tracking detectors for vertex identification and momentum measurement of charged particles, a uranium/liquid argon calorimeter for the energy measurement of electromagnetic and hadronic showers and a muon spectrometer for the detection and momentum measurement of muons. The following chapter will give an overview of the experimental setup in the Run IIa period that lasted from 2001 to 2006, when 1.2 fb^{-1} of data were accumulated, being analyzed in this study.

2.1 The Tevatron Collider

The Tevatron accelerator complex is situated at Fermilab in Batavia, Illinois. To date it is the world's highest energy particle accelerator with a center-of-mass energy of 1.96 TeV and it is the only collider with sufficient energy to produce top quark pairs. Two experiments are located at interaction points on the 6.3 km ring, CDF and D0. The Tevatron is a synchrotron consisting of superconducting magnet coils and warm iron magnets. It started operation as $p\bar{p}$ collider in 1992 with the so-called Run I period lasting until 1996. During Run I, the center-of-mass energy was 1.8 TeV and the collider was filled with six bunches each of protons and anti-protons with 3500 ns between bunch crossings. After the discovery of the top quark in 1995 the Tevatron was upgraded to achieve a higher center-of-mass energy and higher luminosities by increasing the number of particles per bunch and decreasing the bunch spacing. In Run II, started in March 2001, 36 bunches of protons and anti-protons are filled into the Tevatron in each store divided into three bunch trains separated by large abort gaps. The distance between bunches is 396 ns and their length is 38 cm resulting from the accelerator RF system. Peak luminosities lie generally around $100 \cdot 10^{30}\ cm^{-2}s^{-1}$ corresponding to 100 $\mu b^{-1}s^{-1}$. The high bunch rate and large luminosities made substantial upgrades in the two experiments D0 and CDF necessary for Run II. The integrated luminosity design scenario was surpassed in 2005 and up to the end of Run IIa more than 1 fb^{-1} of data was recorded by the experiments. In summer 2006 Run IIb started after upgrades of the accelerator complex and the two detectors to attain even higher luminosities. 4-9 fb^{-1} of integrated luminosity is expected before the end of Tevatron operation in 2008/2009.

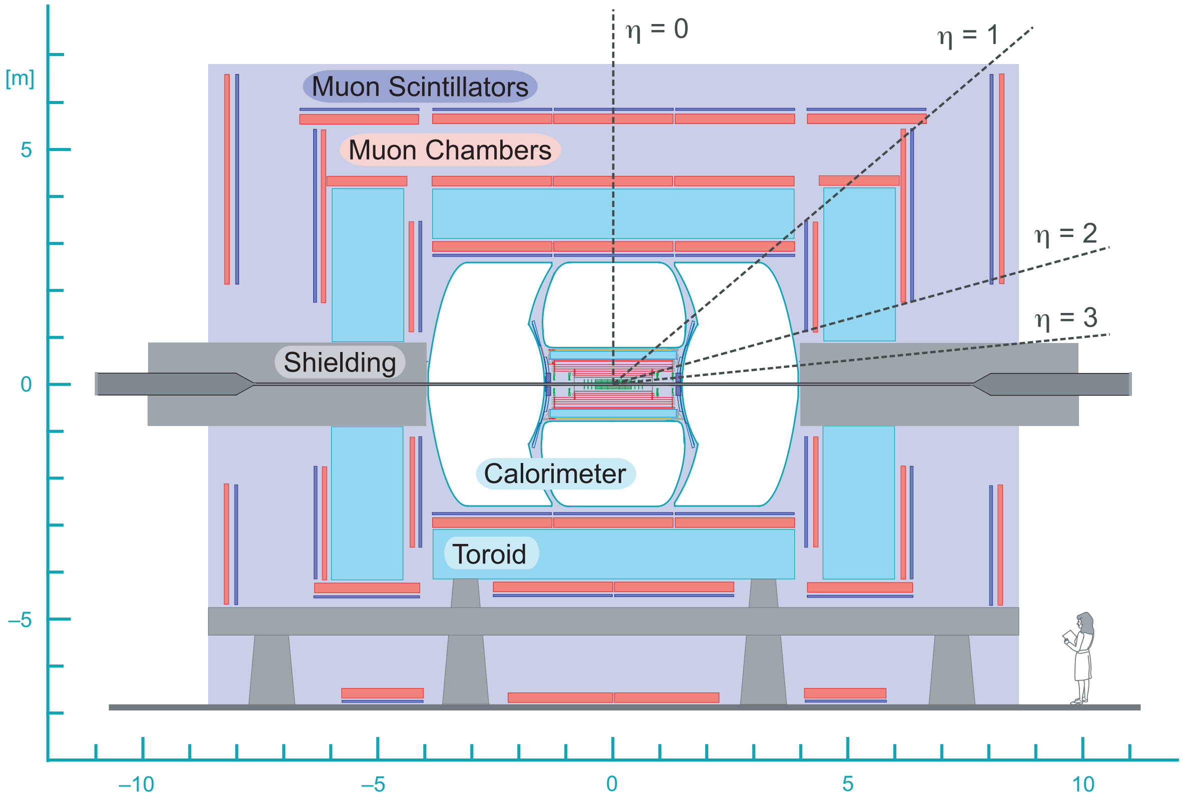

Figure 2.1: D0 detector side view. The tracking detector encloses the beam pipe. It is surrounded by the calorimeter cryostats (white), which are themselves embedded in the toroid (blue). The muon system consists of muon scintillators (violet) for triggering and muon chambers (magenta) for the muon trajectory measurement.

2.2 The D0 Detector

In this section, an introduction to the D0 detector will be given. A more detailed description can be found in [23, 24]. In the first subsection, the coordinate system used throughout this document is defined. The following subsections describe the different detector subsystems. At the end, a short overview of the trigger system is given.

2.2.1 Coordinate System

The coordinate system used for the D0 detector is a right-handed one with its origin at the center of the detector. The z axis is parallel to the proton beam direction, the y axis is vertical and the x axis points towards the middle of the accelerator ring. For particle directions the azimuthal angle ϕ and the pseudorapidity η are widely used. The pseudorapidity is defined as

$$\eta \equiv -\ln(\tan\frac{\theta}{2}) \qquad (2.1)$$

where θ is the polar angle. It is an approximation of the Lorentz-invariant rapidity

$$y = \frac{1}{2}\left(\frac{E + p_z}{E - p_z}\right) \tag{2.2}$$

when the particle mass is ignored, i.e. $p \gg m$. Distances in the detector are typically given in the (η, ϕ) plane by

$$\Delta R = \sqrt{(\Delta\eta)^2 + (\Delta\phi)^2}. \tag{2.3}$$

Attention must be paid to the origin of the coordinate system. Generally, two different systems are in use depending on the purpose. *Physics coordinates* originate in the primary vertex of a hard collision, whereas *detector coordinates* have their origin at the nominal center of the detector. In the remainder of this document a subscript *det* will be given to observables in detector coordinates (e.g. η_{det}). The term *forward* will be used for the detector region at large $|\eta|$. A radius will be denoted by r in contrast to distances indicated by R (see above). A subscript t is given to variables in the transverse plane (like p_t for the transverse momentum).

2.2.2 Tracking System

Excellent tracking is necessary for top quark, electroweak and b physics as well as the search for new phenomena including the Higgs. The central tracking system consists of the Silicon Microstrip Tracker (SMT) and the Central Fiber Tracker (CFT) within a 2 T solenoidal magnet. It surrounds the D0 beryllium beampipe which measures 38.1 mm in diameter, 2.37 m in length and 0.508 mm in thickness. The primary interaction vertex resolution is 35 μm in z-direction and the impact parameter resolution needed for secondary vertex identification is smaller than 15 μm in $r-\phi$ (for $p_t > 10$ GeV/c, $|\eta| = 0$). The high resolution allows good measurements of lepton p_t, jet E_t and missing transverse energy ($\not{E}_t$). The expected transverse momentum resolution $\delta p_t/p_t$ in the central region ($\eta < 1.5$) is as follows:

$$\begin{array}{llll}
\delta p_t/p_t & \geq 2\% & \text{for} & p_t = 1\ GeV \\
\delta p_t/p_t & \geq 4\% & \text{for} & p_t = 10\ GeV \\
\delta p_t/p_t & \geq 10\% & \text{for} & p_t = 100\ GeV
\end{array}$$

Silicon Microstrip Tracker

The SMT allows tracking and vertexing over nearly the full η coverage of the calorimeter and the muon system. Its design was dictated to a large extent by the accelerator environment, e.g. the length of the interaction region ($\approx$ 25 cm) sets the length scale of the device. With such a long interaction region it is a challenge to deploy detectors such that tracks are generally perpendicular to the detector surfaces at all η. This lead to the design of barrel modules interspersed with disks in the central and assemblies of disks in the forward region. The barrel detector measures primarily the $r-\phi$ coordinate whereas the disks can measure both $r-\phi$ and $r-z$. A difficult mechanical challenge was the arrangement of detector components: it should minimize dead areas while providing sufficient space for cooling and cables. Therefore, the SMT consists of three different detector types: 6 *barrels*

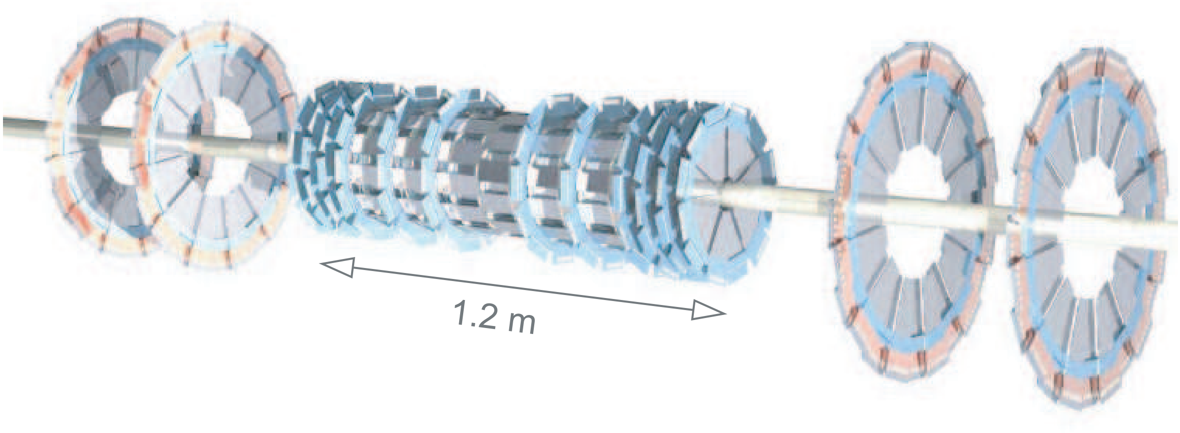

Figure 2.2: The Silicon Microstrip Tracker in a 3D visualization.

in the central region each with 4 readout layers, 12 *F-Disks* each with 12 double-sided wedge detectors and 4 large-diameter *H-Disks* consisting of 24 full wedges each constructed of two single-sided ”half” wedges. This leads to a total of 912 readout modules with 792 576 channels. The inner radius of the SMT detector is about 2.6 cm, the outer radius lies between 10 and 26 cm (barrel/F-Disks and H-Disks, respectively).

Central Fiber Tracker

The CFT consists of scintillating fibers mounted on 8 concentric support cylinders. It occupies the radial space 20 to 52 cm from the beam pipe center. The two innermost cylinders are 1.66 m long to accommodate the SMT H-Disks whereas the six outer cylinders have a length of 2.52 cm. Their coverage extends up to $|\eta| = 1.7$. Per cylinder there is one doublet layer of fibers oriented along the beam direction, the so-called *axial layers*, and one doublet layer at a stereo angle in ϕ, the *stereo layers*. There are two different stereo orientations: +3° (u-layer) and -3° (v-layer). The sequence of layers from innermost to outermost cylinder is the following:

$$zu - zv - zu - zv - zu - zv - zu - zv.$$

The scintillating fibers are optically coupled to clear fiber waveguides carrying the scintillation light to Visible Light Photon Counters (VLPCs) for readout. The inherent doublet layer resolution is about 100 μm under the condition that the location of individual fibers is known to better than 50 μm. The good resolution is due to the small fiber diameter of 835 μm. In total there are 200 km of scintillating and 800 km of clear fibers built into the CFT accounting for 76 800 readout channels.

Solenoid

A superconducting solenoidal magnet with a central field of 2 T was added in the D0 upgrade after Run I. It was designed to optimize the momentum resolution $\delta p_t / p_t$ and improve the tracking pattern recognition. The physical size of the magnet was determined by the available space within the central calorimeter vacuum vessel: 2.73 m in length and 1.42 m in diameter (cf. Sec. 2.2.3). The current density in the magnet windings becomes larger towards the ends of the coil to maximize the field uniformity inside the bore of the magnet. Besides the solenoid, D0 has a toroidal magnet which was installed prior to Run I (cf. Sec. 2.2.4). When only the solenoid is energized the calculated magnetic field needs to be scaled by 0.09% to match the measurements. When both magnets are operating this difference increases to 4.3%. The overall field has (x, z) diagonal symmetry at fixed y meaning

$$|B(+x,+z)| = |B(-x,-z)|.$$

There is no vertical symmetry as the toroid itself is not symmetric and the detector sits on a magnetic steel platform. The relative alignment between solenoid and toroid is known to 0.5-1.0 cm. Based on a $J/\Psi \rightarrow \mu\mu$ mass measurements as function of location within the field, the magnetic field map is estimated to be accurate to better than 0.3% at the detector center.

2.2.3 Calorimeter

Divided into three sampling calorimeters and an intercryostat detector (ICD[1]), the D0 calorimeter is primarily made of uranium as absorber and liquid argon as active medium. It was designed to provide energy measurements for electrons, photons and jets and assist in the identifications of these particles and muons. It is capable of measuring the transverse energy balance in events, needed for neutrino ($\not{E}_t$) measurements (cf. Sec.3.7). The relative E_t resolution for jets at $|\eta| < 0.4$ and a cone size of

---

[1] the intercryostat region is referred to as *ICR* in the remainder of the document

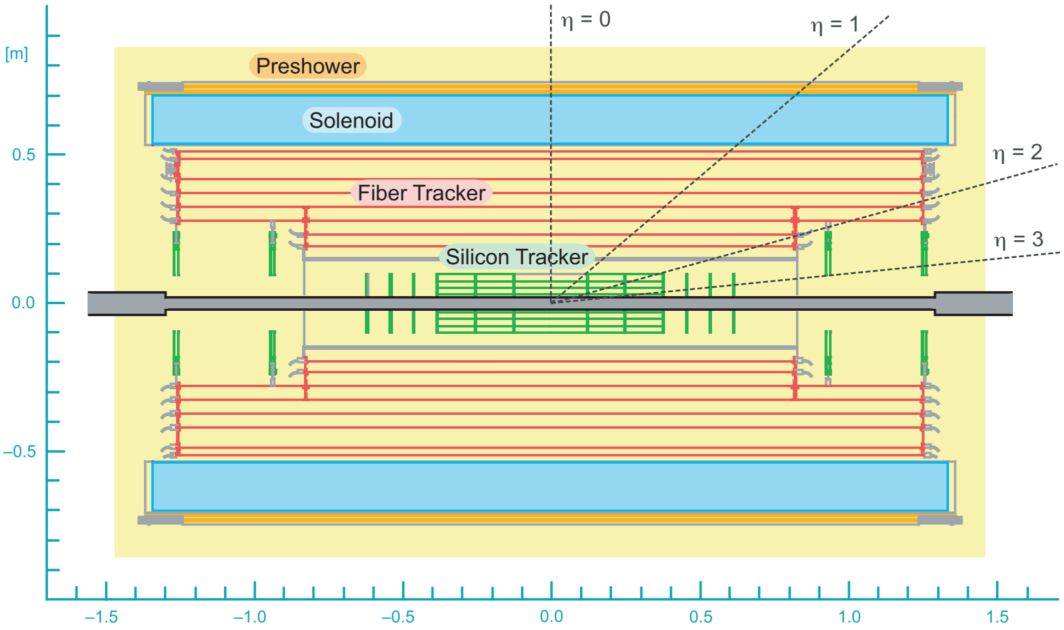

Figure 2.3: Overview of the full tracking system.

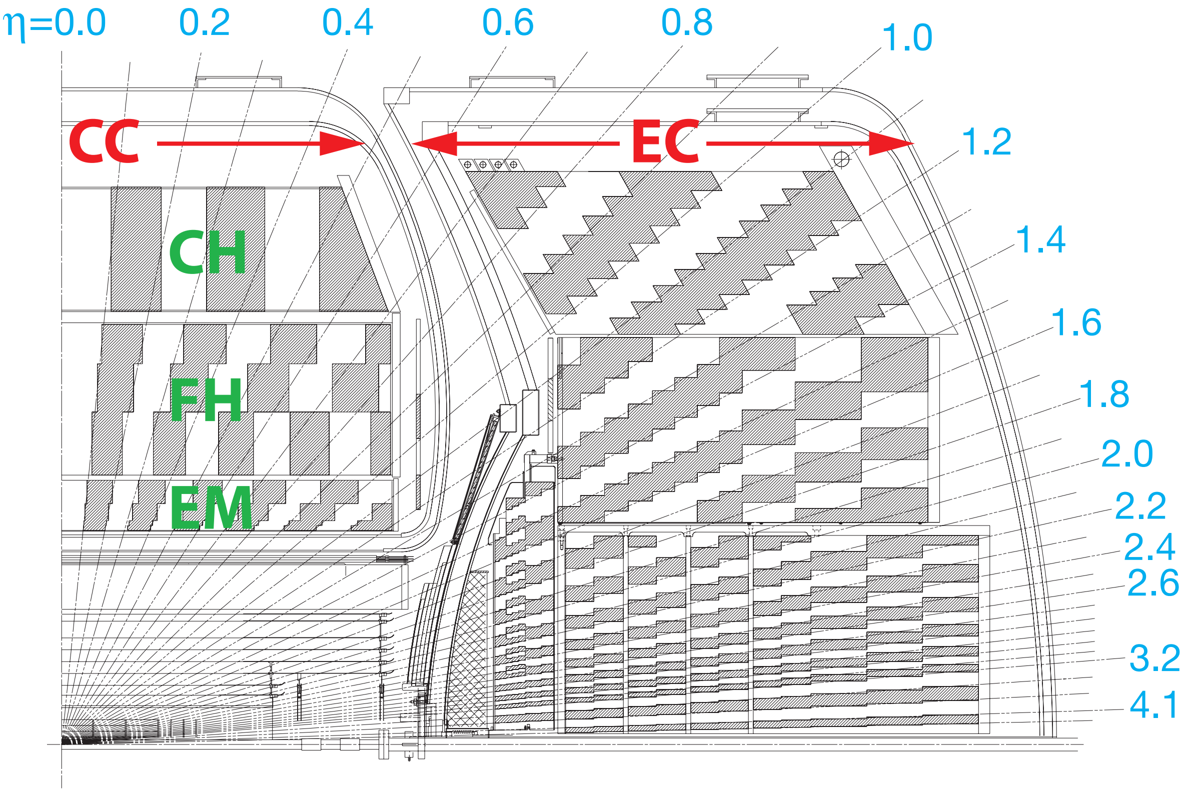

Figure 2.4: Schematic view of a quarter of the D0 calorimeter showing the transverse and longitudinal segmentation pattern. The shading pattern indicates groups of cells ganged together for signal readout. The rays indicate pseudorapidity intervals from the center of the detector.

R = 0.7 (in $\eta - \phi$) is as follows [25]:

$$\begin{aligned} \sigma(p_t)/p_t &\approx 15\% \quad \text{for} \quad p_t = 30\ GeV \\ \sigma(p_t)/p_t &\approx 10\% \quad \text{for} \quad p_t = 100\ GeV \\ \sigma(p_t)/p_t &\approx 5\% \quad \text{for} \quad p_t = 400\ GeV. \end{aligned}$$

The sampling calorimeter consists of three separate cryostats: the central calorimeter (CC) covering a range of $|\eta| \leq 1$ and two end calorimeters ECN and ECS, where *N* and *S* stand for north and south, respectively. They reach up to $|\eta| = 4$. The cryostats maintain a detector temperature of 90 K. Each one is divided into three sections: the electromagnetic (EM) section closest to the interaction region, followed by the fine hadronic (FH) and coarse hadronic (CH) section. The active medium is in all cases liquid argon whereas the absorber plates consist of different materials. The EM is made of thin plates (3 mm) nearly purely depleted uranium, the FH is based on 6 mm thick uranium-niobium (2%) alloy and the CH has 46.5 mm thick copper plates in the CC and stainless steel ones in the ECs. The electric field is established by grounding the metal absorber plates and connecting resistive surfaces of signal boards to positive high voltage, typically 2 kV. The electron drift time across the 2.3 mm

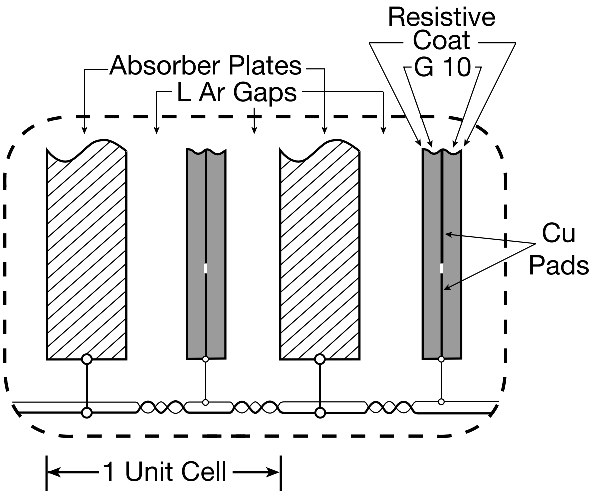

Figure 2.5: Calorimeter unit cell.

wide liquid argon gap is around 450 ns. Readout cells form *pseudo-projective* towers subdivided in depth, meaning the cell centers of increasing shower depth lie on rays projecting from the center of the interaction region but the cell boundaries are aligned perpendicular to the absorber plates. The transverse sizes of the readout cells are comparable to the transverse size of showers: 1-2 cm for electromagnetic showers and $\approx$ 10 cm for hadronic ones. The tower sizes are $\Delta\eta = 0.1$ times $\Delta\phi = 2\pi/64 \approx 0.1$. Only the third of four EM layers (EM3) which is located at the shower maximum is segmentated twice as finely. This allows a more precise location of EM shower centroids. In total the D0 calorimeter has 55 296 electronics channels of which 47 032 are connected to physical readout modules in the cryostats. For Run II completely new preamplifiers and baseline subtractor (BLS) boards were installed to cope with the significant reduction in the Tevatron's bunch spacing.

2.2.4 Muon Spectrometer

The Run II muon spectrometer uses the original Run I central muon system, proportional drift tubes (PDTs) and toroidal magnets. The wire chambers are installed in three layers: the A-layer is located between calorimeter and toroid whereas the B- and C-layers are placed outside the magnets. The central scintillation counters were partly replaced for Run II and a completely new forward muon system was installed. The coverage is up to $|\eta| = 1$ in the central and $|\eta| = 2$ in the forward region. The new forward detector uses mini drift tubes (MDTs) and includes trigger scintillation counters as well as beam pipe shielding. The so-called *cosmic cap* is a set of scintillation counters on top and on the upper sides of the outer layer central PDTs. This was extended to the lower sides and the bottom of the detector in Run II by the *cosmic bottom*. The so-called A-ϕ counters are additional scintillation counters installed on the A-layer PDTs which provide a fast detector for associating muons with the appropriate bunch crossing. The scintillation counters are used for triggering only whereas the wire chambers additionally give a precise coordinate measurement. Background rejection is achieved in the scintillators by considering timing information and in the wire chambers by building track segments. The advantages of a standalone muon system momentum measurement are the possibility of a low-p_t

cutoff in the muon trigger, cleaner matching with central tracks, rejection of π and K decays in flight and an improved momentum resolution at high muon momenta.

Toroidal Magnet

The central toroid is constructed in three sections to allow access to the inner detector. The center-bottom section consists of a 150 cm wide beam, fixed to the detector platform. The annulus is closed by two C-shaped sections, movable perpendicular to the beam axis. The toroidal magnet is completed by two end toroids located between 454 cm and 610 cm in z. Both have a square hole of 183 cm width centered on the beamline and extend up to 426 cm in x and y. The central magnets are wound using 20 coils of 10 turns each; the end toroid windings consist of 8 coils of 8 turns each. As in Run I, the central and end toroids are operated in series but the current was reduced from 2500 A to 1500 A in Run II. This led to a 6% decrease in the 1.9 T magnetic field. The reason is a substantial cost saving due to the reduced current. This is acceptable in Run II as the primary muon momentum measurement is performed by the new central tracking system. The magnet polarity is regularly reversed during run periods.

2.2.5 Trigger Setup

The increased luminosity and higher interaction rate of the upgraded Tevatron made a significantly enhanced trigger necessary for Run II to select interesting physics events to be recorded. This led to the design of three distinct trigger levels with each succeeding level examining fewer events but in greater detail with more complexity.

- **Level 1**
  The first trigger layer L1 is a collection of hardware trigger elements. The input rate is 1.7 MHz based on the bunch crossing frequency. The acceptance rate is around 2 kHz.
- **Level 2**
  L2 is built by hardware engines and embedded microprocessors associated with specific sub-detectors. The trigger decision is based on individual objects as well as correlations between objects. L2 provides information to a global processor. Its acceptance rate is about half the input rate, 1 kHz.
- **Level 3**
  L3 consists of a farm of microprocessors and makes use of sophisticated reconstruction algorithms. At this stage a code similar to the one employed in the offline reconstruction is run. The accept rate is $\approx$ 50 Hz. L3 provides the events to be recorded on tape.

The trigger system is closely integrated with the readout of data. Each event satisfying all three trigger levels is sent by the data acquisition system (DAQ) to long-term storage in Fermilab's Feynman Computing Center where it awaits offline reconstruction and analysis as described in the following sections.

Chapter 3

Event Reconstruction

This chapter will give a brief introduction to the reconstruction of objects as performed at D0. Although the reconstruction details are specific to the experiment, the succeeding chapters only refer generically to jets, charged leptons and $\not{E}_t$ and thus are transferable to other experiments.

Due to the fact that four out of six reconstruction objects in the l+jets final state are jets - of which two are b jets - jet reconstruction and b identification are crucial points for this analysis. They are described in Sec. 3.5 and Sec. 3.6, respectively. A short introduction to the reconstruction of other objects of interest, including a charged lepton (either an electron or a muon) and a neutrino ($\not{E}_t$), is given in Sec. 3.3-3.7.

3.1 Tracks

Since the implementation of a solenoidal magnetic field in D0 Run II, tracks are essential for most of the reconstruction objects. Vertices are reconstructed by clustering of tracks, electron and muon identification (ID) requires a central track match, photons are identified by the absence of a track, and jet reconstruction can be improved by combining calorimeter and tracking information.

Track finding is the process of building tracks from hits, which are energy deposits in the tracking modules, when a charged particle traverses the detector. It consists of two steps. First, pattern recognition builds a list of candidate tracks. This is performed by two distinct algorithms, the AA algorithm [26], finding paths originating in the beam spot layer by layer, and the Histogramming Track Finder [27, 28], making use of the fact that the trajectory of a charged particle is a circle in the plane perpendicular to the magnetic field with its curvature and direction at the distance of closest approach as parameters. Track candidates from the two lists are combined and duplicates are removed. In a second step, a Kalman fit [29–32] is applied to each track facilitating the correct propagation through the detector and calculating final track parameters. Both, tracks with and without SMT hits are considered.

3.2 Primary Vertices

Primary vertices indicate the presence and location of one or several inelastic $p\bar{p}$ collisions along the z direction in a given event. As the luminous region has a Gaussian shape with an RMS of about 30 cm centered around $z \approx 0$, a significant fraction of interactions take place at z positions considerably displaced from the detector center. The position in the transverse plane on the other hand is restricted by the transverse beam size as small as about 40 μm.

Reconstruction of primary vertices comprises three steps: track selection, vertex fitting and vertex selection [33–35]. Track selection requires a p_t larger than 0.5 GeV and 2 or more SMT hits in the SMT fiducial region. Outside this region in the $\eta - z$ plane no SMT requirement is imposed on the tracks. Vertex fitting uses a newly developed method at D0, the Adaptive Vertex Fitting [36,37]. As in the Kalman filter algorithm used previously, tracks are first clustered along z starting with the highest p_t track and including all tracks within 2 cm. In a second step all tracks in a cluster are constrained to a common vertex and the vertex position and track parameters are recalculated. In contrast to the old method where all tracks were weighted equally, the new technique weighs each track according to its χ^2 distance to the new fitted vertex. The fitting is repeated until the weights converge. The hard scatter vertex is finally selected from the list of candidate vertices by finding the vertex with the lowest *minimum bias probability*. Here, minimum bias events refer to all collisions without a hard interaction, i.e. with low transverse momenta. The procedure makes use of a simulated template of the p_t distribution of associated tracks. Additional quality cuts for *good* primary vertices require 3 or more associated tracks and a z distance smaller than 60 cm from the nominal detector center.

The new method significantly improves the primary vertex reconstruction, specially at high luminosities and in heavy flavor decays, where mis-associated tracks from minimum bias interactions and secondary vertices can significantly degrade and bias the vertex resolution and position.

3.3 Electrons

Electrons as electromagnetic objects deposit nearly all their energy in the EM layers of the calorimeter. Thus, they have a large EM fraction $f_{EM} = E_{EM}/E_{CAL}$. In contrast to neutral EM objects like photons and π^0 mesons they produce as charged particles a track in the inner detector. Both features are used to identify electrons [38]. For this analysis the so-called *top_loose* selection is used, it requires:

- $\frac{E}{p}$ track match with $\chi^2 > 0.0$
- $f_{iso} = \frac{E_{tot}(\Delta R<0.4)-E_{EM}(\Delta R<0.2)}{E_{EM}(\Delta R<0.2)} \leq 0.15$
- $f_{EM} \geq 0.9$
- H-matrix(7) ≤ 50
- $p_t^{track} \geq 5$ GeV
- $p_t^{CAL} \geq 15$ GeV

- $\eta_{det} \leq 1.1$

Here, f_{iso} denotes the energy fraction deposited in a hollow cone around the EM candidate. The H-Matrix(7) is calculated for each EM cluster and is based on seven variables describing the shower shape of electrons obtained from simulation [39–41]. Small values indicate electrons. To further decrease backgrounds from neutral particles, a 7-variable likelihood is built, where a value near 1 indicates an electron [41–43]. A *top_tight* electron is required to additionally fulfill:

- Likelihood ≥ 0.85

Since the efficiencies for electron selection are different for data and Monte Carlo (MC) simulation [44, 45], scale factors are applied to Monte Carlo to match the data. Also, the electron resolution is better in Monte Carlo and simulated electrons need to be smeared to reproduce the data resolution [46].

3.4 Muons

In contrast to Run I, where due to the lack of a solenoidal field muon momenta could only be reconstructed from hits in the muon spectrometer, in Run II the additional information from the inner tracker is used. This leads to a much better muon momentum resolution compared to Run I. Muons are classified using two parameters, *type* and *quality* [47]. The muon type is given by the *nseg* variable. A positive value indicates that a *local* muon, i.e. an object reconstructed in the muon system, is matched to a track in the inner detector and thus helps to separate noise and cosmic muons (if these do not fly through the tracker). In this analysis, nseg $= 3$ muons are used, required for the so-called *MediumNSeg3* quality. The latter is defined by the following specifications:

- ≥ 2 A layer wire hits
- ≥ 1 A layer scintillator hits
- ≥ 2 BC layer wire hits
- ≥ 1 A layer scintillator hits

Additionally, requirements on track quality and isolation are made. Medium tracks used here are defined by their distance of closest approach *dca* (in $x - y$) with respect to the primary vertex and the χ^2 per degree of freedom of the central track fit in the following way:

- dca < 0.2 cm (tracks without SMT hits)
- dca < 0.02 cm (tracks with SMT hits)
- $\chi^2/\text{d.o.f.} < 4$

To separate W $\rightarrow \mu\nu$ signal from heavy flavor background (B $\rightarrow \mu X$), isolation cuts are applied, as muons from heavy flavor decays tend to be embedded inside a jet. Both track and calorimeter isolation cuts are used:

- $\Delta R(\mu, \mathrm{jet}) > 0.5$
- $|\sum_{cells} E_t / p_t{}^{\mu}| < 0.08$ (within a hollow cone of $0.1 < \Delta R(track_{\mu}, cell) < 0.4$)
- $|\sum_{other\ tracks} p_t / p_t{}^{\mu}| < 0.06$ (within $\Delta R(track_{\mu}, track_{other}) < 0.4$)

Muons, fulfilling the first isolation cut and all of the other cuts above are called *loose*. Loose muons also fulfilling the other two isolation cuts are labeled *tight*. Both loose and tight muons require:

- $p_t \geq 15$ GeV
- $\eta_{det} \leq 2.0$
- isCosmic = false

where η_{det} is the pseudorapidity at the muon system A-layer ($r = 292.059$ cm). To veto cosmic muons a timing window of 10 ns, starting at the expected time of arrival from the collision, is applied to scintillator hits. If hits in any of the three layers lie outside this window the *isCosmic* flag is set to true.

As for the other reconstruction objects, the simulated resolution is better than the one measured in the actual data and additional smearing needs to be applied to muons in simulation [47]. The parameterization depends on the presence of SMT hits, the $|\eta_{CFT}|$ direction (larger or smaller than 1.6) and the run period. The latter distinction is due to the fact that the resolution in data changed by about 15% in runs taken before and after the fall 2004 shutdown. This is partly due to a change in the toroidal field that was decreased after the shutdown. The run periods are separated by run number 200 000 and will be referred to as *pre*- and *post*-shutdown throughout this document.

3.5 Jets

Energetic quarks and gluons produced in high energy collisions hadronize before entering the detector and are reconstructed as particle jets. Their reconstruction involves several steps from jet building to energy scale corrections described in the following.

3.5.1 Calorimeter Cells Selection

In each $p\bar{p}$ collision energy is deposited in a large number of calorimeter cells. Additionally, cells are subject to all kinds of noise ranging from the intrinsic uranium noise due to uranium decays in the absorbers to electronic noise. Typically, 1000 to 3000 cells are affected by this in each event. To suppress the noise, the average of the pedestal is defined as zero in the hardware. As the noise distribution is asymmetric around zero, with a larger tail to positive energies, the so-called *online zero suppression* sets a threshold at $1.5\,\sigma_{ped}$, where σ_{ped} denotes the RMS of the pedestal distribution. To further improve noise suppression the so-called T42 algorithm is used [48–50]. It rejects all cells with negative energies and positive ones below $2.5\,\sigma_{ped}$. Cells between $2.5\,\sigma_{ped}$ and $4\,\sigma_{ped}$ are only kept if they have a neighboring cell (in 3D space) with an energy above $4\,\sigma_{ped}$. Cells above $4\,\sigma_{ped}$ always pass. The idea behind this method is that in a finely grained calorimeter isolated cells with small energies are likely to originate from noise whereas low-energy cells beside high-energy cells are probably physical energy deposits. The T42 algorithm allows a better rejection of noise and thus better jet energy and missing transverse energy resolutions. It rejects about $30-60\%$ of all cells in each event, in good agreement with the expectation. The term *zero suppression* is used for the combined effect of hardware and T42 thresholds.

3.5.2 Calorimeter Cluster Building

To build calorimeter clusters each cell is first given a ”direction” which is calculated from its detector position and the reconstructed primary vertex in the event under consideration. From the cell energy and its direction the cell transverse energy can be calculated while assuming a massless object. Cells sharing the same $\eta-\phi$ window are combined to form calorimeter towers in the next step. Each tower exceeding $E_t = 500$ MeV is used as seed for cluster forming. Neighboring towers are added to each seed if their energy surpasses 50 MeV and their position lies within a cone of $\Delta R = 0.3$ in the central region (or within a 10 cm cone radius in EM3 of the end caps, cf. Sec. 2.2.3). The obtained *preclusters* are used as starting points for the final clusters if their energy exceeds 1 GeV. To these preclusters any EM tower within $\Delta R < 0.4$ is added. The center of the final cluster is calculated as the energy weighted mean of all cells in EM3 assigned to this cluster.

3.5.3 Jet Reconstruction

In D0 Run II the *Improved Legacy Cone Algorithm* is used for jet reconstruction [51]. As seeds this algorithm uses the final clusters formed as described above. Although a seedless approach is theoretically favored it is computationally very expensive. The precluster approach reduces the number of seeds to a feasible level. The algorithm starts forming a cone of certain radius R_{cone} in $\eta-\phi$ around each precluster centroid. In the next step, a new energy-weighted center is computed from all cells within the cone. The procedure is repeated iteratively until the jet center is stable. These stable solutions are called *protojets*. To reduce sensitivity to soft radiation, E_t-weighted centers between protojets called *midpoints* are used as seeds as well and the iterative procedure is repeated for these. The last step of the algorithm is splitting and merging of overlapping protojets. If more than 50% of the p_t of the least energetic jet is contained in the overlap region, the two protojets are merged into a new jet and the old ones are removed from the list of jets. Otherwise, the two jets are split, meaning the energy of each cell in the overlap region is assigned to the nearest jet. Finally, all jets with $p_t < 6$ GeV are discarded.

The jet algorithm is not only applicable to preclusters but it is also used to form particle jets. This means the algorithm uses *stable* Monte Carlo particles as input, where ”stable” denotes particles with a lifetime long enough to traverse the D0 detector volume without decay. All stable particles from the hard scattering and underlying event are included except for muons and neutrinos. Particle jets are clustered from the list of stable particles and define the particle level jet energy. The goal of the jet energy calibration described in Sec. 3.5.5 is to correct calorimeter jets to the particle jet level.

3.5.4 Jet Identification

The jet identification was revisited recently [52] taking the detailed geometry and noise characteristics of the D0 calorimeter into account. Cuts were optimized to have uniform and high efficiencies for all jet kinematics. The efficiencies for physical jets now lie at the $98-99\%$ level compared to inefficiencies above 10% in the past. In the central region ($|\eta| < 0.8$) the cuts are as follows:

- CHF < 0.44 (coarse hadronic fraction)
- EMF > 0.05 (electromagnetic fraction)
- $\mathrm{L1}_{ratio} > 0.5$ (level 1 confirmation)

where CHF and EMF denote the energy fraction deposited in the coarse hadronic and electromagnetic calorimeter, respectively. The $\mathrm{L1}_{ratio}$ compares the energy obtained from triggered level 1 towers to the energy obtained in the precision readout and helps to discriminate against noise not appearing simultaneously in the two independent readout chains [53]. Similar cuts are applied in the more forward $|\eta|$ regions; the exact criteria are given in [52]. To remove overlap between jets and electrons, all jets matched to a loose electron (see Sec. 3.3) with $\Delta R(e, jet) < 0.5$ are rejected. In this analysis, *good* jets are used, requiring (beside the above):

- $p_t \geq 15$ GeV
- $\eta_{det} \leq 2.5$.

3.5.5 Jet Energy Scale

The goal of the jet energy scale correction is to relate, on average, the measured jet energy in the detector E_{jet}^{meas} to the energy of the final state particle jet E_{jet}^{ptcl}. This can be obtained via the following equation:

$$E_{jet}^{ptcl} = \frac{E_{jet}^{meas} - E_O}{R_{jet} S_{jet}} \tag{3.1}$$

The different terms are defined as follows:

Offset Energy $\mathbf{E_O}$ The offset energy includes contributions from noise, additional $p\bar{p}$ interactions (minimum bias) and previous bunch crossings (pile-up). The energy contributed by spectators (underlying event) is not subtracted as being attributed to the high-p_t event. E_O depends on the cone size R_{cone}, jet pseudorapidity η_{det}, number of primary vertices n_{PV} and instantaneous luminosity L.

Calorimeter Response $\mathbf{R_{jet}}$ The energy response to particle jets is smaller than unity due to energy loss in material in front of the calorimeter, uninstrumented regions, lower response to hadrons compared to EM objects and module-to-module inhomogeneities. It is a function of jet energy, R_{cone} and η_{det}.

Showering Correction $\mathbf{S_{jet}}$ The showering corrections account for the fraction of energy deposited *outside* the jet cone by particles originating from the corresponding particle jet as well as energy deposited *inside* the cone by particles *not* belonging to the particle jet [54]. The net correction is typically smaller than unity. S_{jet} depends strongly on R_{cone} and η_{det} but only mildly on the jet energy.

Since the Monte Carlo simulation does not model all of the effects described above precisely, different jet corrections are applied to data and Monte Carlo. The jet energy scale at D0 is approved for two different cone sizes $R_{cone} = 0.7$ and $R_{cone} = 0.5$ [55]. In this analysis, $R_{cone} = 0.5$ jets are used and the so-called *final p17 JES* is applied.

Heavy flavor jets are expected to have different JES corrections because their harder fragmentation leads to a different response and showering correction. So far, there is no dedicated *b* jet energy scale certified by D0. The only correction applied is concerning jets containing a muon within R_{cone}. In these cases, the muon is supposed to stem from a semi-leptonic *b* decay and the jet is corrected to account for the momentum carried by the muon and the neutrino. In this instance the neutrino is assumed to have the same momentum as the muon.

3.6 Identification of Bottom Quark Jets

At hadron colliders, multijet events have the largest production cross sections and hence constitute a major source of background to many decay signatures. Multijet events can be significantly suppressed by identification of *b* jets in signal final states containing *b* quarks. Due to their relatively long lifetime *b* hadrons can travel several millimeters before decaying. The three main ways to identify *b* jets are i) secondary vertex reconstruction from tracks, ii) large impact parameter significance of tracks with respect to the primary vertex and iii) a muon reconstructed within the jet cone [56, 57]. In the past, four tools were certified at D0 to identify (*tag*) *b* jets:

Counting Signed Impact Parameters (CSIP) Is based on the number of tracks matched to jets (i.e. lying within R_{cone}) with a large impact parameter significance (IP_{sig}) with respect to the primary vertex [58–61].
Tag: $\mathrm{IP}_{sig} > 3$ for ≥ 2 tracks *or* $\mathrm{IP}_{sig} > 2$ for ≥ 3 tracks.

Jet Lifetime Probability Tagger (JLIP) Combines impact parameter information from all tracks belonging to a jet into a single variable, giving the probability of all tracks to originate in the primary vertex [62–65].
Tag: Small probability (e.g. $\leq 0.002 \equiv$ *very tight* tag)

Secondary Vertex Tagging (SVT) Uses tracks significantly displaced from the primary vertex to reconstruct secondary vertices [66–70].
Tag: Secondary vertex is located within R_{cone} of the jet.

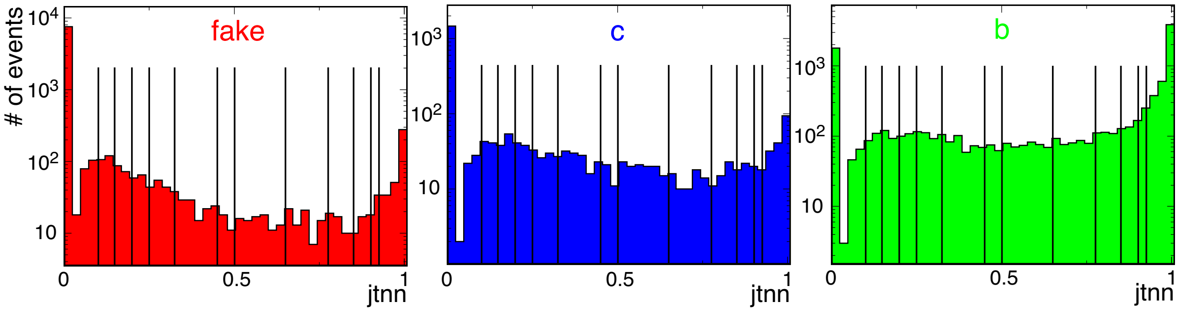

Figure 3.1: Distribution of the neural network output for light, c- and b jets. The cut values of the 12 certified operating points are indicated by the solid lines.

Soft Lepton Muon Tagging (SLT) Identifies muons within R_{cone} of the jet [71].

Tag: Associated muon found in jet.

All taggers calculate different variables containing valuable information on the likelihood of a jet to originate from a b quark and hence lead to a powerful discrimination between u,d,s,g and b,c jets. Combining such variables by means of multivariate techniques can further enhance the descrimination power. In the neural network (NN) b-tagger implemented at D0, seven variables from SVT, JLIP and CSIP enter [72–74]. The SLT does not provide input as it is used later in the determination of b-tagging efficiencies (see below) as independent tagger and only contains information for a small fraction of jets. In order to be independent of any particular jet reconstruction algorithm, variables that depend on the details of the algorithm such as the jet p_t are avoided. The seven input variables ranked by their discrimination power are:

1. Decay length significance of the secondary vertex with respect to the primary vertex (SVT).
2. Combination of all positive and negative decay length significance variables with different weights (CSIP).
3. Probability of a jet to originate from the primary vertex (JLIP).
4. χ^2 per degree of freedom of the secondary vertex (SVT).
5. Number of tracks used for the secondary vertex reconstruction (SVT).
6. p_t corrected mass of the secondary vertex (combined rest mass of tracks, assuming pions and correcting for neutral particles) (SVT).
7. Number of secondary vertices reconstructed within R_{cone} of the jet (SVT).

The output of the neural network is a single value for each jet constrained between 0 and 1 (cf. Fig. 3.1). The distribution for light quark jets (i.e. jets with a fake tag) peaks at values near 0, while that for b quark jets peaks near 1 and c jet distributions exhibit an intermediate behavior. The NN tagger is evaluated and certified for 12 operating points, defined by a lower cut on the NN output.

The b jet efficiencies are determined for all of them from data. The *System8* method described in [75] uses a system of 8 equations with 8 unknowns to solve for the efficiencies of two taggers. For the formalism to work the two chosen taggers need to be uncorrelated, which led to the choice of SLT together with the NN tagger. Efficiencies depend on p_t and η and are assumed to factorize into the corresponding components.

Due to the fact, that effects of dead material and noise in the tracking system are not fully modeled in the D0 Monte Carlo simulation, applying the NN tagger to Monte Carlo leads to significantly higher tagging rates than observed in data ($\approx 10\%$) [75]. Thus, so-called Tag Rate Functions (TRFs) are introduced to tag Monte Carlo events [76]. These consist of the tagging efficiency measured in Monte Carlo multiplied by a scale factor determined in data / MC b efficiency comparisons. It is assumed that the scale factor determined with the System8 method on b jets containing a muon is applicable to any Monte Carlo. With this procedure, tagging rates can be corrected over the full $\eta - p_t$ space. They are derived for both b- and c jets.

To estimate the fake tag rates (FTRs) from data, so-called *negative tag rates* (NTRs) are used. These are obtained by using negative impact parameter significance or negative decay lengths, depending on the tagger, as input to the NN. Thus, every jet is assigned a negative and positive tagged result. Since the negative tag rate is not a perfect approximation of the positive tag fake rate, two correction scale factors are applied to yield the data fake tag rate, both determined on Monte Carlo:

$$\mathrm{FTR} = \mathrm{SF}_{hf} \times \mathrm{SF}_{ll} \times \mathrm{NTR}. \tag{3.2}$$

SF_{hf} denotes the ratio of the light jet negative tag rate to the total negative tag rate and SF_{ll} gives the ratio of the light jet positive tag rate to the light jet negative tag rate.

In order to get the correct tagging probabilities in Monte Carlo samples, the tagging efficiencies need to be multiplied by the *taggability*, the probability to be taggable [77,78]. A jet is called *taggable*, if it is matched to a track jet within R_{cone} which contains at least two tracks. This twofold probability decouples the tagging efficiency from detector effects such as geometric acceptance and calorimeter noise. Taggability depends on the (calorimeter) jet p_t, η and the z position of the primary vertex. The latter one is important due to geometrical constraints of the tracking detector.

3.7 Neutrinos

As a result of their vanishing cross sections for reactions with the detector material, neutrinos escape the detector without producing any signal. Therefore, they can only be reconstructed by considering the assumed momentum balance in the transverse plane. The *escaping* missing transverse energy ($\not{E}_t$) is attributed to neutrinos. This of course has several drawbacks. First of all, the neutrino z momentum remains unknown (or can only be solved with ambiguities), as the momentum of the reacting incoming partons is not measurable. Secondly, several energetic neutrinos cannot be distinguished. Last but not least, the neutrino transverse momentum resolution is affected by calorimeter noise, reconstruction inefficiencies and the resolutions of the other reconstruction objects. Thus, $\not{E}_t$ is subject to multiple corrections including CH correction, EM scale of electrons, JES for good jets and muon corrections [79, 80]. The $\not{E}_t$ is calculated from all cells with the exception of CH calorimeter layers given that these are very noisy. Hence, the $\not{E}_t$ needs to be corrected for the CH energy contained in jets. As the muon is a *mimimum ionizing particle* it hardly deposits energy in the calorimeter. This fake $\not{E}_t$ needs to be subtracted as well. An issue is the treatment of muonic *b* decays. These contain ”real” neutrinos and thus true $\not{E}_t$. In the D0 Top Group this missing energy is attributed to the jet and the jet is corrected for both the missing energy and the muon momentum. The $\not{E}_t$ is therefore only corrected for muons not contained in jets. For the $\not{E}_t$ selection a minimum of 15 GeV is required.

Chapter 4

Top Quark Events

4.1 Top Quark Production

Due to the large mass of top quarks high center-of-mass energies are needed to produce them. These energies can to date only be achieved in proton anti-proton collisions at the Tevatron and will be easily obtained at the even higher energies of the LHC in the near future. As a matter of fact, these high energy collisons can be described by perturbative QCD[1] and the interaction is factorizable into long distance pieces describing the constituents of the incoming hadrons and the hadronization process of the outgoing particles and a short distance part in between describing the hard scattering process producing the top quarks and their decay particles. A schematic view of the factorization approach is shown in Fig. 4.1.

Because of the large amount of energy available in $p\bar{p}$ collisions at the Tevatron, the internal structure of the (anti-) proton is resolved and the interaction takes place between the constituents of the hadron, namely valence quarks, sea quarks and gluons. These objects are modeled by parton distribution functions (PDFs), which cannot be calculated from first principles or perturbatively but are derived from global QCD fits to deep-inelastic scattering and other data. The PDFs give the probability density to find a parton of a certain flavor i and longitudinal momentum fraction x_i in the incoming hadron, probed at a factorization scale μ_f (see Fig. 4.2). This arbitrary scale separates the low momentum (long distance) regime from the high momentum (short distance) one. The dependence on this scale becomes weaker when including higher order terms of the perturbation expansion. In these higher order calculations infinities such as ultra-violet divergences appear, which need to be removed by a renormalization procedure. This introduces another artificial scale, the renormalization scale μ_R, which is typically chosen to be equivalent to the factorization scale, $Q^2 = \mu_f^2 = \mu_R^2$. Although physical observables cannot depend on the scale chosen, an overall dependence remains if calculations are not performed to infinite order. This systematic uncertainty is addressed by probing experimental observables (e.g. the top quark mass) with simulations at different scale values.

The total cross section for a 2→2 process is given by its partonic cross section $\hat{\sigma}$ folded with the appropriate parton distribution functions $f_{p/\bar{p}}(x)$, integrated over the full initial state phase space and

---

[1] Quantum Chromo Dynamics

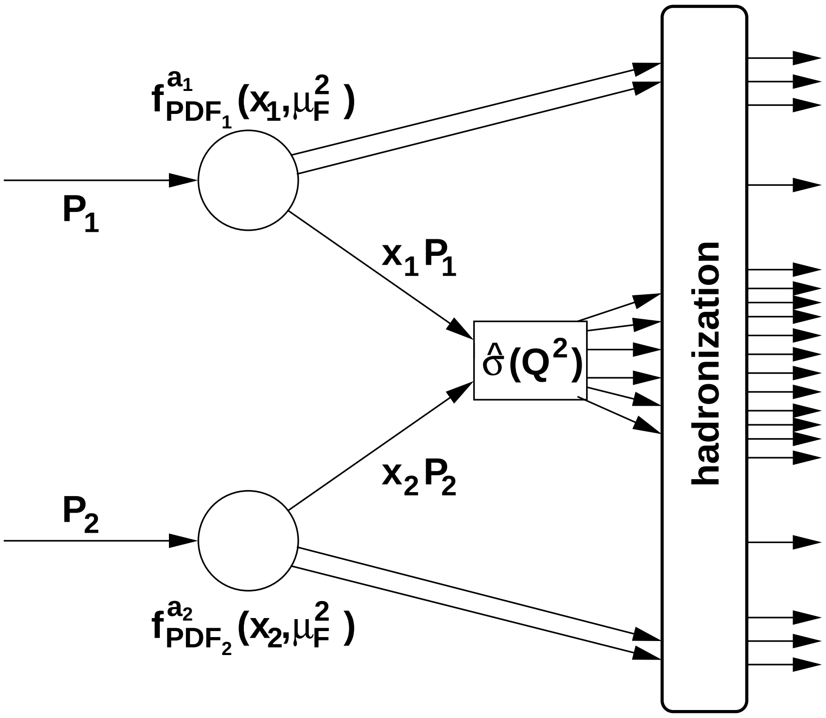

Figure 4.1: Schematic illustration of the factorization approach [81]. Two hadrons with momenta P_1 and P_2 initiate a hard interaction at a scale Q^2. The hard-scattering process takes place between two constituent partons with momentum fractions x_1 and x_2 and is described by the partonic cross section $\hat{\sigma}$, which can be calculated perturbatively. It depends on the renormalization and factorization scales μ_R^2 and μ_F^2. In the hadronization process, independent of the hard process, the particles observable in the detector are produced.

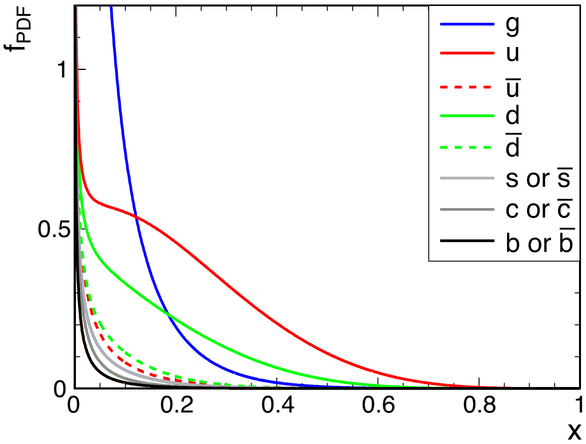

Figure 4.2: The `CTEQ6L` parametrization [82] of the parton distribution functions for different parton flavors in the proton as a function of the momentum fraction x of the proton carried by the parton, for a factorization scale $\mu_F^2 = (170\text{ GeV})^2$.

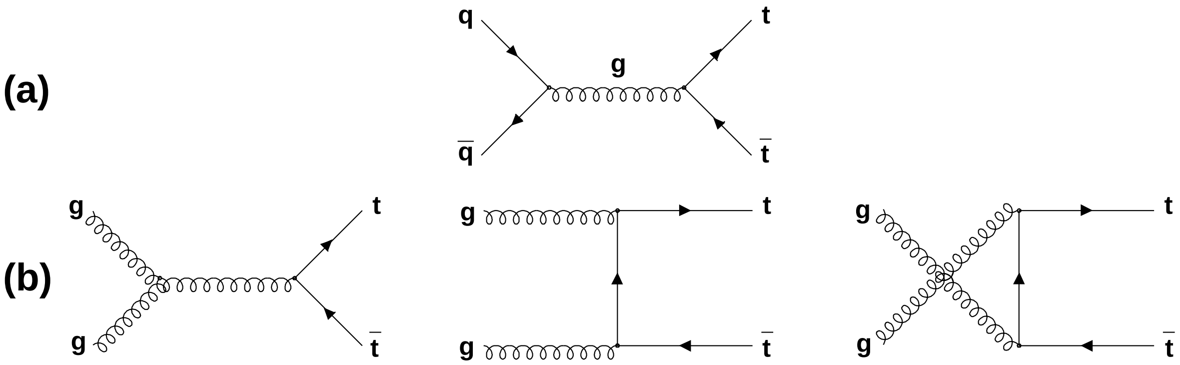

Figure 4.3: Leading order Feynman diagrams for $t\bar{t}$ production at hadron colliders. (a) $q\bar{q}$ annihilation, (b) gluon-gluon fusion.

summed over all contributing incoming parton species:

$$\sigma(p_1,p_2) = \sum_{i,j=q,\bar{q},g} \int dx_i\, dx_j\;\, f_p(x_i,Q^2)\;\, f_{\bar{p}}(x_2,Q^2)\; \hat{\sigma}\left(x_i p_1, x_j p_2, \alpha_s(Q^2), Q^2\right). \tag{4.1}$$

Here, p_1 and p_2 label the momenta of the colliding hadrons, x_i and x_j denote the momentum fraction of the interacting partons and α_s is the strong coupling constant at scale Q^2.

Top quarks can be either produced in pairs at hadron colliders by a 2→2 QCD process as described above or as single tops via the electroweak interaction. The latter one has only recently been observed [83, 84] and has not yet been used for top mass measurements. It is therefore only mentioned for completeness. The $t\bar{t}$ pair production can take place either via gluon-gluon fusion or quark-anti-quark annihilation (cf. Fig. 4.3). The fraction of each contribution depends on the center-of-mass energy available in the interaction. As can be seen in Fig. 4.2 the gluon PDF is steeply rising towards small momentum fractions, whereas at high momentum fractions ($\gtrsim 0.1$) the valence (anti-) quarks of the (anti-) proton dominate. At the Tevatron, the top pairs are produced predominantly at threshold as the probability of finding a parton with a certain momentum fraction falls off with increasing x. Since a momentum fraction of at least 0.18 is needed to produce a top pair, the $q\bar{q}$ annihilation dominates with about 85% of the total $t\bar{t}$ production rate. At LHC energies, the picture looks different as only a momentum fraction of 0.025 is needed for top pair production. In this regime, the gluon PDF prevails and leads to a fraction of about 90% gg-fusion. Due to the increasing PDFs towards small momentum fractions, a small decrease in necessary momentum fraction leads to a sizable effect in production cross section. This was the case at the Tevatron, when switching from 1.8 TeV center-of-mass energy ($x_{min} = 0.19$) in Run I to 1.96 TeV ($x_{min} = 0.18$) in Run II resulted in a cross section increase for top pair production of 30%. At the LHC, the same effect will lead to a cross section that is two orders of magnitude higher than at the Tevatron.

4.2 Top Quark Decay

In the Standard Model the top quark with a mass above the Wb threshold decays almost exclusively to an on-shell W-boson and a b quark via the weak interaction. The branching ratio is predicted to

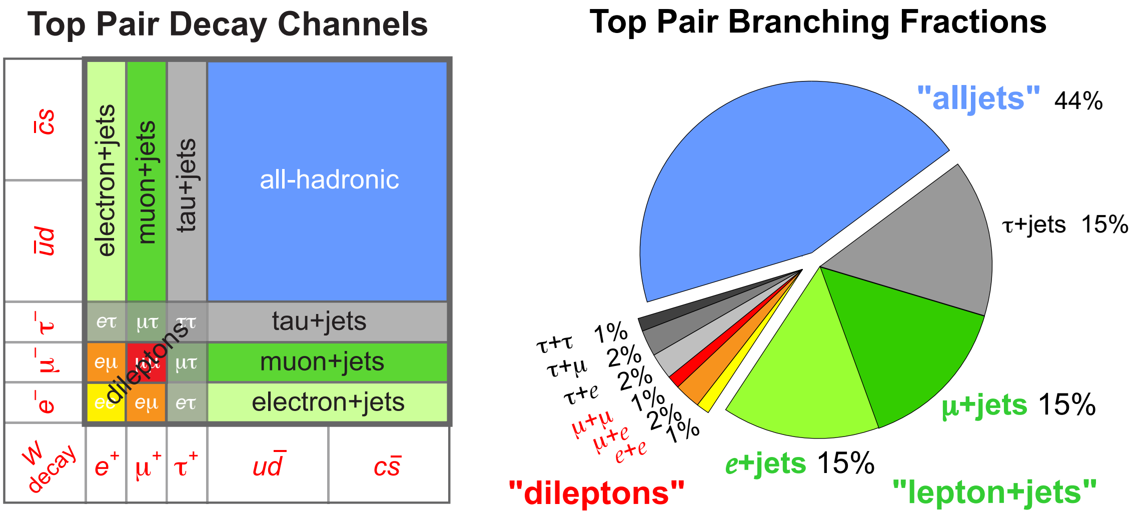

Figure 4.4: Overview of top pair decay channels and branching fractions.

exceed 99.8% at the 95% confidence level. Neglecting higher order terms and assuming the b to be massless the total decay width can be written as [85, 86]:

$$\Gamma_t = \frac{G_F m_t^3}{8\pi\sqrt{2}} \left(1 - \frac{m_W^2}{m_t^2}\right)^2 \left(1 + 2\frac{m_W^2}{m_t^2}\right) \left[1 - \frac{2\alpha_s}{3\pi}\left(\frac{2\pi^2}{3} - \frac{5}{2}\right)\right], \tag{4.2}$$

where G_F denotes the Fermi coupling constant and m_W and m_t indicate the W-boson and top mass, respectively. For an assumed top mass of 170 GeV/c^2 Eqn. 4.2 yields a width of $\Gamma_t \approx 1.5$ GeV/c^2, corresponding to a lifetime of about 0.5 x 10^{-24} s. As Eqn. 4.2 indicates, the top decay width increases with its mass. With the decay width being much larger than $\Lambda_{QCD} = 217^{+25}_{-23}$ MeV the top quark decays before hadronizing and thus not forms any bound states. The event topology of a $t\bar{t}$ decay is thus only determined by the decay modes of the W-boson. The W can decay hadronically into an up- and down-type quark of the first and second generation or leptonically into either electron, muon or tau and their corresponding neutrinos. Fermion universality in the elektroweak interaction leads to an equal rate for each of the leptonic decays. As quarks come in three colors the branching fraction for a leptonic decay is $B(W \rightarrow l\nu) = 3/9 = 1/3$ and for a hadronic decay $B(W \rightarrow q_u q_d) = 6/9 = 2/3$, where q_u and q_d denote up- and down-type quarks, respectively. A detailed overview of the decay channels and their branching fractions is given in Fig. 4.4. The two b quarks plus possible quarks from hadronic W decays hadronize and are reconstructed as jets in the detector. Conventionally, three topologies are classified: the dilepton channel, where both W's decay leptonically, the all-hadronic channel, where both W's decay hadronically and the semi-leptonic (l+jets) channel, where one W decays leptonically and the other one hadronically. All three channels have their advantages and disadvantages in measuring the top quark mass. These together with some details of topology and backgrounds are given in the following:

All-Hadronic Events

Topology 6 jets of which 2 are b jets, no isolated leptons, no $\not{E}_t$

Backgrounds multijet events (i.e. QCD background)

Pros highest branching fraction, over-constrained kinematics

Cons huge multijet background is difficult to model,
large combinatorical background due to 720 possible jet-parton assignments
(can be reduced via identification of b jets)

Semi-Leptonic Events

Topology 4 jets of which 2 are b jets, 1 isolated lepton, $\not{E}_t$

Backgrounds W+jets, multijet events

Pros good branching fraction, nice signature, over-constrained kinematics

Cons dependence on JES and bJES, 24 possible jet-parton assignments

Dilepton Events

Topology 2 b jets, 2 isolated leptons, large $\not{E}_t$

Backgrounds Z+jets, WW+jets

Pros very clean signature, low backgrounds

Cons low branching fraction, under-constrained kinematics

As taus are difficult to identify in the detector, they are not considered in most top mass analyses. They either decay hadronically to form jet-like structures or they decay leptonically, in which case the decay products cannot be distiguished from the products of other leptonic decays. Therefore, the word *lepton* will denote only electrons and muons throughout this document unless stated otherwise.

4.3 Top Mass Measurements

Many properties of the top quark have been studied over the last decade and with higher statistics new possibilities arise. As evidence for single top quark production has been obtained only recently [83, 84], all top properties have been studied in pair production so far. The best studied features are the top pair production cross section and the top quark mass - the latter being described in detail below. Other aspects of top measurements are the determination of the electric charge, investigation of branching fraction ratios, examination of forward-backward charge asymmetry and tests of the helicity of W bosons in top decays. These studies mainly probe and attempt to confirm properties predicted by the Standard Model. Searches for new physics are performed as well. They include searches for anomalous production and decay modes such as decays into Higgs bosons, stop production predicted by supersymmetric models and $t\bar{t}$ resonances from e.g. leptophobic Z' bosons predicted in technicolor models. An overview of the latest results can be found at [87, 88].

The top quark mass is studied with various methods in all three decay channels described in Sec. 4.2 by both the CDF and D0 collaborations. For simplicity only the so-called template method and the matrix element method will be introduced here as they illustrate two somewhat extreme cases. The template method is the classical approach which calculates a mass estimator for each possible permutation. In the semileptonic decay channel there are 24 possible jet-parton assignments of the four jets and 2 solutions for the neutrino z momentum leading to a total of 48 permutations. The mass estimator can either be a single number or a vector of observables. Here, only the simplest estimator shall be considered, in which the invariant masses of the two top quarks are reconstructed explicitly. In this case, one calculates the reconstructed mass for all possible permutations and chooses the kinematic fit with the smallest χ^2. This value is filled into a histogram for every selected event and then compared to template distrubutions. These distribution are obtained from Monte Carlo and predict the reconstructed top mass for various assumed values. The assumed mass of the best fitting distribution (or an interpolation) gives the measured top mass. This method has several drawbacks. First of all, the ”correct” permutation is only chosen in about 40% of the events. Also, each event is weighted equally when filled into the estimator histogram, although the mass prediction obtained from different events are not in general equally accurate. Consider for example a hypothetical two-body decay into a jet and a muon. If the jet carries a large fraction of momentum and the muon a low one, the detector resolutions will be good in both cases (cf. Sec. 3). If the fractions are the other way round, both jet and muon will be poorly reconstructed. Thus, in the first case the mass of the hypothetical particle can be obtained with good resolution whereas in the second case the information is much less precise. Another point is that depending on the kinematics (and *b*-tagging quality) the likelihood to be a top event is different for different events. To circumvent these drawbacks and extract the mass information contained in every single event better, the matrix element method was developed at D0 Run I [89]. It calculates for each event the likelihood to have arisen from a top quark decay under the assumption of different top masses and combines all event likelihoods into a sample likelihood for each assumed mass. The top mass is then extracted as the most likely one (i.e. the one with maximum sample probability). In this method all 48 possible permutations contribute and each possibility and each event is weighted according to its information content. This allows for optimal use of the information in each event.

Chapter 5

The Matrix Element Method

The matrix element method was developed at D0 in Run I after the discovery of the top quark [89]. As statistics were tiny, sophisticated analysis methods were needed to extract the largest possible amount of information out of each event and thereby allow a top mass measurement. Until now, measurements in the semileptonic decay channel performed with the matrix element method were always among the single best measurements in the world and have a strong impact on the world average of the top quark mass. The name matrix element method comes from the fact that it makes use of the topological information concealed in the matrix elements of signal and background reactions. It compares the predicted event topologies to measured ones in order to build likelihoods which distinguish one sort of reaction from another. To yield higher precision measurements, the method has been improved in several ways over the last years, including *b* identification and a simultaneous fit of the top mass and a jet energy scaling factor [90, 91]. This study will show how further improvements can be achieved by including *b* identification probabilities and another fit dimension, namely a specific energy scaling factor for *b* jets.

5.1 Topological Likelihood

The key element of the matrix element method is the calculation of a sample likelihood whic is maximized with respect to the observables s to be measured. This sample likelihood decouples into likelihoods for each event in the data sample:

$$\mathscr{L}(y_1,\ldots,y_n;s_1,\ldots,s_m) = \prod_{i=1}^{n} \mathscr{L}_{evt}(y_i;s_1,\ldots,s_m)\ . \tag{5.1}$$

Here, n stands for the number of events in the sample, y_i for the measured kinematic quantities in a certain event, and m is the number of observables s.

The event likelihood in principle needs to be composed of all possible processes leading to the final state under consideration

$$\mathscr{L}_{evt} = \sum_{proc} f_{proc}\, \mathscr{L}_{proc} \tag{5.2}$$

with $\mathscr{L}_{proc}$ being the likelihood of one such process and f_{proc} denoting the corresponding event fraction in the sample. Nevertheless, in practice only one signal and one background process is calculated explicitly leading to

$$\mathscr{L}_{evt} = f_{t\bar{t}}\, \mathscr{L}_{t\bar{t}} + (1 - f_{t\bar{t}})\, \mathscr{L}_{bkg} \tag{5.3}$$

for $t\bar{t}$ decays. Other background processes with small fractions are neglected and the fit results need to be corrected accordingly (cf. Sec. 6.3). The calculation of $\mathscr{L}_{t\bar{t}}$ and $\mathscr{L}_{bkg}$ is described in Sec. 5.3 and 5.4, respectively.

According to Fermi's Golden Rule, transition rates, i.e. event likelihoods, are proportional to the differential cross section of the corresponding reaction. In collider experiments, where two initial state particles are involved in a hard scattering and produce an n-body final state, the differential cross section can be expressed as

$$\mathrm{d}\sigma_{2\to n} = \frac{(2\pi)^4 |\mathscr{M}_{2\to n}|^2}{4\sqrt{(p_1 p_2)^2 - m_1^2 m_2^2}}\, \mathrm{d}\Phi_n\ , \tag{5.4}$$

where p_1 and p_2 denote the four-momenta of the two initial state particles with masses m_1 and m_2 and $\mathscr{M}_{2\to n}$ is the matrix element of the process incorporating all its kinematics. The n-body phase space $d\phi_n$ for final state momenta $q_1, \ldots, q_n$ is given by

$$\mathrm{d}\Phi_n(p_1 + p_2; q_1, \ldots, q_n) = \delta^4\left(p_1 + p_2 - \sum_{i=1}^{n} q_i\right) \prod_{i=1}^{n} \frac{\mathrm{d}^3 q_i}{(2\pi)^3 2E_i}\ . \tag{5.5}$$

At hadron colliders, the initial state of the two colliding partons is not known precisely and must be described by Parton Density Functions (PDFs) taking all possible parton flavors and initial state momentum fractions x_i into account. Thus, the differential cross section (5.4) needs to be convoluted with the PDFs in the following way:

$$\mathrm{d}\sigma^{hc}_{2\to n}(y_{parton}) = \int\limits_{x_1,x_2} \sum_{flavors} \mathrm{d}x_1 \mathrm{d}x_2\ f_{\mathrm{PDF}}(x_1)\ f_{\mathrm{PDF}}(x_2)\ \mathrm{d}\sigma_{2\to n}\ . \tag{5.6}$$

As any real detector leads to finite energy resolutions for the measured particles, the energy of the final state partons is also not known precisely. The function relating the true energy of an incident parton to its measured energy is known as *detector response* or *transfer function*. It gives the probability density of a certain partonic state y_{parton} to be measured as y_{evt}. In our case, the observed energy does not refer to the energy deposit in the detector alone but to the reconstructed energy with all corrections applied, e.g. jet energy scale corrections (see Sec. 3.5.5). According to that, the differential cross section (5.6) leading to a certain final state y_{parton} needs to be convoluted with a transfer function $W(y_{parton}, y_{evt})$ to give the differential cross section for observing a given reconstructed event y_{evt}:

$$\mathrm{d}\sigma^{hc}_{2\to n}(y_{evt}) = \int\limits_{y_{parton}} \mathrm{d}\sigma^{hc}_{2\to n}(y_{parton})\, W(y_{evt}, y_{parton})\ . \tag{5.7}$$

A description of transfer functions and their determination for this analysis is given in Sec. 5.2. In general, the transfer functions themselves can depend on the parameters to be fitted, $W(y_{evt}, y_{parton}; s_1, \ldots, s_m)$.

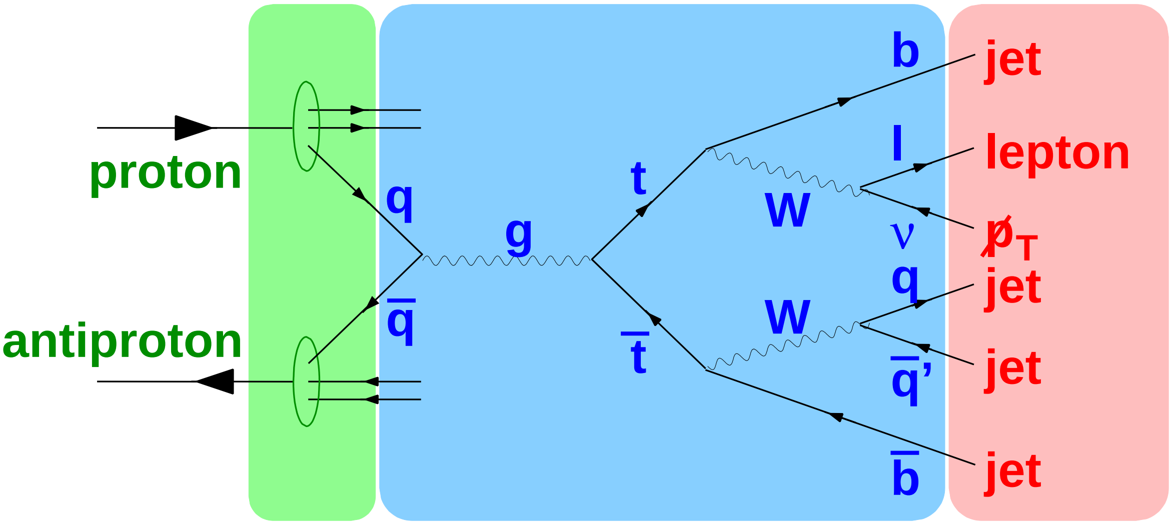

Figure 5.1: Schematic overview of the signal probability evaluation. *green:* The initial state consisting of the colliding proton and anti-proton, of which two constituent quarks take part in the reaction. This part is described by the **Parton Density Functions**. *blue:* The hard scattering interaction leading to a partonic final state with 2 b quarks, 2 light quarks, a lepton and a neutrino. The tree level process is encoded in the **matrix element**. *red:* The measured event in the detector consisting of four jets, a lepton and $\not{E}_t$. The transition from the partonic final state to the reconstructed objects is given by the **transfer functions**.

In order to properly normalize the sample likelihood this differential cross section must be divided by the total *observable* cross section $\sigma^{obs}_{2\to n}$, i.e. the production cross section within the acceptance. Due to both the intrinsic geometrical detector acceptance and the applied selection cuts, this is smaller than the theoretically predicted cross section for the process under consideration:

$$\sigma^{obs}_{2\to n} = \int_{y_{evt}} dy_{evt} \int_{y_{parton}} d\sigma^{hc}_{2\to n}(y_{parton})\; W(y_{evt}, y_{parton})\; f_{acc}(y_{evt})\;, \tag{5.8}$$

where $f_{acc}(y_{evt}) = 1$ for selected events and $f_{acc}(y_{evt}) = 0$ otherwise.

Bringing all bits and pieces together we finally arrive at the likelihood for observing an event of a certain process, e.g. $t\bar{t}$ production, as y_{evt} in the detector under the assumption of certain values of the observables s_i to be fitted:

$$\begin{aligned}
&\mathscr{L}(y_{evt}; s_1, \ldots, s_m) \\
&= \frac{d\sigma_{2\to n}(y_{evt}; s_1, \ldots, s_m)}{\sigma^{obs}_{2\to n}(s_1, \ldots, s_m)} \qquad\qquad (5.9) \\
&= \frac{1}{\sigma^{obs}_{2\to n}} \int_{x_1, x_2} \sum_{flavors} dx_1 dx_2\, f_{PDF}(x_1)\, f_{PDF}(x_2) \int_{y_{parton}} d\sigma^{hc}_{2\to n}(y_{evt}; s_1, \ldots, s_m)\;\; W(y_{evt}, y_{parton})\;.
\end{aligned}$$

Figure 5.1 depicts a schematic representation of the different parts in the above equation. How these likelihoods are evaluated for signal and background processes and which observables are included in the fitting procedure will be discussed in Sec. 5.3-5.4 and Sec. 5.7.

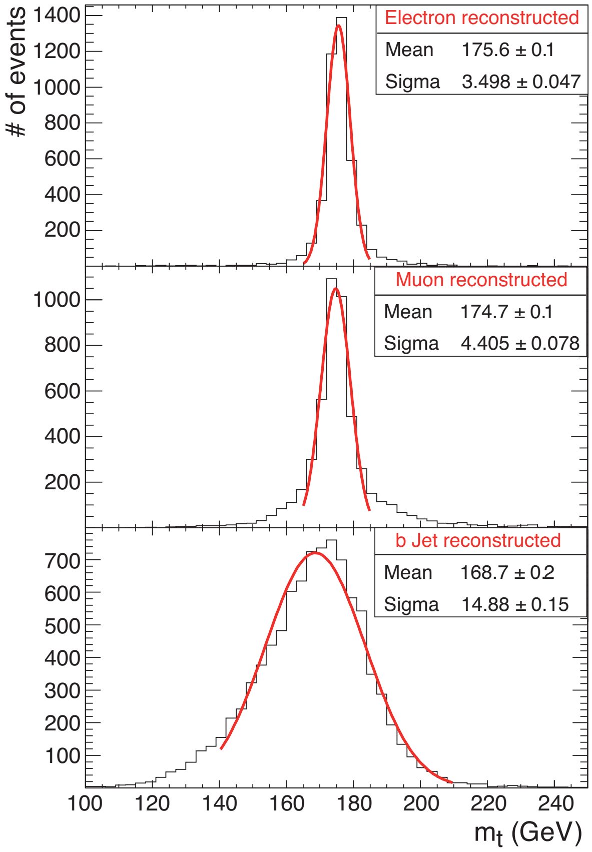

Figure 5.2: Top mass resolution with *top:* electron reconstructed, *middle:* muon reconstructed, *bottom:* *b* jet reconstructed.

5.2 Transfer Functions

The matrix element method likelihood procedure only yields a trustworthy error estimate if the finite object resolutions are accurately described. In this section it will be shown which transfer functions need to be considered and how they are determined by means of Monte Carlo events. As described above, the transfer functions $W(y_{evt}, y_{parton})$ yield the normalized likelihood for a parton with kinematics y_{parton} to be reconstructed with kinematics y_{evt}:

$$\mathrm{d}P = W(y_{evt}, y_{parton}; s_0, \ldots, s_m) \tag{5.10}$$

$$\text{normalized as:} \quad \int \mathrm{d}P = \int_{y_{evt}} \mathrm{d}y_{evt}\, W(y_{evt}, y_{parton}; s_0, \ldots, s_m) \equiv 1\,. \tag{5.11}$$

In the above normalization it is assumed that any partonic final-state leads to some measured event y_{evt} (cf. Sec. 5.5).

In order to judge which transfer functions must necessarily be incorporated into the analysis and which ones are negligible, one can study the impact of the different decay products on the top mass

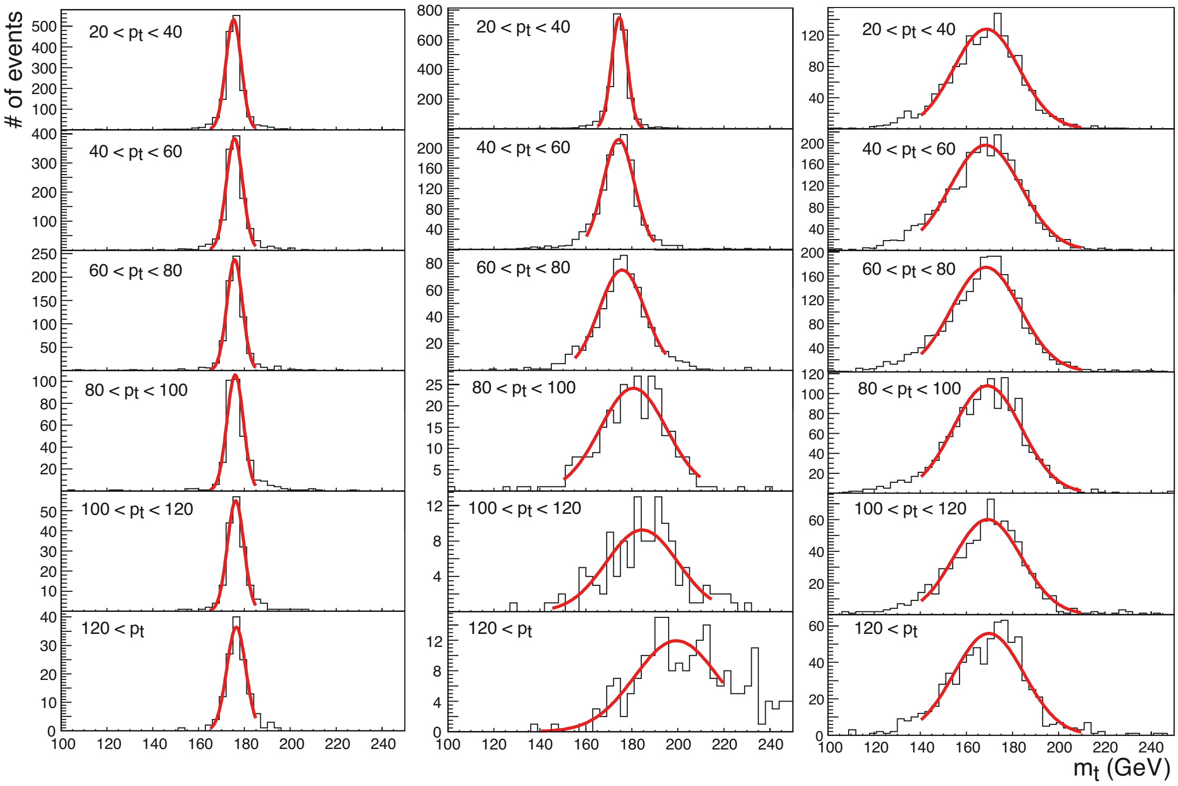

Figure 5.3: Top mass resolution for several energy intervals with *left:* electron reconstructed, *middle:* muon reconstructed, *right:* b jet reconstructed.

resolution. This is done by means of $t\bar{t}$ Monte Carlo events decaying semileptonically in order to have access to the generated energy of the final state partons. In the leptonic decay branch, the four-momentum q_t of the top quark is the sum of the four-momenta of the decay products b, ν and l:

$$q_t = q_b + q_\nu + q_l, \tag{5.12}$$

where b denotes the b quark (b jet), ν the neutrino ($\not{E}_t$) and l the lepton (μ or e). The top quark mass can be deduced from its four-momentum. In order to reveal the effect on the mass resolution of one decay product individually, the generated four-momenta of two decay products and the reconstructed four-momentum of the one under consideration are used. In Figure 5.2 the results are shown for reconstructed electrons, muons and b jets. As expected from the known detector resolutions (cf. Chapter 3), the jet reconstruction widens the top mass peak most significantly. The electron and muon resolutions are nearly a factor of 4.6 and 2.7 better, respectively.

For evaluating the importance of a certain resolution not only the average behavior is important but the energy dependence needs to be considered as well. This is done by dividing the sample into subsamples of certain energy ranges of the generated particles. The results can be seen in Fig. 5.3. The plots show that the energy dependence of the muon resolution is much stronger than for electrons and jets and becomes comparable to jet resolutions above 100 GeV. This is due to the fact that electron and jet energies are reconstructed from calorimeter energies, whose resolution improves with higher energies (cf. Sec. 2.2.3) due to the decreasing importance of noise contributions and stochastic fluctuations in the showering process. For muons, whose momenta are mainly measured in the tracking system the trend is reversed (see Sec. 2.2.2). The momentum measurement is based on the curvature of tracks in the solenoidal field. Although the absolute error on the curvature is constant, its relative importance increases with straighter tracks, i.e. more energetic particles, since a small absolute error on the track curvature leads to large uncertainties on the muon momentum.

As jets have by far the worst resolutions their inclusion into the probability calculation by transfer functions is most important. In early top mass measurements the finite resolutions of electrons and muons were neglected and they were assumed to be ”perfectly” measured compared to jets. From the energy dependence of the resolutions it becomes clear that this assumption for muons only holds at low energies. Therefore, muon transfer functions were developed and included in the latest measurements with the matrix element method. Studies with electron transfer functions were also performed but no significant improvement could be achieved [92]. Thus, it was decided to keep the assumption of perfectly measured electron energies and save the computation time that would be needed for another integration over the electron energy.

In principle, transfer functions should consider all aspects of particle detection, i.e. energy resolutions, directions and particle identification. Due to limited computing resources, in practice all particle directions are assumed to be identical to the measured ones. This is a good assumption because small effects on the top mass arising from this approximation are corrected for in the calibration with fully simulated Monte Carlo events. An example how to account for particle identification in the case of *b* jets is given in Section 5.6. For all other measured particles, the probability to have arisen from the corresponding final state particle is supposed to be 1. It is assumed that all transfer functions factorize into contributions from each measured final state particle and hence can be treated separately. In the following two sections the determination of jet and muon transfer functions will be described with emphasis on the latter as they were developed most recently [93]. For both cases, `PYTHIA` [94] Monte Carlo samples were used due to their larger available statistics compared to `ALPGEN` [95] samples at the time of these studies.

5.2.1 Jet Transfer Functions

For describing jet resolutions a double gaussian as a function of the energy difference $\Delta E = E_{jet} - E_{parton}$ between the parton and the jet energies is used, with parameters depending linearly on the parton energy:

$$W(\Delta E) = \frac{1}{\sqrt{2\pi}(p_2 + p_3 p_5)} \left[\exp\left(-\frac{(\Delta E - p_1)^2}{2p_2^2} \right) + p_3 \exp\left(-\frac{(\Delta E - p_4)^2}{2p_5^2} \right) \right] \tag{5.13}$$

$$p_i = a_i + b_i \cdot E_{\text{parton}} \tag{5.14}$$

Different transfer functions are derived for four η_{det} ranges:

$$\begin{aligned} |\eta_{det}| &< 0.5 \\ 0.5 < |\eta_{det}| &< 1.0 \\ 1.0 < |\eta_{det}| &< 1.5 \\ 1.5 < |\eta_{det}| &< 2.5 \end{aligned}$$

and three different jet types:

light partons	$(u, d, s, c$ and $g)$
b-quarks	without soft muon tag
b-quarks	with soft muon tag

leading to 120 parameters describing the jet transfer functions. The soft muon tag is used as indication for a semimuonic b or c decay. The corresponding transfer function accounts on average for the energy carried away by the unreconstructed neutrino. Semielectronic decays are not treated explicitly as it is much more complicated to identify an electron lying in or near a jet. This is because both objects are reconstructed in the calorimeter and, in contrast to the muon system, no external trigger identification is available. These decays are corrected for on average in the generic b transfer function.

Studies on `PYTHIA` $t\bar{t}$ Monte Carlo have shown [96] that jet masses are an important issue in the reconstruction of masses. If one assumes perfectly measured transfer functions, these would correct all jet energies back to the parton level. However, if one uses only Monte Carlo events where all jets could be matched to a generated parton and replaces the jet energies by the parton energies to see what is the best one can achieve, one obtains the di-jet invariant mass distribution shown in Fig. 5.4, left. As one can see, the reconstructed W mass is shifted by more than 1 GeV. This effect can be explained by parton showering in the Monte Carlo due to final state radiation. If for instance the b quark from the top decay radiates gluons, the resulting parton shower will have a mass which is significantly different from the original mass of the parton (e.g. $\approx$ 15 GeV instead of 4.75 GeV). Due to this, the energy and direction of the b shower will no longer be identical to that of the b quark it started from. As a result of energy and momentum conservation of the parent top, this is also true for the W, which ”recoils” against the b shower. The same explanation holds for the two quarks from the W decay shown in Fig. 5.4. Therefore, in contrast to former analyses, the transfer functions are derived in such a way that they correct the jets back to the parton shower level, not to the parton level. This means the reconstructed jet masses are assumed to be correct and are used instead of the parton masses in the matrix element (cf. Equations (5.23-5.25)). With this change applied, the di-jet invariant mass distribution looks like in Fig. 5.4, right. It can be seen that the W mass is much more accurately reconstructed than it was using parton masses.

The jet transfer functions used in this analysis are derived on fully simulated `PYTHIA` events. Nine samples with top masses ranging from 155 GeV to 195 GeV in 5 GeV steps are included in the fit. The events are selected according to the preselection described in Sec. 6.1. This implies that all events containing at least one good jet are included in the transfer function determination. As the momentum cut for good jets is 15 GeV compared to 20 GeV in the final selection, this requirement assures a smooth behavior of the jet transfer functions below the final jet momentum cut. The jet and parton

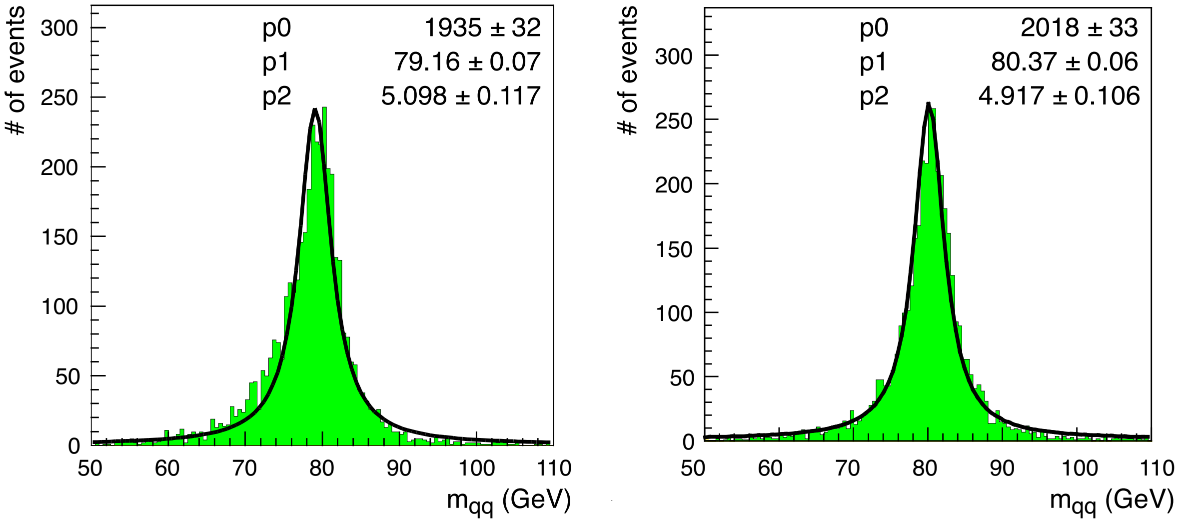

Figure 5.4: Di-jet invariant mass distributions for the two quarks of the W decay for jet-parton matched events. Left: generated parton energies and quark masses used. Right: generated parton energies and reconstructed jet masses used.

energies of all jets in the Monte Carlo sample are fed into an unbinned likelihood fit, minimizing the product of $W(\Delta E)$ for all jets in a certain event with respect to a_i and b_i. The parameters obtained for the four η_{det} regions and three jet flavors listed above can be found in in Tbl. 5.1. Plots of the jet transfer functions as a function of E_{jet} for different input values of E_{parton} are shown in Fig. 5.5.

In general, the jet transfer functions can depend on all observables that should be fitted in the mass measurement. The dependence on the top mass is due to changes in the event topology leading to a varying angular separation of the jets. However, this effect is small [81] and can be dealt with in the calibration with fully simulated events at different generated top masses. In contrast, the dependence on jet parameters such as (b-) jet energy scaling factors is much larger and needs to be accounted for properly in the transfer functions. In this analysis, the scaling factors s_{jes} and s_{bjes} are chosen to be independent for technical reasons. The parameter s_{jes} is only applicable to light partons, s_{bjes} only to b quarks. Thus, the light transfer function depends on s_{jes} in the following way:

$$W_{light}(\Delta E, s_{jes}) = \frac{W(\frac{E_{jet}}{s_{jes}} - E_{parton})}{s_{jes}} \tag{5.15}$$

and the b transfer function is defined analogously as:

$$W_b(\Delta E, s_{bjes}) = \frac{W(\frac{E_{jet}}{s_{bjes}} - E_{parton})}{s_{bjes}} . \tag{5.16}$$

The transfer functions depend on the scaling factors as these are on top of the nominal D0 jet energy scale and change the energy difference ΔE between parton and jet energies. Additionally, the normalization of the transfer functions is s_{jes} and s_{bjes} dependent as well. This is due to the fact that, according to Eqn. (5.11), any partonic final state leads to a measurable event. Since jet selection cuts

	$0.0 \leq \lvert\eta_{det}\rvert < 0.5$		$0.5 \leq \lvert\eta_{det}\rvert < 1.0$		$1.0 \leq \lvert\eta_{det}\rvert < 1.5$		$1.5 \leq \lvert\eta_{det}\rvert < 2.5$	
	a_i	b_i	a_i	b_i	a_i	b_i	a_i	b_i
p_1	-1.51×10^{0}	-7.54×10^{-3}	4.18×10^{-1}	-3.42×10^{-2}	7.91×10^{0}	-2.13×10^{-1}	1.55×10^{1}	-2.26×10^{-1}
p_2	3.78×10^{0}	1.09×10^{-1}	3.20×10^{0}	1.40×10^{-1}	2.93×10^{0}	1.35×10^{-1}	3.90×10^{0}	1.39×10^{-1}
p_3	0.00×10^{0}	3.64×10^{-4}	0.00×10^{0}	3.55×10^{-4}	0.00×10^{0}	7.34×10^{-3}	0.00×10^{0}	3.60×10^{-3}
p_4	2.34×10^{1}	-2.29×10^{-1}	2.47×10^{1}	-1.46×10^{-1}	7.90×10^{0}	1.93×10^{-2}	2.25×10^{1}	-4.63×10^{-2}
p_5	1.89×10^{1}	1.34×10^{-1}	1.91×10^{1}	1.21×10^{-1}	1.10×10^{1}	8.19×10^{-2}	1.68×10^{1}	7.45×10^{-2}

(a) Light quarks.

	$0.0 \leq \lvert\eta_{det}\rvert < 0.5$		$0.5 \leq \lvert\eta_{det}\rvert < 1.0$		$1.0 \leq \lvert\eta_{det}\rvert < 1.5$		$1.5 \leq \lvert\eta_{det}\rvert < 2.5$	
	a_i	b_i	a_i	b_i	a_i	b_i	a_i	b_i
p_1	-6.91×10^{0}	6.47×10^{-3}	-4.60×10^{0}	-4.68×10^{-2}	2.75×10^{0}	-2.24×10^{-1}	8.00×10^{0}	-2.18×10^{-1}
p_2	4.41×10^{0}	9.84×10^{-2}	3.26×10^{0}	1.41×10^{-1}	3.33×10^{0}	1.32×10^{-1}	2.77×10^{0}	1.57×10^{-1}
p_3	0.00×10^{0}	1.23×10^{-3}	0.00×10^{0}	1.57×10^{-3}	0.00×10^{0}	7.62×10^{-3}	0.00×10^{0}	3.28×10^{-3}
p_4	9.24×10^{0}	-2.96×10^{-1}	-3.29×10^{0}	-3.69×10^{-2}	-4.70×10^{-1}	-3.92×10^{-3}	1.24×10^{1}	-3.38×10^{-2}
p_5	1.69×10^{1}	8.43×10^{-2}	1.70×10^{1}	4.23×10^{-2}	1.10×10^{1}	9.95×10^{-2}	1.78×10^{1}	7.40×10^{-2}

(b) *b* quarks.

	$0.0 \leq \lvert\eta_{det}\rvert < 0.5$		$0.5 \leq \lvert\eta_{det}\rvert < 1.0$		$1.0 \leq \lvert\eta_{det}\rvert < 1.5$		$1.5 \leq \lvert\eta_{det}\rvert < 2.5$	
	a_i	b_i	a_i	b_i	a_i	b_i	a_i	b_i
p_1	5.87×10^{0}	-1.35×10^{-1}	7.46×10^{0}	-1.50×10^{-1}	1.01×10^{1}	-1.68×10^{-1}	2.31×10^{1}	-3.12×10^{-1}
p_2	2.18×10^{0}	1.59×10^{-1}	2.57×10^{0}	1.62×10^{-1}	3.67×10^{0}	1.57×10^{-1}	1.09×10^{1}	8.91×10^{-2}
p_3	0.00×10^{0}	8.09×10^{-5}	0.00×10^{0}	1.56×10^{-4}	0.00×10^{0}	1.85×10^{-4}	0.00×10^{0}	2.18×10^{-3}
p_4	4.32×10^{1}	1.74×10^{-1}	3.03×10^{1}	1.58×10^{-1}	3.72×10^{1}	1.82×10^{-1}	2.67×10^{1}	-5.67×10^{-2}
p_5	1.92×10^{1}	-1.26×10^{-1}	2.00×10^{1}	-5.39×10^{-2}	1.95×10^{1}	-6.95×10^{-2}	2.24×10^{1}	1.24×10^{-2}

(c) *b* quarks with soft muon tag.

Table 5.1: Jet transfer function parameters derived for the three jet types considered in four η_{det} ranges.

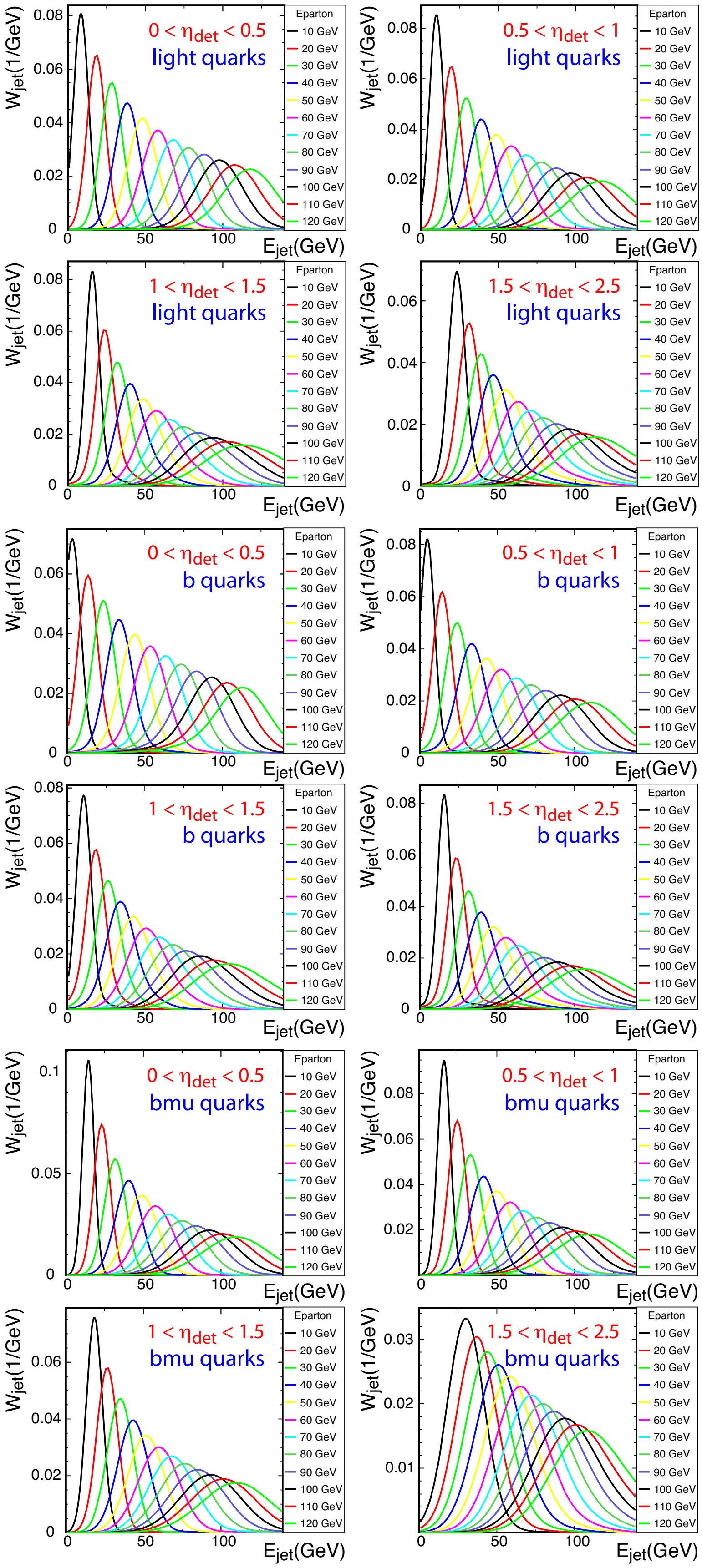

Figure 5.5: Jet transfer functions for the three jet flavors in four η_{det} regions.

x_{cut} are applied to reconstructed events, this leads to the following normalization:

$$\int \mathrm{d}P = \int\limits_{y_{evt}>y_{cut}} \mathrm{d}y_{evt} W(\Delta E; s_{jes}, s_{bjes}) = 1\ . \tag{5.17}$$

As the transfer functions are factorizable into individual components from each final state particle, Eqns. 5.15 and 5.16 are used respectively for each particular jet depending on the jet-parton assignment under consideration.

5.2.2 Muon Transfer Functions

The muon transfer function gives the probability density to reconstruct a certain muon momentum $p_{t,evt}$ for a given muon momentum in the final state of the top decay $p_{t,fs}$. The resolution is parameterized in terms of the muon charge q divided by its transverse momentum p_t:

$$\Delta\left(\frac{q}{p_t}\right) = \left(\frac{q}{p_t}\right)_{evt} - \left(\frac{q}{p_t}\right)_{fs} \tag{5.18}$$

This is chosen because the resolution in the tracking detector depends on the track curvature in the magnetic field, which is proportional to q/p_t. The inclusion of the muon charges takes charge misidentification, whose probability increases at larger momenta, properly into account.

To obtain an appropriate muon sample, the same selection cuts as in the top mass measurement are used. A transverse momentum $p_t \geq 20\,\mathrm{GeV}$ is required, corresponding to $1/p_t \leq 0.05\,\mathrm{GeV}^{-1}$. The pseudorapidity cut is $|\,\eta\,| \leq 2.0$. The distance between the generated and reconstructed muon track should be small in order to obtain matching tracks. A value of $\Delta R \leq 0.005$ is required, where ΔR denotes (cf. Eqn. 2.3):

$$\begin{aligned} \Delta R &= \sqrt{(\Delta\varphi)^2 + (\Delta\eta)^2} \\ \text{with} \quad \Delta\varphi &= \varphi(\mu_{evt}) - \varphi(\mu_{fs}) \\ \text{and} \quad \Delta\eta &= \eta(\mu_{evt}) - \eta(\mu_{fs})\ . \end{aligned} \tag{5.19}$$

Different cut values of ΔR were studied and no bias depending on this choice was found.

An important step is to map corresponding generated and reconstructed muons. This is done on a one-to-one basis using their topological information. For every generated muon the reconstructed muon with the closest track is chosen. Afterwards for every reconstructed muon the closest generated one is searched for. The muon is selected only if this mapping is unambiguous. In contrast to the mass measurement more than one muon is allowed in a single event if the above selection requirements are fulfilled to enhance statistics. For the same reason not only $t\bar{t}$ Monte Carlo samples generated at different top masses are used but other samples such as $Z \rightarrow \mu\mu$ leading to muonic final states are included as well. To study potential biases, transfer function parameters for samples with and without top quarks were derived separately and compared. Within statistical uncertainties no significant effect was found.

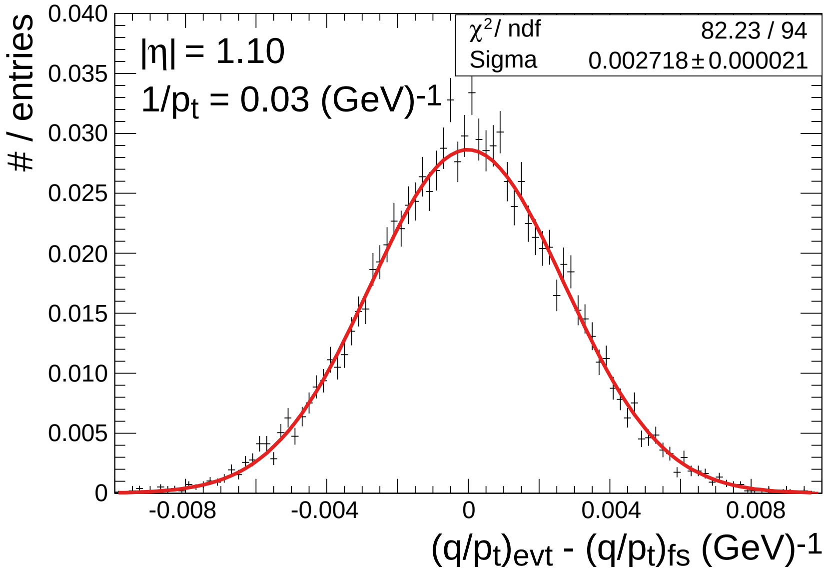

Figure 5.6: Muon resolution fitted by a gaussian for $1.0 \leq |\eta_{evt}| \leq 1.2$ and $0.025 \leq (1/p_t)_{evt} \leq 0.030\ \text{GeV}^{-1}$.

The muon transfer function is parameterized by a single Gaussian:

$$W_\mu\left(\left(\frac{q}{p_t}\right)_{fs}, \left(\frac{q}{p_t}\right)_{evt}, \eta_{evt}\right) = \frac{1}{\sqrt{2\pi}\,\sigma_\mu}\exp\left(-\frac{1}{2}\left(\frac{(q/p_t)_{evt} - (q/p_t)_{fs}}{\sigma_\mu}\right)^2\right), \tag{5.20}$$

with the muon resolution σ_μ depending on the measured η_{evt} and $(1/p_t)_{evt}$. The full Monte Carlo sample is divided into 10×10 bins of these two parameters and a Gaussian is fitted to each distribution. Figure 5.6 shows an example. To stabilize the fits of the η_{evt} and $(1/p_t)_{evt}$-dependencies a cut is introduced on the number of events per bin. If less than 10 events are within a certain bin, the bin is excluded from further fitting.

In Figure 5.7 the Gaussian widths for each of the bins are shown in dependence of η_{evt} and $(1/p_t)_{evt}$. One observes that the muon resolution is almost constant in the whole $(1/p_t)_{evt}$-range. The main dependence lies in a strong rise above $\eta_{evt} \geq 1.4$. At smaller pseudorapidity values the resolution is constant as well. This strong η dependence can be explained by the tracking detector geometry. Above a certain pseudorapidity value the tracks can no longer produce hits in all detector layers. Hence, the resolution degrades. The muon resolution is therefore parametrized by a transfer function with a constant value σ_0 beneath a threshold η_0 and above this is given by the quadratic sum of the constant σ_0 and a straight line with slope c (cf. Fig. 5.8):

$$\sigma_\mu = \begin{cases} \sigma_0 & \text{for } |\eta_{det}| \leq \eta_0 \\ \sqrt{\sigma_0^2 + [c \cdot (|\eta_{det}| - \eta_0)]^2} & \text{for } |\eta_{det}| > \eta_0 \end{cases}. \tag{5.21}$$

Due to the effect caused by the tracking detector geometry it is important to use the pseudorapidity in the (tracking) detector coordinate system η_{det} for the parameterization and evaluation of the muon

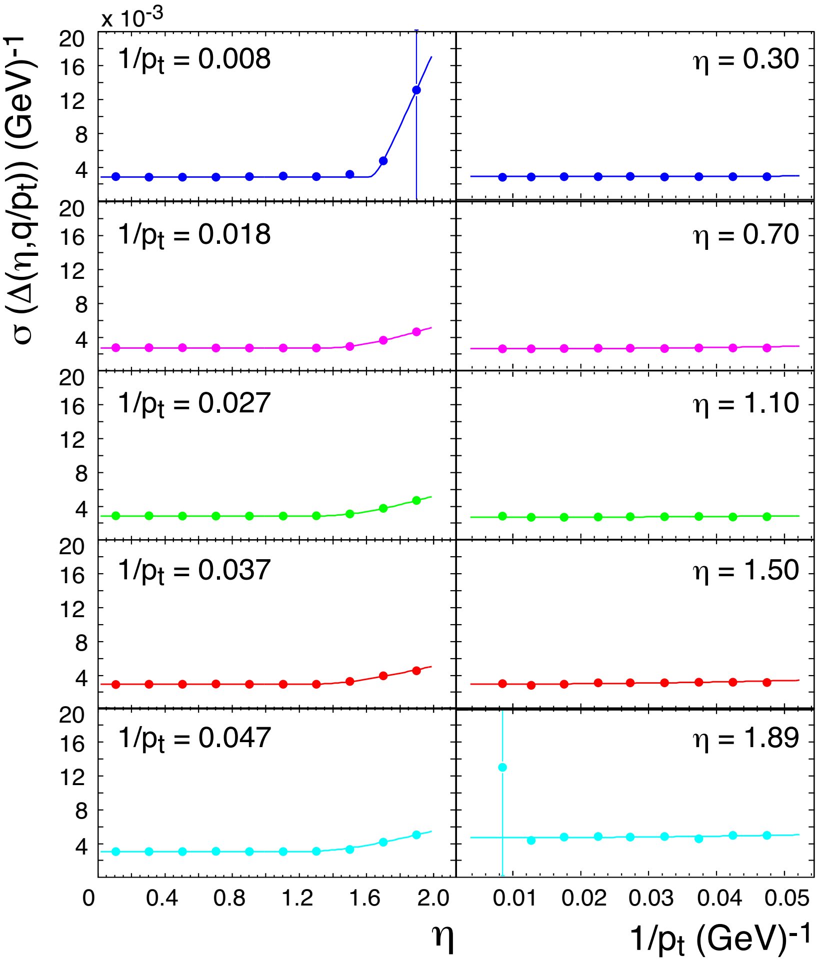

Figure 5.7: Muon resolution dependence on η_{evt} and $(1/p_t)_{evt}$ for muons including SMT hits in the post-shutdown period.

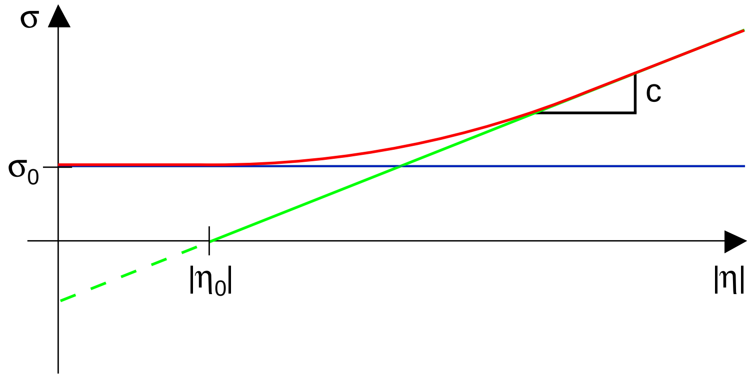

Figure 5.8: Schematic of muon transfer function described by the quadratic sum of a constant and a straight line.

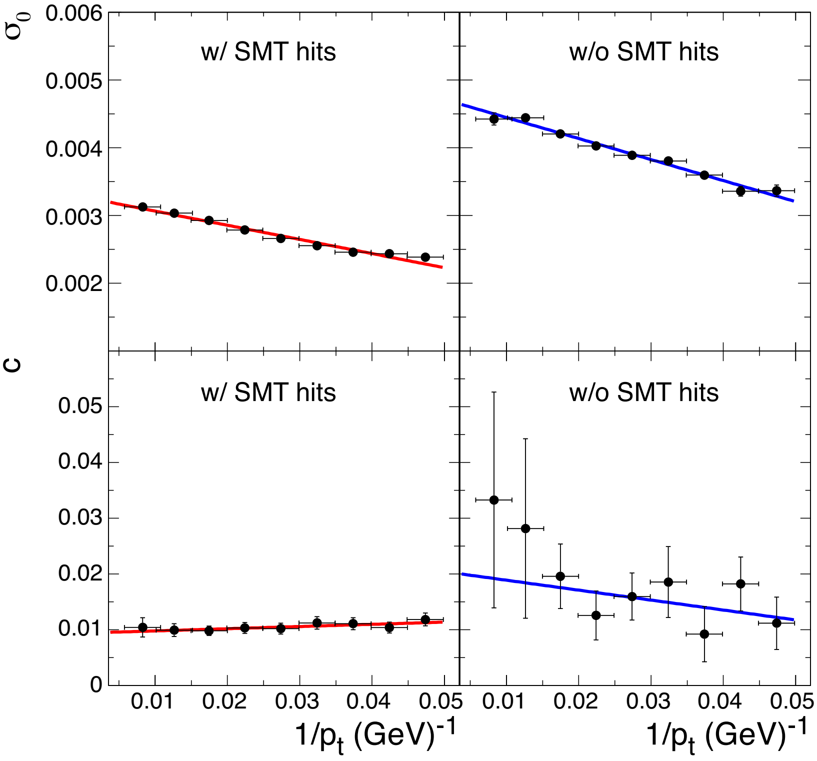

Figure 5.9: Dependence of the σ_0 and c parameters on $(1/p_t)_{evt}$ for the post-shutdown period. *Left*: Muons without SMT hits. *Right*: Muons with SMT hits.

transfer function. The threshold η_0 is fixed to a value of 1.4, corresponding to the region where the muon track resolution becomes worse due to CFT detector fringe effects. As the parameters η_0 and c are correlated, the fit otherwise is unstable and leads to unphysical values for η_0 instead of varying the slope c.

To allow for a weak $1/p_t$-dependence of the muon transfer function, the two free parameters σ_0 and c are permitted to vary with $(1/p_t)_{evt}$ and are fitted by a straight line (see Fig. 5.9). Equation (5.21) is extended as follows (with $x_i \in \{\sigma_0, c\}$):

$$x_i = a_i + b_i \cdot \left(\frac{1}{p_t}\right)_{evt} . \qquad (5.22)$$

As described in Sec. 2.2.2, the D0 tracking system consists of a silicon microstrip tracker (SMT) surrounded by a central fiber tracker (CFT). Since the simulation incorporates an idealized geometry of the tracking system and some of the dead material is not fully implemented, the Monte Carlo is tuned to describe the data by smearing the transverse muon momentum. For the muon identification only a CFT track is required and therefore about 10% of the muons in the samples lack SMT hits. As these muon tracks do not contain inner hits the track curvature and thus the track p_t is less precisely known. Therefore, the resolution is worse than for muon tracks incorporating SMT hits. To improve their resolution, the muons without SMT hits are constrained to come from the primary vertex and the p_t is corrected accordingly. The smearing on Monte Carlo is performed for all muons regardless of SMT hits and it is carried out after applying the primary vertex constraint for muons without inner hits. The influence of the smearing (*smear*) and primary vertex constraint (*pvtx*) for muons with and without SMT hits was studied and the results are shown in Fig. 5.10. It is apparent that the primary vertex constraint improves the resolution of muons without SMT hits by a factor of three whereas it has much less influence ($\approx$ 5%) on muons with SMT hits. The smearing corrects the intrinsic Monte Carlo resolution by about 40%. Due to the strong influence of the presence or absence of SMT hits, separate transfer functions are determined for the two subsamples and applied to the corresponding muons.

Another non-negligible effect on the muon resolution is seen in two different run periods. Following a shutdown in fall 2004 the muon resolution degraded by $\approx$ 15%. This was partly due to a reduction in the magnetic field. The resolutions before and after the shutdown are shown in Fig. 5.11. For this reason, transfer function parameter sets are derived for each run period and referred to as *pre-* and *post-shutdown* throughout the rest of this document. In order to take this effect properly into account all muon samples need to be divided into subsamples according to the two run periods and have to be treated separately.

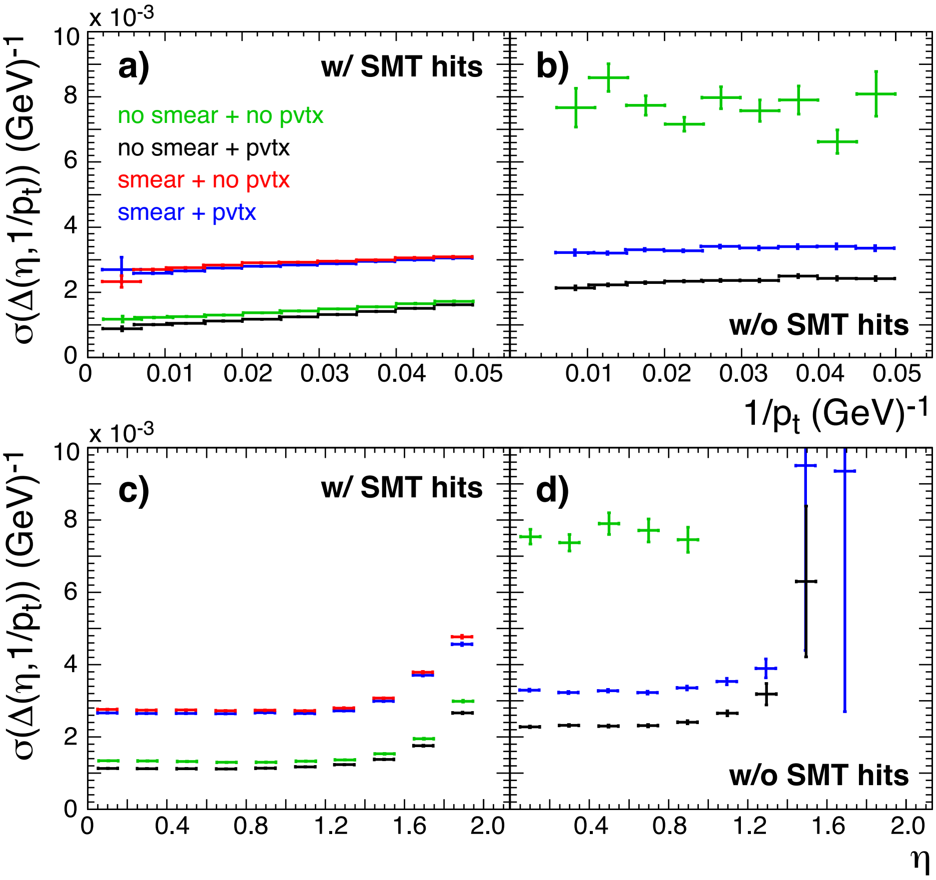

Figure 5.10: Muon resolution vs. $1/p_t$ (a, b) and η (c, d) with and without SMT hits (smear = MC smearing, pvtx = primary vertex constraint).

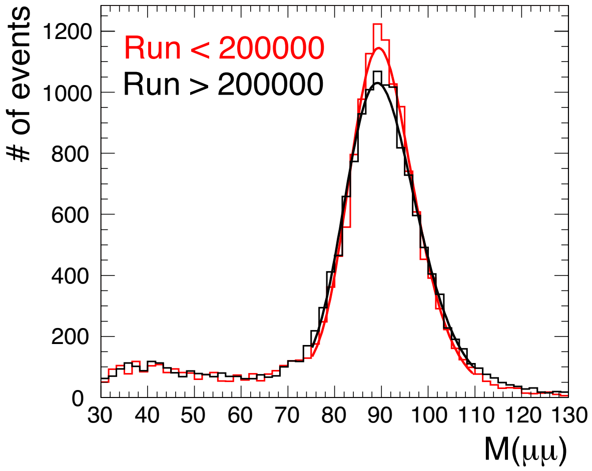

Figure 5.11: Comparison of the muon resolution for pre- and post-shutdown data, separated by run number 200 000.

In total there are 20 parameters specifying the muon transfer functions for muons with and without SMT hits, before and after the 2004 shutdown. They can be found in Table 5.2.

	$N_{SMT} > 0$		$N_{SMT} = 0$	
Parameter	pre	post	pre	post
σ_0, a	3.16e-03	3.27e-03	5.23e-03	4.76e-03
σ_0, b	-2.77e-02	-2.09e-02	-5.27e-02	-3.11e-02
c, a	4.24e-03	9.40e-03	2.04e-02	2.07e-02
c, b	1.38e-01	3.87e-02	-1.73e-01	-1.78e-01
η_0	1.4	1.4	1.4	1.4

Table 5.2: Muon transfer function parameters for muons with and without SMT hits in the pre -and post shutdown run periods.

5.3 Topological Signal Likelihood

The topological signal likelihood is calculated according to Eqn. (5.9) with the differential cross section obtained from the matrix element for $t\bar{t}$ production. Although $t\bar{t}$ pairs can be produced either via quark-antiquark annihilation or gluon-gluon fusion, the latter production mechanism is neglected in (most) top mass measurements at the Tevatron. This is justified, as it contributes only 10% of the top pairs and most of the top mass information resides in the decay parts of the matrix element, which are the same for both production mechanisms. For the evaluation of the differential cross section Eqn. (5.4), correlations between the top and antitop quarks are neglected and a leading order matrix element for $q\bar{q} \to t\bar{t}$ is used [97]:

$$|\mathscr{M}_{q\bar{q}\to t\bar{t}}|^2 = \frac{g_s^4}{9} F\overline{F} \left(2 - \beta^2 s_{qt}^2\right) \ . \tag{5.23}$$

Here, $g_s^2/(4\pi) = \alpha_s$ denotes the strong coupling constant, β is the velocity of the top quarks in the $t\bar{t}$ rest frame, and s_{qt} stands for the sine of the angle between the incoming parton and the outgoing top quark in the $t\bar{t}$ rest frame. The factors F and $\overline{F}$ incorporate the kinematics of the top and antitop decays. If one chooses an event, in which the top quark decay products include a leptonically decaying W boson, while the antitop decay includes a hadronically decaying W, they are given by:

$$F = \frac{g_w^4}{4} \left(\frac{m_{bl\nu}^2 - m_{l\nu}^2}{\left(m_{bl\nu}^2 - m_t^2\right)^2 + (m_t\Gamma_t)^2} \right) \left(\frac{m_{bl\nu}^2 \left(1 - \hat{c}_{bl}^2\right) + m_{l\nu}^2 \left(1 + \hat{c}_{bl}\right)^2}{\left(m_{l\nu}^2 - m_W^2\right)^2 + (m_W\Gamma_W)^2} \right) , \tag{5.24}$$

$$\overline{F} = \frac{g_w^4}{4} \left(\frac{m_{\bar{b}d\bar{u}}^2 - m_{d\bar{u}}^2}{\left(m_{\bar{b}d\bar{u}}^2 - m_t^2\right)^2 + (m_t\Gamma_t)^2} \right) \left(\frac{m_{\bar{b}d\bar{u}}^2 \left(1 - \hat{c}_{\bar{b}d}^2\right) + m_{d\bar{u}}^2 (1 + \hat{c}_{\bar{b}d})^2}{\left(m_{d\bar{u}}^2 - m_W^2\right)^2 + (m_W\Gamma_W)^2} \right) , \tag{5.25}$$

where g_w denotes the weak charge ($G_{\mathrm{F}}/\sqrt{2} = g_w^2/8m_W^2$), m_t and m_W are the masses of the top quark and the W boson, respectively, and Γ_t and Γ_W are their corresponding decay widths. Invariant top and W masses in a particular event are denoted by m_{xyz} and m_{yz}, respectively, where x, y, and z are their decay products. The cosine of the angle between particles x and y in the W rest frame is denoted by $\hat{c}_{xy}$. Here and in the following, d and $\bar{u}$ denote down-type and up-type quarks, respectively, and stand as placeholders for all possible hadronic W decay products (i.e. u, d, c, s and b quarks).

For the reverse case, in which the top quark decay products include a hadronically decaying W, and the antitop decay the leptonically decaying one, the following substitutions need to be applied to Eqns. (5.24, 5.25):

$$b \leftrightarrow \bar{b} \qquad\qquad l \leftrightarrow d \qquad\qquad \nu \leftrightarrow \bar{u} \, . \tag{5.26}$$

The correct assignment of reconstructed jets to the final state quarks is not known. Thus, all 24 possible jet-parton assignments need to be taken into account. Eqn. (5.9) is evaluated for each combination and the signal likelihood is given by the sum of all permutations. An overview of these jet-parton assignments (in the order used in this analysis) is given in Fig. 5.18. The jet transfer functions are evaluated according to this assignment as well. In former analyses [98], a symmetrized matrix element was used which reduced the number of permutations to 12. It combined analytically the two solutions where the quarks from the hadronically decaying W are interchanged. Due to the use of b identification in this analysis as described in Sec. 5.6, this conversion is no longer applicable, since the W decay products contain c (and a very small fraction of b) quarks and it is therefore important to know which jet was assigned to which of these quarks.

As mentioned before, besides the top mass, a jet energy scaling factor s_{jes} and a b jet energy scaling factor s_{bjes} shall be measured in a 3-dimensional fit. The dependence of the topological likelihood on the assumed top mass can be seen in Eqns. (5.24, 5.25), directly. For the other two observables the influences are not as obvious. The JES scaling factor is constrained by the nominal mass of the W boson which is incorporated in the matrix element. Thus, configurations in which the light quarks from the hadronic decay yield too high or too low invariant W masses result in lower likelihood values. Over many events, the scaling factor which must be applied to obtain the nominal W mass can be deduced. The more events used, the better the estimate. Therefore, the JES uncertainty is not systematically but statistically limited. The s_{jes} factor as given in Eqn. (5.15) is constructed such that a factor of 1.1 means that the D0 jet energy scale overestimates the jet energies by 10% and they need to be scaled down by this factor. On the other hand a factor of 0.9 indicates an underestimation of the jet energy scale by 10%.

For the constraint of the observable s_{bjes} not only the hadronic W decay but the full event kinematics need to be taken into account. If both the (light) jet energy scale and b jet energy scale were known precisely, the event would be balanced in the $q\overline{q}$ rest frame and the two top masses from the top and antitop decay would be approximately equal (despite the intrinsic top mass resolution). If the b jet energy scale is not perfectly corrected for, the b jets are reconstructed with too high or too low momenta and the balance is disturbed. As all decay products must be considered for this constraint, it is weaker than the JES one but still contributes valuable information. Also, the s_{bjes} fit is more correlated with the top mass than the s_{jes} fit is. This is due to the fact that the first two are based on the same information, whereas for s_{jes} only part of the event information is needed.

A visualization of the two constraints is given in Figure 5.12. In the first plot, Fig. 5.12 a) a fictitious event display of particle four-vectors projected onto a 2-dimensional plane is shown. The event contains the two light quarks from the hadronic W decay, the lepton and neutrino from the leptonic W decay and the b jets from the two top decays. For simplification, particles and antiparticles are not distinguished. The neutrino direction and momentum are derived from the balance of the other decay products in the transverse plane. The kinematics can be solved up to two possible solutions for the neutrino z momentum. As another simplification, from these two possible solutions only one is considered here. In Fig. 5.12 b) the construction of the W momenta from the u- and d-quark on the one hand and the lepton and neutrino on the other hand is shown. To reconstruct the top quarks, the two W bosons (or rather their decay products) and the two b jets are needed. This is shown in Fig. 5.12 c). To simplify the picture, the decay products from which the two W bosons were reconstructed in 5.12 b) are not drawn. As one can see from this picture, the two reconstructed top quarks have the same four-momenta and are balanced (i.e. back-to-back). Here and in the following explanations, a total transverse momentum equal to zero is assumed for simplicity for the $t\overline{t}$ system. For a four-vector $p = (E, \vec{p})$, the following equation holds for the mass of the particle:

$$p^2 \equiv E^2 - |\vec{p}|^2 = m^2 \; . \tag{5.27}$$

Thus, if the four-momentum of a particle is reconstructed too high or too low, the same is true for its mass (in the limit of massless jets). This is sketched in the lower two plots for overestimated jet energy scales.

In Fig. 5.12 d), the D0 jet energy scale is assumed to overestimate the light jet energies by 50%. This not only affects the two quarks in the hadronic decay branch, but also the neutrino in the leptonic one, as it is obtained from the balance of all other objects in the transverse plain. To reduce the complexity of the picture, the neutrino (i.e. $\not{E}_t$) is also scaled by 1.5. This of course does not hold in reality, as the vectors are four-dimensional and the neutrino momentum could change by any amount in this two-dimensional projection. The important point is that due the overestimation of the jet energies, the W mass in the hadronic decay branch is overestimated as well. When comparing the reconstructed W mass with the mass intrinsic in the matrix element, it is found that a factor of $s_{jes} = 1.5$ would regain the ”correct” picture in Fig. 5.12 b). That means, on average, all light jets need to be scaled down by 1.5 to reconstruct the correct W mass.

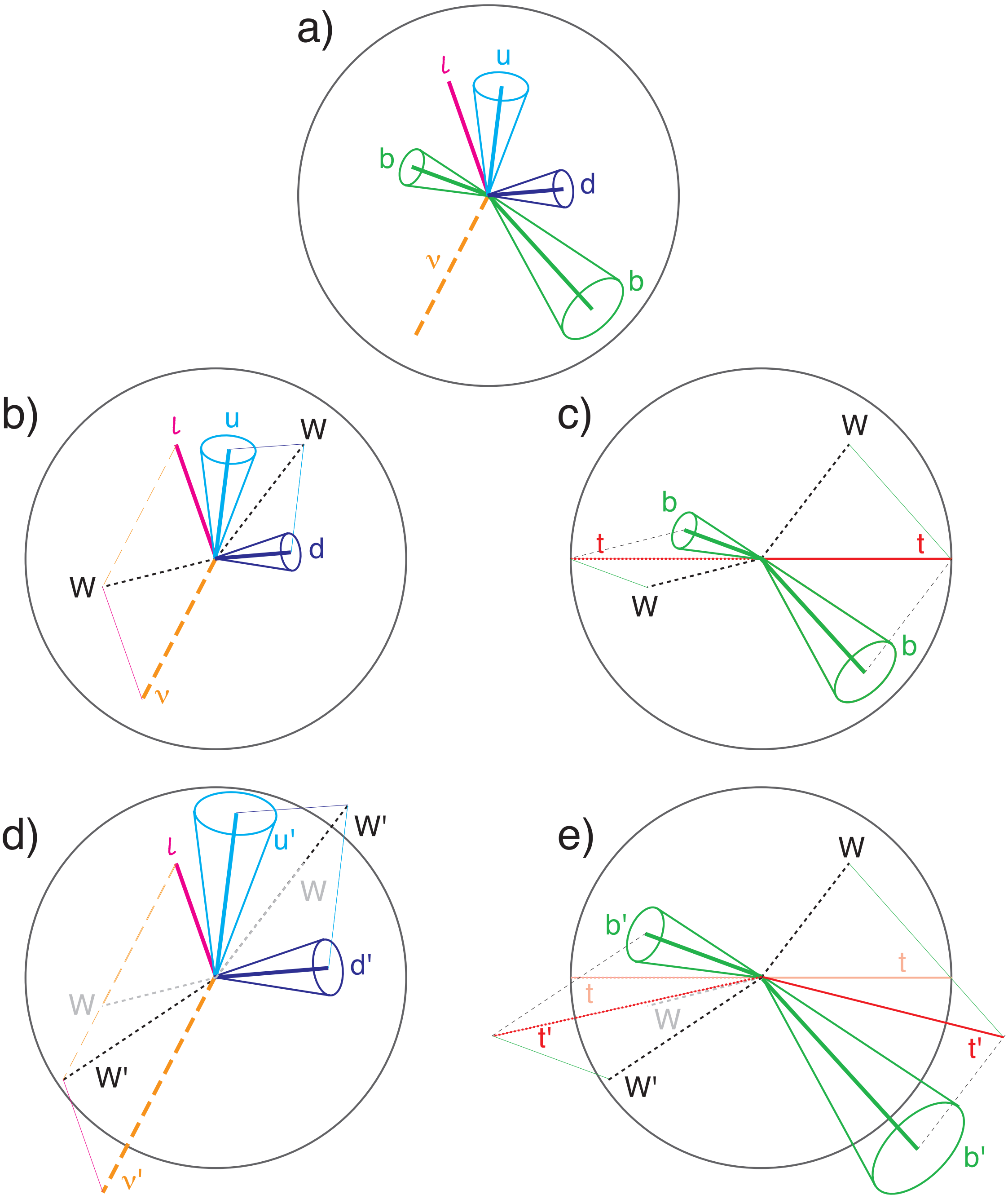

Figure 5.12: Schematic representation of the s_{jes} and s_{bjes} constraints in the topological signal likelihood evaluation. See the text for details.

a) Fictitious event display of a semileptonic $t\bar{t}$ decay.

b) $s_{jes} = 1$. Reconstruction of the W momenta from their decay products.

c) $s_{bjes} = 1$. Reconstruction of the top quarks from the b jets and W bosons reconstructed in b).

d) $s_{jes} = 1.5$, $s_{bjes} = 1$. The u-jet, d-jet and $\not{E}_t$ are affected by an overestimated JES. In grey the nominal W momenta from b) are sketched. The reconstructed momenta W' are overestimated.

e) $s_{jes} = 1$, $s_{bjes} = 1.5$. The b jets and $\not{E}_t$ are affected by an overestimated bJES. They lead to overestimated top momenta t' that are not balanced in contrast to the correct ones (indicated in light red).

The same would hold true for the top masses, but unfortunately, these are the ones to be measured! Nevertheless, Fig. 5.12 e) shows how the b scaling factor can be constrained. If the b jet energy scale overestimates the b jet energies by 50%, the reconstructed top mass would be too high, as in the previous example for the W mass. As stated, this does not help, since the true top mass is not known. But this is not the only effect. In addition, the reconstructed top momenta are no longer balanced in p_t. When assuming different s_{bjes} values, it is found in this case, that a factor of 1.5 on average leads to a balanced event as in Fig. 5.12 c). This factor would hence lead to higher likelihoods, i.e. it would have the highest probability to be the correct one. It should be mentioned that once again the neutrino is affected by the overestimation of the b energies. The effect could be different from the case where the light jets are overestimated. This is disregarded here, and the same reconstructed (leptonic) W' is taken as in Fig. 5.12 d).

For underestimated jet energy scales s_{jes} and s_{bjes}, the picture is qualitatively the same. Jet momenta are underestimated and thus the reconstructed W (and top) momenta are also too small. As in the case of overestimated bJES, the $t\bar{t}$ pair is no longer balanced in the transverse plane. Again, the appropriate correction factors can be derived by assuming the correct W mass and $t\bar{t}$ p_t balance.

It should be stated clearly that Figure 5.12 only gives a qualitative representation of the scaling factor constraints. The real picture is much more complex without the simplifications made here, however all necessary information is still encoded in the matrix element.

With all the ingredients described above, the signal likelihood for $t\bar{t}$ production can be calculated according to Eqns. (5.4), (5.9) and (5.15), (5.16), (5.20):

$$\begin{aligned}\mathscr{L}_{t\bar{t}}(y_{evt}; m_t, s_{jes}, s_{bjes}) = {} & \frac{1}{\sigma^{obs}_{q\bar{q}\to t\bar{t}}} \int\limits_{x_1,x_2} \sum_{flavors} \mathrm{d}x_1 \mathrm{d}x_2\, f_{\mathrm{PDF}}(x_1)\, f_{\mathrm{PDF}}(x_2) \\ & \times \int\limits_{y_{parton}} \mathrm{d}\Phi_n \, \frac{(2\pi)^4 \left|\mathscr{M}_{q\bar{q}\to t\bar{t}}\right|^2}{4\sqrt{(p_1 p_2)^2 - m_1^2 m_2^2}} W(y_{evt}, y_{parton}; [s_{jes}], [s_{bjes}]) \; .\end{aligned} \tag{5.28}$$

This means that a multidimensional integral over 6-body phase space and all possible final states needs to be evaluated. To reduce the integration dimensions, several assumptions are made:

- $p_t(q\bar{q}) = p_t(t\bar{t}) = 0$
  The transverse momentum of the initial state quark system and hence of the final state $t\bar{t}$ system is zero.

- $\vec{n}(jet) = \vec{n}(q_{fs})\ ,\ \vec{n}(l_{evt}) = \vec{n}(l_{fs})$
  The particle directions (symbolized by their normal 3-vector $\vec{n}$) of the final state quarks and lepton are assumed to be perfectly measured.

- $E(e_{evt}) = E(e_{fs})$
  The energy resolution of electrons from leptonic W decays is neglected, i.e. the reconstructed electron energy is assumed to be exact.

The first assumption of zero transverse momentum is applicable, as most of the top quark pairs at Tevatron energies are produced at threshold and the phase space for an additional jet in the final state is small. The second assumption is only an approximation because the reconstruction of the jet directions has a finite resolution just as the jet momenta do. However, compared to the jet momentum resolution the effect is small and can be neglected. In addition to this detector effect, there is also a physical uncertainty in the jet direction. First of all, the hadronization process itself can lead to differences between the jet and the quark direction. Secondly, effects of color reconnection between the parton shower and the beam remnant can influence the jet direction. Studies of color reconnection with several test models in Monte Carlo simulations are currently underway [99]. Nevertheless, the effect is supposed to be tiny and will be neglected until the studies indicate the contrary or a realistic model is found and is incorporated into the simulations. The third assumption is a trade-off between a more correct description of detector effects and computing requirements for the multidimensional integration as mentioned in Sec. 5.2.

With these simplifications, an integration over the quark momenta, the lepton momentum (in the μ-channel only) and the longitudinal neutrino momentum remains. It is performed numerically by the Monte Carlo routine `VEGAS` [100–102]. This algorithm works most efficiently if the integration variables exhibit well localized peaks. For the signal likelihood this is the case for the transfer functions and even better for the Breit-Wigner peaks of the W boson and top quark masses. Thus, to satisfy this criterion, the following integration variables (and corresponding limits) are chosen:

- $0 \leq |\vec{p}^{\,d}| \leq 500$ GeV
  the magnitude of one of the quark momenta from the hadronic W decay
- $0 \leq m^2_{d\bar{u}} \leq (400 \text{ GeV})^2$
  the squared mass of the hadronically decaying W
- $0 \leq m^2_{bd\bar{u}} \leq (500 \text{ GeV})^2$
  the squared mass of the top quark with the hadronic W decay branch
- $0 \leq m^2_{bl\nu} \leq (500 \text{ GeV})^2$
  the squared mass of the top quark with the leptonic W decay branch
- $-500 \text{ GeV} \leq p_z^{b\nu} \leq +500 \text{ GeV}$
  the longitudinal projection of the momentum sum of the b quark and neutrino in the leptonic decay branch
- $-1/(100 \text{ GeV}) \leq (q/p_t)^\mu \leq +1/(100 \text{ GeV})$
  the charge over transverse momentum ratio of the muon (if applicable)

For details about the choice of variables refer to [98].

In each integration step, the kinematics need to be solved from the integration variable values, the measured directions and the electron energy (if applicable). The matrix element and the parton density functions can then be evaluated. The transfer functions give the probability to observe the kinematic final state y_{parton} under consideration as the measured state y_{evt} in the detector. Finally, a Jacobian determinant is included for the transformation from measured Cartesian coordinates and momenta to the 6-dimensional integration space variables.

The event likelihood (5.28) is computed on a 3-dimensional grid of hypotheses for m_t, s_{jes} and s_{bjes}. For each of these grid points, the 24 possible jet-parton assignments have to be considered. For every one of those, numerous points in the 6-dimensional integration space spanned by $\{|\vec{p}^{d}|, m^2_{d\bar{u}}, m^2_{bd\bar{u}}, m^2_{bl\nu}, p_z^{b\nu}, (q/p_t)^{\mu}\}$ are evaluated, as described above. This necessitates a huge amount of computing power for the full likelihood evaluation. Thus, only a limited number of hypotheses and a highly optimized code environment make this calculation feasible (cf. Sec. 6.2).

5.4 Topological Background Likelihood

In principle, the topological background likelihood can be calculated exactly as the signal one according to Eqn. (5.28) by using the corresponding matrix element for the background process. Nevertheless, for the background likelihood there are several drawbacks:

- Many different background processes may contaminate the data sample. For the semileptonic decay signature W production in association with (four) jets (W+jets) and QCD multijet production (where one jet is misidentified as a lepton) are the most important ones.
- Even at leading order hundreds of Feynman diagrams contribute to electroweak W+jets production and need to be evaluated in the matrix element.
- In contrast to $t\bar{t}$ production, the W mass leads to the only well localized Breit-Wigner peak in W+jets events. In multijet background there is none at all.

These three points would lead to a significant enhancement in computing time which cannot be provided even by large computing farms. Thus, several simplifying assumptions have to be made:

- Consider only W+jets background in the likelihood evaluation and weigh it by the full number of all background events (cf. Eqn. (5.3)). This assumption holds as W+jets and QCD background have similar event kinematics. However, this approximation needs to be validated in pseudoexperiments and incorporated in the calibration.
- Use the `VECBOS` generator [103] to evaluate the background likelihood. This Monte Carlo generator accounts for the relative importance of different subprocesses and performs a statistical sampling of all possible spin, flavor and color configurations.
- Neglect contributions from subprocesses other than W+4lp (i.e. W production in association with 4 light partons). These can be either subprocesses containing more (or fewer) partons or contributions with heavy flavor content. Again, this needs to be studied and corrected for in pseudoexperiments and the calibration.
- Assume the background likelihood does not depend on the observables to be fitted. For m_t this is true. For the scaling factors s_{jes} and s_{bjes} it is an approximation (see Sec. 6.2). This means in practice that the likelihood is only evaluated for $s_{jes} = s_{bjes} = 1$ but is used in combination with all assumed values in the signal likelihood in Eqn. (5.3).

To obtain the background likelihood, `VECBOS` evaluates the matrix element $\mathscr{M}_{W+4lp}$ at N phase space points that are randomly chosen according to the transfer functions. The likelihood $\mathscr{L}_{bkg}$ is then estimated as the mean of all evaluations. Between 100 and 1000 iterations are performed until the result is stable. The minimum of 100 iterations corresponds to a statistical uncertainty of 10%. As will be shown in the next chapter, despite these simplifying assumptions the fitting procedure shows much better results when including this background likelihood than when neglecting it completely. Also, the calibration demonstrates a very good performance and is able to cope with the approximations made here.

5.5 Normalization

The topological likelihoods for signal and background need to be normalized by the total observable cross section, i.e. the cross section of events within detector and selection cuts acceptance (cf. Eqn. (5.8)):

$$\sigma^{obs}_{2\to n}(m_t, s_{jes}, s_{bjes}) = \int\limits_{y_{evt}} \mathrm{d}y_{evt} \int\limits_{y_{parton}} \mathrm{d}\sigma^{hc}_{2\to n}(y_{parton}; [m_t])\, W(y_{evt}, y_{parton}; s_{jes}, s_{bjes})\; f_{\mathrm{acc}}(y_{evt}; s_{jes}, s_{bjes}) \;. \tag{5.29}$$

The normalization is not only top mass dependent through the cross section (in the signal case), but due to the jet energy selection cuts, the acceptance f_{acc} becomes dependent on the scaling factors s_{jes} and s_{bjes} as well. That would make a 3-dimensional normalization necessary. However, this can be circumvented by normalizing the jet transfer functions themselves. Instead of normalizing as

$$\int \mathrm{d}P = \int\limits_{y_{evt}=0}^{\infty} \mathrm{d}y_{evt}\; W(\Delta E; s_{jes}, s_{bjes}) = 1 \;, \tag{5.30}$$

by integrating from zero to infinite momentum, the normalization given in Equation (5.17) runs from the momentum cut to infinity. This makes use of the fact that only jets with momenta above the cut threshold have a non-vanishing probability to be reconstructed. Hence, it is sufficient to calculate a 1-dimensional normalization depending only on the top mass. This is verified by the following calculation for the signal likelihood and is visualized in Fig. 5.13.

The event likelihood $\mathscr{L}_{t\bar{t}}$ is such that the probability to observe *any* event y_{evt} above the selection cut is equal to one:

$$\int\limits_{E_j=20\,\mathrm{GeV}}^{\infty} \mathrm{d}E_j\; \mathscr{L}_{t\bar{t}} \equiv 1 \tag{5.31}$$

For the following consideration, only the parts depending on the scaling factor, i.e. the jet transfer functions, are taken into account. For these, y_{evt} is equivalent to the reconstructed jet energy E_j. According to Sec. 5.1, $\mathscr{L}_{t\bar{t}}$ can be written in the following way (with the unit GeV omitted for

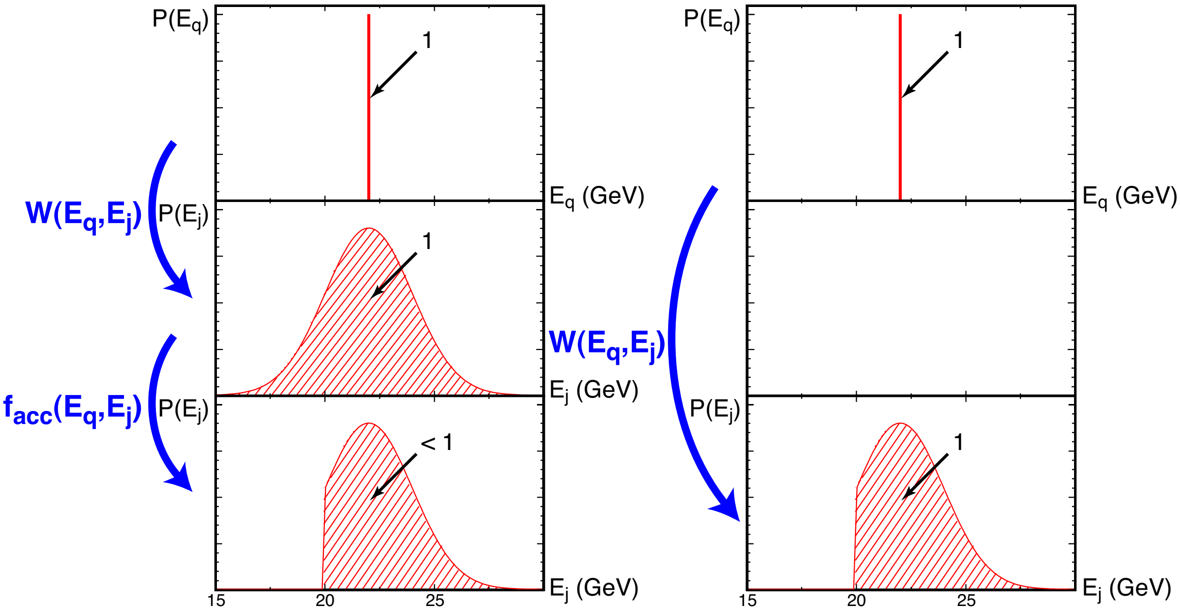

Figure 5.13: Schematic comparison between 3D and 1D normalization. The plots show the probability density versus the quark or jet energy. *Left:* with a jet transfer function normalized according to Eqn. (5.30), any partonic state E_q has a probability of 1 to be reconstructed as a jet with $0 \leq E_j \leq \infty$. When the acceptance cut is applied, the probability to be reconstructed is smaller than 1. *Right:* if the jet transfer function is normalized according to Eqn. (5.17), the probability for any partonic state E_q to produce a measured event $E_{cut} \leq E_j \leq \infty$ is 1. No additional acceptance cut for the jet energy needs to be applied in this case.

abbreviation):

$$\begin{aligned}
\int\limits_{E_j=20}^{\infty} \mathrm{d}E_j\, \mathscr{L}_{t\bar{t}} &\overset{(5.6-5.9)}{=} \frac{1}{\sigma_{norm}} \int\limits_{E_j=20}^{\infty} \mathrm{d}E_j \int\limits_{E_q=0}^{\infty} \mathrm{d}\sigma_{p\bar{p}\to t\bar{t}}(E_q)\; W(E_j,E_q;s_{jes},s_{bjes}) \qquad (5.32)\\
&= \frac{1}{\sigma_{norm}} \int\limits_{E_q=0}^{\infty} \mathrm{d}\sigma_{p\bar{p}\to t\bar{t}}(E_q) \int\limits_{E_j=20}^{\infty} \mathrm{d}E_j\, W(E_j,E_q;s_{jes},s_{bjes})\\
&\overset{(5.17)}{=} \frac{1}{\sigma_{norm}} \int\limits_{E_q=0}^{\infty} \mathrm{d}\sigma_{p\bar{p}\to t\bar{t}}(E_q)\\
&= \frac{1}{\sigma_{norm}} \sigma^{total}_{p\bar{p}\to t\bar{t}}\,.
\end{aligned}$$

With Eqn. (5.31) it follows:

$$\sigma_{norm} \equiv \sigma^{total}_{p\bar{p}\to t\bar{t}}\,. \qquad (5.33)$$

That means the jet acceptance is absorbed by the jet transfer function normalization and no scaling factor dependence remains in the likelihood normalization. Of course, this is only correct, if none of the other kinematic quantities depend on the jet scales. As the missing transverse energy is derived from the jet momenta and thus indirectly depends on the jet scales, this is only an approximation. However, this small dependence can be handled in the calibration, as $\not{E}_t$ is only used for the cut. For the normalization, the acceptance cuts for all final state particles except the jets and also for the jet directions, i.e. η_{jet} cuts, still need to be applied. This decreases the observed cross section compared to the total cross section for $t\bar{t}$ production. However, these selection cuts no longer exhibit a dependence on the scaling factor:

$$\sigma^{obs}_{p\bar{p}\to t\bar{t}} = \int\limits_{y_{evt}} \mathrm{d}y_{evt} \int\limits_{y_{parton}} \mathrm{d}\sigma_{p\bar{p}\to t\bar{t}}(y_{parton};m_t)\; f_{\mathrm{acc}}(y_{evt})\,. \qquad (5.34)$$

In the case of the muon transfer function, no integration over $(q/p_t)_{evt}$ is performed as the muon transverse momentum resolution is very narrow in the region of the applied selection cut and hence can be neglected. The normalizations for the e+jets and μ+jets $t\bar{t}$ decay channels with respect to the top mass are evaluated in Sec. 6.2.3 and Sec. 6.3.3 for the parton level studies and Monte Carlo calibration, respectively.

For the background likelihood, the dependence on the scaling factors is neglected as described before (cf. Sec. 5.4). The normalization could be obtained analogously to the signal normalization according to Eqn. (5.34). However, as for the likelihood itself, this would be computationally intensive and thus a different approach is chosen. It makes use of the fact that the fitted signal fraction in Eqn. (5.3) will be underestimated if the background likelihood is overestimated and vice versa. Therefore, the relative background normalization can be adjusted in pseudoexperiments by varying it until the correct signal fraction is obtained. This approach is only valid if no external constraints on the signal fraction are applied (e.g. from the measured signal and background cross sections), which is the case for this analysis.

It should be noted, that both signal and background likelihoods can only be calculated up to some constant factors. In the estimate of the background normalization as described above, these relative

Name	L6	L5	L4	L3	L2	Loose
Cut	0.1	0.15	0.2	0.25	0.325	0.45

Name	oldLoose	Medium	Tight	VeryTight	UltraTight	MegaTight
Cut	0.5	0.65	0.775	0.85	0.9	0.925

Table 5.3: Operating points and cut values certified for the NN b-tagger.

constant factors are taken care of as well. For the likelihood fits of the observables to be measured only the relative difference between various hypotheses is important. Therefore, an overall constant factor (and hence the absolute normalization of the event likelihood) is irrelevant.

5.6 b Identification Probabilities

Using b identification in top measurements has several advantages. The signature of top pair decays contains two b quarks which form jets. In semileptonic decays there are additionally two jets from light quarks. In contrast, the background stemming from W+jets or multijet background contains very few hard b jets. Thus, b-tagging helps to separate signal from background and enhances the sample purity. Additionally, identifying b jets allows one to find the best jet-parton assignments and hence reduces combinatorial background as well. This is due to the fact that combinations in which a tagged jet is assigned to a b quark are much more likely to be the correct combination than permutations where tagged b jets are assigned to light quarks from the W decay.

In former studies, various b identification methods, and also a combination of them utilizing a neural net (cf. Sec. 3.6), were used. In all cases, the data sample was split into subsamples according to the number of b-tagged jets per event. Samples with 0, 1 and 2 or more tagged jets per event were commonly used. Events without b-tagged jets or with only one were then either dropped completely, e.g. in the all-hadronic channel [104], or measurements were performed on all subsamples and combined afterwards with higher weights for samples with more tagged jets. Details given for the top mass analysis in the semileptonic decay channel can be found in [90, 91]. As a rule of thumb, at most $\approx 50\%$ of true b jets are tagged in b identification algorithms, leading to largely reduced statistics in tagged samples and a substantial amount of signal in 0-tagged subsamples.

In this analysis, a qualitative improvement over the above concept is achieved. For each jet, the b-tagging neural network output is used directly to calculate a probability for the jet to stem from a bottom, charm or light quark. In each jet-parton assignment, the probabilities of all four jets are combined, leading to a separation of ”good” and ”bad” permutations. Thereby, combinatorial background is reduced. In addition, different flavor combination assumptions for signal and background b identification probabilities improve the discrimination power of the method. As the neural network output for b identification is only certified for several individual operating points (i.e. cut values) at D0, the b identification probabilities are not fully continuous but are used in a binned manner.

In Figure 5.14 the neural net output is exemplified for a $t\bar{t}$ Monte Carlo sample. The NN output is restricted between 0 and 1, entries at -1 correspond to jets not being taggable (see Sec. 3.6, last

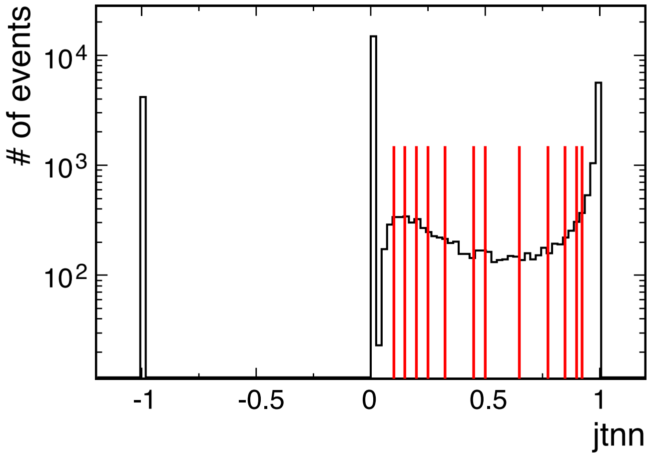

Figure 5.14: Distribution of the neural network output for a $t\bar{t}$ MC sample ($m_t = 170$ GeV). The red lines indicate the position of the cut values for the 12 operating points.

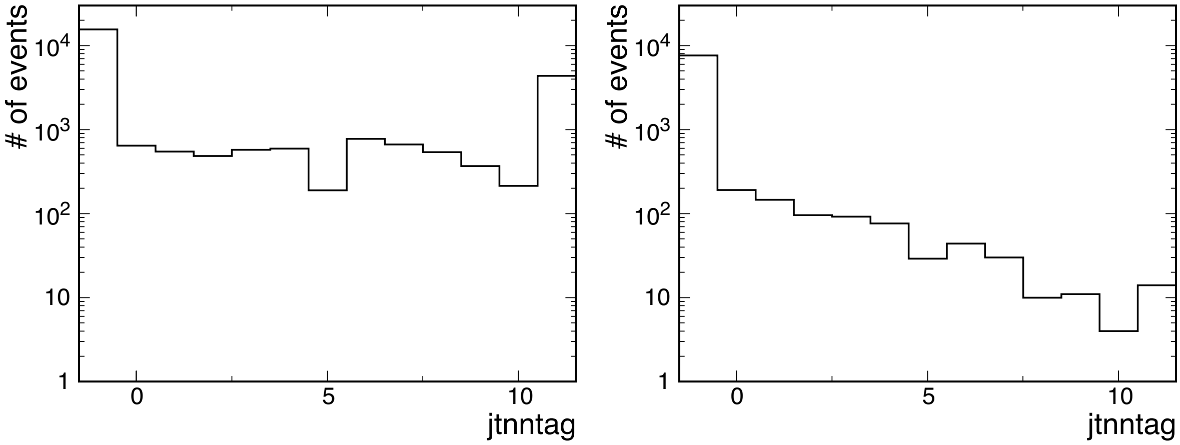

Figure 5.15: Distribution of the highest operating point giving a tag for MC samples with and without b jets. *Left:* $t\bar{t}$ sample ($m_t = 170$ GeV). *Right*: W+jets sample.

paragraph). The large peak at 0 is due to events where the NN failed and did not give any output. An operating point is defined as a certain cut value on the NN output, where all events with an output above that threshold are called tagged and all events with output below the threshold are untagged. This means b-tagging is defined inclusively so that a ”tight” b jet fulfills all looser requirements. So far, 12 operating points were studied and certified at D0 [75], given in Table 5.3. As the cut values are non-equidistant to allow for cross-checks with older studies, the number of entries in exclusive b-tagging bins, given in Figure 5.15, shows artefacts of the binning (see bin 5 for example). In this plot, only the number of the highest operating point giving a tag is stored for each jet, leading to exclusive b-tagging bins (numbered from 0 to 11). Jets in the bin ’-1’ are either non-taggable, failed the NN or have a NN output below the loosest possible threshold (i.e. no tag at all).

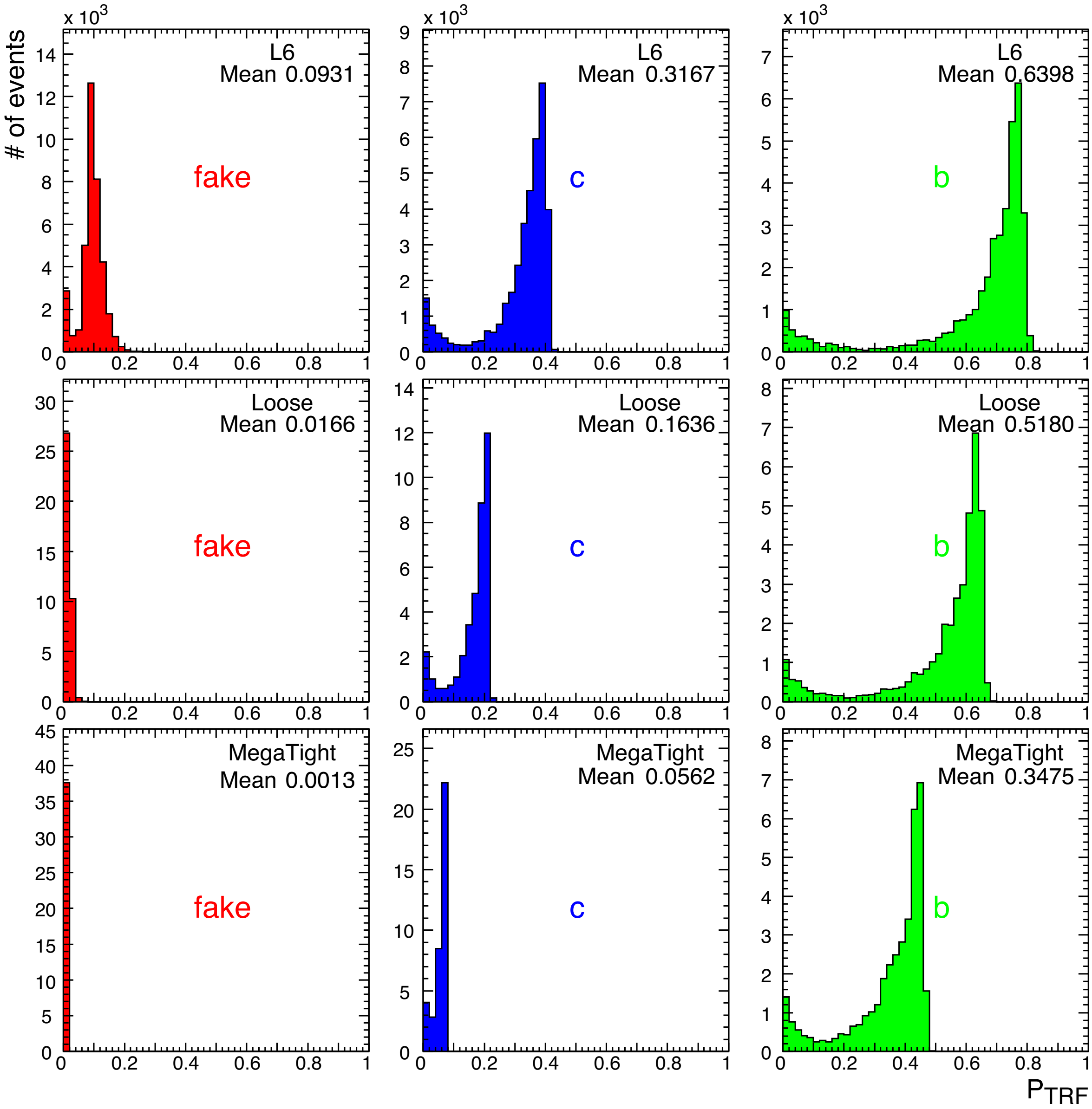

Figure 5.16: Tag Rate Function (TRF) output for three example operating points: *Top*: L6, *Middle*: Loose, *Bottom*: MegaTight; for the three possible parton flavors: *Left*: fake, *Middle*: *c* quark, *Right*: *b* quark.

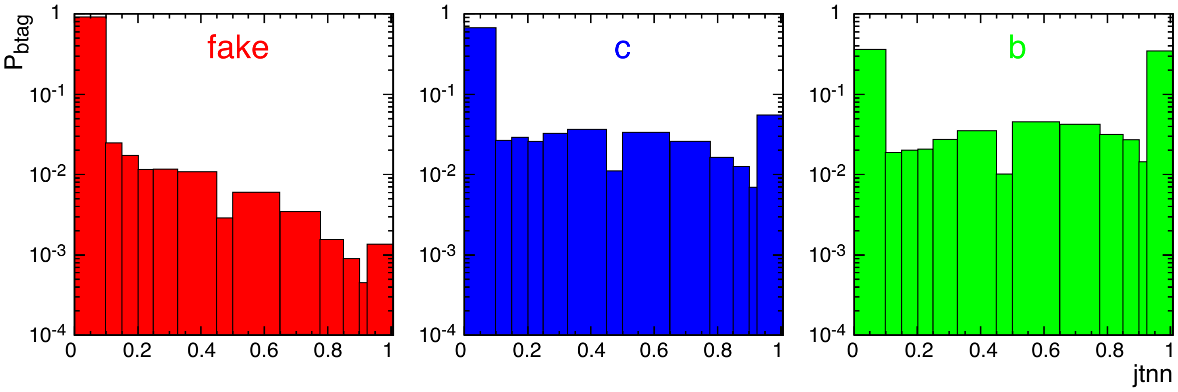

Figure 5.17: b-tagging probabilities vs. NN output of all operating points for the three jet flavors fake, *c*, *b*. The first bin contains non-tagged jets.

There are two possible methods for applying *b*-tagging to Monte Carlo. The obvious way is to apply the same *b*-tagging algorithm on Monte Carlo as the one used for analyzing the data and ”really tag” the Monte Carlo jets. Studies have shown [75], that this procedure leads to overestimated tagging rates on Monte Carlo compared to data due to various detector effects not modeled perfectly in the simulation. To address this issue, tag rate functions (TRFs) were developed [76], parameterizing the tag rates in the full $\eta - p_t$ space (cf. Sec 3.6). With those, the second way to apply *b* identification to Monte Carlo is ”random tagging”. For this procedure, a random number uniformly distributed between 0 and 1 is thrown and compared to the probability to be tagged according to the TRF for each operating point. If the random number is smaller than the TRF probability, the jet is called tagged and untagged otherwise. Again, only the tightest operating point giving a tag is used for each jet to yield exclusive bins. As the tag rate functions are flavor dependent (*b*, *c* or fake, i.e. *u*/*d*/*s*/*g*), the flavor of the generated Monte Carlo parton is used for finding the tightest possible tagging point.

The next step is to calculate b-tagging probabilities for all permutations and events under different flavor assumptions. As the TRFs only give *inclusive* probabilities $P_{trf}(i)$, the *exclusive* probabilities for each b-tagging bin $P_{btag}(i)$ need to be calculated in the following manner:

$$\begin{aligned} P_{btag}(-1) &= 1 - P_{trf}(0) \\ P_{btag}(n) &= P_{trf}(n) \\ P_{btag}(j) &= P_{trf}(j) - P_{trf}(j+1) \qquad j \in \{0, 1, ..., n-1\} \end{aligned} \tag{5.35}$$

Here, $i = -1$ denotes ’no tag’ as stated above and n stands for the highest operating point. Figure 5.16 shows the TRF probabilities for the three different flavors *b*, *c* and fake in three example *b*-tagging bins *L6*, *loose* and *megatight* (cf. Tbl. 5.3). As mentioned before, even with loose operating points one hardly exceeds 50% tagging probability for b-jets (see right column, top and middle plot), leading to reduced statistics in tagged data samples. If one goes from loose to tight operating points, i.e. from top to bottom in the plots, one sees that the tagging probabilities decrease with tighter cuts but much faster for fakes and *c* quarks than for *b* quarks. This leads to the good discrimination power between signal and background mentioned above. In Fig. 5.17 the *b* identification probabilities are shown for all operating points according to equations (5.35). These plots are based on the mean values of

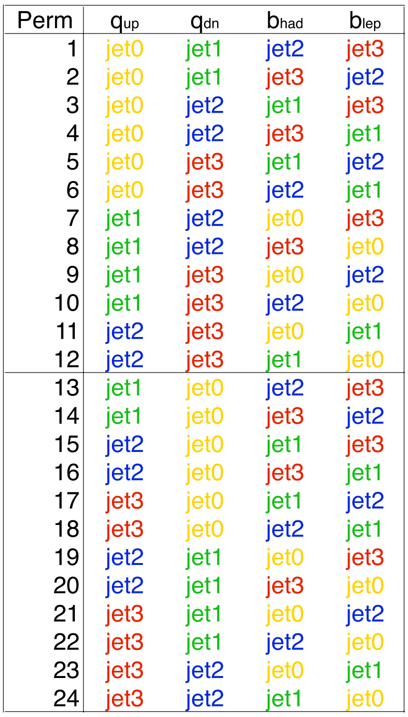

Perm	q_{up}	q_{dn}	b_{had}	b_{lep}
1	jet0	jet1	jet2	jet3
2	jet0	jet1	jet3	jet2
3	jet0	jet2	jet1	jet3
4	jet0	jet2	jet3	jet1
5	jet0	jet3	jet1	jet2
6	jet0	jet3	jet2	jet1
7	jet1	jet2	jet0	jet3
8	jet1	jet2	jet3	jet0
9	jet1	jet3	jet0	jet2
10	jet1	jet3	jet2	jet0
11	jet2	jet3	jet0	jet1
12	jet2	jet3	jet1	jet0
13	jet1	jet0	jet2	jet3
14	jet1	jet0	jet3	jet2
15	jet2	jet0	jet1	jet3
16	jet2	jet0	jet3	jet1
17	jet3	jet0	jet1	jet2
18	jet3	jet0	jet2	jet1
19	jet2	jet1	jet0	jet3
20	jet2	jet1	jet3	jet0
21	jet3	jet1	jet0	jet2
22	jet3	jet1	jet2	jet0
23	jet3	jet2	jet0	jet1
24	jet3	jet2	jet1	jet0

Figure 5.18: Possible 24 jet-parton assignments in the semileptonic $t\bar{t}$ decay channel.

Fig. 5.16 and only serve illustrative purposes. For individual jets the b identification probabilities are calculated from the appropriate TRF values based on the jet energy and pseudorapidity.

To combine the different jet b identification probabilities to form a permutation probability, flavor assumptions need to be made. In the $t\bar{t}$ semi-leptonic decay channel the assumption for the four jets is u-d-b-b, meaning two b-quarks stemming from the (anti-)top decay and an up-type and down-type quark from the W decay. The up-type quark can be either a u quark or a c quark (and the down-type quark either a d or s, neglecting b contributions), each with a probability of 50%. Hence, these two flavor assumptions need to be properly combined:

$$P_u = \frac{1}{2}\left(P_{fake} + P_c\right) . \tag{5.36}$$

The down-type quark probability is simply given by the probability for a fake tag which can be used for all light flavor assumptions q. Accordingly, the flavor assumption for background is q-q-q-q in the l+jets channel, neglecting contributions from real heavy flavor content.

In Figure 5.18 the 24 possible jet-parton assignments for the $t\bar{t}$ semileptonic decay channel are given. For each of these permutations a b identification probability is calculated in the following way:

$$P_{sgn}(j_i, j_k, j_l, j_m) = P_u(j_i) \cdot P_d(j_k) \cdot P_b(j_l) \cdot P_b(j_m) \tag{5.37}$$

$$P_{bkg}(j_i, j_k, j_l, j_m) = P_q(j_i) \cdot P_q(j_k) \cdot P_q(j_l) \cdot P_q(j_m) \ , \tag{5.38}$$

for signal and background, respectively. A concrete example is examined in Appendix A.

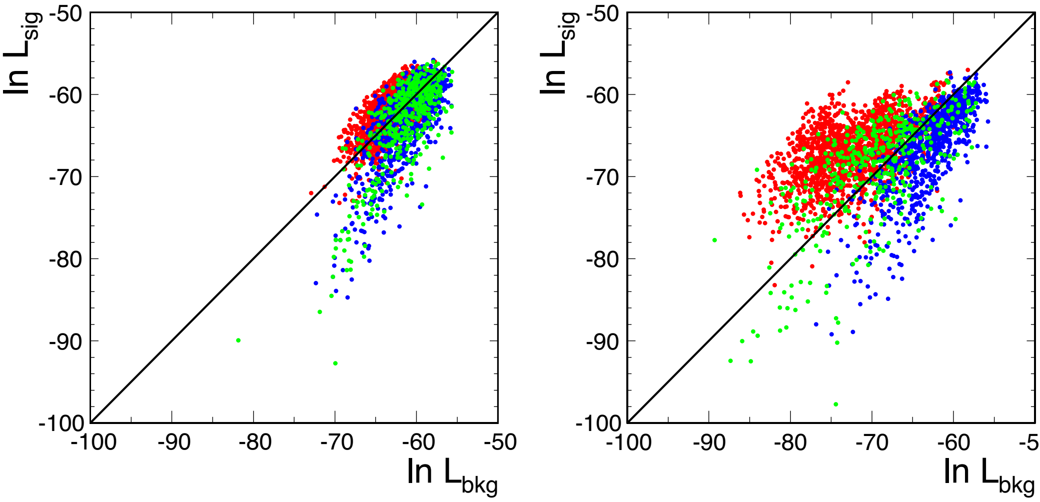

Figure 5.19: Descrimination power of signal vs. background likelihoods between $t\bar{t}$ signal (red), W+4lp background (blue) and W+bb+jj background (green). *Left*: Topological likelihoods alone. *Right*: Topological and b identification likelihoods combined. The study is performed on parton level events, where the correct jet permutation is known (cf. Sec. 6.2).

Including the b identification probabilities into the matrix element method is simply done by multiplying them with the topological probabilities described in Section 5.1 for each permutation individually, both for the signal and background assumption. In Figure 5.19 the discrimination power between $t\bar{t}$ semileptonic events, W+4lp events and W+bb+jj events is shown. Here, 'j' indicates a light parton (lp). It can be seen that the discrimination against W+4lp becomes orders of magnitudes better by including b identification probabilities, whereas the W+bb+jj background cannot be removed by b-tagging, as expected. The separation of $t\bar{t}$ and W+bb+jj is caused only by the topological differences. As events with heavy flavor content account for less than 20% of the W+jets background, this does not indicate a general drawback of the method. Even for these events it is at least as good as previous analyses which did not include b identification probabilities.

The good discrimination power against combinatorial background by combining topological and b-tagging probabilities can be seen in Fig. 5.20. For these plots the number of permutations needed to obtain 95% of the full event probability is calculated. For the b-tagging probabilities alone there is a strong peak at 12 permutations. This can be explained by the fact that on average one of the b-jets is identified while the other one is not. The 12 permutations where the "tagged" jet is assigned to a b quark therefore have high b-tagging probabilities, whereas the other permutations are negligible. For the topological probabilities there is a strong peak at 4 permutations and smaller ones at 6 and 8. As the exchange of the two light quarks stemming from the W decay leads to very similar topologies these permutations have similar probabilities as well, which leads to an even number of permutations being preferred. The strong peak at 4 permutations corresponds to the four cases where the b jets are correctly assigned to b quarks and the light jets to the decay products of the W. All other permutations are much more unlikely. The combination of both probabilities shows that the average number of permutations which must be summed to obtain 95% of the event probability is only 2.8 with peaks at

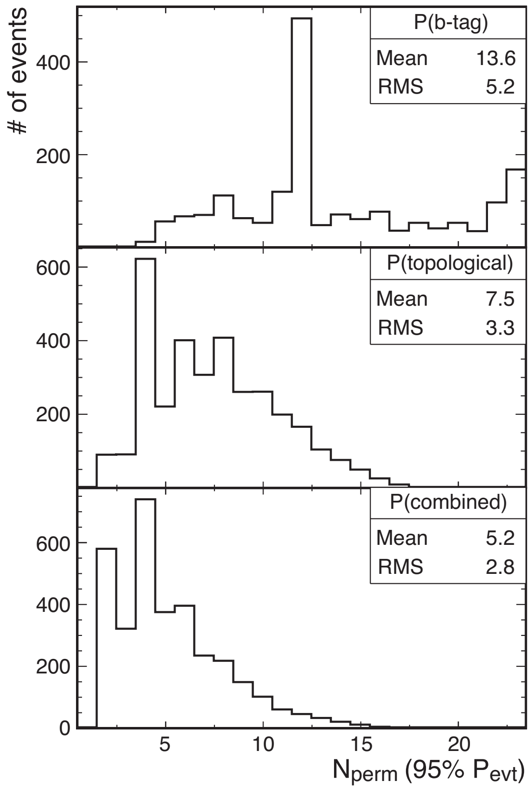

Figure 5.20: Number of permutations needed to obtain 95% of the full event probability in a $t\bar{t}$ parton level test. Top: b-tagging probabilities, middle: topological probabilities, bottom: combined probabilities.

2 and 4. This indicates that both *b* identification and topological probabilities tend to prefer the same ("good") permutations and lead to a very good discrimination against the other ones.

As a consequence of the inclusion of *b* identification information and the hence better background separation, the expected measurement uncertainties for the three fit observables m_t, s_{jes} and s_{bjes} decreases by about 15% as will be shown in Section 6.2.4.

5.7 The Fitting Procedure

The aim of the matrix element method as described here, is the simultaneous measurement of the top mass m_t, the jet energy scaling factor s_{jes}, the *b* jet energy scaling factor s_{bjes} and the fraction of $t\bar{t}$ events $f_{t\bar{t}}$ in the event sample. For the signal likelihood a 3-dimensional grid of hypotheses for m_t, s_{jes} and s_{bjes} is evaluated. At each grid point, the following calculations are performed:

1. Determination of the signal likelihood for all 24 possible jet-parton assignments and the two solutions for the longitudinal component p_z of the neutrino momentum according to Eqn. (5.28).

2. Calculation of the background likelihood for all 2×24 kinematic solutions. This is performed only once for $s_{jes} = s_{bjes} = 1$ and is applied to all signal hypotheses.
3. Evaluation of the b identification probabilities for all 24 jet permutations with both signal and background assumptions. Multiplication with the corresponding topological likelihoods.
4. Computation of the mean signal and background event likelihood using all 2×24 individual solutions.
5. Combination of $\mathscr{L}_{t\bar{t}}$ and $\mathscr{L}_{W+4lp}$ to an event likelihood according to Eqn. (5.3).
6. Combination of all event likelihoods to a sample likelihood $\mathscr{L}(m_t, s_{jes}, s_{bjes}, f_{t\bar{t}})$ according to Eqn. (5.1).
7. Identification of the top fraction f_{tt}^{best} which maximizes the sample likelihood. Use of the corresponding likelihood value and signal fraction for all further calculations.

To obtain the final result for the signal fraction, all likelihood values in the 3-dimensional hypotheses grid are compared and the global maximum is determined. The $t\bar{t}$ fraction corresponding to this maximal likelihood value is the quoted one. Its uncertainty is evaluated by varying the signal fraction at fixed (m_t, s_{jes}, s_{bjes}) until $\Delta(-\ln\mathscr{L}) = +\frac{1}{2}$. In this approach, no correlations between $f_{t\bar{t}}$, m_t, s_{jes} and s_{bjes} are accounted for.

For the fits of the other three observables m_t, s_{jes} and s_{bjes}, the likelihoods of all hypotheses in the grid are transformed into $-\ln\mathscr{L}$ values. With these, projections onto each observable axis are obtained in the following way for the example of the top mass (cf. Fig. 5.21):

1. For each m_t hypothesis find the minimum $-\ln\mathscr{L}$ value in the $s_{jes} - s_{bjes}$ plane.
2. Fill the according $-\ln\mathscr{L}$ value into a 1-dimensional plot versus m_t.
3. Fit the $-\ln\mathscr{L}$ distribution with a second order polynomial in a symmetric range around the minimal value. This corresponds to a Gaussian in the likelihood $+\mathscr{L}$.
4. The m_t value that maximizes the fitted likelihood $+\mathscr{L}$ is taken to be the measured value of the top mass.
5. The upper and lower uncertainty is determined such that 68% of the total likelihood integral is enclosed by the corresponding top mass values, with equal likelihood values at both limits.

For the other two observables, s_{jes} and s_{bjes}, the fits are performed correspondingly.

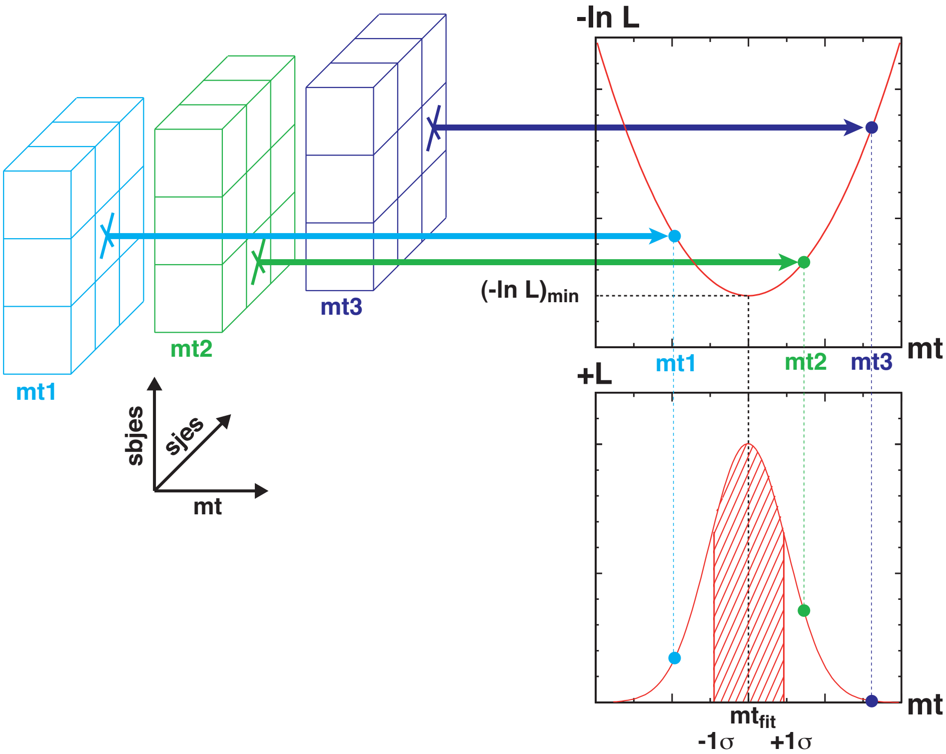

Figure 5.21: Overview of the fitting procedure for the example of the top mass. The minimal $-\ln\mathscr{L}$ value (marked by 'X') in each $s_{jes} - s_{bjes}$ plane for several top mass hypotheses mt1, mt2, mt3, ... is filled into a 1-dimensional plot and fitted by a parabola. The fitted minimum gives the measured value of the top mass $\mathrm{mt}_{\mathrm{fit}}$. Its uncertainty is derived as the $\pm 1\sigma$ region of the corresponding likelihood Gaussian.

Chapter 6

Top Mass Measurement

To measure the top mass in data, several studies on Monte Carlo samples are required beforehand. In a first step, a validation of the method on so-called parton level events is performed, described in Sec. 6.2. Parton level events are simulated events which are not run through any detector simulation but are simply smeared according to the transfer functions. Thus, they represent an idealized test case. In a second step, the method is tested on fully-simulated Monte Carlo events including a complete detector simulation. This is described in Sec. 6.3. These Monte Carlo samples are used to derive a calibration curve that can finally be applied to data events as explained in Sec. 6.4. For all studies and the final measurement events are selected following the criteria given in Sec. 6.1.

6.1 Event Selection

In order to reduce the total number of events and increase the signal purity, the event selection is performed in several steps. The preselection stage is a common selection developed by the top group for the semileptonic top pair decay channel. It is performed with `top_cafe` in the Common Analysis Framework (`CAF`). The D0 software release p18.10.00 is utilized together with the packages listed in App. C. For the jet energy scale the analysis could rely on the final JES for the considered run period, published in [55]. The event preselection comprises the object quality cuts described in Chap. 3 and the following selection cuts:

- e+jets channel
  - one loose electron
  - no second loose electron
  - no loose muon
  - vertex cut: $\Delta z(e, PV) < 1$ cm
  - triangle cut: $\Delta\phi(e, \not{E}_t) > 0.7 \cdot \pi - 0.045 \cdot [\not{E}_t / \text{GeV}]$
- μ+jets channel

  - one loose muon
  - no second loose muon
  - no loose electron
  - vertex cut: $\Delta z(\mu, PV) < 1$ cm
  - triangle cut: $\Delta\phi(\mu, \not{E}_t\ ) > 2.1 - 0.035 \cdot [\not{E}_t/\ \mathrm{GeV}]$
  - Z veto: $70 < m_{\mu\mu} < 110$ GeV

Both channels require at least one good jet. The triangle cut for electrons and muons helps to suppress multijet background. It makes use of the fact that $\not{E}_t$ in such events tends to be small and points along the direction of the lepton. The Z veto rejects events where the loose muon and any second muon (with even looser requirements) have an invariant mass in the Z mass window. This is to suppress $Z \to \mu\mu$+jets background.

The preselected events are written into smaller `ROOT` trees called `METrees` that contain only the information needed for the matrix element method and are thus easier to handle than `CAF` trees. On these, the final selection is applied. It contains the following cuts:

- e+jets channel
  - exactly one tight electron
  - electron in the fiducial calorimeter volume
  - exactly four jets
  - $p_t(e) > 20$ GeV
  - $p_t(jet) > 20$ GeV
  - $\not{E}_t > 20$ GeV
- μ+jets channel
  - exactly one tight muon
  - exactly four jets
  - $p_t(\mu) > 20$ GeV
  - $p_t(jet) > 20$ GeV
  - $\not{E}_t > 20$ GeV

Requiring exactly four jets helps to reduce the systematic uncertainty due to initial and final state radiation. The selection of electrons in the fiducial calorimeter volume ensures that only well measured electrons for which smearing and scale factors were derived enter our samples. This cut replaces the integration over an electron transfer function, which was tested in another analysis [92].

6.2 Method Validation

As described in Chapter 5, the matrix element method is a complex tool to extract the top quark mass and other parameters of interest. In this analysis, several modifications to the method have been applied for the first time. Therefore, an accurate validation that the method behaves as expected is essential.

To create an idealized test case, parton level events are studied. These events are generated with the Monte Carlo simulator `Madgraph` [105] for the signal process and `ALPGEN` [95] for the W+jets background, respectively. In order to accurately reflect the model used in the method, leading-order generators are chosen and no initial or final state radiation is included in the events. For the same reason, the events are not run through a detector simulation but the particle momenta are only smeared according to the corresponding transfer functions. Thus, the energy resolutions observed in data are modeled correctly, but the particle directions remain unchanged from the parton ones as assumed by the method. With this procedure, there exists a one-to-one map between quarks produced at tree-level and ”jets”, i.e. smeared partons. The same holds true for leptons and $\not\!\!E_t$ ($\equiv$ smeared neutrinos).

In order to get a good coverage of the phase space of signal and background decays a large number of Monte Carlo events is necessary. Nevertheless, the possible event pool sizes are limited to the order of thousands of events. For the background process this is due to the fact that the selection requirements of exactly four jets and momenta above 20 GeV are hard cuts for W+jets production. Thus, no larger background samples can be practically achieved. In the case of the signal process this is not an issue. However, for these events the computing time becomes a limiting factor. The calculation of signal and background likelihoods for a large number of Monte Carlo events in a three-dimensional grid is highly CPU intensive. Therefore, only a limited amount of Monte Carlo events can be analyzed with the matrix element method even though large computing farms are available.

6.2.1 Ensemble Testing Procedure

For measuring the top quark mass and jet energy scale factors as in data, *pseudo-experiments* or *ensembles* need to be created from Monte Carlo event pools. This is done by randomly drawing events from the pools. The total number of events taken from the different pools is chosen to reflect the number observed in data. In order to make optimal use of the limited available Monte Carlo statistics resampling techniques are applied. These allow an individual event to appear in different ensembles as well as several times in one ensemble (redrawing). As was shown in [106, 107] resampling helps to reduce the bias and improves the precision of the estimated error significantly. Generally speaking, it is always best to have the largest Monte Carlo statistics possible. In case of limited statistics, however, increasing the number of ensembles will always help to improve the estimate of the uncertainties. In the Monte Carlo studies presented in the following, one thousand ensembles are used for each ensemble test. The number of events in each ensemble varies for different tests and will be given for each case.

In order to obtain calibration curves, ensemble tests are performed for several calibration points, representing different input parameters. For a mass calibration curve, for example, events at five different top masses between 160 GeV and 180 GeV in 5 GeV steps are generated. As defaults a top

Parameter	Default	Range	Step Size	N_{hypo}
m_t	170 GeV	± 9 GeV	1.5 GeV	13
s_{jes}	1.0	± 0.06	0.01	13
s_{bjes}	1.0	± 0.12	0.02	13

Table 6.1: Parameters for the three-dimensional grid of hypotheses. The default values (i.e. origin), range, step size and number of hypotheses in each dimension are given.

mass of 170 GeV and scaling factors of $s_{jes} = s_{bjes} = 1.0$ are assumed. The three-dimensional grid of m_t, s_{jes} and s_{bjes} assumptions in the likelihood integration is chosen to be symmetric around the corresponding generated values. Table 6.1 gives an overview of the parameters of the hypotheses grid used in all ensemble tests. The total number of hypotheses in this grid is $13^3 = 2,190$, leading to $52,718$ signal likelihoods to be calculated for each event with 24 jet permutations per event considered.

To summarize, Fig. 6.1 gives an overview of the three necessary steps for a full Monte Carlo test:

1. Likelihood Fit
    - build one ensemble with N events
    - fit $f_{t\bar{t}}$, m_t, s_{jes} and s_{bjes} (see Sec. 5.7)
2. Ensemble Test
    - repeat Step 1 with 1000 ensembles
    - fit mean results, expected errors and pull widths
3. Calibration
    - repeat Step 2 for all generated input values
    - parameterize calibration curve to obtain biases and slopes

The relevant quantities for ensemble tests are the fitted means of the three observables under study (m_t, s_{jes}, s_{bjes}), their expected statistical error as estimated by the likelihood fit, and their pull width, the latter one being a measure of the quality of the error estimate. The pull is defined as:

$$\text{pull} = \frac{\langle x^{rec} \rangle - \overline{x^{rec}}}{\sigma_x} \qquad \text{with} \qquad x \in \{m_t, s_{jes}, s_{bjes}\} \tag{6.1}$$

Here, $\langle x^{rec} \rangle$ denotes the mean of the fit of one individual ensemble, σ_x the corresponding fit error (i.e. the width of the parabola in Fig. 6.1, top left) and $\overline{x^{rec}}$ the mean of the fits of all ensembles in the test. In the case of parton level tests, $\overline{x^{rec}}$ is replaced by the generated value x^{gen} of the fit observables to show a possible deviation of the fit from the input. When calculating the errors of the ensemble tests, resampling has to be taken into account. For the mean of the distributions, the error is simply given by the width divided by the number of *independent* ensembles that can be built out of the event pool:

$$\bar{x}_{err} = \frac{\sigma_x}{N_{ind}} \qquad \text{with} \qquad N_{ind} = \frac{N_{pool}}{N_{evts}} \ . \tag{6.2}$$

The following naming convention is used here and throughout this document:

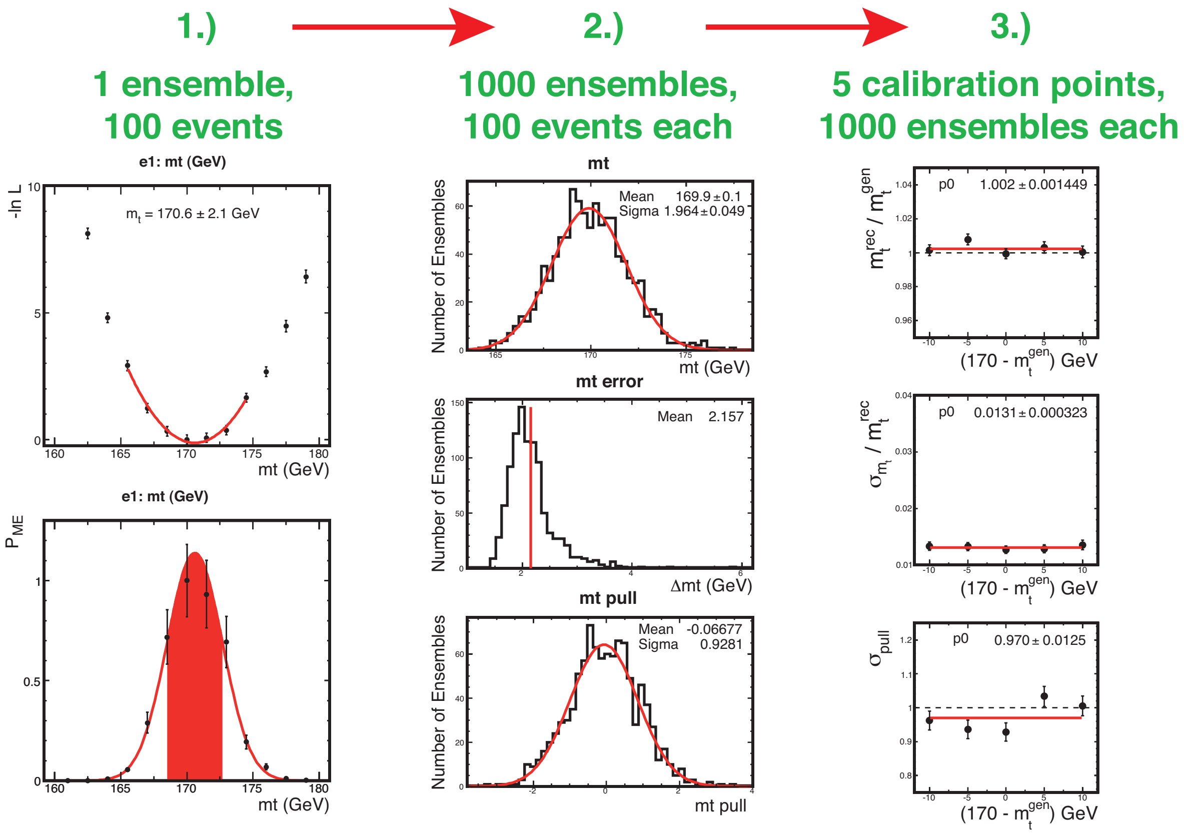

Figure 6.1: Overview of the ensemble testing procedure for the example of the top mass. 1.) likelihood fit of 1 ensemble, 2.) ensemble test with 1000 ensembles 3.) calibration curves for 5 calibration points. See text for details.

N_{pool}	Number of events in the event pool
N_{evts}	Number of events in one ensemble
N_{ens}	Number of ensembles in the test
N_{ind}	Number of possible independent ensembles

As stated above, redrawing improves the estimate on the statistical error. According to [106] the error on the width of the pull distribution is given by:

$$(\sigma_{pull})_{err} = \sigma_{pull} \cdot \sqrt{\frac{1}{2}\left(\frac{1}{N_{pool}} + \frac{1}{N_{ens}-1}\right)}\,. \tag{6.3}$$

6.2.2 Overview of the Event Pools

As stated above, only a limited number of Monte Carlo events can be achieved in the event pools. In this study, pool sizes of around 2000 events for the $t\bar{t}$ signal process (*ttlj*) and 1000 events of

Decay	ttlj	ttljj	wjjjj	wbbjj
e+jets	1500	800	850	425
μ+jets	2000	—	1000	500

Table 6.2: Event pool sizes available for the parton level studies.

W+4lp background (*wjjjj*) are available. Here, the background only contains light partons. Half of the background sample is ”reused” as W+bb+2lp events (*wbbjj*) by randomly assigning two light partons as b partons and smearing them according to the b transfer functions. With this sample, effects of heavy flavor content in the background not modeled by the ME method can be tested. Another test sample is composed of 800 semileptonic $t\bar{t}$ events, which contain an additional parton in the final state (labelled *ttljj* in the following). These decays serve as a test case for events with initial or final state radiation in data, also not modeled by the method. In order to minimize computing time, the parton level studies were mostly performed on e+jets events. This means the generated lepton was not smeared according to the muon transfer functions, avoiding the additional integration over the muon momentum resolution. Nevertheless, a mass calibration test was performed for smeared lepton events to show that the method works for semileptonic decays containing muons as well. An overview of the pool sizes used for the parton level studies is given in Table 6.2.

6.2.3 Normalization

The normalization of the signal and background likelihoods for the parton level studies follows the procedures described in Sec. 5.5. For the signal likelihood normalization the observable cross section was calculated by applying all kinematic selection cuts given in Sec. 6.1 and Chap. 3 except the jet momentum cut. These are as follows:

- $p_t(l) > 20$ GeV
- $\not{E}_t > 20$ GeV
- $\Delta R(l, jet) > 0.5$
- $\Delta R(jet, jet) > 1.0$
- $\eta_{det}(e) < 1.1$
- $\eta_{det}(\mu) < 2.0$
- $\eta_{det}(jet) < 2.5$

The ΔR cuts follow from the minimal possible distance to jets, being restricted by the chosen jet cone size of 0.5. To model the initial state $p\bar{p}$ system with a center-of-mass energy of 1960 GeV, parton density functions of the `CTEQ` Collaboration in the version `CTEQ5L` are applied [108]. Because the matrix element method uses leading order matrix elements in the current version leading order PDFs are chosen. Figure 6.2 shows the signal likelihood normalization as a function of top quark mass for

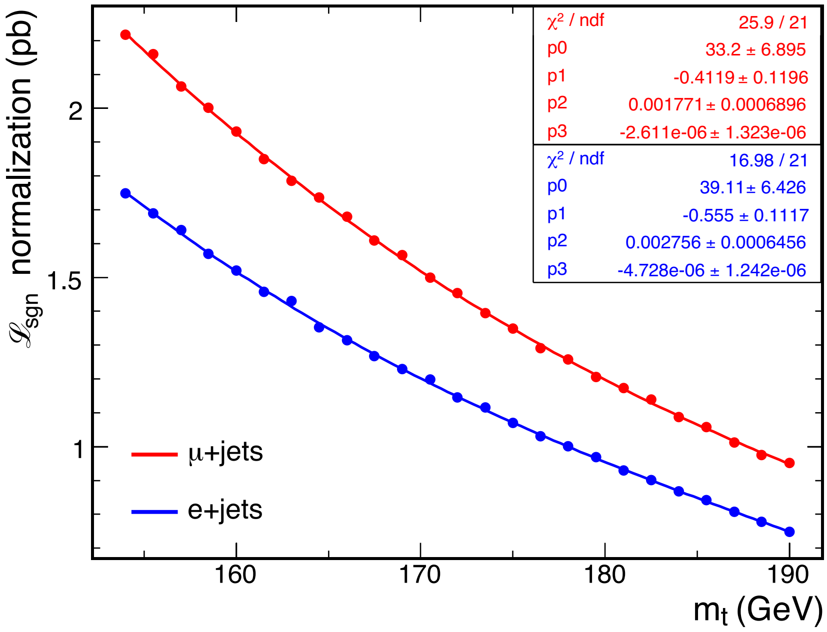

Figure 6.2: Normalization of the signal likelihood for the parton level studies.

the e+jets and μ+jets decay channels. The normalization is fitted by a 3^{rd}-order polynomial with the parameters given in the same figure. The difference between the two decay channels results from the different η_{det} cuts for electrons and muons, limiting the respective phase space.

For the background likelihood normalization, ensembles with different signal fractions are generated. To minimize statistical fluctuations, the ensemble size is maximized with respect to the available pool sizes. In this case, the ensembles contain 1000 events allowing for background fractions of up to 85% in the e+jets channel. Ensembles are generated with signal fractions of 20% to 80% in steps of 10% in the e+jets and between 10% and 70% in the μ+jets channel. The background likelihood normalization is fitted with a 1^{st}-order polynomial. The normalization and its parameterization is shown in Fig. 6.3. The dashed line indicates the signal fraction used in the ensemble tests. It is apparent that the background normalization depends slightly on the signal fraction. This might be caused by the fact that the background likelihoods are evaluated with `VECBOS`, whereas the simulated samples are produced with `ALPGEN`. As described in Sec. 5.4, several approximations are made in the calculation of background likelihoods which could influence the background normalization as well. Nevertheless, this effect does not represent a possible source of uncertainty as the method and thus the normalization need to be fixed, whereas all possible systematics have to be evaluated by changing the input parameters. Hence, this effect is taken care of by the calibration of the signal fraction and its systematic uncertainty (cf. Fig. 6.29 and Sec. 6.5.1).

6.2.4 Pure Signal Studies

As the method contains several innovations compared to earlier measurements the parton level studies are used to validate the method. In a first step, tests are performed on ensembles being composed of

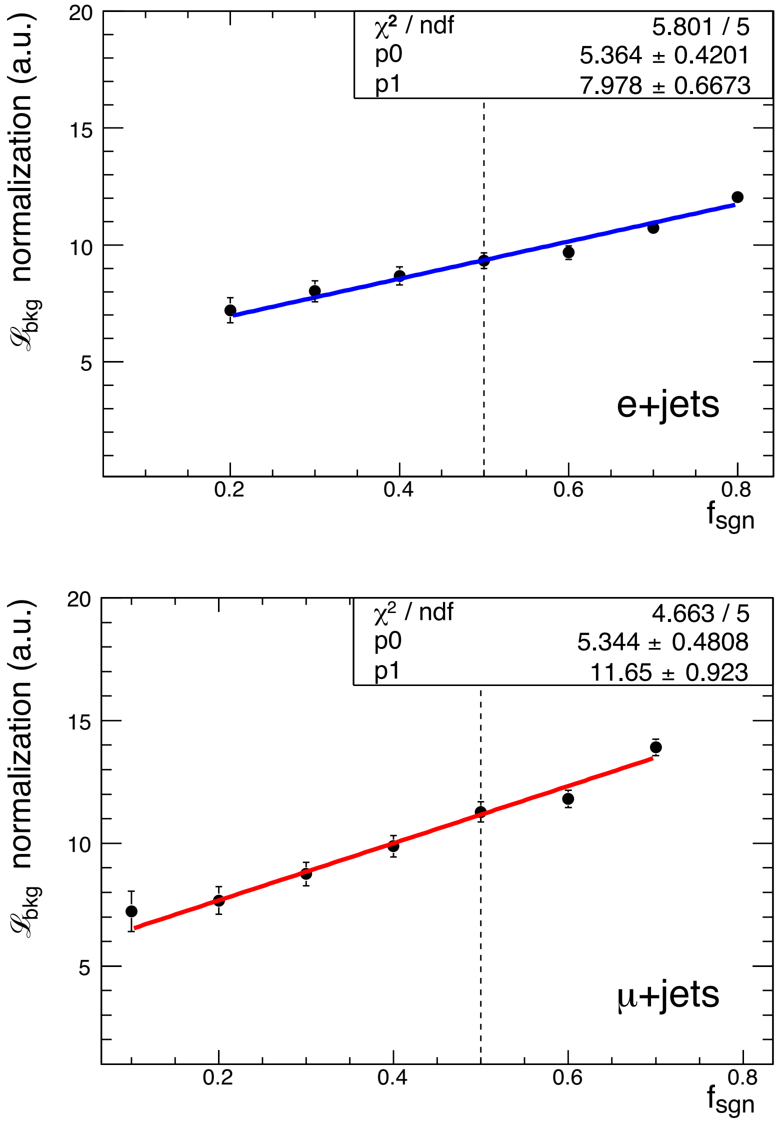

Figure 6.3: Normalization of the background likelihood for the parton level studies.

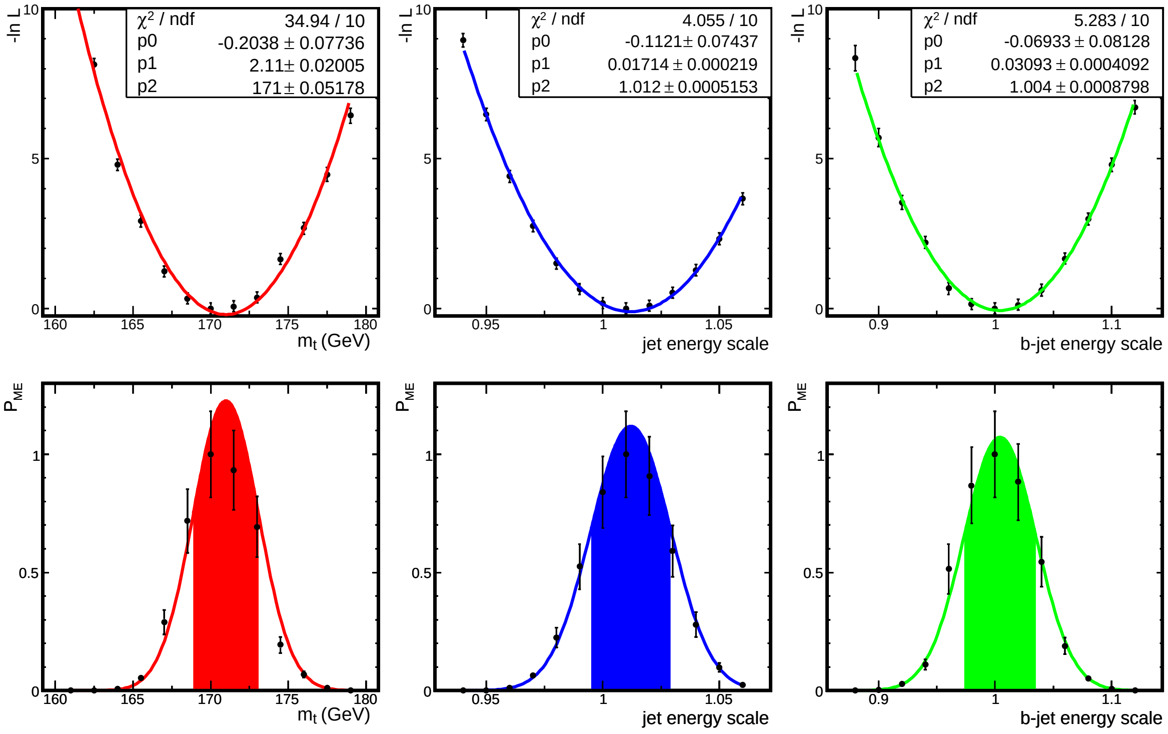

Figure 6.4: Ensemble fit for an arbitrary ensemble with generated values of m_t = 170 GeV, s_{jes} = 1.0 and s_{bjes} = 1.0. *Top*: negative signal log-likelihood. *Bottom*: signal probability, with the filled area indicating the integral of 68% probability.

pure signal events. This is the most idealized test case and should show no deviations from the expectations. Thus, the reconstructed fit observables should resemble the generated input values within statistical uncertainties and the pull widths are expected to be equal to unity (within errors). For these studies, ensembles are composed of 100 events each. A total of 1000 ensembles is produced and fitted per calibration point. If not stated otherwise, the ensembles contain e+jets events only as there is no intrinsic difference for the method between the two types of decays. The background likelihoods are not included in this study.

Mass Calibration

Masses are generated at 160 GeV, 165 GeV, 170 GeV, 175 GeV and 180 GeV. The 170 GeV mass point with $s_{jes} = s_{bjes} = 1$ is taken as default. Figure 6.4 shows the likelihood fit for an arbitrarily chosen ensemble. The minima of the log-likelihoods are set to zero as the absolute likelihood normalization is unimportant. The error bars indicate the integration uncertainty and are considered by the fit. However, the statistical uncertainty of the fit observables is based on the width of the likelihood gaussians. As one can see, the log-likelihood points agree well with a parabola. No deviations in the tails can be found in this ideal case. The fluctuations in the top mass points are larger than for the

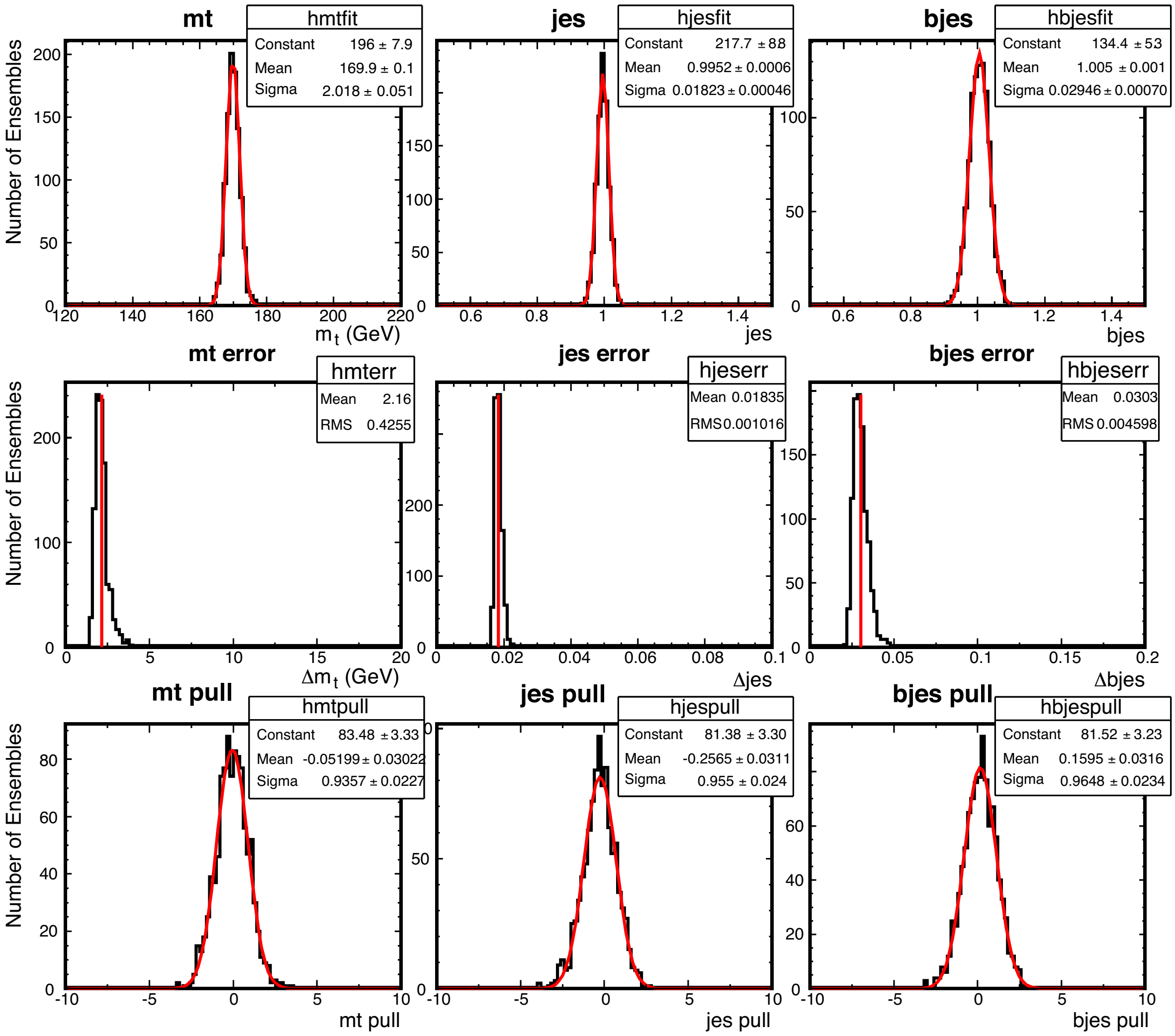

Figure 6.5: Ensemble test for the m_t = 170 GeV calibration point. For each of the observables m_t, s_{jes} and s_{bjes} the distributions of the reconstructed value, its error and the pull are shown.

other two fit observables. This can be explained by the fact that the integrations for all s_{jes} and s_{bjes} points are performed in one turn, whereas for the top mass the integration is restarted for each input value. The sampling points used by the numerical integration are thus fixed for s_{jes} and s_{bjes}, but they are rederived for every m_t hypothesis. This is due to technical reasons. In the ensemble tests, these integration fluctuations cancel out on average due to the large number of ensembles included.

In Fig. 6.5 the ensemble test for all 1000 ensembles for the m_t = 170 GeV calibration point is shown. In order to prevent any biases due to quality cuts, the fit range for the different observables is very wide, as shown in the histograms. It is chosen such that even for extreme conditions where the distributions become very wide not more than about 10% of the ensembles are lost. These extreme cases are for instance background tests, where the signal fractions approach zero. For the same reason and in contrast to former measurements [98] no cut on the χ^2 of the likelihood fit is applied.

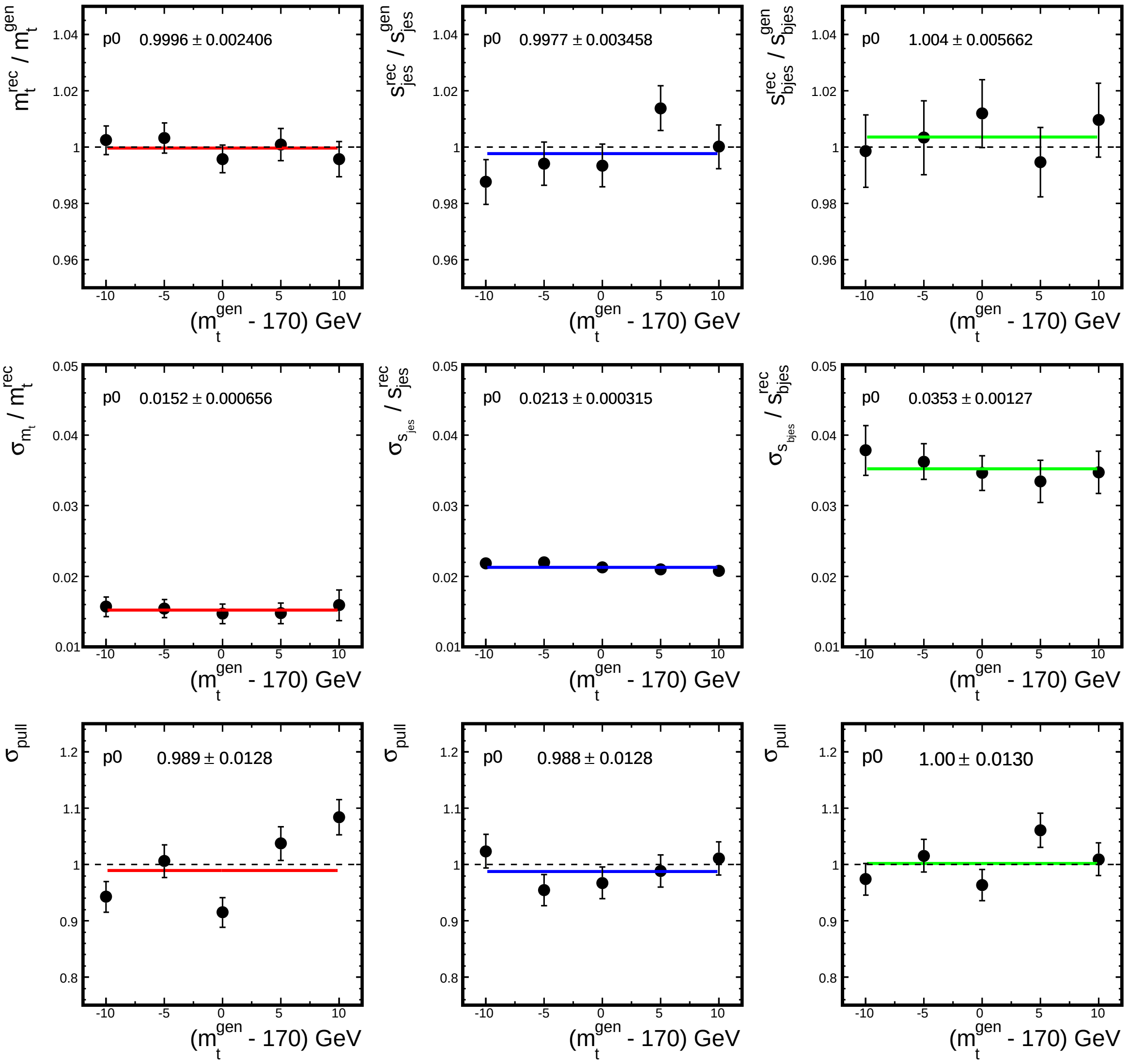

Figure 6.6: Mass calibration for pure *e*+jets signal events without *b* identification probabilities included.

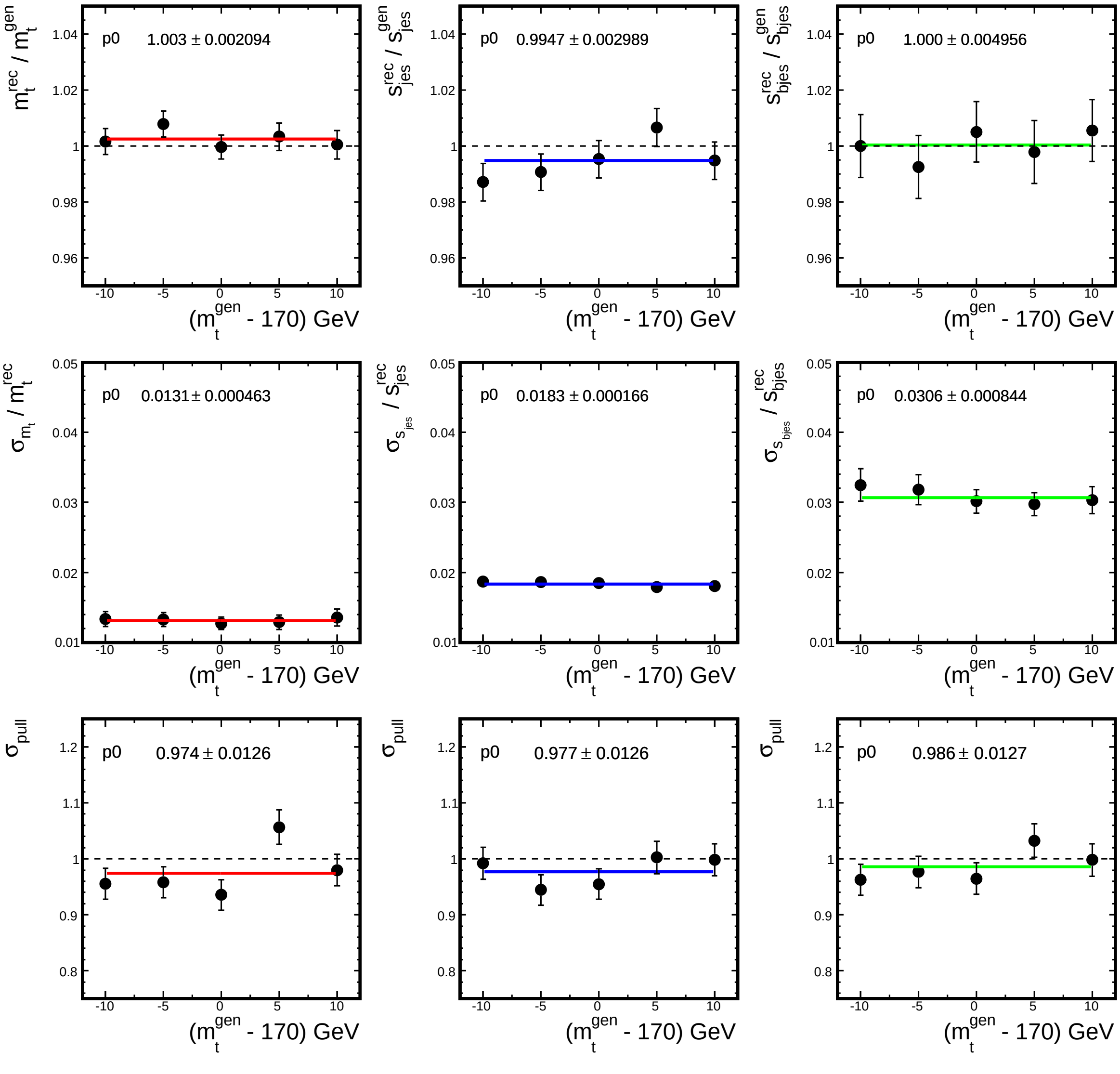

Figure 6.7: Mass calibration for pure e+jets signal events including b identification probabilities.

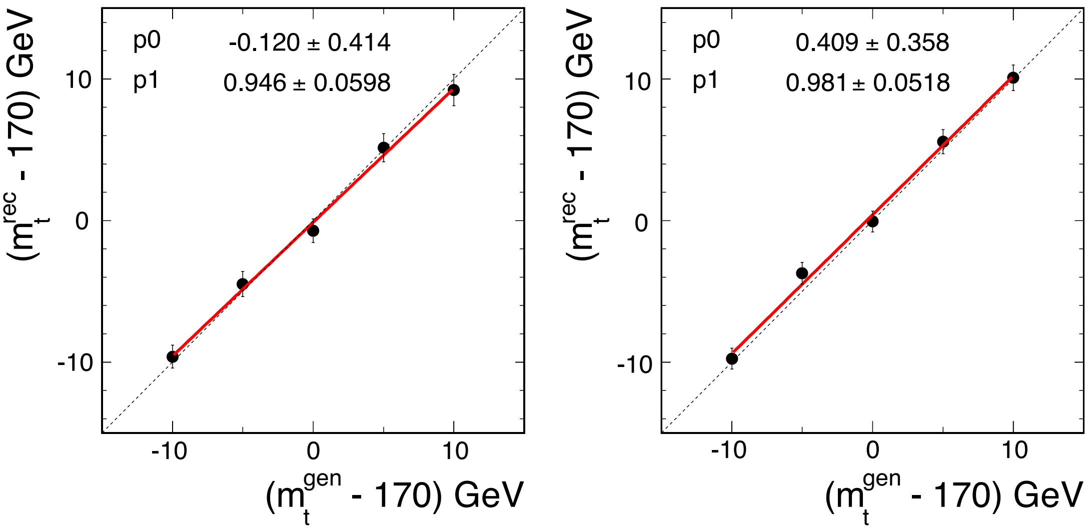

Figure 6.8: Mass calibration curves. *Left*: e+jets, without use of b identification probabilities. *Right*: e+jets, with use of b identification probabilities.

The full mass calibration can be found in Fig. 6.6 and Fig. 6.7. The first figure only includes the topological signal likelihoods, whereas the second one makes use of the b identification probabilities introduced in this analysis as well. The top row shows the fitted values of the three observables m_t (red), s_{jes} (blue) and s_{bjes} (green) divided by their respective input values. Thus, the expectation is a flat line at the value of 1.0 for all calibration points (indicated by the dashed lines). It can be seen that this expectation is well fulfilled within errors. The middle row gives the relative statistical errors for the three fits. They lie in the range between 1.5% and 3.5% for the three observables. The bottom row presents the pull widths. As stated above, if the method works, they should be equal to one (indicated by the dashes line). Again, within errors this expectation is well fulfilled. Due to the additional information used, the statistical errors in the middle row decrease as expected. The effect is about 16% for all three fit observables. In addition to this reduction of the expected statistical uncertainties, the inclusion of b identification information also improves the quality of the calibration. This effect is shown in Fig. 6.8, where the mass calibration, i.e. reconstructed versus the generated top mass, is presented for the two cases. The fit with solely topological likelihoods exhibits a slope of 0.94 ± 0.06. The fit with b identification probabilities included improves that to 0.98 ± 0.05. Although the difference is small and the two values agree with each other and with unity within errors, this is a general trend in all calibrations.

Jet Energy Scales Calibration

The jet energy scale factors are set up in such a way that they are independent from each other: s_{jes} only applies to light jets, s_{bjes} only affects b jets. Therefore, the calibration can vary one of them exclusively or both simultaneously. These three cases are shown in Fig. 6.9-6.11. In the first one s_{jes} is varied between 90% and 110% in steps of 5%, where 100% stands for the nominal D0 jet energy scale. Fig. 6.10 modifies the jet energy scale for b jets between 80% and 120% in 10% increments.

point #	1	2	3	4	5
s_{jes}	0.9	0.9	1.0	1.1	1.1
s_{bjes}	0.8	0.9	1.0	1.1	1.2

Table 6.3: Calibration points for the simultaneous variation of s_{jes} and s_{bjes}.

The larger range and step size in s_{bjes} compared to s_{jes} is motivated by the fact that the constraint for s_{bjes} is weaker and thus the likelihood distributions are wider. The other scale factor is fixed to 1.0 in both cases. As the nominal jet energy scale represents a special point in the hypotheses grid, also a simultaneous variation (from unity) of both scale factors is studied. The five calibration points in Table 6.3 are chosen to allow such a simultaneous variation while still keeping them reasonably similar. As the nominal D0 jet energy scale is a good approximation for all jets (in first order), the difference between the two is not expected to be large.

Figures 6.9-6.11 exhibit a good agreement of the fits with the expectations. The statistical errors agree in all three calibrations. The pull widths are somewhat smaller than the expectations of one (0.92-0.99) indicating that the statistical errors have been overestimated slightly. The calibration curves for the same three cases are drawn in Fig. 6.12. As for the mass calibration, the slopes exhibit perfect agreement with unity and the biases lie in the permille range.

μ+jets Mass Calibration

In order to show that the method works for smeared lepton events, i.e. μ+jets decays as well, a mass calibration is performed (cf. Fig. 6.13). It demonstrates again the power of the method, although the fluctuations especially in the pulls are somewhat larger than in the case of e+jets events. A possible explanation is the additional muon momentum integration which introduces a new source of fluctuations. The s_{jes} fit agrees very well with the fits in the e+jets case as it is only constrained by the two jets stemming from the W decay. In contrast, the m_t and s_{bjes} fits incorporate the (smeared) lepton in their constraints and are thus affected by the additional source of uncertainty. It is apparent that in these cases the statistical errors are underestimated by around 7%. Nevertheless, the calibration curves in Fig. 6.14 with a comparison of the e+jets and μ+jets mass calibration still exhibit a reasonable slope of 0.97 ± 0.04 for the latter decay. The bias increases from about 400 MeV to 700 MeV when switching the lepton smearing on.

6.2.5 Studies Including Background

For the studies including background the 1000 ensembles are composed of 200 events each. Due to the limited statistics available for the W+jets sample, ensemble tests are performed for a signal fraction of 50%. This corresponds to the same number of signal events as in the pure signal studies. In the following, the dependencies on various sources of background and on the estimated signal fraction are studied. For completeness, the calibrations for the three fit observables are added in App. B. As they give no qualitatively new information compared to the studies presented so far, they are not discussed further.

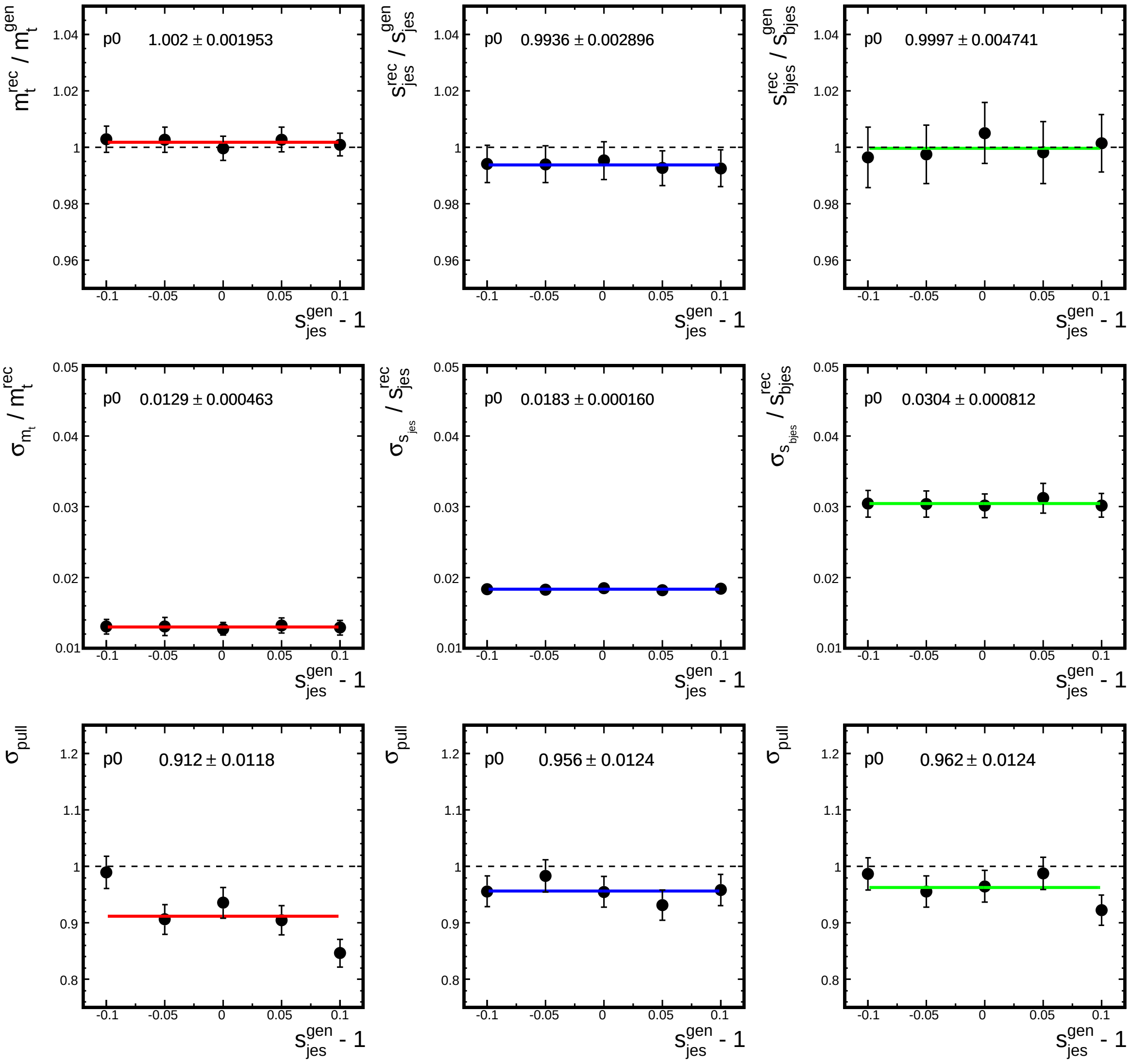

Figure 6.9: s_{jes} calibration for pure e+jets signal events.

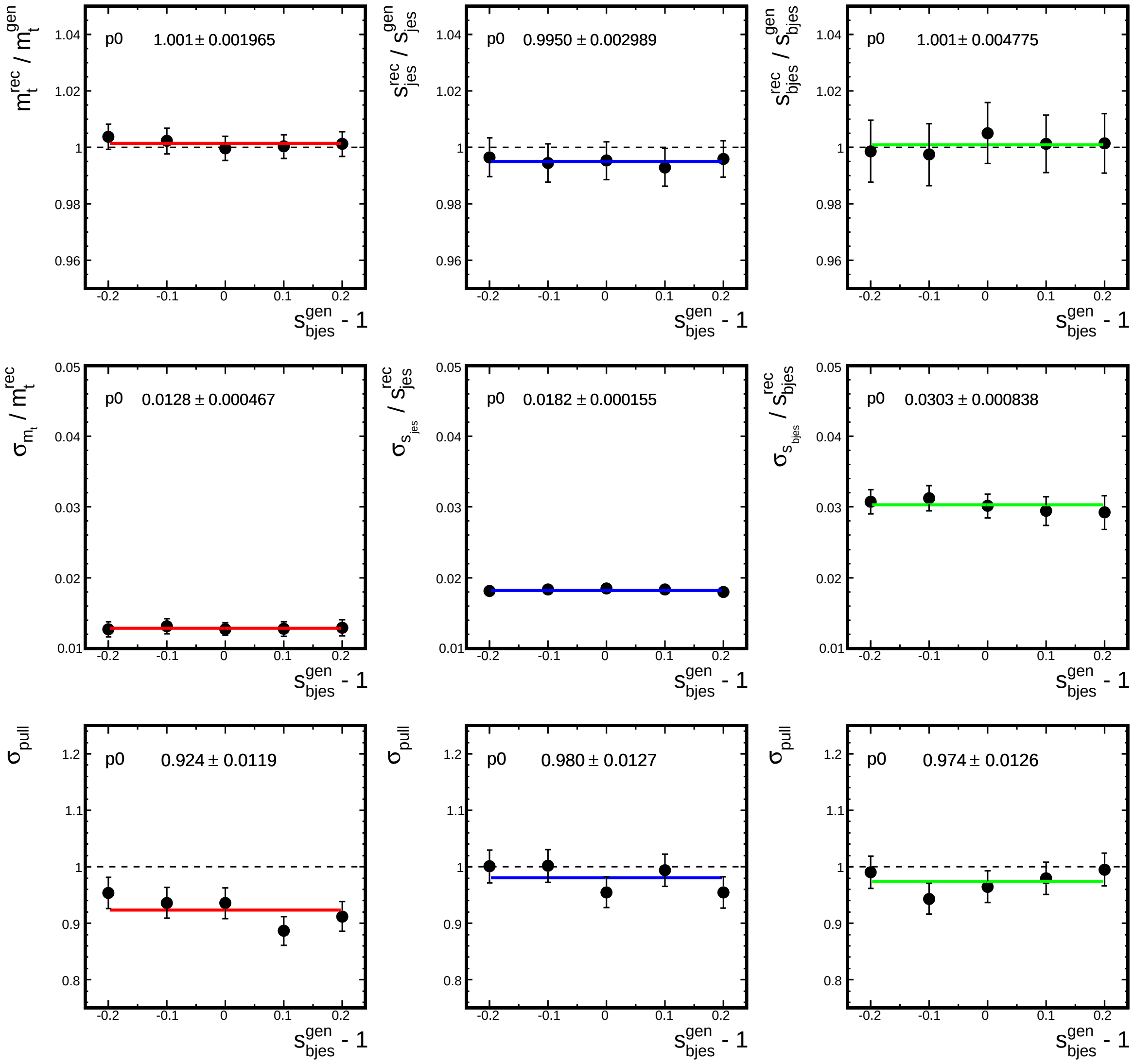

Figure 6.10: s_{bjes} calibration for pure e+jets signal events.

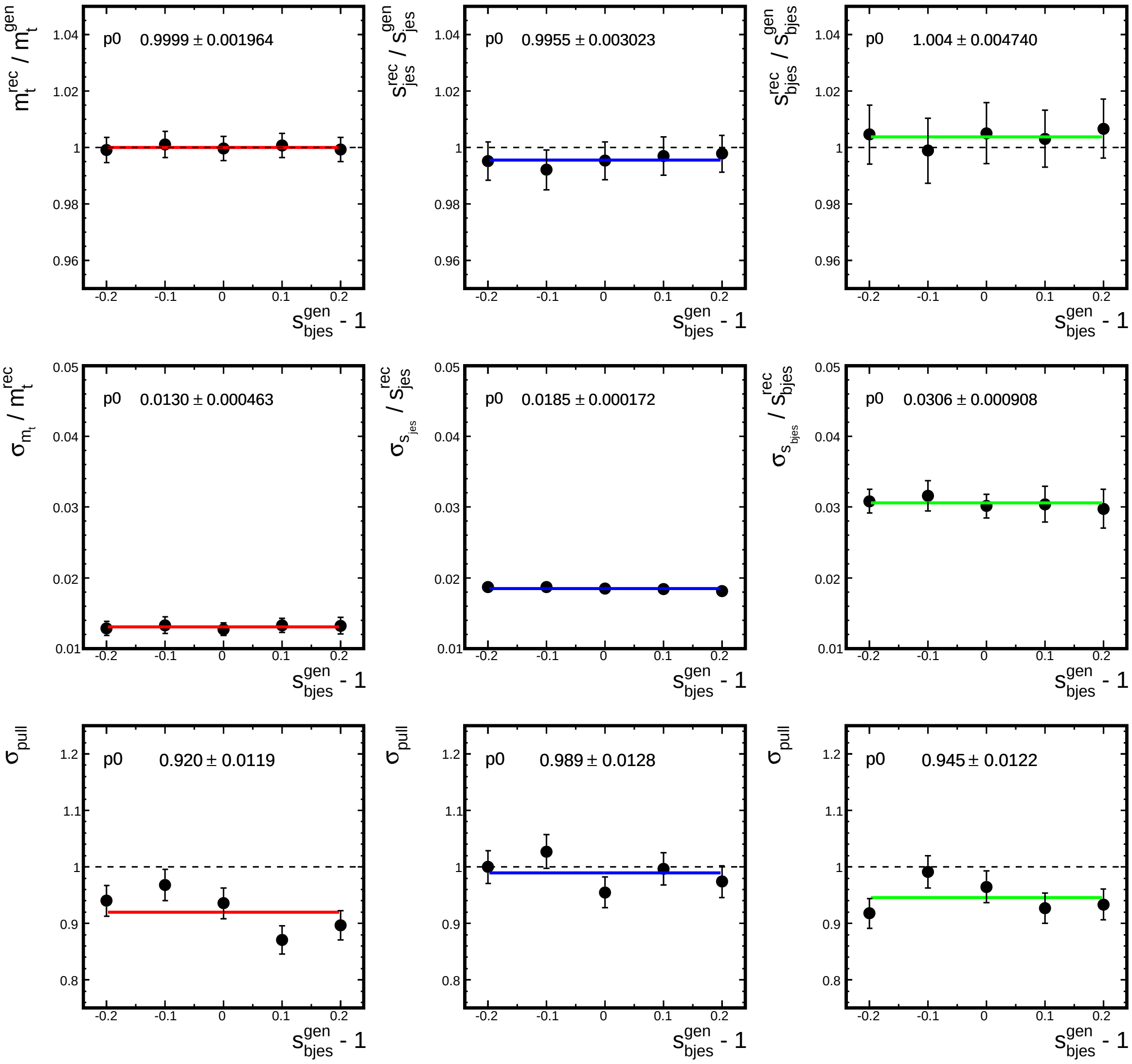

Figure 6.11: s_{bjes} calibration for pure e+jets signal events. s_{jes} and s_{bjes} are varied simultaneously according to Table 6.3.

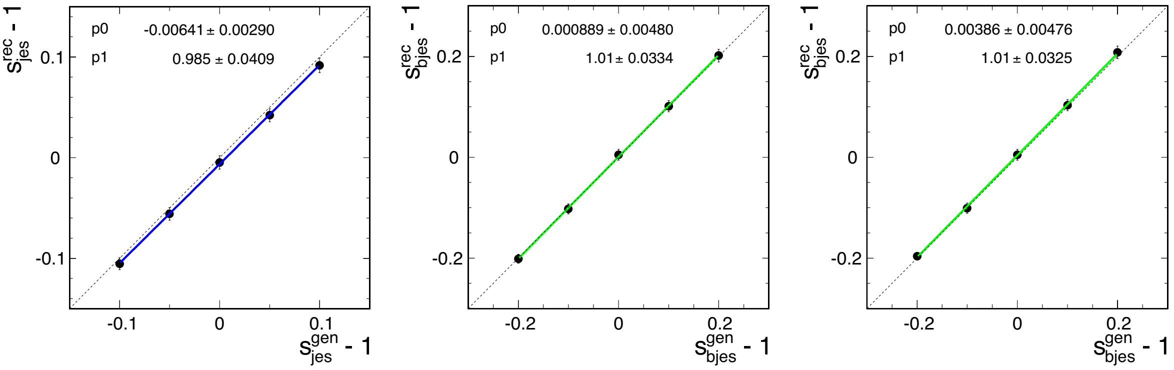

Figure 6.12: Calibration curves for pure e+jets signal events. *Left*: s_{jes} variation. *Middle*: s_{bjes} variation. *Right*: s_{jes} and s_{bjes} variation.

W+4**lp Background**

In order to study the effects of background on the fits and to find out how much the introduction of background likelihoods helps, Fig. 6.15 and Fig. 6.16 show calibrations with the fraction of W+4lp events varied between 0% and 90% in 10% steps. The first figure only includes signal likelihoods whereas the second calibration additionally makes use of the background likelihoods. When background likelihoods are not included, the mass fit starts to significantly deviate from the generated values at fractions of around 30% background. At 90% background fraction the deviation reaches 6%. The s_{jes} and s_{bjes} fits exhibit a more linear behavior, leading to deviations of 6% and 4%, respectively, at $f_{bkg} = 90\%$. The pull widths of up to 1.5-2.0 show that the error estimate fails in this case as well.

On the other hand, if background likelihoods are included as depicted in Fig. 6.16, the top mass fit works very well up to background fractions of 80%. The reconstructed mass agrees with the expectation and the error estimates are much better as demonstrated by the nearly flat distributions of the pull widths. Only the s_{jes} and s_{bjes} fits still exhibit steeply falling distributions. This should be attributed to the fact that the background likelihoods are not varied in the two s_{jes} and s_{bjes} hypothesis dimensions. As stated before, the independence of the background likelihood on the top mass is a good assumption, whereas it is only an approximation for the other two observables.

W+bb+**jj Background**

An important aspect of the background which was not considered until now is the fraction of W+bb+jj events. As these contain two ”real” b quarks, they resemble the signal more than W+4lp events do and the b identification probabilities cannot help in their case. Figure 6.17 depicts the dependence on the (absolute) W+bb+jj fraction. The ensembles are built in such a way that the signal fraction is fixed at 50%, while the W+bb+jj fraction varies between 0% and 50%. The rest of the events are drawn from the W+4lp pool so that the total background fraction is fixed to 50% as well. The calibration makes clear that the dependence on this background component is small. Even if the background consists of 100% W+bb+jj events, the top mass deviates less than 1% from the generated value. The

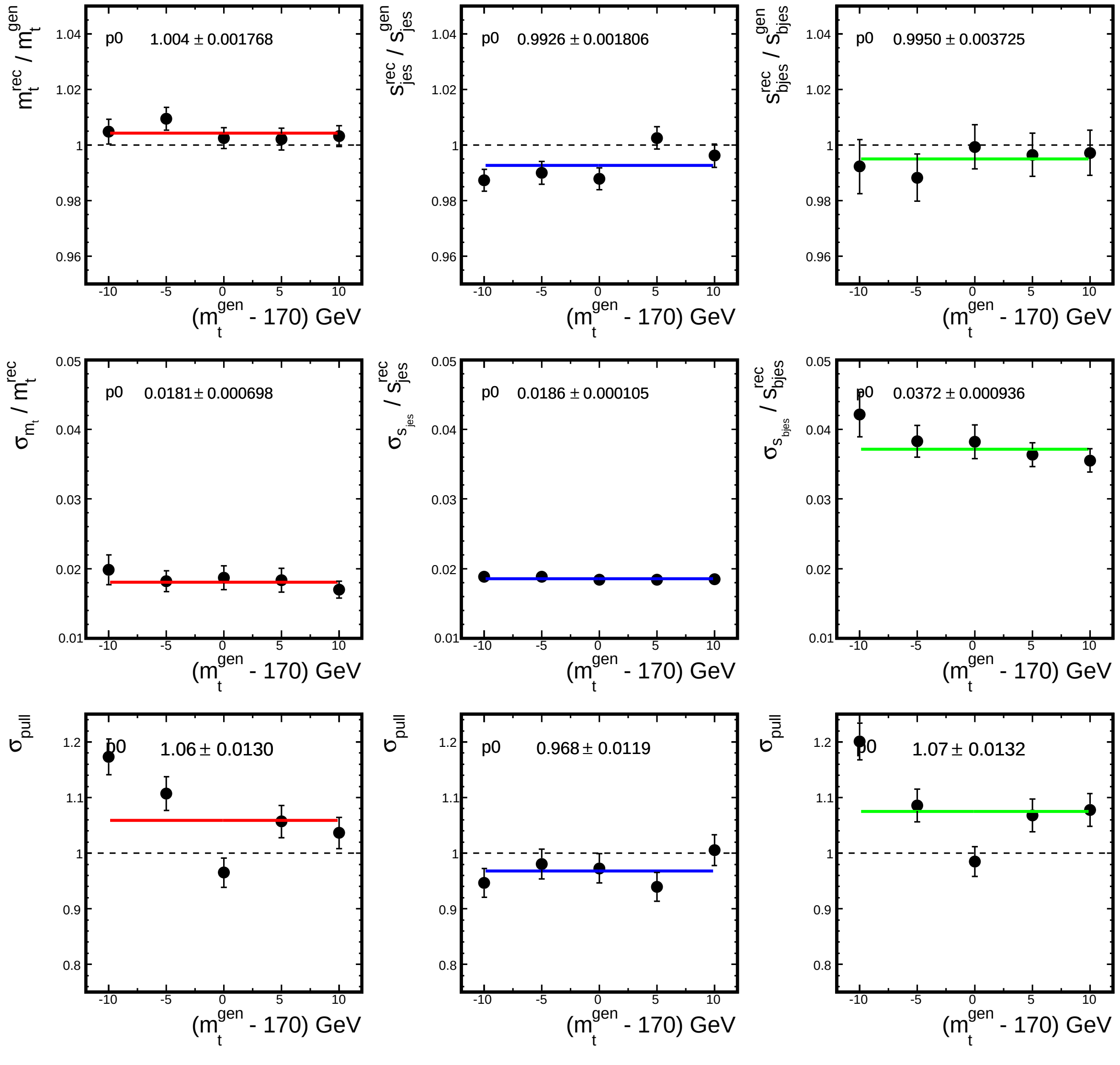

Figure 6.13: Mass calibration for pure μ+jets signal events.

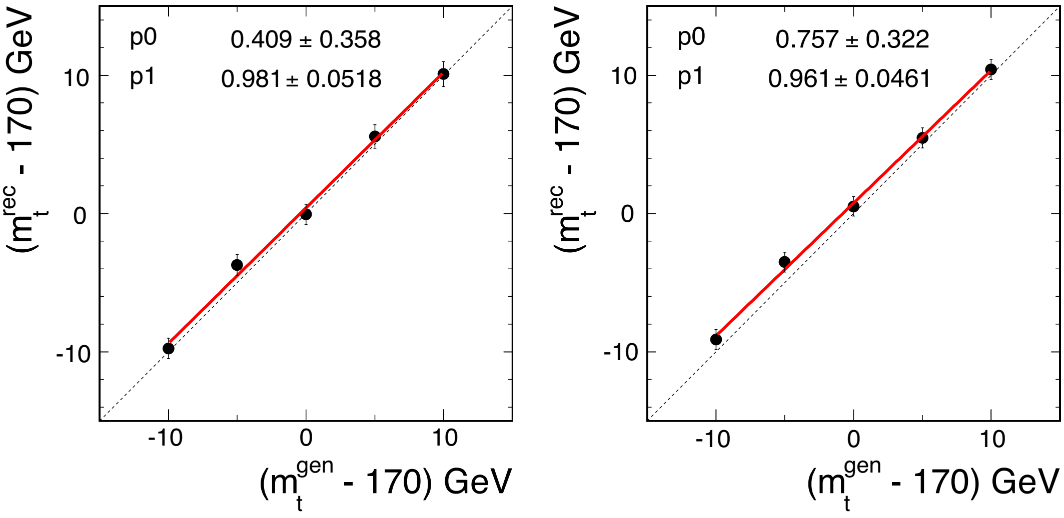

Figure 6.14: Mass calibration curves. *Left*: e+jets decay. *Right*: μ+jets decay.

distributions for the s_{jes} and s_{bjes} fits show the same behavior: they are almost flat compared to the large dependence of the fits on the total background fraction.

$t\bar{t}$ Events with an Additional Parton

A different kind of background are $t\bar{t}$ events with an additional parton from initial or final state radiation (*ttljj*, following the nomenclature in Table 6.2). In this case, the transverse momentum of the $t\bar{t}$ system is nonzero and the balance in the transverse plane becomes disturbed. Thus, neither the top mass fit nor the s_{bjes} fit are expected to work perfectly. Figure 6.18 contains the calibration versus (absolute) ttljj fraction. Again, the signal and background fractions are fixed to 50%, but in this case the signal part is mixed from the standard $t\bar{t}$ pool (*ttlj*) and the ttljj pool, whereas the background contains only W+4lp events. The plots exhibit a similar behavior as in the case of including background events without background likelihoods (cf. Fig. 6.15). This is not surprising because the situation is comparable: the signal events with an additional parton constitute a new source of background which is not described by the method (i.e. neither signal nor background likelihoods). Thus, with growing fractions of this process the deviations from the expectation increase. However, as this ”background” is more signal-like and the additional parton is considered in the s_{jes} and s_{bjes} hypotheses, their fits are hardly affected, exhibiting nearly flat distributions.

Signal Fraction Dependencies

When background is included, the reconstructed signal fractions become an important aspect of the fits. Figure 6.19 gives an overview of the reconstructed versus generated fractions for the three different types of background discussed above. In Fig. 6.19(a), the calibration of the signal fraction itself is shown. As the matrix element method only considers W+4lp events in the background likelihood, the signal fraction calibration contains only W+4lp background as well. It can be seen that the calibration

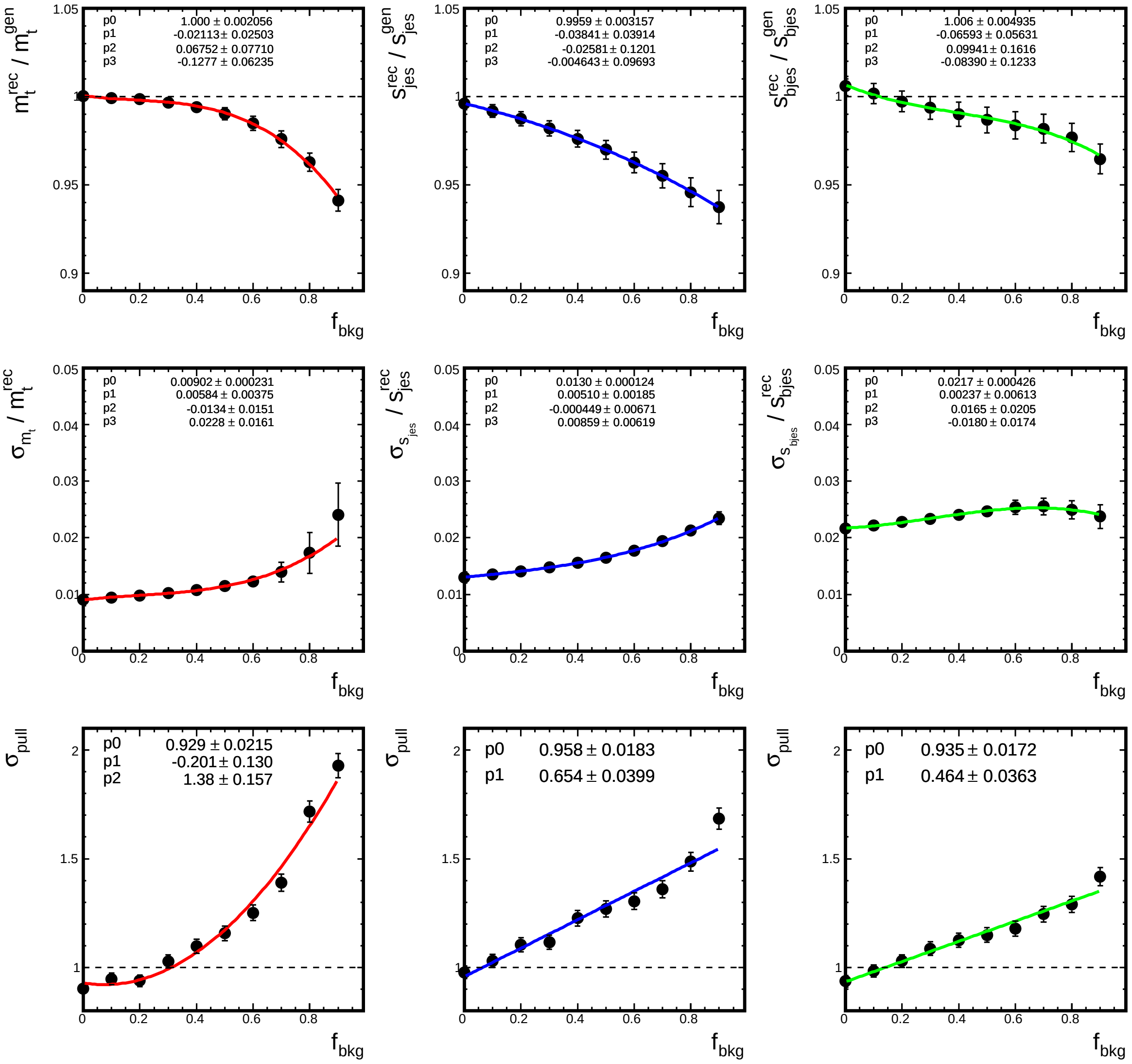

Figure 6.15: Background fraction calibration for pure e+jets events. No background likelihoods are included.

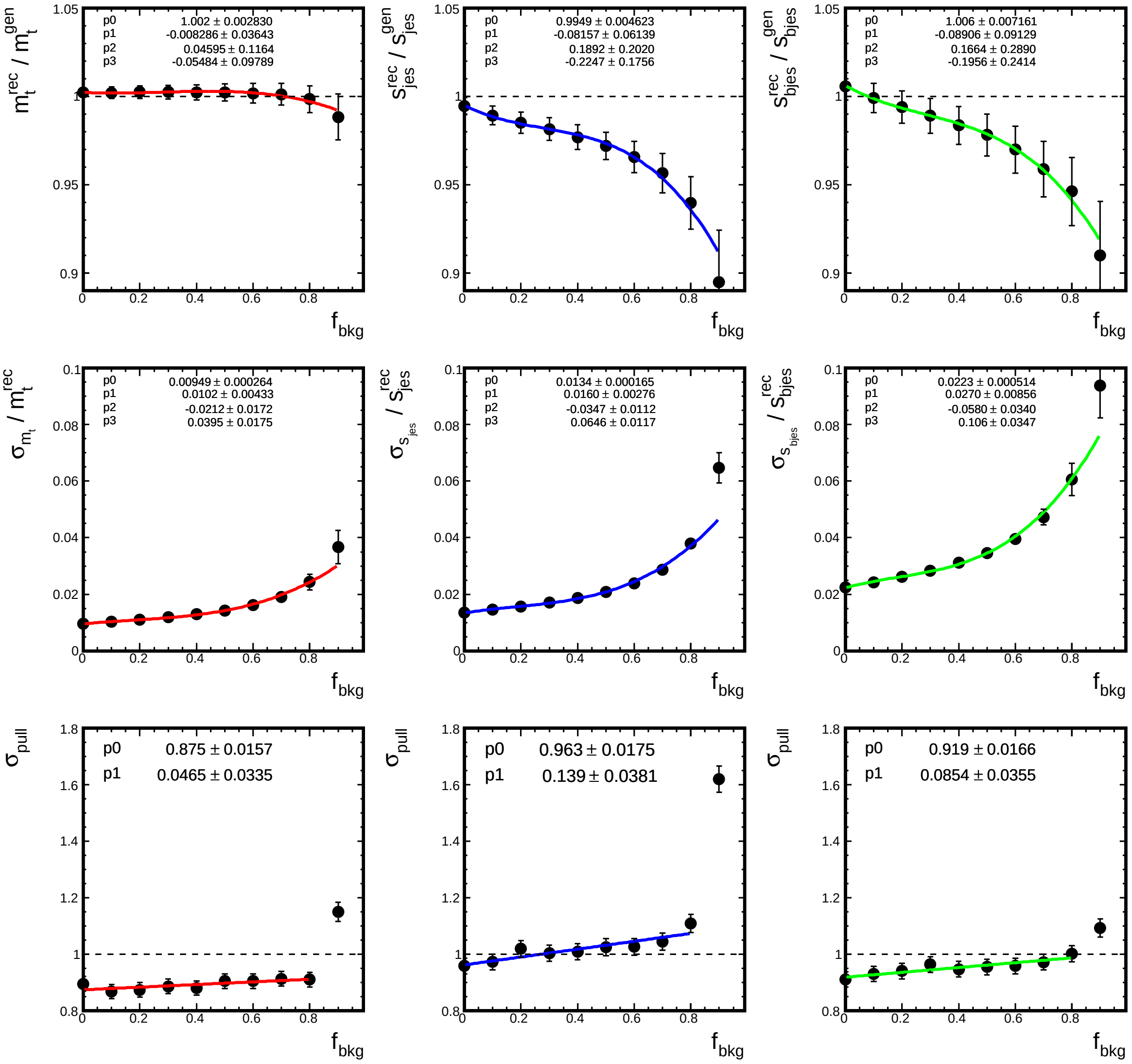

Figure 6.16: Background fraction calibration including background likelihoods.

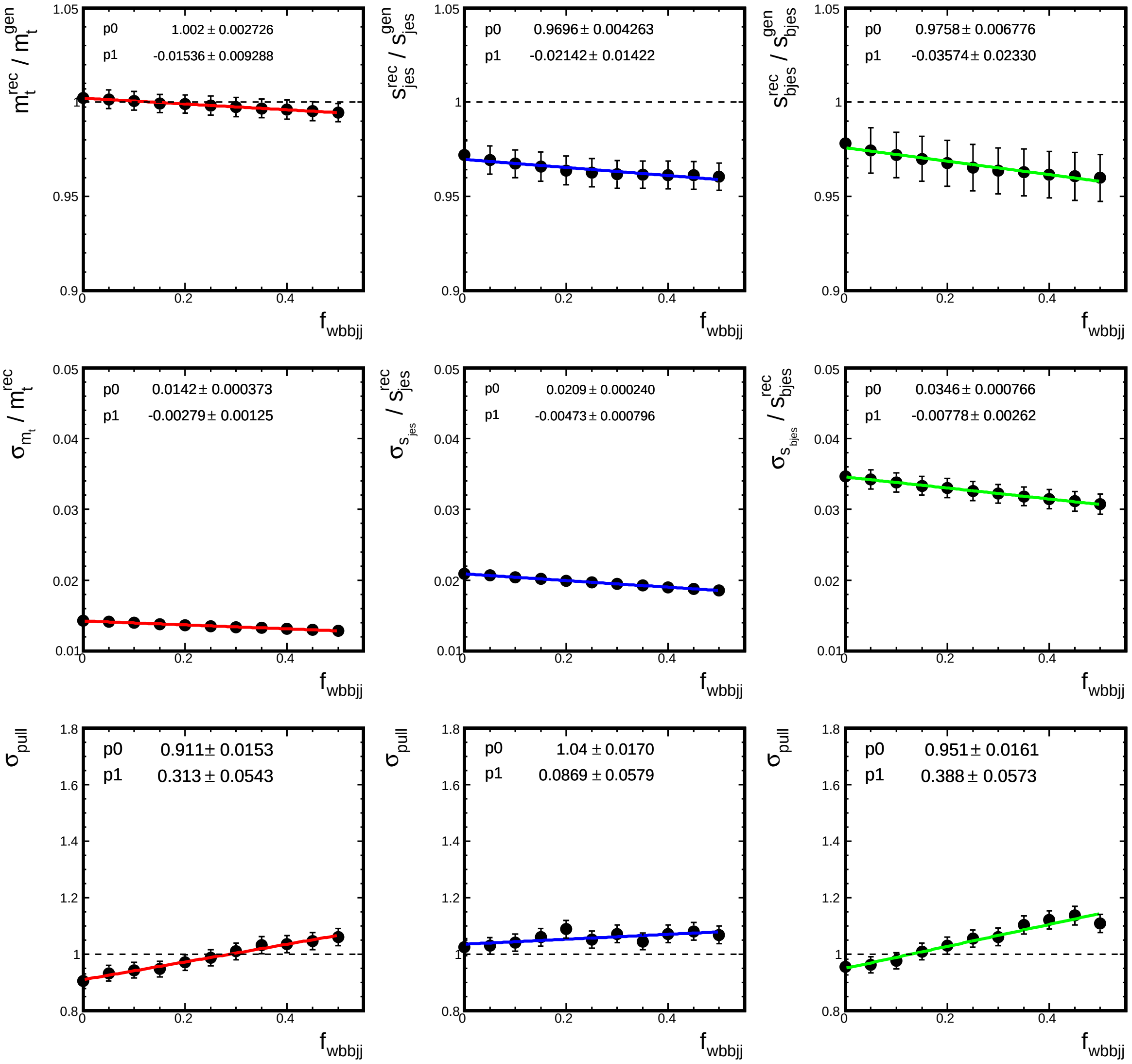

Figure 6.17: Calibration for the W+bb+jj fraction.

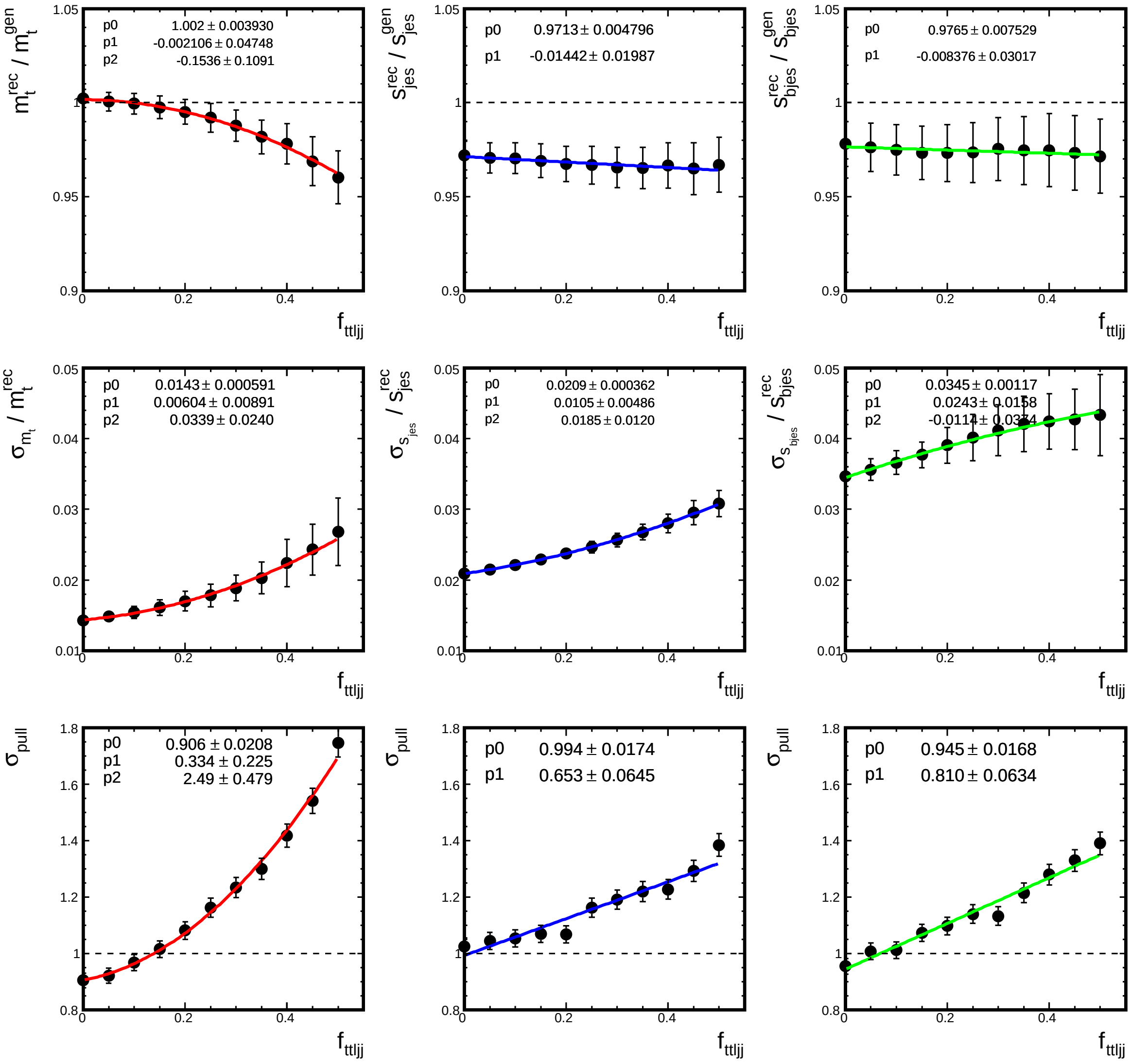

Figure 6.18: Calibration including events with an extra parton in the final state (ttljj). Background likelihoods are included.

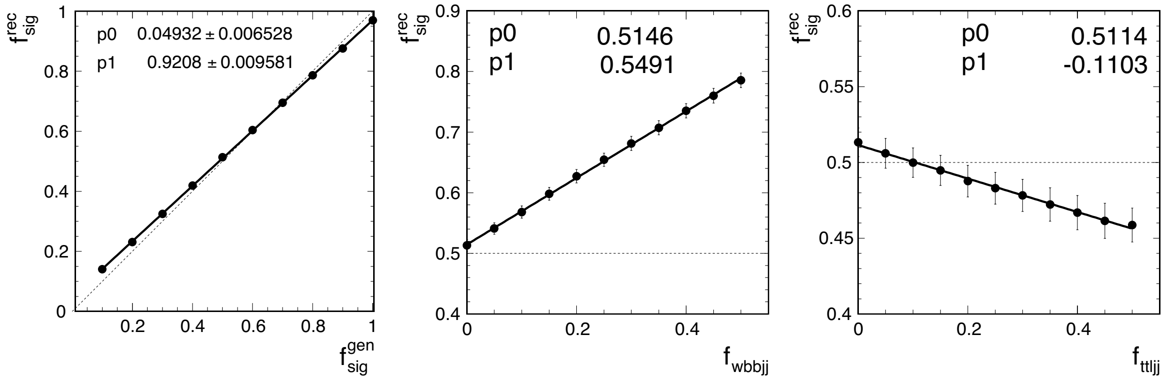

(a) $W+$4lp calibration (b) $W+bb+$jj calibration (c) ttljj calibration

Figure 6.19: Signal fraction calibration curves for the different types of background.

curve follows the ideal case with a slope of 1.0 quite well, although its slope of 0.92 is slightly smaller. The discrepancy to the ideal curve can be explained by the fact that the background normalization is only correct for the assumed signal fraction of 50%. For other values the background normalization deviates as can be seen in Fig. 6.3. In the opposite sense, because the background normalization is a constant factor in the method, the signal fraction is not perfectly reconstructed for values other than 50%. If one checks Fig. 6.19a in detail, one observes a small bias at the nominal signal fraction of 50%. Here, the reconstructed signal fraction gives 50.97%. Such small discrepancies can be easily explained by fluctuations in the background normalization as can be found in Fig. 6.3 for the $f_{sgn} = 0.6$ point.

For the other two types of background shown in Fig. 6.19(b) - (c) their different nature becomes visible in the signal fraction calibration. If none of these $W+bb+$jj or ttljj events are included, the signal fraction is reconstructed at the 51% value expected from the $W+$4lp calibration. However, as more of these events are included the reconstructed signal fraction diverges from this expectation. Due to the fact that the $W+bb+$jj background looks more signal like than $W+$4lp, the reconstructed signal fraction rises with higher f_{wbbjj}. In contrast, the ttljj signal process resembles the background more than pure $l+$jets events. Thus, the signal fraction falls with higher f_{ttljj}. In addition, the figure reveals that the effect of $W+bb+$jj events on the signal fraction is stronger than for ttljj events. At $f_{wbbjj} = 0.5$ (absolute), which corresponds to a background composition of 100% $W+bb+$jj events, the signal fraction is 27% higher than for pure $W+$4lp background. In the ttljj case, the difference is only 5.5%.

In Figure 6.20 the reconstructed signal fraction is shown versus the m_t, s_{jes} and s_{bjes} calibration points. For the default value (m_t = 170 GeV, $s_{jes} = s_{bjes} = 1$), the reconstructed signal fraction is 51% as for the background calibrations mentioned above. Nevertheless, deviations from this default value yield different reconstructed fractions. All three distributions exhibit a falling behavior, i.e. the signal fraction decreases with higher values of m_t, s_{jes} or s_{bjes}. For m_t and s_{jes} the deviation in f_{sig}^{reco} between the default and the most extreme input values is 3.8%. In the s_{bjes} case one obtains a difference of 5.8%. Thus, for the matrix element method the signal looks more background like for higher values of the fit observables.

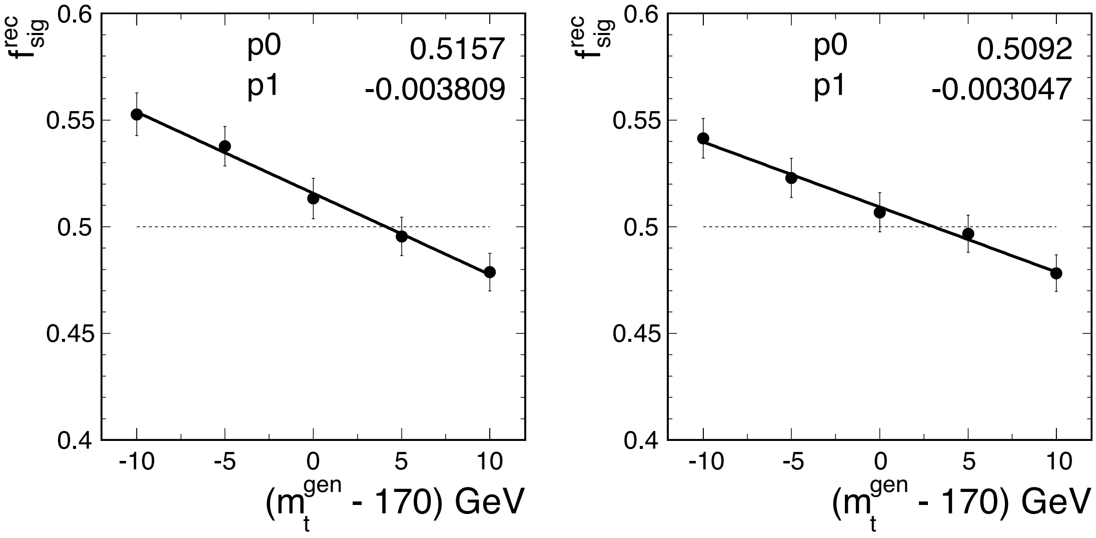

(a) m_t calibration (e+jets)

(b) m_t calibration (μ+jets)

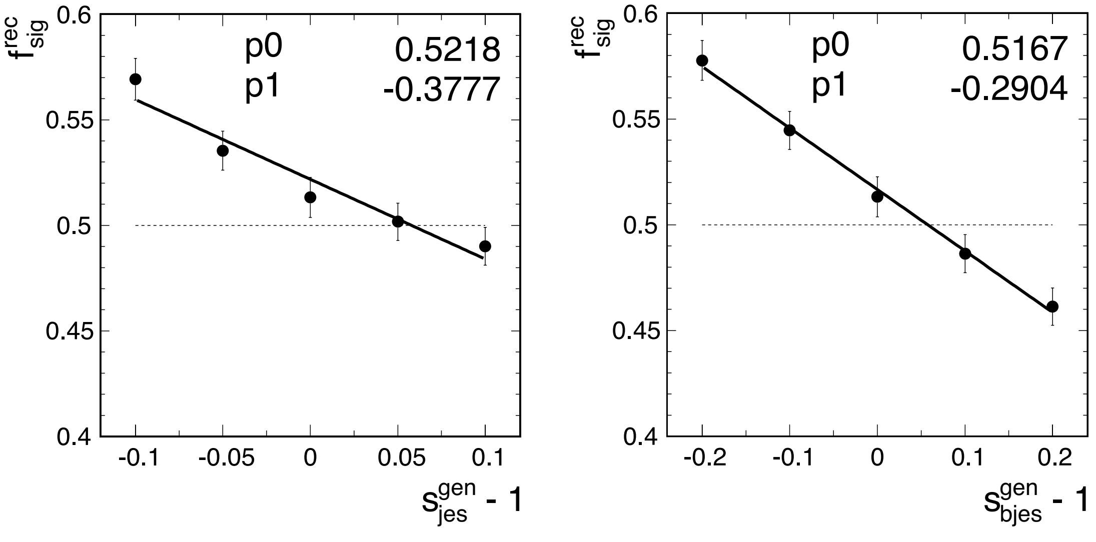

(c) s_{jes} calibration (e+jets)

(d) s_{bjes} calibration (e+jets)

Figure 6.20: Signal fraction calibration curves for the three fit observables. The ensembles include 50% W+4lp background.

6.3 Method Calibration

In order to obtain a calibration applicable to measured data, ensemble tests on fully simulated events need to be performed. For this analysis, Monte Carlo samples of W+jets background and $t\bar{t}$ signal are used. They are generated according to the ”matched `ALPGEN` + `PYTHIA`” scheme. This means `ALPGEN` [95] is used to generate the parton-level matrix elements, `PYTHIA` [94] performs the shower evolution and hadronization and the `MLM` matching scheme [109] is applied afterwards. The matching removes possible overlap between the hard partons created by the matrix elements and the parton shower in an event. The `MLM` matching also attempts to fill gaps in the phase space left unpopulated by less sophisticated event generators.

An overview of the Monte Carlo samples used in this analysis is given in Sec. 6.3.1. The determination of the signal and background fractions can be found in Sec. 6.3.2, followed by the normalization of the signal and background likelihoods in Sec. 6.3.3. The ensemble tests are constructed according to these fractions and the calibration curves for the data measurement are finally derived in Sec. 6.3.4.

6.3.1 Overview of Monte Carlo Samples

To obtain a meaningful Monte Carlo sample exclusive and inclusive light parton multiplicity bins must be combined. For the signal process these are $t\bar{t}+0lp$, $t\bar{t}+1lp$ (both excl.) and $t\bar{t}+2lp$ (incl.). The $t\bar{t}$ system is forced to decay semileptonically in the event generator and the number of light partons indicates the presence of additional partons in the hard process. For the event generation a scale defined by $m_t^2+\sum p_T^2(\text{jets})$ is used. Five signal samples at generated top quark masses of 160 GeV, 165 GeV, 170 GeV, 175 GeV and 180 GeV are available. An overview of the subsample composition and size of the event pools for the different input masses can be found in Table 6.4. As is the case for the parton level studies, the event pool sizes are limited by the computation time needed for the likelihood evaluation in the signal process case and by the total number of selected events in the background process case.

Both signal and background samples are produced with `CTEQ6L1` parton density functions [82] and run through a full `GEANT3` [110] detector simulation with `D0gstar` [111]. The reconstruction and analysis chain described in Sec. 6.1 is the same one as used for the data samples.

The W+jets background is composed of 11 subsamples listed in Table 6.5, combining W+jj, $W+b\bar{b}$ and $W+c\bar{c}$ contributions. The W is forced to decay leptonically during the generation, the jets stem from the additional light or heavy partons. In order to obtain a clean sample in which all heavy flavor contributions are produced by the `ALPGEN` generator, events in which heavy flavor quarks result from the `PYTHIA` showering are removed from the samples. For the W+jets generation a scale of $m_W^2+\sum p_T^2(W)$ is applied. As a result of the hard requirements in the event selection, it is not possible to produce enough statistics in the $W+0lp$ and $W+1lp$ subsamples to obtain reasonable (selected) event numbers. Thus, the handful of events selected would require extremely high weights compared to the other subsamples. This would lead to artefacts in the kinematic distributions and finally in the mass fit. As this is not a physical effect but is simply caused by the low statistics, the two subsamples are excluded from the analysis.

Due to differences in the produced statistics compared to their respective cross sections the subsamples are given a Monte Carlo weight. As this leads to complications throughout the analysis, the

Top Mass	Sample	cross section (pb)	N_{evt}			
			e+jets		μ+jets	
			pre	post	pre	post
tt160	ttlj+0lp	2.042	610	1220	900	1286
	ttlj+1lp	0.866	251	503	334	476
	ttlj+2lp	0.665	139	277	167	238
	Total	3.573	1000	2000	1400	2000
tt165	ttlj+0lp	1.732	622	1244	905	1291
	ttlj+1lp	0.735	248	495	331	474
	ttlj+2lp	0.556	130	261	164	235
	Total	3.023	1000	2000	1400	2000
tt170	ttlj+0lp	1.505	629	1258	924	1320
	ttlj+1lp	0.629	239	479	322	459
	ttlj+2lp	0.469	132	263	154	221
	Total	2.603	1000	2000	1400	2000
tt175	ttlj+0lp	1.300	629	1258	920	1315
	ttlj+1lp	0.540	284	569	379	459
	ttlj+2lp	0.265	86	173	101	221
	Total	2.105	999	2000	1400	2000
tt180	ttlj+0lp	1.122	638	1275	941	1343
	ttlj+1lp	0.468	241	482	318	455
	ttlj+2lp	0.345	121	243	141	201
	Total	1.935	1000	2000	1400	1999

Table 6.4: Event pool sizes of the $t\bar{t}$ signal available for the MC calibration.

Subsample	cross section (pb)	HF scale factor	N_{evt} e+jets pre	e+jets post	μ+jets pre	μ+jets post
$W+2$lp	298.6	—	22	41	24	34
$W+3$lp	70.56	—	36	68	40	60
$W+4$lp	15.83	—	113	210	129	193
$W+5$lp	5.760	—	202	375	227	341
$W+b\bar{b}+0$lp	19.18	1.17	1	2	1	2
$W+b\bar{b}+1$lp	7.939	1.17	6	10	6	9
$W+b\bar{b}+2$lp	2.637	1.17	9	16	11	17
$W+b\bar{b}+3$lp	1.069	1.17	32	60	33	50
$W+c\bar{c}+0$lp	71.15	1.17	1	1	3	4
$W+c\bar{c}+1$lp	29.85	1.17	8	14	11	17
$W+c\bar{c}+2$lp	13.74	1.17	95	177	115	172
Total	536.3		525	974	600	899

Table 6.5: Overview of the W+jets background available for the MC calibration. Cross sections, heavy flavor (HF) scale factors, sample composition and pool sizes are listed.

event pools are constructed with respect to the subsample cross sections and their acceptance in such a way that an unweighted W+jets sample is achieved. The cross sections taken for this are listed in Table 6.5. As this analysis makes use of b identification, the relative fraction of heavy flavor versus light flavor contributions in the background becomes important. It is known [112] that Monte Carlo and data samples disagree in the amount of heavy flavor when b-tagging is applied. This is partly caused by the fact that `ALPGEN` uses leading order cross sections and the heavy flavor contributions are expected to be higher at next to leading order. To deal with this discrepancy heavy flavor scale factors are derived [112] and applied to increase the relative contribution of the $W+b\bar{b}$ and $W+c\bar{c}$ subsamples. For this analysis, it was decided to use a heavy flavor scale factor of 1.17 with a relative uncertainty of 25% for all heavy flavor subsamples [113].

For the s_{jes} and s_{bjes} shifted samples, the reconstructed (b-) jets of the $t\bar{t}$ sample with $m_t = 170$ GeV and the W+jets sample are multiplied with the respective scaling factors before the selection and $\not{E}_t$ is corrected for the shifted jets. After the selection, the sample composition with respect to the different subsample fractions is slightly changed due to the shifts. Thus, the $t\bar{t}$ and W+jets pool composition is adapted accordingly for each calibration point.

6.3.2 Signal Fraction Determination

Before ensemble tests can be performed to obtain calibration curves that can be applied to a data measurement, the ensemble composition needs to be estimated from data. The procedure described in this section was developed for the top quark cross section analyses at D0. Since these analyses use slightly different event selections and in particular only require four or more jets, the method needs to be reapplied to this analysis. The signal fraction determination procedure makes use of kinematic quantities that show reasonable separation between signal and background processes and combines them into a topological likelihood discriminant. The following variables are included:

$\mathbf{H_T}$ The scalar sum of the p_T of the four jets.

Centrality The scalar sum of transverse energies divided by the scalar sum of energies of the four jets.

$\Delta\phi(\mathbf{l},\not\!\!E_t)$ Azimuthal opening angle between the lepton and $\not\!\!E_t$.

$\mathbf{K'_{T,min}}$ Defined as

$$K'_{T,min} = \Delta R^{min} E_T^{min} / E_T^W \ . \tag{6.4}$$

Here, ΔR^{min} denotes the minimum separation between any pair of jets, E_T^{min} is the minimum transverse energy of these two jets and $E_T^W = E_T^l + \not\!\!E_t$.

Aplanarity The normalized momentum tensor $\mathcal{M}$ is defined as:

$$\mathcal{M}_{jk} = \frac{\sum_i p_j^i p_k^i}{\sum_i |\vec{p}^i|^2} \ , \tag{6.5}$$

where $\vec{p}^i$ is the momentum vector of a reconstructed object and j and k are Cartesian coordinates. By standard diagonalization of $\mathcal{M}$ one may obtain three eigenvalues $\lambda_{1,2,3}$, which fulfill $\lambda_1 + \lambda_2 + \lambda_3 = 1$. The aplanarity is defined as $\mathcal{A} = \frac{3}{2}\lambda_3$, where λ_3 is the smallest eigenvalue. Therefore, it is restricted to the range $0 \leq \lambda_3 \leq 0.5$.

Sphericity Defined as $\mathcal{S} = \frac{3}{2}(\lambda_2 + \lambda_3)$ with λ_2 and λ_3 being the smallest eigenvalues of $\mathcal{M}$. The sphericity is defined in the range $0 \leq \mathcal{S} \leq 1$.

The aplanarity is a measure of the flatness of an event. Small values correspond to planar events, whereas large values indicate more spherical events. $t\bar{t}$ events tend to be spherical as is typical for decays of heavy objects. In contrast, W+jets and multijet QCD backgrounds demonstrate more planar event topologies caused by the fact that the jets in these events arise predominantly from initial state radiation. The sphericity essentially gives the summed $p_\perp^2$ with respect to the event axis. Thus, a 2-jet event corresponds to $\mathcal{S} \approx 0$ and an isotropic event to $\mathcal{S} \approx 1$. As in the case of the aplanarity, decays of a heavy object such as $t\bar{t}$ tend to be more isotropic than the background processes.

In order to obtain probability density functions for signal (S_i) and background (B_i), the variables given above (x_i) are histogrammed for $t\bar{t}$ signal and W+jets background and normalized to unity. To be less sensitive to statistical fluctuations of any of the input variables, these are transformed in the following way for the histograms:

$$\ln(\mathcal{A}) \qquad \ln(\mathcal{S}) \qquad \ln(\mathcal{C}) \qquad \ln(H_T) \qquad \ln(K'_{T,min}) \qquad \Delta\phi(l,\not\!\!E_t) \ .$$

The logarithms of the probability ratios $\ln\left(\frac{P_{t\bar{t}}}{P_{W+jets}}\right)$ are parameterized with functional fits to obtain probability density functions $\ln\left(\frac{S_i}{B_i}\right)$ for the input variables. The likelihood function can be approximated in the following way, if the input variables are assumed to be uncorrelated:

$$\mathcal{L} = \frac{S(x_1,...,x_6)}{S(x_1,...,x_6) + B(x_1,...,x_6)} \approx \frac{\prod_i S_i}{\prod_i S_i + \prod_i B_i} = \frac{\exp(\sum_i (\ln \frac{S_i}{B_i}))}{\exp(\sum_i (\ln \frac{S_i}{B_i})) + 1} \ . \tag{6.6}$$

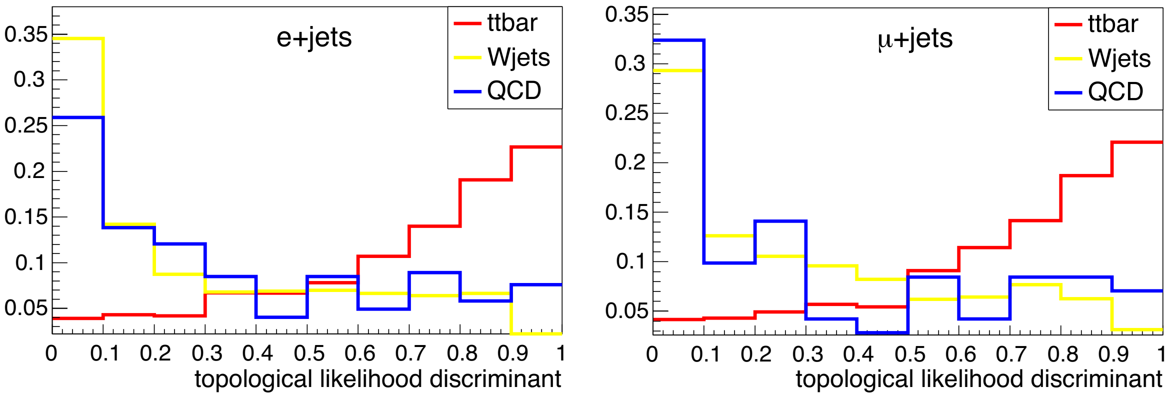

Figure 6.21: Templates for the topological likelihood fits in the e+jets and μ+jets decay channels.

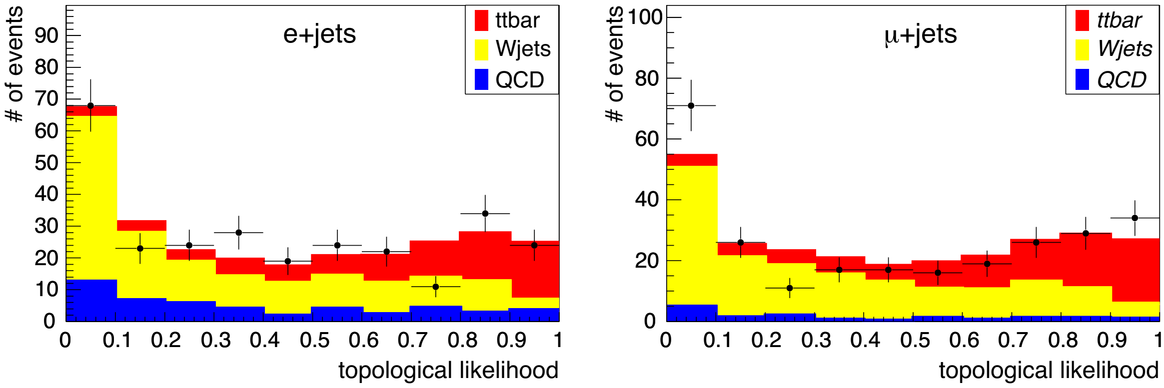

Figure 6.22: Topological likelihood fits or the e+jets and μ+jets decay channels.

The QCD multijet background tends to be small and of similar topology as the W+jets background. Hence, it is not treated separately in the fits of the topological likelihood input variables. Nevertheless, it is included in the topological likelihood fit for measuring the signal fraction. Since QCD multijet background is not easy to model by Monte Carlo, the QCD sample is obtained from data by inverting the tight isolation cut for the lepton, i.e. selecting loose-but-not-tight leptons. The topological likelihood discriminant (6.6) is calculated for all events in the $t\bar{t}$, W+jets and QCD multijet samples. In this way one obtains the likelihood discriminant templates shown in Fig. 6.21 for the three processes.

For estimating the signal fraction in data, the three templates are fitted to the data distribution of the likelihood discriminant. The fit results for the e+jets and μ+jets decay channels are depicted in Fig. 6.22. In the fit, the ratio of W+jets and QCD multijet background is not varied freely. Instead, their relative fractions are fixed to the values obtained from the so-called matrix method (cf. App. G). The absolute event numbers and obtained fractions of the three samples together with their one sigma errors are given in Table 6.6. For the e+jets channel a signal fraction of 28.6% is determined and 35.5% is measured for the μ+jets channel.

Decay		$t\bar{t}$	W+jets	QCD
e+jets	N_{evt}	$79.1^{+16.2}_{-15.5}$	$149.3^{+18.1}_{-17.8}$	$48.9^{+4.4}_{-4.2}$
	f_N (%)	$28.6^{+5.8}_{-5.6}$	$53.9^{+6.5}_{-6.4}$	$17.6^{+1.6}_{-1.5}$
μ+jets	N_{evt}	$94.6^{+15.8}_{-15.3}$	$156.0^{+17.9}_{-17.5}$	$15.2^{+5.4}_{-5.0}$
	f_N (%)	$35.5^{+5.9}_{-5.7}$	$58.6^{+6.7}_{-6.6}$	$5.7^{+2.0}_{-1.9}$

Table 6.6: Fitted fractions of $t\bar{t}$ signal, W+jets and QCD multijet background.

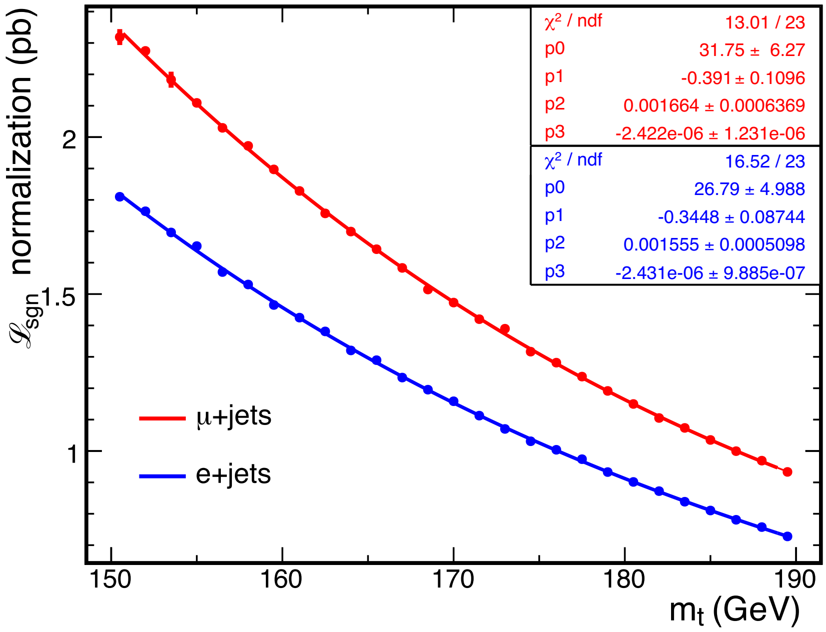

Figure 6.23: Normalization of the signal likelihood for the calibration.

As both the procedure described above to determine the signal fraction in data and the whole matrix element method rely heavily on Monte Carlo samples, it should be shown that the Monte Carlo simulation describes the data, in the first place. A data / MC comparison study is performed and the results for all relevant kinematic quantities are shown in App. G for the four jet exclusive bin with the Monte Carlo sample fractions fixed to the values determined in this section. The same studies were performed for events with fewer jets as well and are summarized in [114]. All data / MC comparisons show good agreement for the kinematic distributions and no larger discrepancies are observed in any of them.

6.3.3 Normalization

The normalization for the fully simulated events follows the same procedure as described in Sec. 5.5 and Sec. 6.2.3. It needs to be rederived as several differences in the simulation and likelihood calcu-

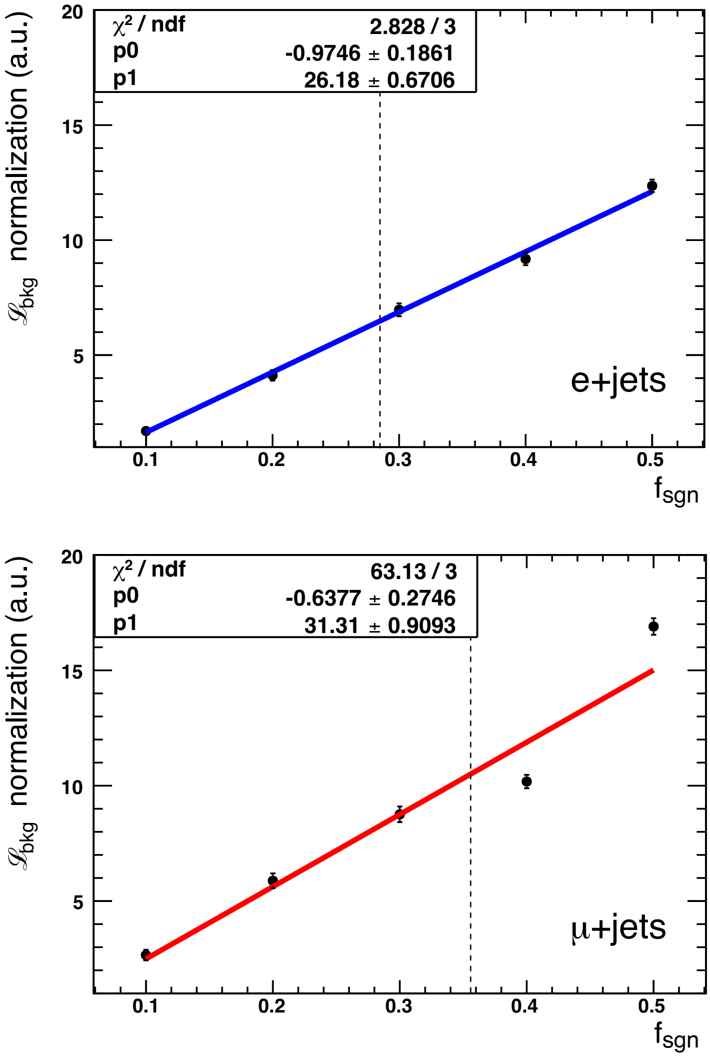

Figure 6.24: Normalization of the background likelihood for the calibration.

Subsample	e+jets		μ+jets	
	pre	post	pre	post
$t\bar{t}$	28	54	39	56
W+jets	67	128	70	101
Total	95	182	109	157
Sum	277		266	

Table 6.7: Event numbers for the eight event pools used to compose the calibration ensembles.

lation between the parton level studies and the fully simulated samples exist, e.g. the versions of the `CTEQ` parton density functions. The result and parametrization for the signal likelihood normalization are given in Fig. 6.23. The normalization of the background likelihood can be found in Fig 6.24. As was shown in Sec. 6.3.2, the signal fraction in data is 28.6% for e+jets and 35.5% for μ+jets. Hence, the background normalization is performed for these points.

6.3.4 Calibration for the Data Measurement

The ensembles used for the data calibration are composed in such a way, that they resemble the observed data contributions. As will be shown in Sec. 6.4, the selected data sample consists of 543 events distributed over pre- and post run periods and e+jets and μ+jets decay channels. Table 6.7 lists the respective event numbers for the eight event pools. The signal fraction is fixed to the values for e+jets and μ+jets derived in Sec. 6.3.2.

As stated in the description of the matrix element method (cf. Chap. 5), several assumptions made in the calculations of signal and background likelihoods are not perfectly true. For instance, the background is assumed to be independent of s_{jes} and s_{bjes}. Furthermore, the fully simulated Monte Carlo contains contributions from underlying event, pile-up and initial and final state radiation, which are not modeled in parton level events. Finally, as was shown in the parton level studies (see Sec. 6.2.5), the method degrades if processes are present which are not modeled by the likelihoods, e.g. $W+b\bar{b}$ or $t\bar{t}$+Nlp contributions. Both processes are included in the fully simulated events. Hence, perfect agreement between generated and reconstructed observables cannot be achieved in the calibration and the calibration slopes, offsets and pull widths are expected to degrade compared to the parton level studies.

Figure 6.25 shows the background calibration. The W+jets background fraction is varied between 0% and 90%, the other events are $t\bar{t}$ signal with $m_t = 170$ GeV and $s_{jes} = s_{bjes} = 1$. It is apparent, that the relative offsets with pure signal events are below or around 1% for the three fit observables, showing good agreement with the expectation. When increasing the background fraction, the same effects observed in parton level studies occur: the s_{jes} and s_{bjes} reconstructed values instantly start to decrease, whereas the m_t reconstruction shows a flat distribution (meaning good reconstruction) up to background fractions of around 60%. At higher f_{bkg}, the m_t fit starts to degrade as well. At $f_{bkg} = 90\%$ the reconstructed values are about 95% of the generated ones. The pull widths are around or below 1.1 without background included, indicating a good error estimation. Again, for higher background

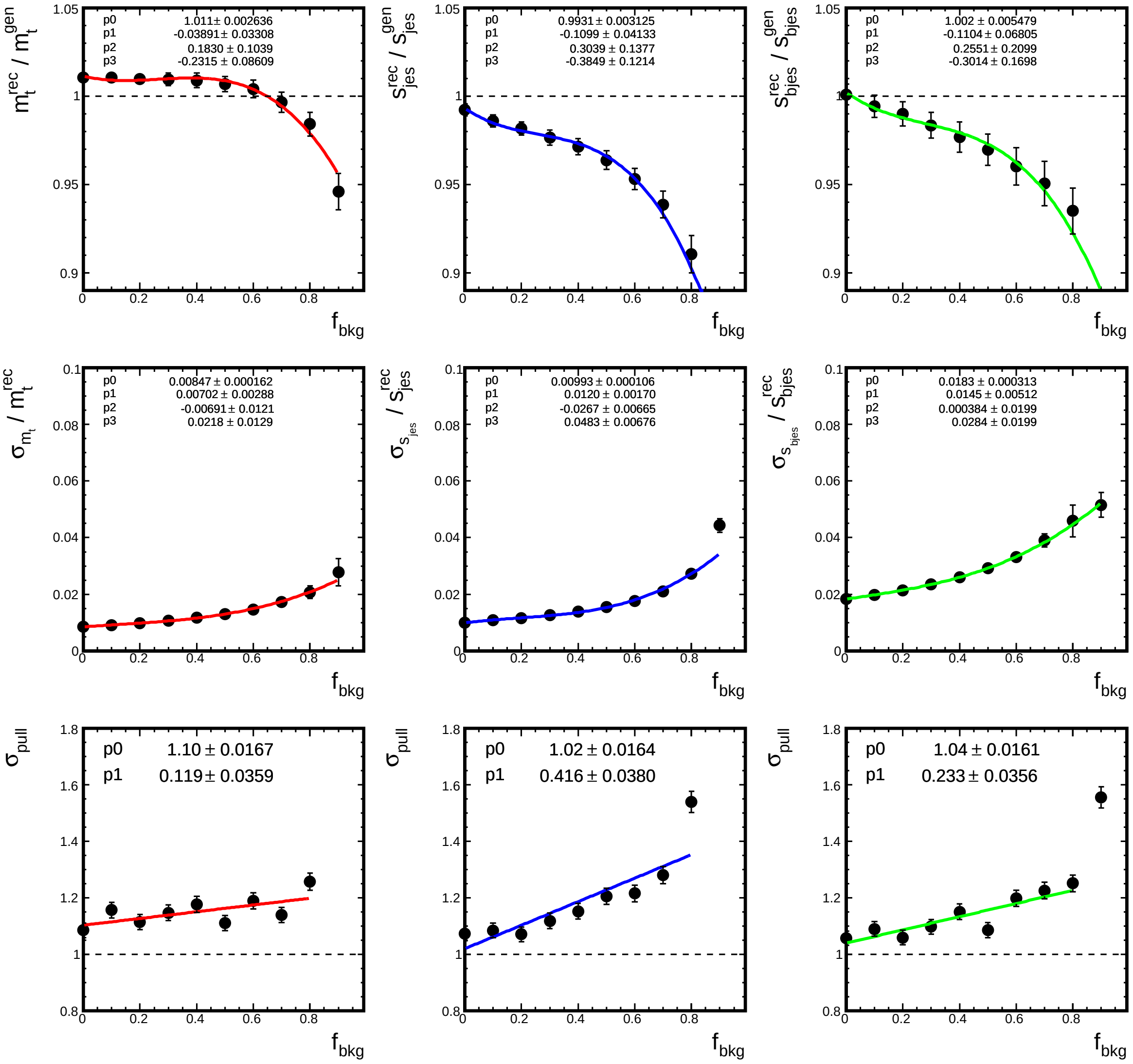

Figure 6.25: Background calibration for fully simulated events.

fractions the pulls start to degrade slowly, reaching values of around 1.2 at $f_{bkg} = 70\%$. At higher background fractions, the error estimate for s_{jes} and s_{bjes} can no longer be trusted.

The mass calibration is depicted in Fig. 6.26. The mass fit shows perfect agreement with the expectation, whereas the s_{jes} and s_{bjes} fits exhibit reconstructed values which are too low ($\approx 95\%$). This is in good agreement with the offset seen for the background fraction used in the background calibration curve given above. The errors and pulls are flat with respect to the generated top mass, despite statistical fluctuations. The pull widths are 1.16, 1.26 and 1.22 for m_t, s_{jes} and s_{bjes}, respectively. These are still very good values if the drawbacks described at the beginning of this section are taken into account.

The next picture, Fig. 6.27, depicts the s_{jes} calibration. The distributions show in general the same

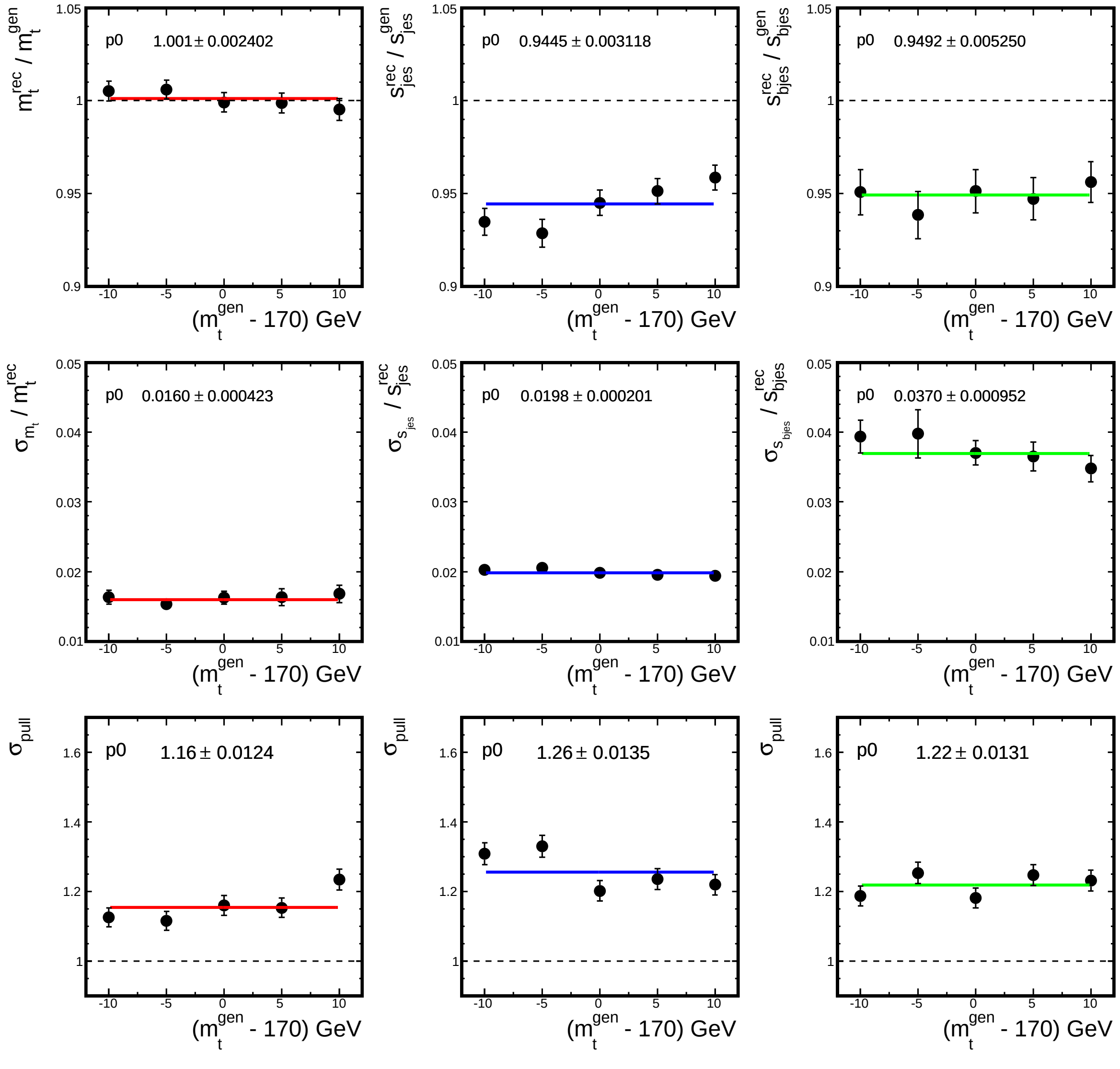

Figure 6.26: Top mass calibration for fully simulated events.

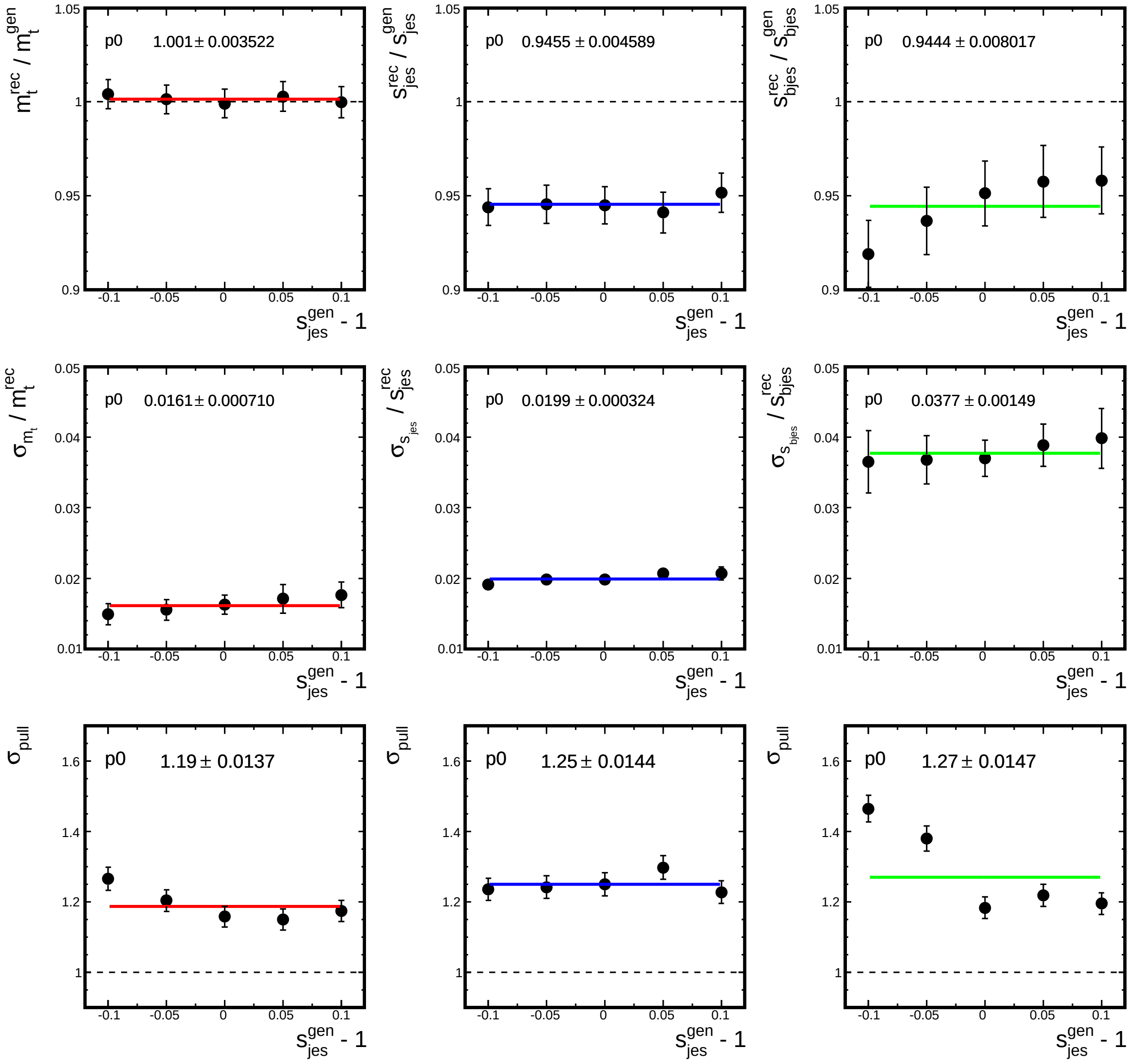

Figure 6.27: s_{jes} calibration for fully simulated events.

flat behavior as in the top mass calibration. Nevertheless, there is a rise in the pull widths in the m_t and s_{bjes} fit for low generated s_{jes} values. Also, the reconstructed s_{bjes} decreases towards lower s_{jes} inputs. This trend is already indicated in the parton level studies including background (cf. Fig. B.5), although it is not as striking due to the larger statistical uncertainties. In contrast, it is not visible in the parton level studies on pure signal events (cf. Fig. 6.9). This leads to the conclusion, that the behavior might be connected to the assumptions made in the background likelihood, in particular the neglected dependence on the JES scaling factors s_{jes} and s_{bjes}. However, this effect only appears at large deviations from the nominal jet energy scale (-5% to -10%), whereas the uncertainty on the jet energy scale lies in the few percent range (cf. Table 6.32). In addition, previous measurements have shown, that the s_{jes} fit for $t\overline{t}$ events tends to the direction of high s_{jes} values [92]. Thus, it is not a drawback for the data measurement, in which the main focus is on the fitted top mass. The fact, that deviations only appear in the s_{bjes} fit can be explained by the strong constraint of the W mass in the s_{jes} fit and the weaker constraint of the s_{bjes}. Thus, if events are deformed in such a way that they appear ”unphysical” to the matrix element method fit, distortions are likely to show up in s_{bjes}, first.

The last calibration, Fig. 6.28, gives the results for the fits versus s_{bjes}. Again, the reconstructed fit values show no (significant) dependence on the input values of s_{bjes}. The error and pull width distributions are also flat. Only in the m_t pull width a dependence on s_{bjes} is visible. However, no distortions such as those in the s_{jes} case are found in the ensemble tests. Instead, both the m_t fit distribution width and the error estimate increase with lower values of s_{bjes}. It can thus be concluded that the fluctuations in m_t increase with decreasing input values of s_{bjes}.

For completeness, the reconstructed signal fractions versus the m_t, s_{jes} and s_{bjes} calibration points are displayed in App. H, Fig. H.1. The distributions exhibit the same behavior as in the parton level studies. The reconstructed signal fractions decrease with increasing input values for all three fit observables. At the default calibration point $m_t = 170$ GeV, $s_{jes} = s_{bjes} = 1$, the reconstructed values agree perfectly with the expected value of 32.6% within errors. This implies, that the calibration samples are very well normalized.

The calibration curves which can finally be applied to data are depicted in Fig. 6.29. They show the reconstructed versus generated values for the four fit observables f_{sig}, m_t, s_{jes} and s_{bjes} and are parameterized by a straight line. With their help, any reconstructed value x_{rec} can be turned into a calibrated value x_{cal} by the following equation:

$$x_{cal} = \frac{x_{rec} - x_{off} - p_0(x)}{p_1(x)} + x_{off} \qquad x \in \{f_{sig}, m_t, s_{jes}, s_{bjes}\} \,. \tag{6.7}$$

Here, $p_0(x)$ and $p_1(x)$ are the respective parameters of the straight line fit given in Fig. 6.29, and x_{off} is the offset subtracted from each input value in the graphs, i.e. $f_{sig,off} = 0$, $m_{t,off} = 170$ GeV and $s_{jes,off} = s_{bjes,off} = 1$.

6.4 Data Measurement

For the top mass measurement presented in this analysis data taken with the D0 detector during the so-called Run IIa between 2002 and 2006 is used. It amounts to about 1 fb^{-1} of integrated luminosity, split into electron and muon decay signatures and run periods before and after a Shutdown in 2004

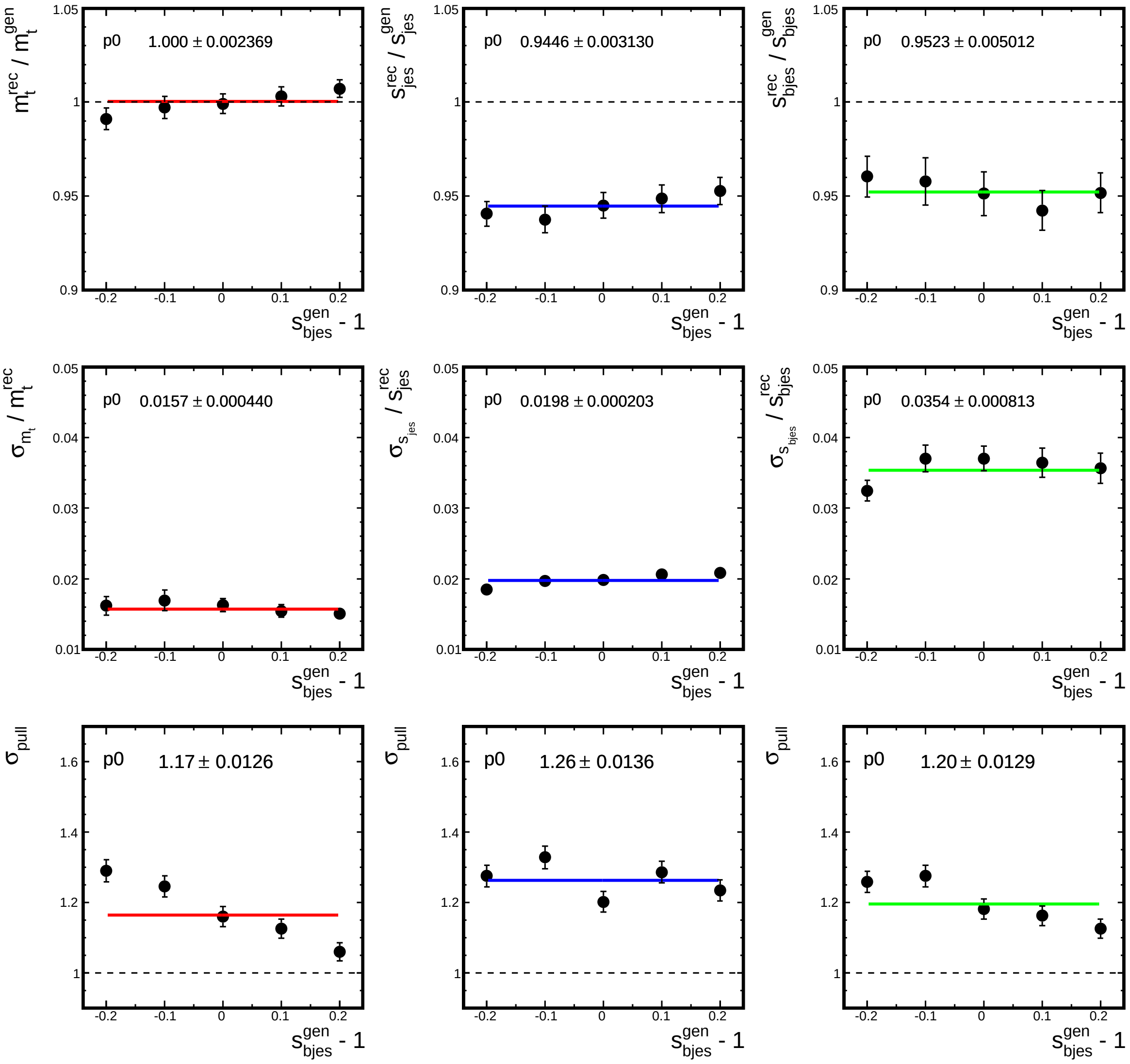

Figure 6.28: s_{bjes} calibration for fully simulated events.

Signature	Delivered	Recorded	Good Quality
e+jets	1312.14	1195.82	1035.64
μ+jets	1349.20	1146.31	994.14

Table 6.8: Integrated luminosities in pb^{-1}.

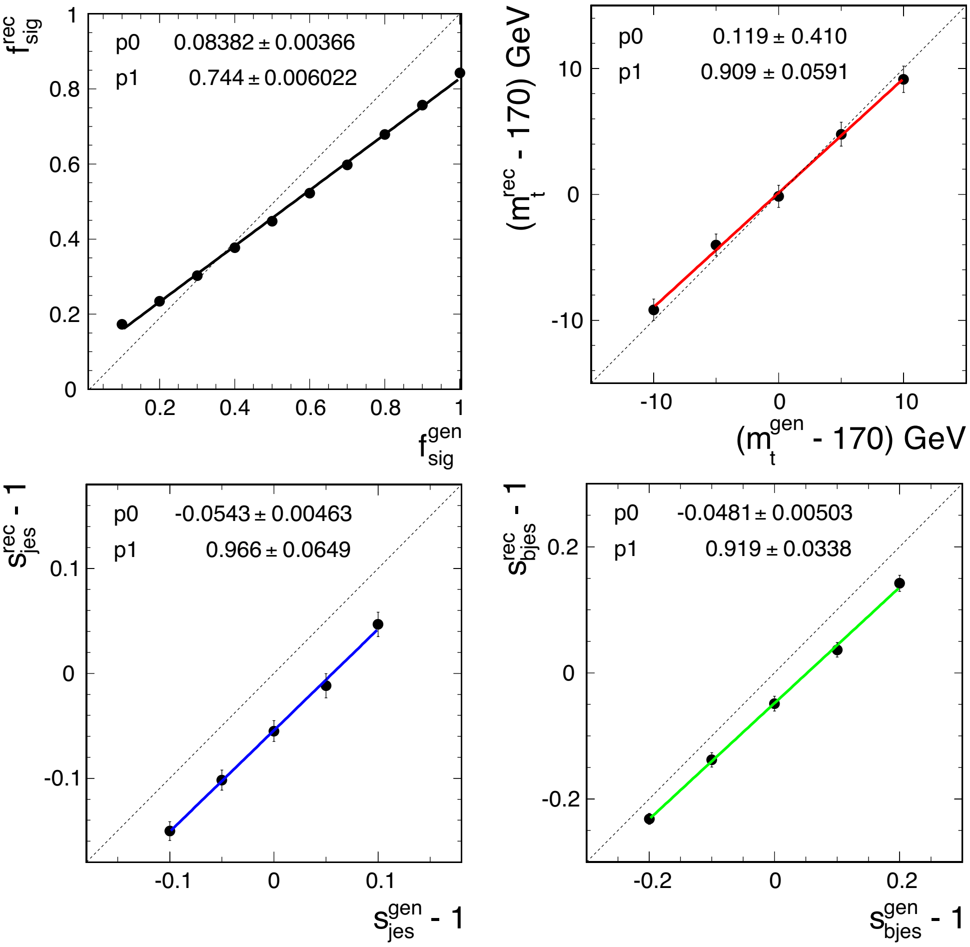

Figure 6.29: Calibration curves for the four fit observables for fully simulated events.

Decay	pre	post	Total
e+jets	95	182	277
μ+jets	109	157	266
Total	204	339	543

Table 6.9: Selected event numbers for the e+jets and μ+jets decay signatures in the pre- and post-shutdown run periods.

Fitrange N_{pt}	m_t (GeV)	σ_{mt} (GeV)	s_{jes}	σ_{sjes}	s_{bjes}	σ_{sbjes}
3	169.4	2.9	0.981	0.018	0.999	0.037
4	169.5	2.9	0.982	0.018	1.002	0.036
5	169.4	3.3	0.982	0.018	1.005	0.038
6	169.4	3.1	0.982	0.018	1.007	0.038
7	169.1	2.9	0.982	0.018	1.009	0.038
Mean	169.4	3.0	0.982	0.018	1.004	0.037

Table 6.10: Measurement results vs. fit range. The range always consists of $(2N_{pt}+1)$ points to be fitted and is symmetric around the absolute likelihood minimum.

Observable	Reconstructed	Calibrated	External	$\Delta\sigma$	Ref.
m_t	(169.4 ± 3.0) GeV	(169.2 ± 3.5 GeV)	(172.6 ± 1.4 GeV)	0.9	[115]
s_{jes}	0.982 ± 0.018	1.038 ± 0.023	1.030 ± 0.017	0.3	[55, 92]
s_{bjes}	1.004 ± 0.037	1.056 ± 0.045	1.048 ± 0.018	0.2	[92, 116]
f_{sig}	(34.6 ± 2.4)%	(35.2 ± 2.4)%	(32.0 ± 8.1)%	0.4	Sec. 6.3.2

Table 6.11: Reconstructed and calibrated data measurement results and external measurements for comparison. The $\Delta\sigma$ values between this analysis and the external results are obtained by adding both uncertainties in quadrature.

(referred to as *pre* and *post*). An overview of the delivered, recorded and good quality integrated luminosities can be found in Table 6.8. As stated in Chap. 3, only runs in which all detector components were working well during data taking are used for a top mass measurement, as all subdetectors are needed for reconstructing the top decay products. A more detailed list of the l+jets triggers used and their specific integrated luminosities is given in App. E. Out of 1,849,900,000 events initially recorded, 143,399 are preselected, separated in e+jets (99,473) and μ+jets (43,926) decays. Only 543 events, nearly equally distributed between the two decay signatures, survive the final selection stage. The final event numbers are listed in Table 6.9.

Figure 6.30 shows the uncalibrated result of the likelihood fit for 15 data points being fitted. As described in Sec. 6.2.4, statistical fluctuations of the numerical integration especially show up in the top mass likelihoods. This effect can be seen here as well. While possible biases in the top mass estimate cancel out on average in ensemble tests, this is not necessarily true for individual pseudo-experiments or correspondingly for the data set. In order to reduce a possible effect on the data result, the data measurement is repeated for several fit ranges. The results are listed in Table 6.10. It can be seen that, as expected, the fluctuations in m_t are indeed larger than those in the other two observables. To average over the fluctuations, the mean values of these results are quoted as the reconstructed values.

Table 6.11 applies the calibration derived in Sec. 6.3 to obtain the final results. The statistical uncertainties of the fit observables are inflated by the average pull widths obtained in the calibration. The external results listed for comparison are the current world average for the top mass (as of March

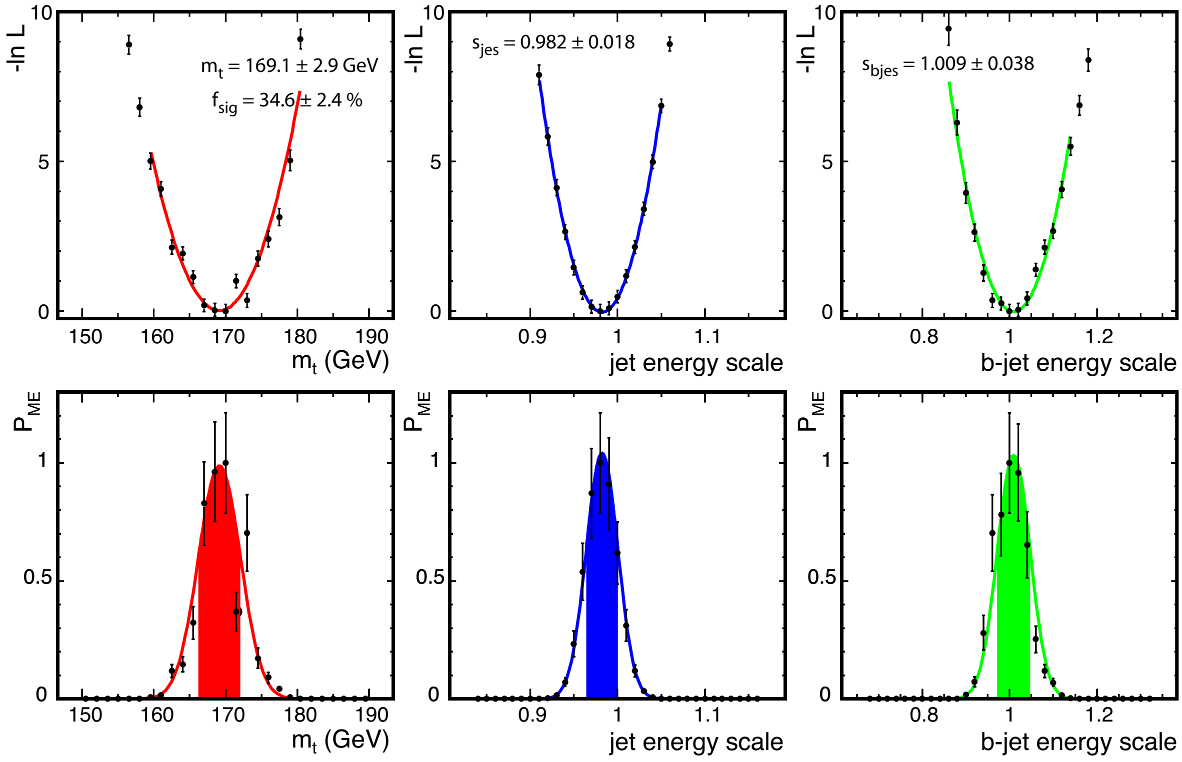

Figure 6.30: Likelihood fits of m_t, s_{jes} and s_{bjes} for the data measurement (uncalibrated). *Top*: negative log likelihoods. *Bottom*: Probability distributions.

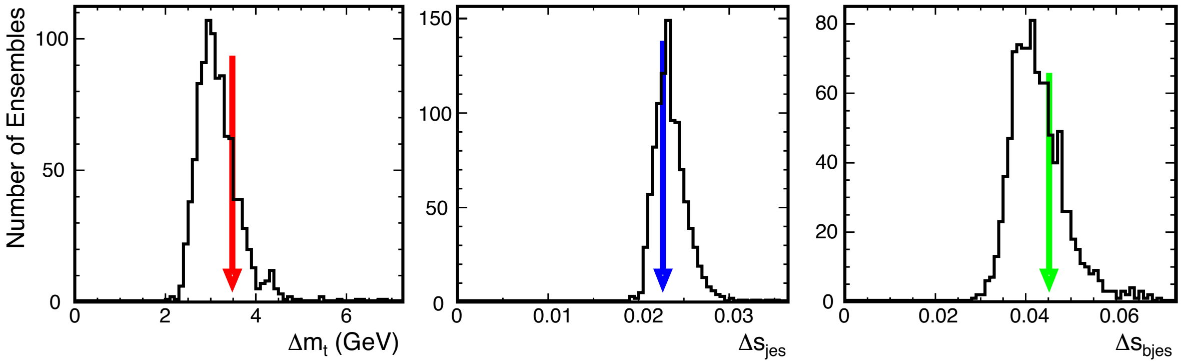

Figure 6.31: Fitted statistical uncertainties for m_t, s_{jes} and s_{bjes} (arrows) compared to the error distributions in MC ensembles (histograms). All uncertainties are inflated by the average pull widths obtained in the calibration.

2008) [115], the jet energy scale and its error provided by the JES group for s_{jes} (derived for a γ+jets sample) [55], the expected discrepancy in the jet response of b versus light jets for s_{bjes} [116] and the signal fraction obtained from the topological likelihood fit for f_{sig} (cf. Sec 6.3.2).

The measurement yields:

$$m_t = (169.2 \pm 3.5)\ \text{GeV} \tag{6.8}$$

$$s_{jes} = 1.038 \pm 0.023 \tag{6.9}$$

$$s_{bjes} = 1.056 \pm 0.045 \tag{6.10}$$

$$f_{sig} = (35.2 \pm 2.4)\%\ . \tag{6.11}$$

As one can see, the results agree very well with the external measurements, showing deviations that are around or below 1σ. Figure 6.31 shows a comparison between the extracted statistical uncertainty in data and the error distribution obtained in Monte Carlo (at the default calibration point).

6.5 Systematic Uncertainties

For the studies of systematic uncertainties different sources concerning detector and physics modeling and the uncertainties of the method itself need to be taken into account. The procedure for extracting the individual components is described in the following section with a summary of all significant systematic uncertainties given at the end.

Due to the fact that most of the uncertainties involve either reweighting of events or reintegration of likelihoods, the ensembles need to be redrawn for the uncertainty evaluation. Thus, the statistical uncertainty in the m_t estimate needs to be taken into account. For the 1000 pseudo-experiments used in each ensemble test, the uncertainty on the mean of the gaussian fitted to the m_t distribution is about 0.1 GeV. For the two ensemble tests used to evaluate an uncertainty (the default and the modified one), the quadratic sum yields 0.14 GeV. Hence, shifts in m_t much less than this value can be completely attributed to the statistical uncertainty of the evaluation. Such small uncertainties indicate that the method is insensitive to their source and thus they are neglected in the total systematic uncertainty. Nevertheless, for completeness their studies will be discussed in the following as well.

The uncertainties that involve either reweighting of events or a change in the sample composition are determined by rederiving the mass calibration curve and evaluating it at the reconstructed top mass in data (169.4 GeV). The attributed systematic uncertainty is defined as the difference between this slightly shifted value and the default calibrated mass (169.2 GeV). Systematic uncertainties that require reintegration are instead evaluated at a single calibration point. Here, the $m_t = 170$ GeV, $s_{jes} = s_{bjes} = 1$ point serves as reference since the background normalization is derived for it and it is the origin of the hypotheses grid. In this case, the difference in the fitted top mass between the default ensemble test and the modified one is taken as systematic uncertainty.

6.5.1 Method

In this section all systematic uncertainties caused by the matrix element method as it is applied in this analysis are derived.

	Reco.	Calibr.	p_0		p_1		Δ_{sys}
			up	down	up	down	
f_{sig}	0.346	0.3524	0.3475	0.3573	0.3496	0.3553	0.006
m_t	169.4	169.209	168.758	169.660	169.257	169.154	0.454
s_{jes}	0.982	1.0376	1.0328	1.0424	1.0373	1.0378	0.005
s_{bjes}	1.004	1.0559	1.0477	1.0642	1.0530	1.0593	0.009

Table 6.12: Systematic variation of the calibration curve parameters. *up* and *down* denote a variation in positive or negative direction.

Calibration

As shown in Fig. 6.29, the calibration applied to the data is derived by a straight line fit to the calibration points of all four fit observables. The two parameters of the fit can only be derived with a certain accuracy caused by the statistical errors of the calibration points. To extract the uncertainty on the top mass that is caused by the calibration, the calibrated results are rederived by scaling the two parameters up and down by their uncertainties one at a time. The results are listed in Table 6.12. A systematic uncertainty of 0.454 GeV is assigned to the top mass due to this source.

Signal Fraction

The ensemble tests for extracting the calibration curves are constructed with a signal fraction fixed to the value measured in data. This signal fraction can only be measured with an accuracy of 3.5% for e+jets events and 3.7% for μ+jets events. The mass calibration curve is rederived with the respective fractions varied up and down by this amount. The extracted top mass varies by 0.340 and 0.605 GeV, respectively. A symmetrized uncertainty of 0.473 GeV is assigned to the top mass due to this source.

Luminosity Reweighting

As the underlying event models in the Monte Carlo generators used for this analysis do not perfectly describe the data, a zero bias overlay is applied to the Monte Carlo samples [117]. This means, ”events” measured in the detector when no hard collision is triggered, are added to the generated Monte Carlo events to simulate the underlying event. As the properties of the underlying event (e.g. total transverse energy) are luminosity dependent, the zero bias data set used for the overlay should resemble the luminosity distribution of the full data set in which the top mass is measured. As this is not exactly the case, Monte Carlo events with zero bias overlay are reweighted to match the ”correct” luminosity distribution. In order to study the effect of this reweighting on the top mass, the mass calibration curve is rederived with these weights removed. This leads to a shift in the top mass of 0.178 GeV being assigned as systematic uncertainty due to this source.

QCD Contamination

In the description of the matrix element method (Chap. 5), it was stated that the kinematic distributions of W+jets and QCD multijet background events look very similar and the QCD background does not need to be modeled separately in the method. Thus, all ensemble tests are performed with a background composed of pure W+jets events. To study the effect of this assumption on the top mass, the ensemble tests for deriving the mass calibration curve are repeated with QCD events included. The QCD fraction is hereby fixed to the value obtained in the topological likelihood fit (cf. Sec. 6.3.2, App. G). As QCD multijet Monte Carlo simulation does not perfectly describe the kinematic distributions observed in data, the QCD events are drawn from a QCD enriched data sample instead. This sample is selected by applying all selection requirements but reversing the lepton isolation cut (i.e. selecting loose but *not tight* leptons). The comparison of the top mass measurement with and without QCD multijet events being included in the calibration yields a systematic uncertainty of 0.268 GeV due to this source.

Signal Contamination

Since `ALPGEN` $t\bar{t}$ samples used in this analysis are exclusive samples consisting only of l+jets events, possible contamination from the other decay channels is not taken into account in the ensemble tests. To evaluate the effect of this contamination on the top quark mass, the ensemble test for the $m_t =$ 175 GeV mass point is repeated while including $t\bar{t}$ events in the dilepton channel. This mass point is chosen for practical reasons.

Like the l+jets samples, the dilepton sample used also consists of `ALPGEN` $t\bar{t}$ events composed of the following three parton multiplicity subsamples: $t\bar{t}+0lp$, $t\bar{t}+1lp$, and $t\bar{t}+2lp$. The total number of dilepton events to be included in the background is determined from the relative weights of the dilepton to l+jets samples:

$$R(ll\ :\ l+jets) = \frac{\sum_{i=t\bar{t}+0lp}^{t\bar{t}+2lp} \sigma_i(t\bar{t}\to ll)\times\varepsilon_i(t\bar{t}\to ll)}{\sum_{i=t\bar{t}+0lp}^{t\bar{t}+2lp} \sigma_i(t\bar{t}\to l+jets)\times\varepsilon_i(t\bar{t}\to l+jets)} \tag{6.12}$$

where the sum runs over the three parton multiplicity subsamples and the σ_i's and ε_i's represent, respectively, the `ALPGEN` cross sections and efficiencies to pass the final selection. The total number of $t\bar{t}$ dilepton events (N_{dilep}) is then given by:

$$N_{dilep} = R(ll\ :\ l+jets) \times N_{l+jets} \tag{6.13}$$

$$= R(ll\ :\ l+jets) \times (f_{top}\times N_t) \tag{6.14}$$

where N_{l+jets} is the total number of $t\bar{t}$ l+jets events, f_{sig} is the signal fraction used in the ensemble tests and N_t is the number of events passing the final selections. Including dilepton events in the background shifts the top mass by -0.190 GeV [92], which is assigned as the systematic uncertainty in both directions due to this source.

6.5.2 Detector Modeling

In this section all systematic uncertainties attributed to the imperfect modeling of the D0 detector are derived.

Residual JES Uncertainty

In the analysis presented here, the jet energy scaling factor s_{jes} is a free parameter in the top mass fit. Thus, absolute shifts between the JES derived in D0 and the ”true” jet energy scale in our (top-enriched) data sample are measured (with statistical uncertainty) and do not harm the top mass measurement as has been shown in the ensemble tests. Nevertheless, there is still the possibility that the real jet energy scale cannot be achieved by a simple scale factor but shows a more complicated behavior over the jet energies. To study such contributions to the JES, the uncertainties provided by the D0 JES group are parameterized versus the jet energy separately for the four η_{det} regions used in the jet transfer functions. Figure 6.32 shows the results for the relative JES error σ_{jes}/jes. As one can see, in general the errors range between 1.2% and 3% depending on the detector region. However, they display a non-trivial behavior with respect to E_{jet}. For the determination of the systematic uncertainty on the top mass, all jets in the Monte Carlo calibration pools (for $m_t = 170$ GeV) are scaled up by the parameterized errors on the jet energy scale. For these JES-shifted samples, the signal and background likelihoods are recalculated. An ensemble test performed with these pools results in a top mass shift of 0.265 GeV compared to the standard pools. This shift is assigned as residual JES uncertainty.

Residual bJES Uncertainty

As for the general jet energy scale (JES), absolute shifts in the JES for *b* jets (bJES) are accounted for in the top mass fit by the free s_{bjes} parameter. Therefore, only differences in the responses of *b* jets (R_b) compared to all jets (R_j) which vary with the jet energy represent a possible source of uncertainty for the measurement presented here. As studies of such an effect have just been started by the JES group [118], no estimate of the residual bJES uncertainty exists so far. Hence, several slope values and their effect on the top mass fit are evaluated and presented in Fig. 6.33. Here, a slope of 0.1, for example, stands for a 10% increase in R_b/R_j per 100 GeV in the jet transverse momentum p_t^{jet}. It is apparent that for a slope of 10% or less the effect on m_t is small, whereas at higher values the mass estimate degrades. As the s_{bjes} parameter can only cope with a constant shift between the light and the *b* JES, the matrix element method fails, whenever large differences in the responses between two (*b*-) jets exist. One could argue that a slope as applied here creates ”unphysical” events, which can no longer be made to agree with the matrix element by the fit (see also Sec 6.3.4). The method thus breaks down when the slope is large. For small slopes, the fit works well as it simply averages the bJES over the two *b* jets in each event.

For the residual JES uncertainty described above, slopes are in the range of $\lesssim 0.5\%$ per 100 GeV as can be inferred from Fig. 6.32. Therefore, a slope of 5% in the bJES should give a conservative estimate of the mass uncertainty due to this source. The shift in m_t for this slope is 0.145 GeV, listed as residual bJES uncertainty in Table 6.13.

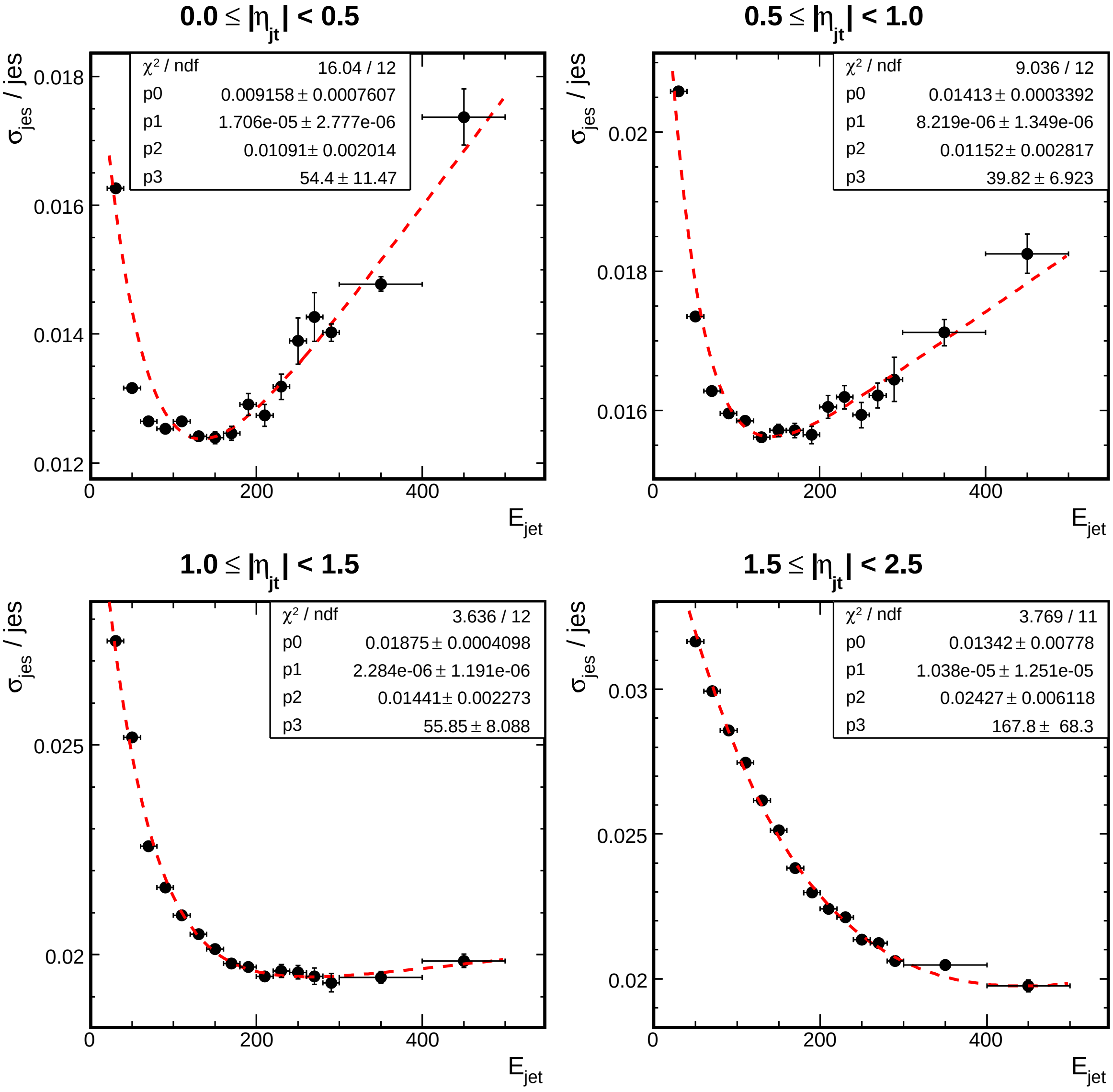

Figure 6.32: Parameterized distributions of the relative JES error for the four η_{det} regions used in the jet transfer functions.

Jet Resolution

The reconstructud jets used in this analysis include an additional smearing which improves the data / MC agreement in the jet resolution (cf. Chap. 3). To evaluate the effect of a residual uncorrected difference between data and Monte Carlo, the standard sample is resmeared with a resolution increased by its uncertainty [92]. Likelihoods are reevaluated and the ensemble test for the $m_t = 170$ GeV sample is repeated, leading to a top mass measurement differing by 0.061 GeV compared to the default [92]. As this shift is smaller than the statistical uncertainty on the top mass estimate (≈ 0.1 GeV), it is not considered in the total systematic uncertainty.

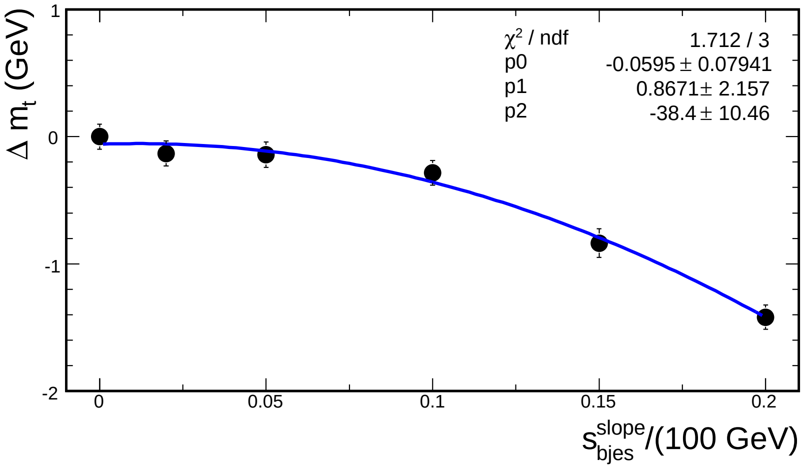

Figure 6.33: Uncertainty on m_t caused by a slope in bJES vs. p_t^{jet}. The shift in m_t is parameterized by a second-order polynomial.

Jet Identification

The scale factors used to achieve good data / MC agreement in the jet identification efficiencies represent another source of uncertainty. To study this, the efficiencies are decreased according to their uncertainties separately for the CC and ICR calorimeter regions and likelihoods are evaluated for events migrating into the ensemble pools due to this correction. An ensemble test is performed on the events surviving the final selection and the top mass is rederived. It is shifted by 0.072 GeV and 0.317 GeV for the CC and ICR test, respectively [92]. Adding these shifts in quadrature leads to a total systematic uncertainty of 0.325 GeV.

b identification

In order to estimate the uncertainty on the top mass caused by the use of tag rate functions, the *b* identification probabilities are recalculated on tagged Monte Carlo. This means that *b*-tagging based on the jet properties is applied the same way on the Monte Carlo samples used for the ensemble tests as on data. As stated before, this is known to overestimate the tag rates in Monte Carlo compared to data (cf. Sec.3.6). Hence, on average it leads to shifts of the jets to higher working point bins. Redoing the ensemble test for the default calibration point leads to a shift of 0.041 GeV on the top mass compared to the case with tag rate functions applied. This is much smaller than the statistical uncertainty of the top mass estimate. This study and the parton level tests (cf. Fig. 6.6 - 6.7) show that the *b* identification probabilities do not lead to a bias on the top mass. Hence, no systematic uncertainty due to this source is considered in the total systematic uncertainty of the top mass measurement.

Trigger

The effect of the trigger on our Monte Carlo samples is modeled by applying a weight which represents the probability for a certain Monte Carlo event to be triggered, if it was real data. This information affects the frequency of the event to be drawn into the ensembles. The influence of possible discrepancies between the trigger probabilities in data and Monte Carlo can be studied by omitting these weights in the ensemble drawing. Ensemble tests performed on the non trigger-weighted samples are used to rederive the mass calibration curve. A shift in the top mass of 0.688 GeV compared to the default measurement is observed. As there is no estimate on the uncertainty of the trigger weights available, but not applying them at all certainly overestimates their uncertainty, half that shift (0.344 GeV) is attributed as systematic uncertainty due to this source.

Lepton Identification

As for the trigger probability, the efficiency for a (MC) lepton to be identified if it were a measured lepton in data is modeled by assigning an event weight. The effect is evaluated again by excluding this weight in the ensemble drawing process and rederiving the mass calibration curve. The top mass shift obtained is 0.141 GeV. As for the trigger weights, not using lepton identification weights at all is an overestimation of their uncertainty. Again, half the shift (0.071 GeV) is attributed as systematic uncertainty due to this source.

Primary Vertex z-Reweighting

In order to reproduce the primary vertex z-profile measured in data, Monte Carlo events are reweighted according to their primary vertex z-position. To determine wether this procedure has any influence on the top mass measurement, ensemble tests without this weight are performed and the mass calibration curve is rederived. The non z-weighted calibration yields a shift on the top mass of 0.056 GeV. With a statistical uncertainty of ≈ 0.1 GeV on this value, no significant systematic uncertainty due to this source can be found and it is neglected in the total systematic uncertainty.

6.5.3 Physics Modeling

This section lists systematic uncertainties attributed to physics effects which are only known to a certain precision.

Signal and Background Modeling

The composition of signal and background samples is determined by the cross sections built into the Monte Carlo generators. The differences between leading-order and next-to-leading order cross sections on the theoretical side and the uncertainties on measured cross sections on the experimental side lead to uncertainties in the compositions. For instance, the quantity of $t\bar{t}$ events with additional light partons is known to be higher at next-to-leading order. Also, estimates evaluated on b-tagged data samples show that the amount of $W+b\bar{b}$ in the W+jets process is higher than expected. Several studies were performed on ensembles by varying the signal and background compositions, all showing shifts on the top mass smaller than the statistical uncertainty of the estimate. As an example, the heavy flavor scale factor applied to increase the contribution of $W+b\bar{b}$ and $W+c\bar{c}$ in the background is shifted by its uncertainty of 25% resulting in a top mass shift of only 0.076 GeV. In addition, the ensemble tests described in Sec. 6.2.5 which consider the influence of different sources of background, have shown that their effects on the top mass are small up to fractions of several times higher than the expected ones. Since none of the backgrounds in question has such large uncertainties, there is no systematic uncertainty included due to this source.

b Fragmentation

Uncertainties in the simulation of b fragmentation can affect the top mass measurement through its effect on various aspects of the analysis such as b-tagging and the b jet transfer functions used in the likelihood calculations. Such effects are studied by reweighting the simulated $t\bar{t}$ events used in the calibration of the method to simulate the choice of other fragmentation models for the b jets. All the default Monte Carlo samples used in this analysis consist of events that have been reweighted from the default `PYTHIA` b fragmentation function to a Bowler scheme [119] tuned to LEP (ALEPH, OPAL, and DELPHI) data [120]. To evaluate the systematic uncertainty caused by the choice of the fragmentation model, these events are further reweighted to account for differences in SLD and LEP data [121]. Ensemble tests are repeated to derive a modified calibration curve resulting in a shift of 0.327 GeV on m_t relative to the calibration with standard b fragmentation.

PDF Uncertainty

The uncertainty of the parton distribution functions is parametrized by 2×20 error PDFs provided for `CTEQ6L` [82]. Ensemble tests are repeated for each of these variations and the uncertainty is evaluated using the following formula [92]:

$$\Delta m_t = \frac{1}{2}\left(\sum_{i=1}^{20}[m_t(S_i^+) - m_t(S_i^-)]^2\right)^{1/2} , \tag{6.15}$$

where the sum runs over the 20 error PDF eigenvectors in the plus (S_i^+) and minus (S_i^-) directions. Δm_t is found to be 0.240 GeV [92], indicating the systematic uncertainty due to this source.

6.5.4 Summary of Systematic Uncertainties

Table 6.13 summarizes the systematic uncertainties derived in the last sections and lists the total uncertainty. Systematic shifts smaller than the statistical uncertainty of the mass estimate are not considered in the total as explained above.

Source	Uncertainty (GeV)
Method:	
Calibration	0.454
Signal Fraction	0.473
Luminosity Reweighting	0.178
QCD contamination	0.268
Signal contamination	0.190
Detector Modeling:	
Residual JES	0.265
Residual bJES	0.145
Jet Resolution	(0.061)
Jet identification	0.325
b identification	(0.041)
Trigger	0.344
Lepton identification	(0.071)
Primary Vertex z Reweighting	(0.056)
Physics Modeling:	
Heavy Flavor Scale Factor	(0.076)
b Fragmentation	0.327
PDF uncertainty	0.240
Total systematic	**1.02**
Total statistical	**3.5**
Total uncertainty	**3.6**

Table 6.13: Overview of the systematic uncertainties of the top mass measurement presented in this analysis and their combination with the statistical uncertainty. Systematic uncertainties listed in brackets are not considered in the total as they are statistically insignificant.

Chapter 7

Conclusions

In the previous chapters, it was shown how the matrix element method for a top mass measurement can be improved by optimizing the use of b identification information and by simultaneously measuring the top mass m_t, a scaling factor for the jet energy of light jets s_{jes} and a scaling factor for the JES of b jets. The D0 experiment, the reconstruction objects of the semileptonic decay channel and their selection were introduced. The method was validated on parton level events and calibration curves were derived on fully simulated Monte Carlo events including detector simulation. The analysis was applied to about 1 fb^{-1} of D0 Run II data. Possible sources of systematic uncertainties were studied. The measurement yields:

$$m_t = (169.2 \pm 3.5\,(stat.) \pm 1.0\,(syst.))\ \text{GeV} \tag{7.1}$$

$$m_t = (169.2 \pm 3.6)\ \text{GeV}\ . \tag{7.2}$$

In order to illustrate the power of the newly developed b identification likelihoods, Table 7.1 compares this result to the result one would obtain in a b-tagging analysis. The latter is derived by requiring two b-tags at the loosest possible operating point (L6) (cf. App. I). This selection reduces the statistics from 543 events to 164 events while increasing the signal purity substantially. However, it can be seen that the result in all three observables is hardly affected and the statistical errors are nearly the same. This indicates that the likelihoods alone contain all necessary information about b identification and thus that the result cannot be improved by applying a tag. The improvement one would expect due to the higher purity is obscured by the greatly decreased statistics. It should be noted that no full analysis as in Chap. 6 was performed for the b-tagging result. In particular, no calibration curves were derived. Instead, the ”calibration” was determined from Fig. 6.25 and Fig. 6.29 for the fitted signal fraction. Therefore, the result permits only a qualitative statement about the effect of b-tagging.

As the statistics of the selected $t\bar{t}$ sample were tiny in Run I of the Tevatron, the matrix element method was developed at D0 in order to gain as much information about the top mass out of an individual event as possible [89]. In Run II, the method was improved to address the then largest systematic uncertainty, the absolute jet energy scale. It was extended to simultaneously measure the top mass and the jet energy scale. The method thereby turned the systematic JES uncertainty into a statistical one. This analysis has shown how this approach can be extended to constrain the absolute

Analysis	f_{sig}	m_t	s_{jes}	s_{bjes}
ibidem	$(35.2 \pm 2.4)\%$	$(169.2 \pm 3.5 \pm 1.0)$ GeV	1.038 ± 0.023	1.056 ± 0.045
btag*	$(94.7 \pm 3.8)\%$	$(169.0 \pm 3.5 \pm$ n.a.) GeV	1.017 ± 0.025	1.054 ± 0.046
2D	$(32.5 \pm 8.5)\%$	$(170.6 \pm 2.2 \pm 1.1)$ GeV	1.030 ± 0.017	—

Table 7.1: Comparison of the measurement presented in this analysis to the result one would obtain by requiring two *b*-tags and the 2D measurement of m_t and s_{jes} on the same data set [92]. (*) For the *b*-tagging result no calibration curves and systematics are rederived (cf. App. I).

jet energy scale of *b* jets as well. With a three dimensional fit of m_t, s_{jes} and s_{bjes}, the systematic uncertainty of the bJES is reduced from 800 MeV to 150 MeV at the cost of increasing the statistical uncertainty. From Table 7.1 it can be seen that the 2D analysis (m_t, s_{jes} measurement) and the 3D analysis (m_t, s_{jes}, s_{bjes} measurement) presented here have similar uncertainties. This analysis has a slightly larger statistical uncertainty, which can be partly explained by a statistical fluctuation, as the expected uncertainty from Monte Carlo simulation is 2.5 GeV. Although both analyses are performed on the same data set, they are not 100% correlated because the 2D analysis utilizes a preliminary version of the D0 jet energy scale while this analysis can rely on the final JES for the corresponding data taking period. Therefore, about 10% of the selected events differ. The statistical uncertainty will of course be reduced when more statistics are available. As of now, 4 fb^{-1} have already been delivered to D0. This means four times the statistics analyzed here is available. With the plan to double this amount of data again before the end of the Tevatron run, there are good prospects to reduce the statistical uncertainty by a factor of about three. For this analysis, the statistical uncertainty would then decrease to about 1 GeV. If no further improvements concerning the method were developed, the systematic uncertainty would stay in the same range. According to this conservative estimate, it will be possible to determine the top mass with less than 1% total precision in a single measurement.

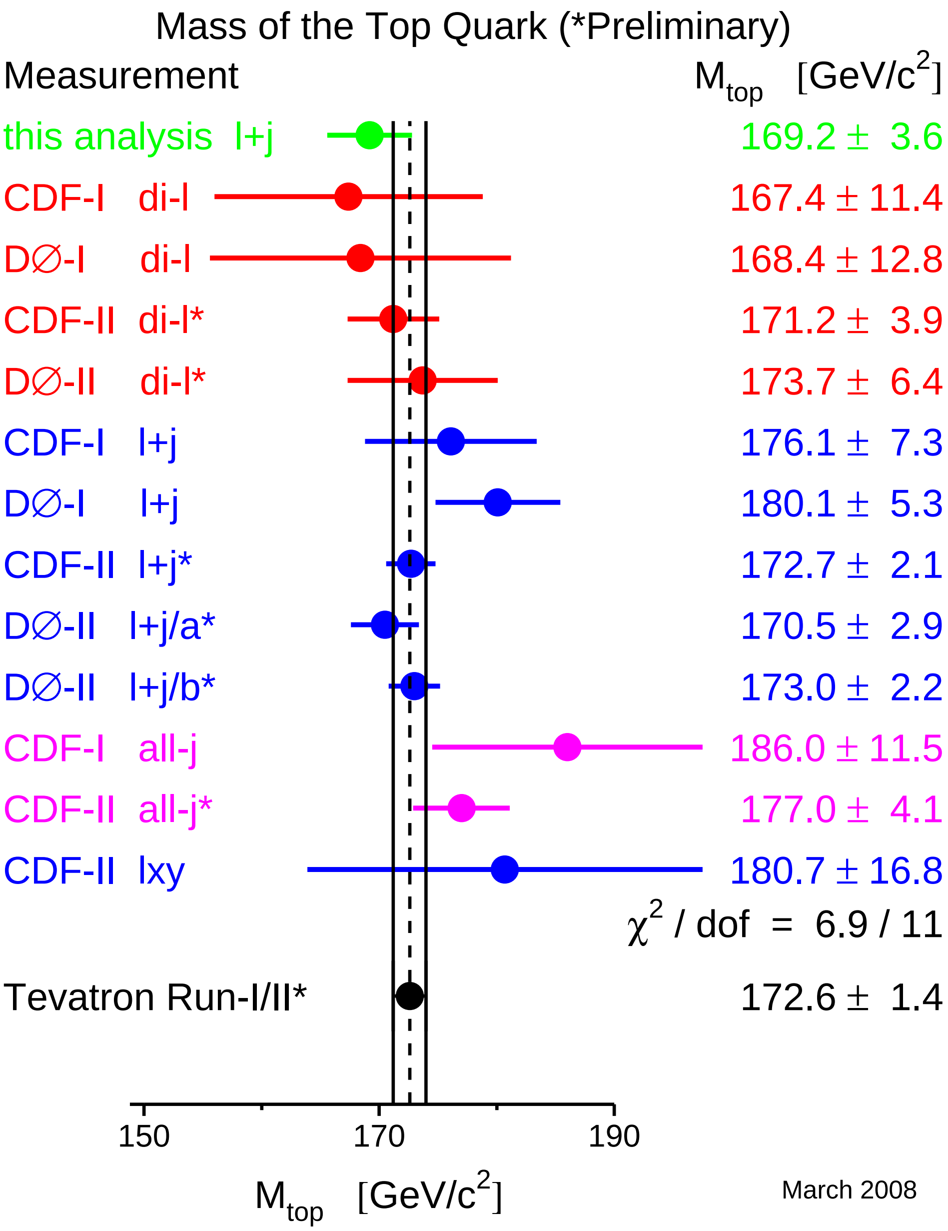

Figure 7.1: World average of the top quark mass as of March 2008 [115]. Preliminary results are indicated by a star. The result of this analysis is plotted for comparison.

Chapter 8

Outlook

In this analysis, several assumptions and approaches are applied which will no longer be valid in the high energy, high luminosity environment of the LHC. At Tevatron energies, there is hardly any phase space for the production of an additional (energetic) jet. Furthermore, the selection requirement of exactly four reconstructed jets reduces the fraction of events with initial or final state radiation. Thus, the assumption of zero transverse momentum of the $t\bar{t}$ pair is a valid approximation. In addition, the effects of next-to-leading order vs. leading-order calculations in the Monte Carlo generators and the matrix element implemented in the method are kept small, justifying the usage of leading-order terms.

Another important point is the statistics of the data sample. At the LHC, the $t\bar{t}$ cross section is two orders of magnitude higher than at the Tevatron. Much higher statistics will therefore be available within a comparably short runtime. This allows for simpler cut-based analyses. The matrix element method was developed in order to obtain as much information from a low statistics sample as possible. However, the increase in information is associated with the requirement of large computing resources (both CPU power and storage capacities). With the three-dimensional fit presented here and the Monte Carlo statistics needed for the calibration of 543 events, the method is at the limit of today's available computing capacities. A much larger data set and larger MC calibration samples can no longer be easily accommodated. The future of the matrix element method therefore probably lies in other regimes with low statistics data sets. At D0, it is for example adapted to single top analyses which have smaller cross sections than $t\bar{t}$ production and a difficult background environment. For the LHC, it will surely play a major role in first mass estimates of whatever new particles or excited states might appear. Especially in the startup phase, when the detector calibration is still converging and b identification is being developed, the method of b identification likelihoods can be useful. As this analysis has shown, such methods help to profit from b identification without the drawbacks of a hard cut concerning loss of statistics and systematic uncertainty. Hence, b identification likelihoods represent a valuable tool for all signatures including b quarks.

Appendix A

Example Calculation for *b* Identification Probabilities

Let’s assume for the real tagging case the fictitious NN outputs given in Table A.1. If one compares these outputs with the cut values for the operating points listed in Table 5.3, one obtains the highest operating points with tag levels given in the row labelled ’OP’ in Table A.1. The next step is to read the probabilities for these operating points from Fig. 5.17 for a fake and a b-quark assumption. This leads to the numbers in the last two lines of Table A.1. For simplicity the *c* probabilities are neglected in this example. One should note that the probability to be in any of the (exclusive) operating point bins for each jet is equal to unity (including the non-tagged bin) but the sum of the probabilities for the different flavors for a specific operating point need not to be unity. For the non-tagged bin the sum reaches nearly 200% as there is a substantial probability for all flavors not to be tagged. On the other hand the probability to be in the highest bin reaches less than 50% in the sum of all flavors. If one calculates the probabilities for the first and the last permutation given in Fig. 5.18 and assumes

jet	0	1	2	3
NN_{out}	0.12	0	0.99	0.58
OP	0	-1	11	6
P_b	0.02	0.30	0.35	0.05
P_{fake}	0.03	0.90	0.001	0.006

Table A.1: Example of b-tagging probabilities for 4 fictitious jets.

d-d-b-b as parton flavors, one obtains the following result:

$$\begin{aligned}
P_{ddbb}^{\text{perm1}} &= P_{fake}^{0}(0)\cdot P_{fake}^{1}(-1)\cdot P_{b}^{2}(11)\cdot P_{b}^{3}(6) \\
&= 0.03\cdot 0.9\cdot 0.35\cdot 0.05 && = 0.47\cdot 10^{-3} \\
P_{ddbb}^{\text{perm24}} &= P_{fake}^{0}(0)\cdot P_{fake}^{1}(-1)\cdot P_{b}^{2}(11)\cdot P_{b}^{3}(6) \\
&= 0.02\cdot 0.30\cdot 0.001\cdot 0.006 && = 0.36\cdot 10^{-7} \\
P_{dddd} &= P_{fake}^{0}(0)\cdot P_{fake}^{1}(-1)\cdot P_{fake}^{2}(11)\cdot P_{fake}^{3}(6) \\
&= 0.03\cdot 0.9\cdot 0.001\cdot 0.006 && = 0.16\cdot 10^{-6}
\end{aligned}$$

The last two lines give the b-tagging probability for a background assumption of d-d-d-d, being of course independent of any permutation. This simplified example shows that including *b* tagging probabilities into the analysis can separate the signal from both the combinatorical and physics background. This is confirmed by studies on parton level events with the full *b* tagging probabilities (including *c* quarks) described in Sec. 6.2.4, where random tagging is applied.

Appendix B

Parton Level Studies Including Background

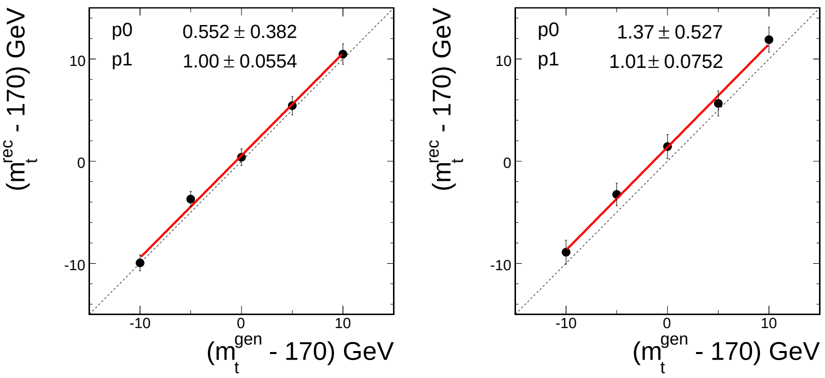

(a) m_t calibration (e+jets)

(b) m_t calibration (μ+jets)

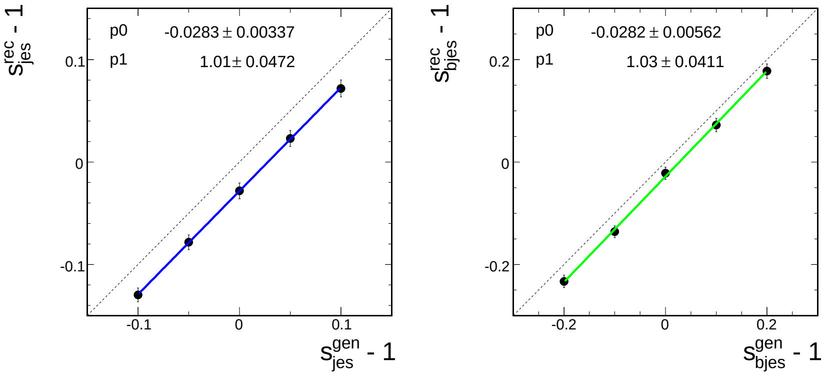

(c) s_{jes} calibration

(d) s_{bjes} calibration (50% W+4lp)

Figure B.1: Parton level calibration curves including background likelihoods.

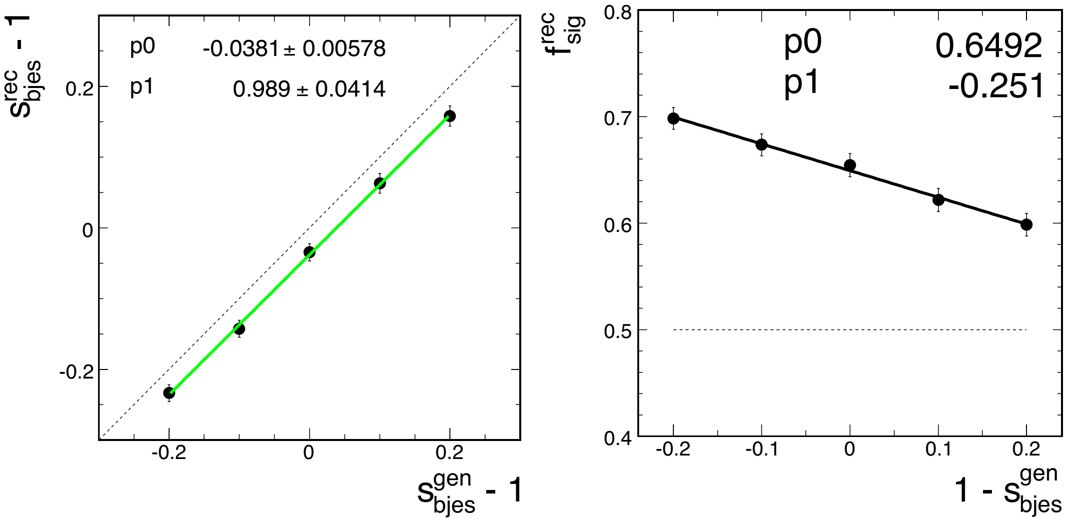

Figure B.2: s_{bjes} calibration including background likelihoods. The ensembles contain 25% $W+4$lp and 25% $W+bb+$jj events. Due to the more signal-like background the signal fraction is about 15% higher than in the case of pure $W+4$lp background.

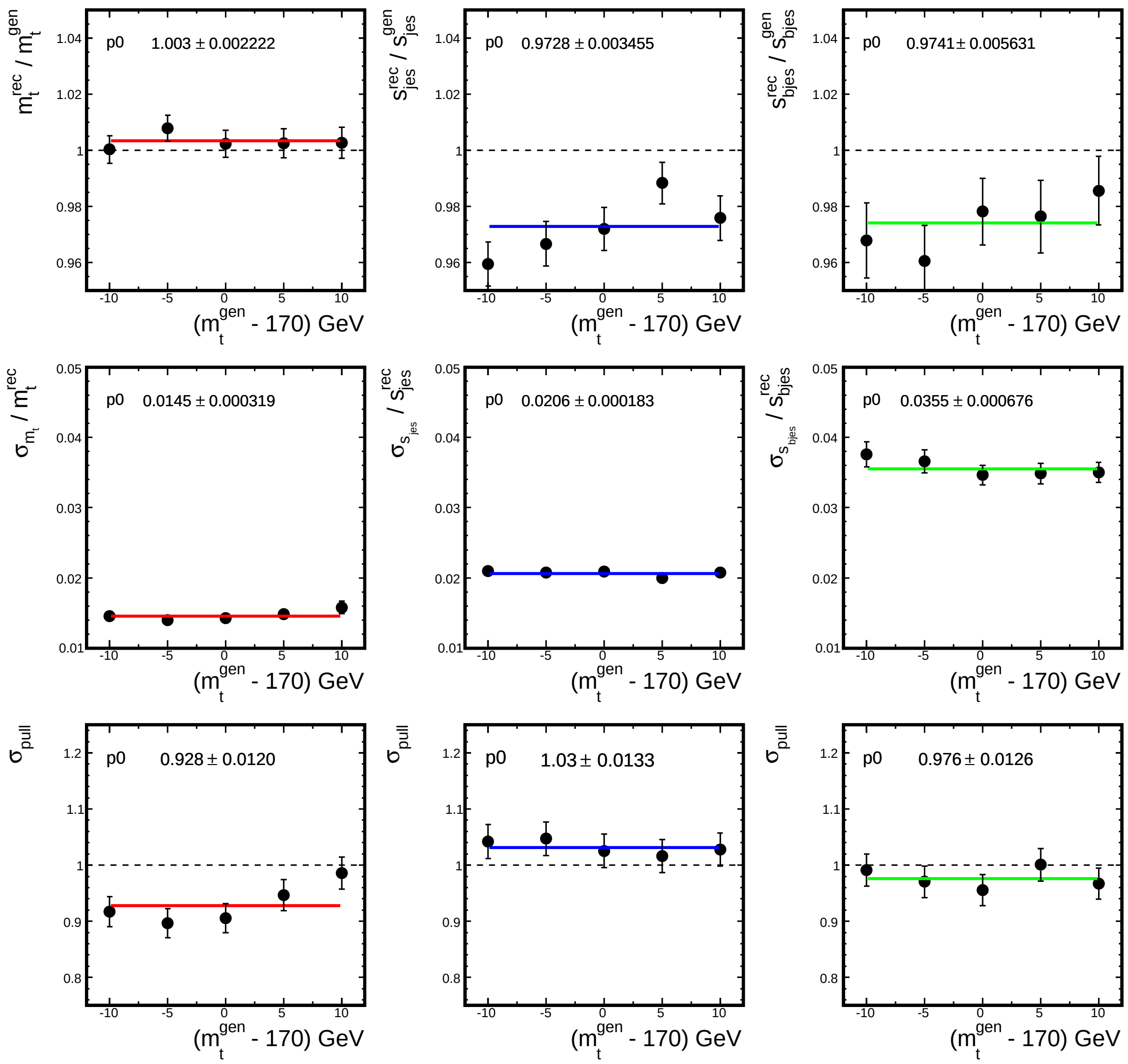

Figure B.3: Mass calibration including *W*+4lp events.

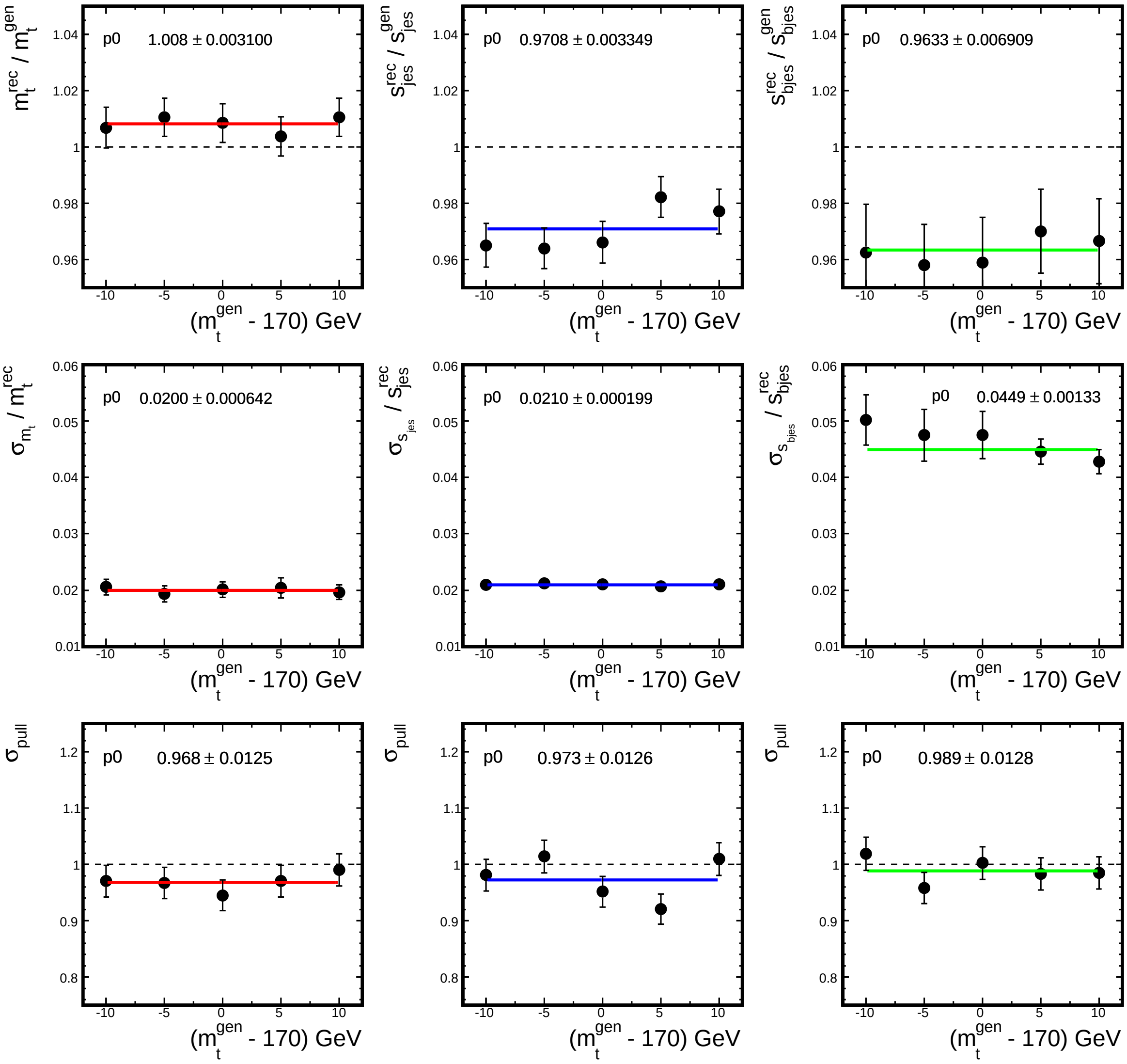

Figure B.4: Mass calibration for the μ+jets channel including W+4lp events.

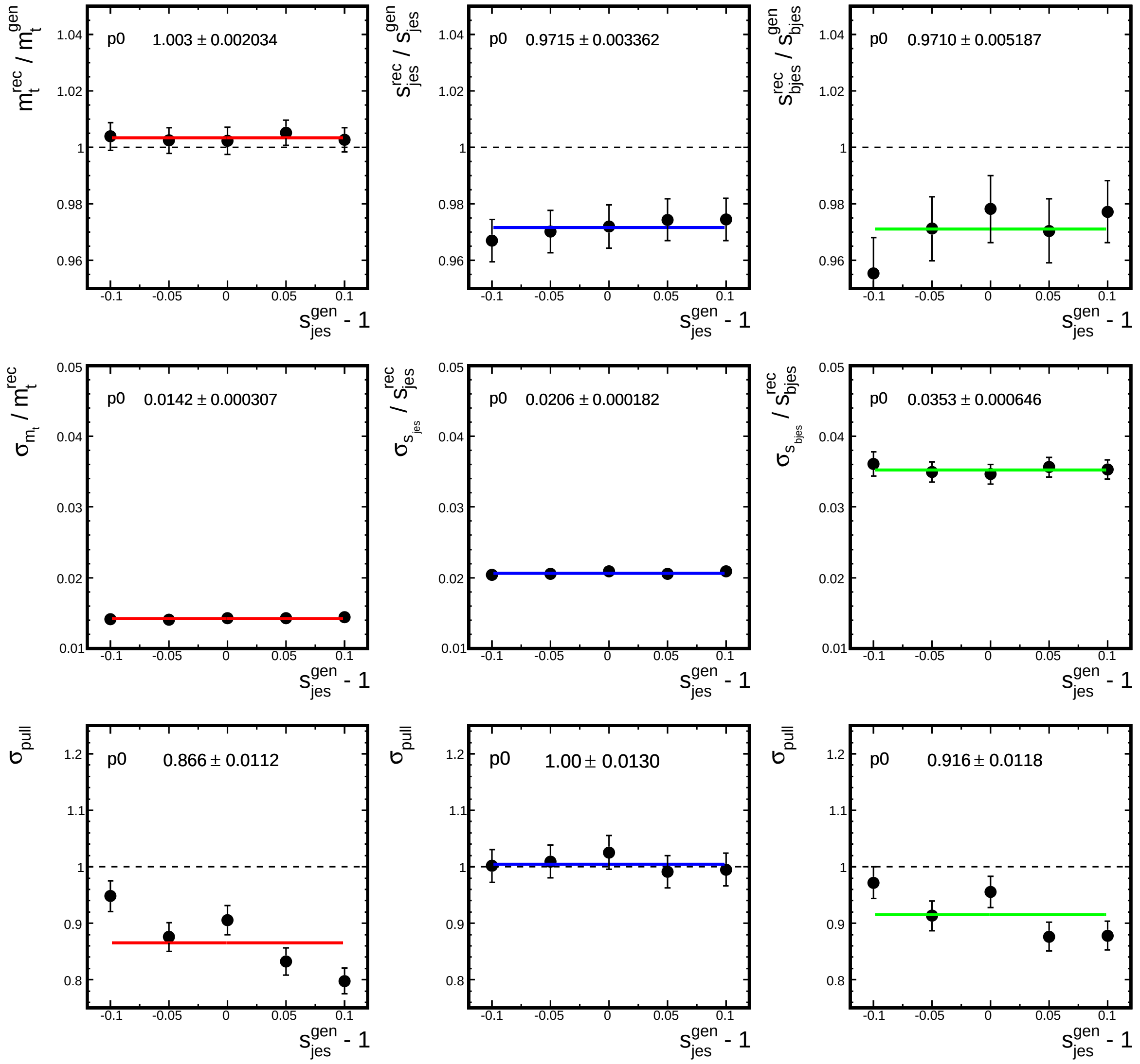

Figure B.5: s_{jes} calibration including W+4lp events.

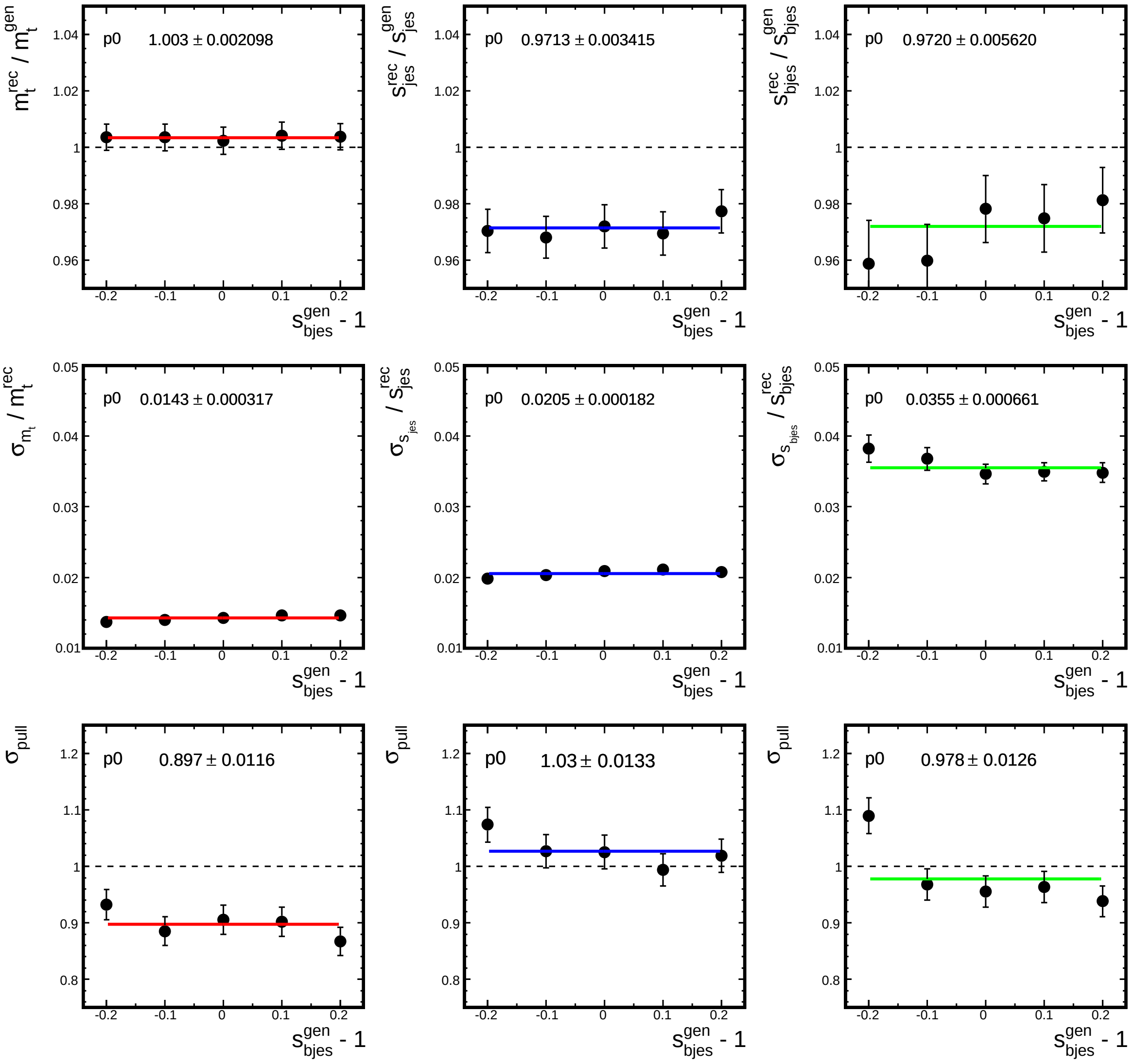

Figure B.6: s_{bjes} calibration including W+4lp events.

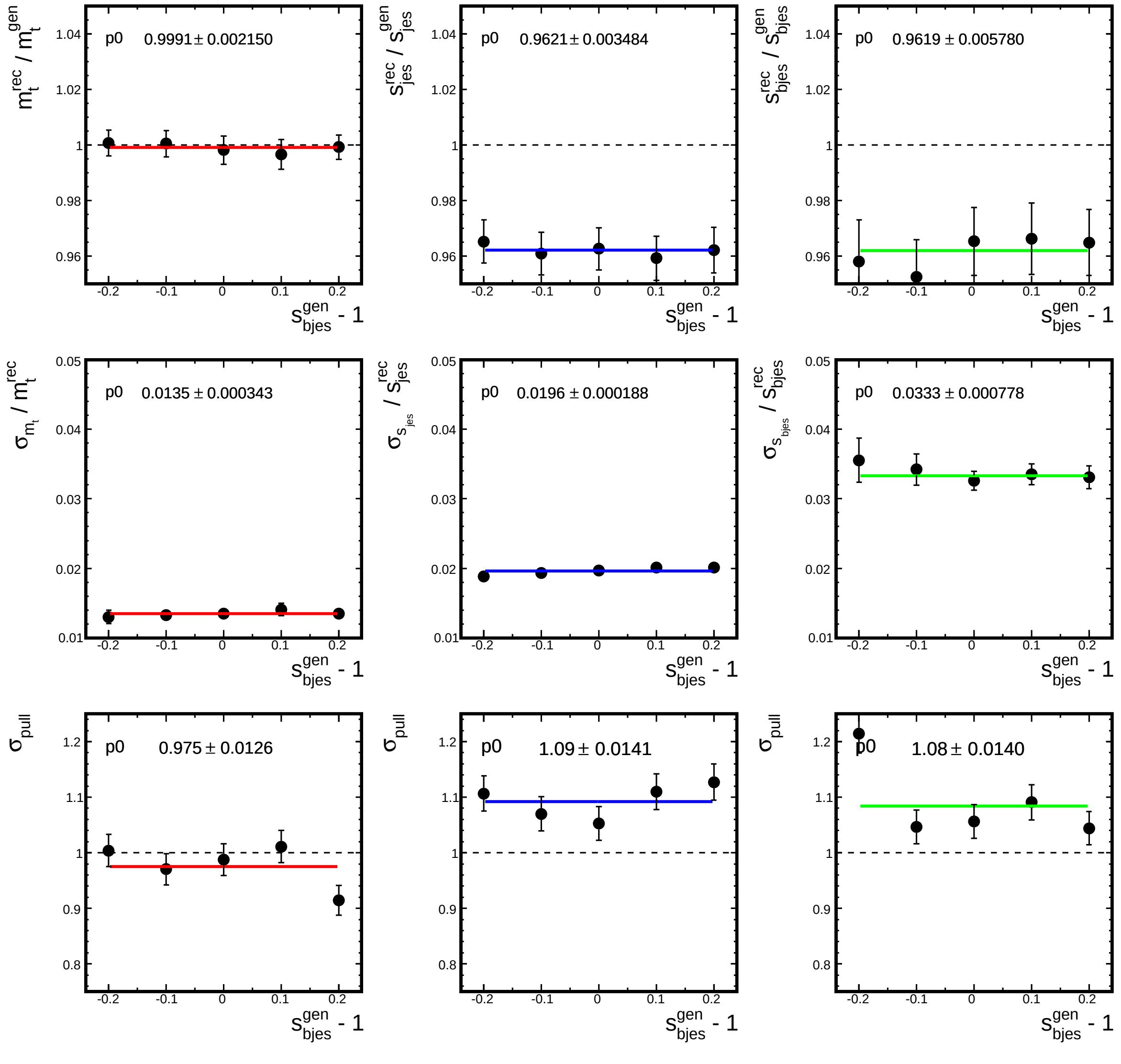

Figure B.7: s_{bjes} calibration including 25% W+4lp and 25% W+bb+jj events.

Appendix C

CAF Package List

Package	Version	Comment
D0RunII	p18.10.00	
cafe	p18-br-132	
tmb_tree	p18-br-91	
cafe_sam	p18-br-07	
met_util	p18-br-01	
emid_cuts	p18-br-03	
caf_util	p18-br-47	
caf_mc_util	p18-br-51	final JSSR
mc_dup_evt	p18-br-01	
caf_pdfreweight	v00-00-05	
caf_dq	v02-02-02	
dq_util	v02-03-00	
dq_defs	v2007-03-09	
caf_trigger	p18-br-15	
caf_eff_utils	p18-br-07	
eff_utils	p18-br-13	
emid_eff	v7-preliminary-06	
muid_eff	v04-00-06	
jetid_eff	v01-01-03	
jetcorr	p18-br-11	final JES
top_cafe	v01-03-00	
top_me_cafe		

Table C.1: List of all CAF packages used in this analysis.

Appendix D

Monte Carlo Request IDs

Subsample	Request IDs
tt160+0lp	72866-72868
tt160+1lp	72872
tt160+2lp	72875
tt165+0lp	32384-32385, 34188-34189
tt165+1lp	32386, 34190-34191
tt165+2lp	32387
tt170+0lp	38689
tt170+1lp	38691
tt170+2lp	38692
tt175+0lp	29249-29250, 29265-29268, 37340-37341
tt175+1lp	29251, 29269
tt175+2lp	29888, 29890
tt180+0lp	72893-72895
tt180+1lp	72896-72897
tt180+2lp	72912

Table D.1: List of D0 Monte Carlo request IDs for the $t\bar{t}$ sample.

Subsample	SAM-Definition	Request IDs
W+0lp, excl.	TOP_w0lp_qMWPtW_ph*_v1	28472-28473, 28864, 28894-28895, 28914-28915, 29152-29153, 31063-31064, 31067-31068
W+1lp, excl.	TOP_w1lp_qMWPtW_ph*_v1	28474-28475, 28895-28897, 28916-28917, 29154-29155, 30176-30179
W+2lp, excl.	TOP_w2lp_qMWPtW_ph*_v1	28476-28479, 28866-28869, 28898-28901, 28918-28921, 29156-29159
W+3lp, excl.	TOP_w3lp_qMWPtW_v1	28908-28913, 28922-28923, 29160
W+4lp, excl.	TOP_w4lp_qMWPtW_v1	28752-28753, 28874-28881, 28904-28907, 28924-28927, 29161-29162
W+5lp, incl.	TOP_w5lp_qMWPtW_v1	28754, 28863, 34959
W+bb+0lp, excl.	TOP_w2b0lp_qMWPtW_v1	28548-28551, 28892-28893, 30779-30780, 30803-30804
W+bb+1lp, excl.	TOP_w2b1lp_qMWPtW_v1	29252-29255, 30801-30802
W+bb+2lp, excl.	TOP_w2b2lp_qMWPtW_v1	29258-29261
W+bb+3lp, incl.	TOP_w2b3lp_qMWPtW_v1	29881-29884
W+cc+0lp, excl.	TOP_w2c0lp_qMWPtW_v1	31707-31711
W+cc+1lp, excl.	TOP_w2c1lp_qMWPtW_v1	31712-31718
W+cc+2lp, incl.	TOP_w2c3lp_qMWPtW_v1	31732 - 31739

Table D.2: List of D0 SAM-Definitions and the corresponding Monte Carlo request IDs for the W+jets sample.

Appendix E

Overview of Trigger Lists and Integrated Luminosities

e+jets			μ+jets		
Trigger List	Trigger	$\int$ Lumi (pb^{-1})	Trigger List	Trigger	$\int$ Lumi (pb^{-1})
V8.0 - V9.0	EM15_2JT15	23.35	V8.0 - V9.0	MU_JT20_L2M0	24.63
V9.0 - V10.0	EM15_2JT15	24.73	V9.0 - V10.0	MU_JT20_L2M0	24.77
V10.0 - V11.0	EM15_2JT15	9.81	V10.0 - V11.0	MU_JT20_L2M0	10.70
V11.0 - V12.0	EM15_2JT15	63.40	V11.0 - V12.0	MU_JT20_L2M0	65.83
V12.0 - V13.0	E1_SHT15_2J20	227.35	V12.0 - V13.0	MU_JT25_L2M0	231.14
V13.0 - V13.3	E1_SHT15_2J_J25	54.86	V13.0 - V13.2	MUJ2_JT25	31.84
			V13.2 - V13.3	MUJ2_JT25_LM3	15.74
TOTAL	Pre-Shutdown	403.50	TOTAL	Pre-Shutdown	404.64
V13.0 - V13.3	E1_SHT15_2J_J25	0.35	V13.2 - V13.3	MUJ2_JT25_LM3	0.35
V13.3 - V14.0	E1_SHT15_2J_J30	298.21	V13.3 - V14.0	MUJ2_JT30_LM3	255.33
V14.0 - V15.0	E1_SHT15_2J_J25	333.57	V14.0 - V14.2	MUJ1_JT25_LM3	0.01
			V14.2 - V14.3	MUJ1_JT25_ILM3	21.89
			V14.3 - V15.0	MUJ1_JT35_LM3	311.92
TOTAL	Post-Shutdown	632.14	TOTAL	Post-Shutdown	589.50

Table E.1: Trigger Lists and the corresponding integrated luminosities for the e+jets and μ+jets channel of the data sample used in this analysis.

Appendix F

Input Variables for Topological Likelihood Fits

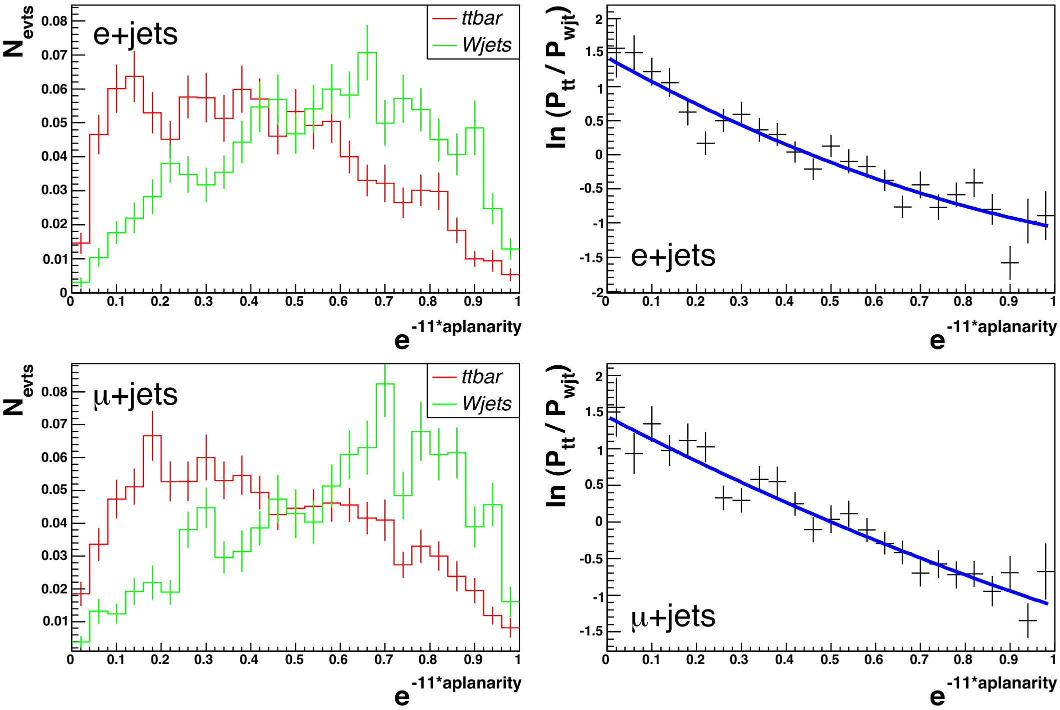

Figure F.1: Aplanarity.

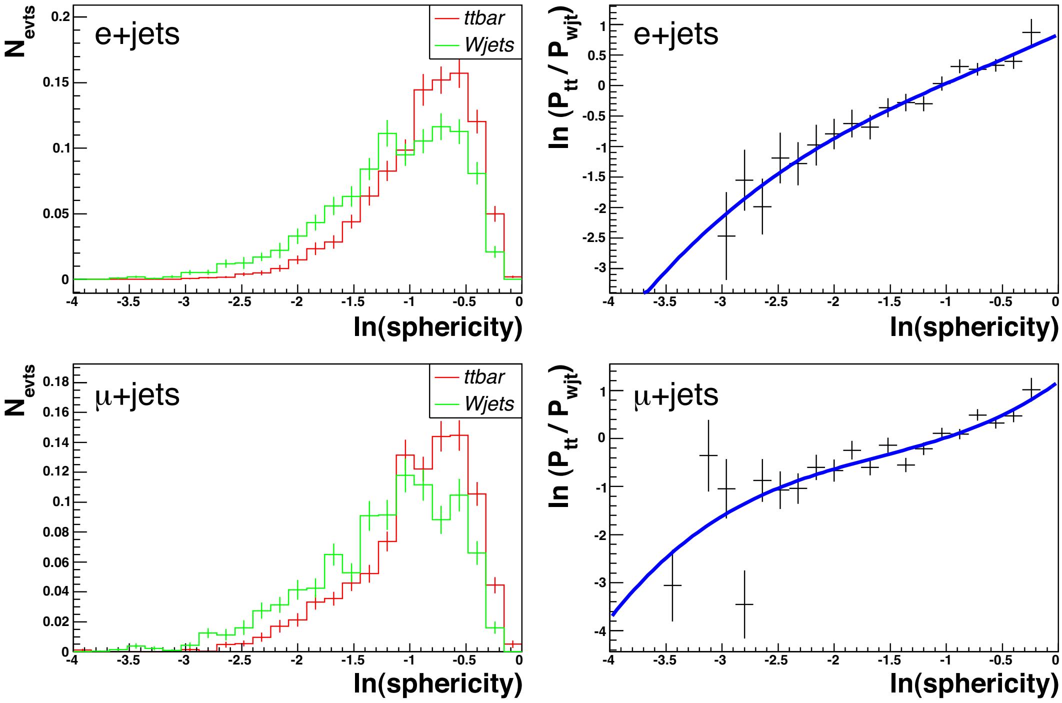

Figure F.2: Sphericity.

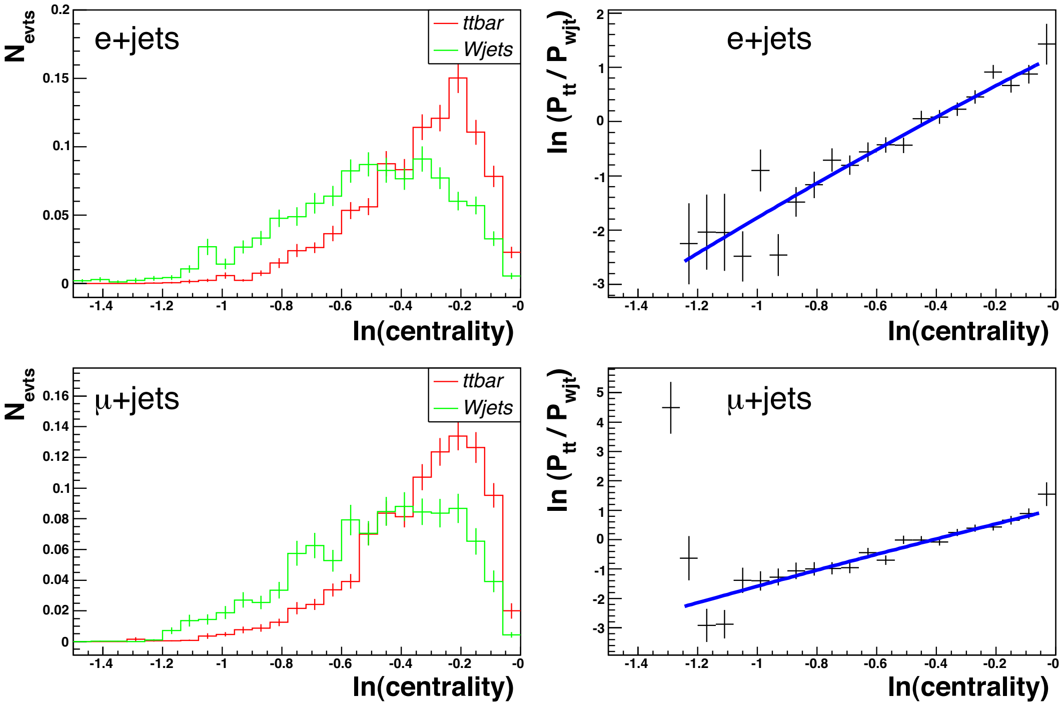

Figure F.3: Centrality.

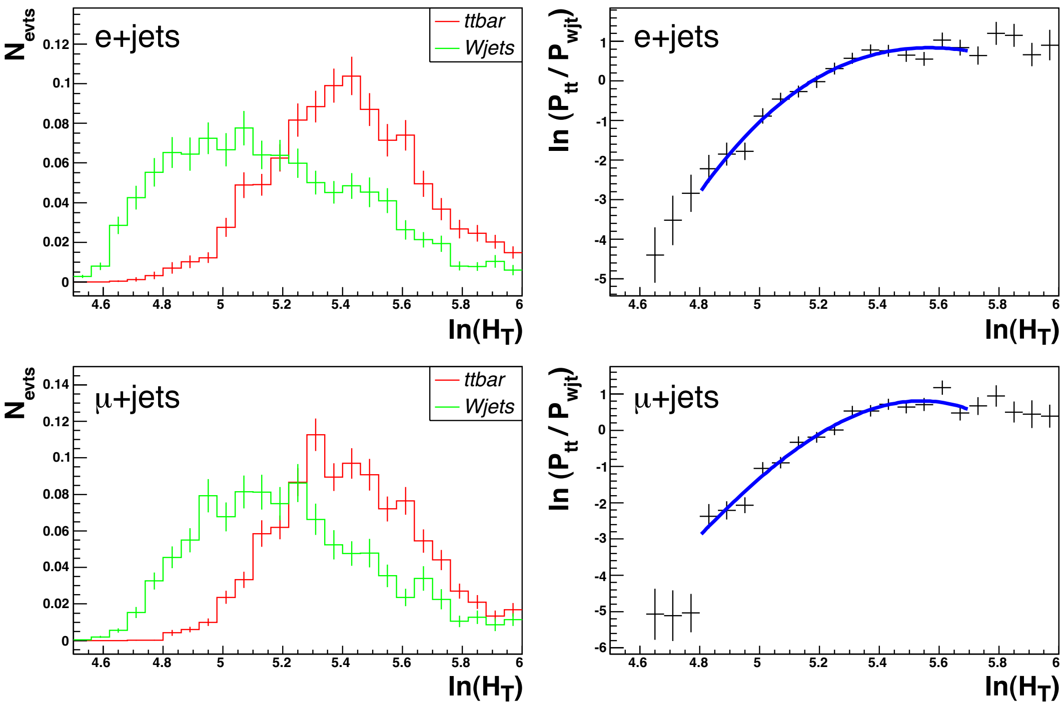

Figure F.4: H_T.

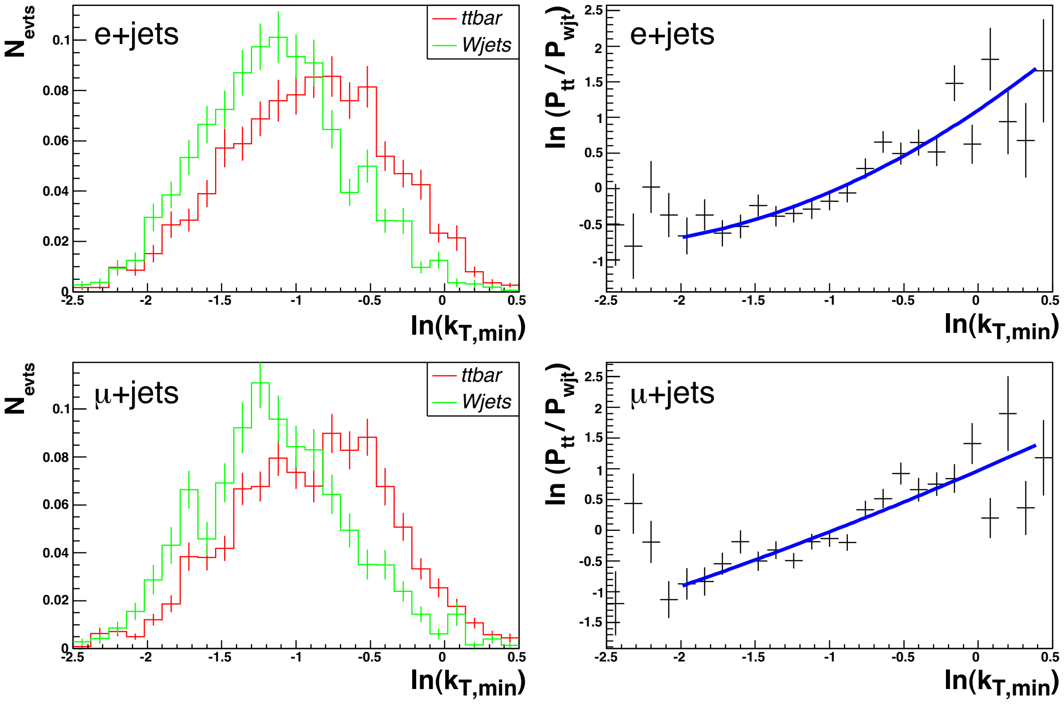

Figure F.5: $k_{T,min}$.

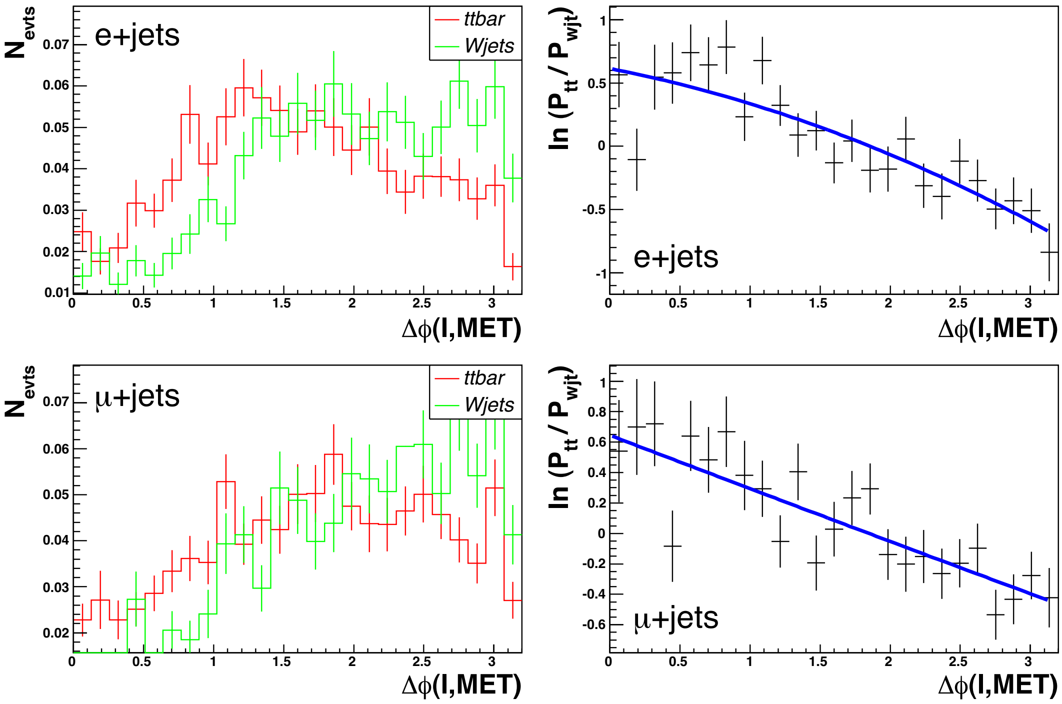

Figure F.6: $\Delta\phi(l, \not{E}_t)$.

Appendix G

Data to Monte Carlo Comparisons

In order to compare kinematic distributions between data and Monte Carlo simulation, the different signal and background processes need to be combined according to their measured fractions. As stated in Sec. 6.3.2, the QCD multijet background is difficult to simulate and therefore is estimated from data. This is done by selecting a loose and a tight sample. Here, the loose sample selection comprises all cuts described in Sec. 6.1 despite the tight lepton isolation cut. The tight sample is obtained from the loose one by applying that cut. To estimate the QCD multijet background fraction from these samples, the so-called *matrix method* [122] is used (not to be confused with the matrix *element* method!).

The number of events in the loose and tight data samples are denoted with N_l and N_t, respectively. $N^{W+t\bar{t}}$ indicates the combined number of $t\bar{t}$ and W+jets events and N^{QCD} gives the event number of QCD multijet events, all in the loose data sample. To obtain the respective numbers in the tight sample, the efficiency for a real lepton to pass the tight selection cut ε_{sig} and the efficiency for a fake lepton to pass the same cut ε_{qcd} are required. These are listed in Table G.1. Their derivation is described in [123, 124]. With these definitions, the event numbers of the loose and tight sample can be written as:

$$N_l = \varepsilon_{sig} N_l^{W+t\bar{t}} + \varepsilon_{qcd} N_l^{qcd} \tag{G.1}$$

$$N_t = \varepsilon_{sig} N_l^{W+t\bar{t}} + \varepsilon_{qcd} N_l^{qcd} \; . \tag{G.2}$$

The number of multjet events is extracted by solving this linear system. One gets:

$$N^{qcd} = \frac{\varepsilon_{sig} N_l - N_t}{\varepsilon_{sig} - \varepsilon_{qcd}} \tag{G.3}$$

$$N^{W+t\bar{t}} = \frac{N_t - \varepsilon_{qcd} N_l}{\varepsilon_{sig} - \varepsilon_{qcd}} \; . \tag{G.4}$$

As no efficiencies for the four jet exclusive bin are available, the values from the four jet inclusive bin are used to derive the number of QCD multijet events used in this analysis. The fitted QCD multijet fractions for the e+jets and μ+jets channels from the topological likelihood fit are given in Table 6.6, together with the respective W+jets and $t\bar{t}$ fractions. The following data / MC comparison plots for the four jet exclusive bin use these compositions. For the other jet bins, the contribution of $t\bar{t}$ signal is expected to be negligible. Thus, the QCD multijet background is subtracted bin-by-bin from the data sample and the result is compared to the W+jets Monte Carlo sample. The plots can be found in [114].

Efficiency	N_{jet}	e+jets	μ+jets
ε_{sig}	1	0.836 ± 0.035	0.915 ± 0.011
	2	0.846 ± 0.015	0.887 ± 0.008
	3	0.848 ± 0.003	0.873 ± 0.006
	≥ 4	0.840 ± 0.018	0.845 ± 0.022
ε_{qcd}	1	0.207 ± 0.003	0.350 ± 0.010
	2	0.192 ± 0.004	0.285 ± 0.014
	3	0.200 ± 0.010	0.235 ± 0.030
	≥ 4	0.213 ± 0.026	0.351 ± 0.082

Table G.1: Efficiencies for signal and QCD background to pass the tight lepton isolation cut for e+jets and μ+jets.

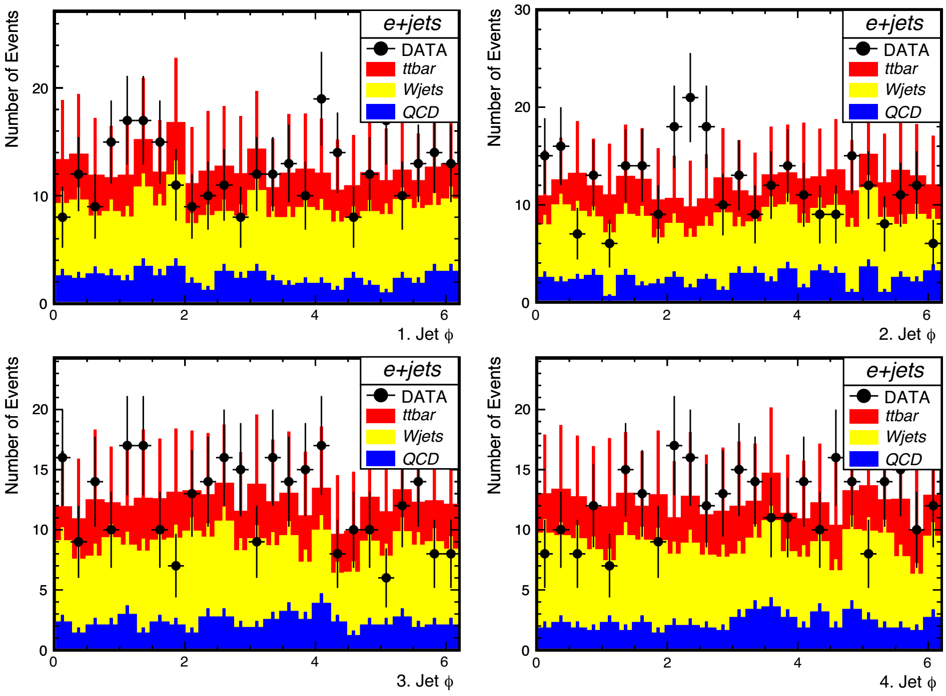

Figure G.1: Data-MC jet ϕ comparison for the e+jets channel.

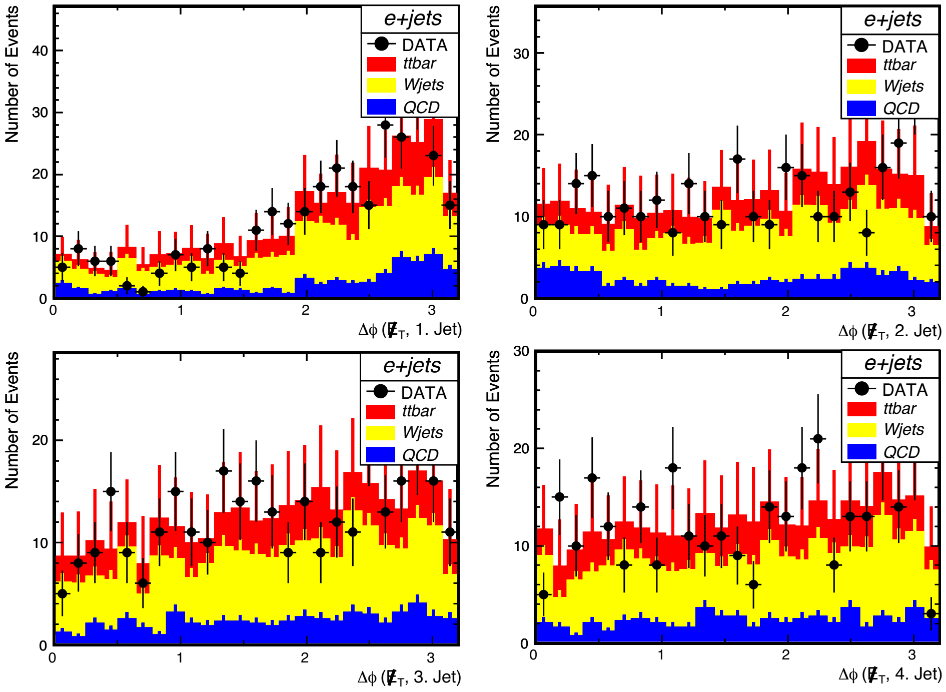

Figure G.2: Data-MC $\Delta\phi$(jet, $\not{E}_t$) comparison for the e+jets channel.

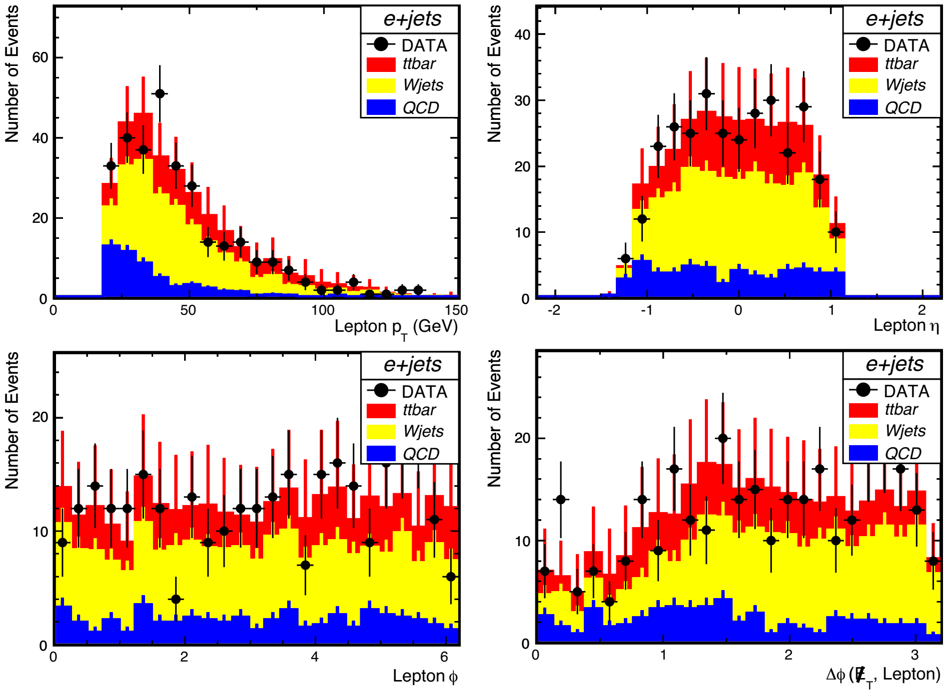

Figure G.3: Data-MC lepton comparisons for the e+jets channel.

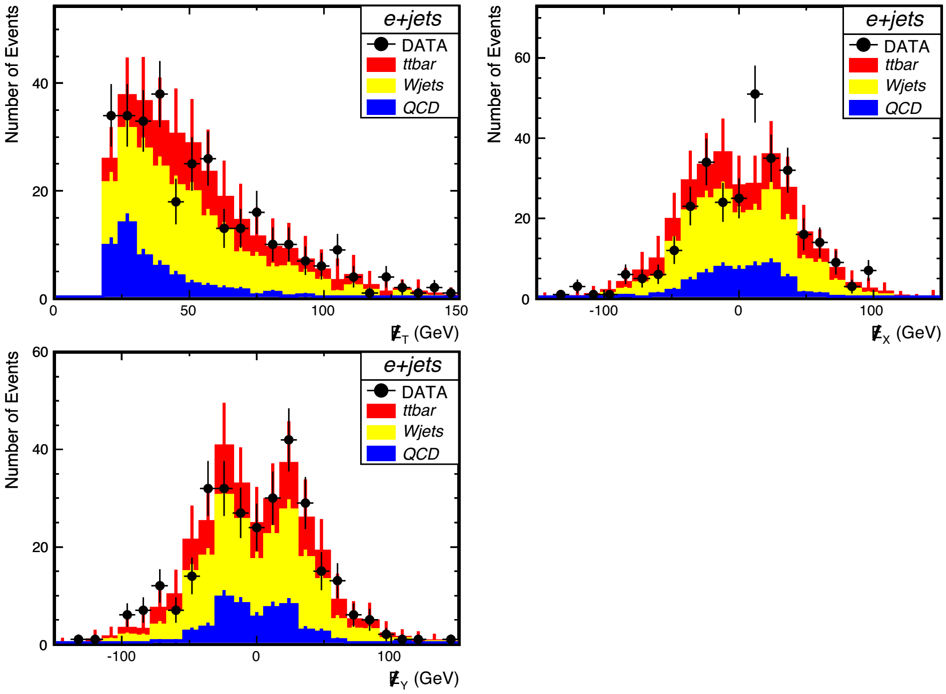

Figure G.4: Data-MC $\not\!\!E_t$ comparisons for the e+jets channel.

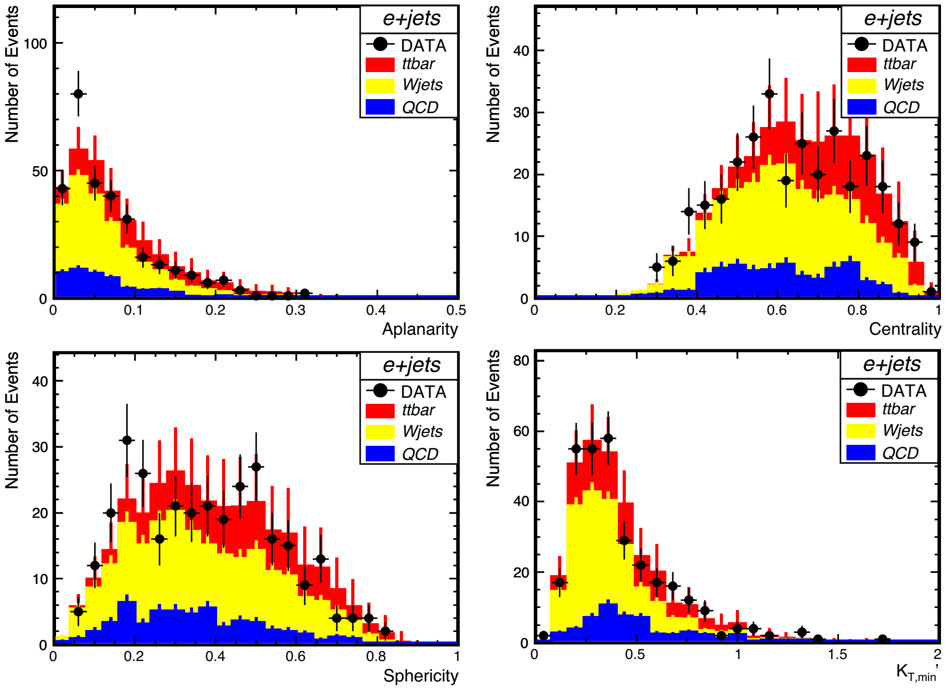

Figure G.5: Data-MC topological variable comparisons for the e+jets channel.

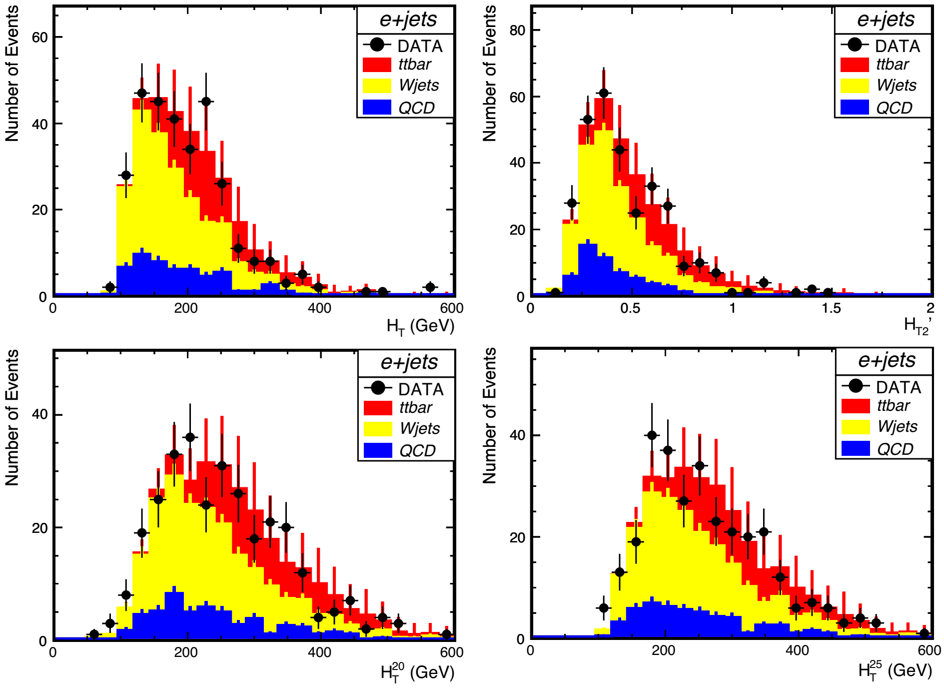

Figure G.6: Data-MC H_T variable comparisons for the e+jets channel.

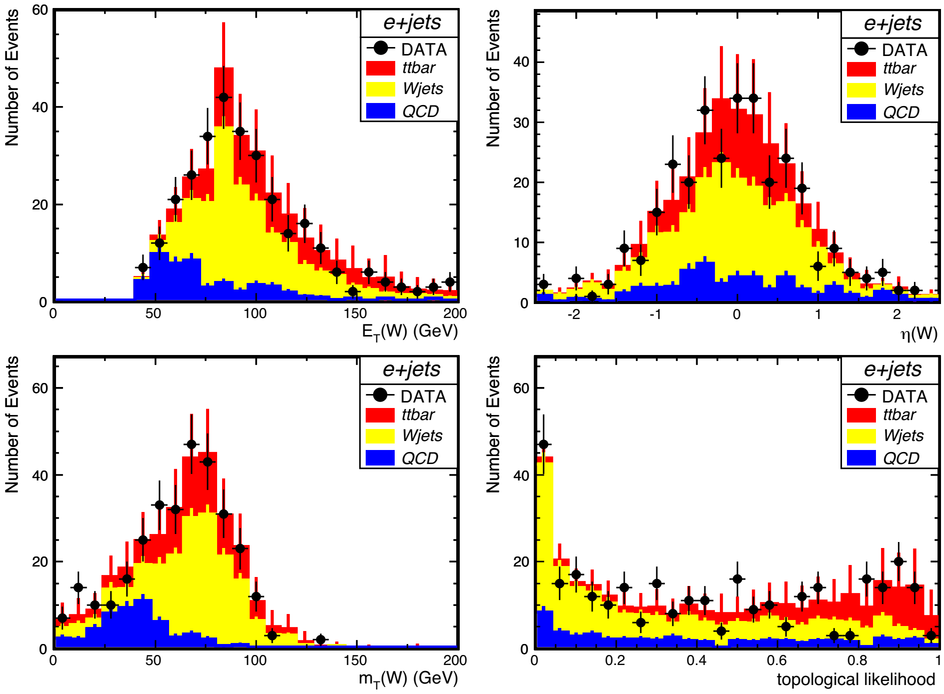

Figure G.7: Data-MC W variable comparisons for the e+jets channel.

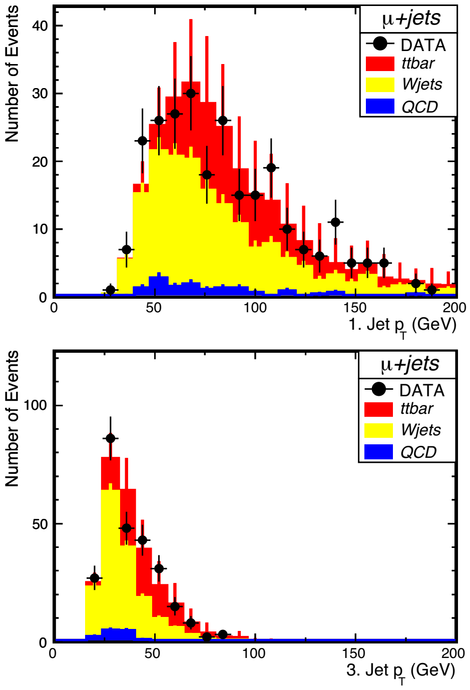

Figure G.8: Data-MC jet p_t comparison for the μ+jets channel.

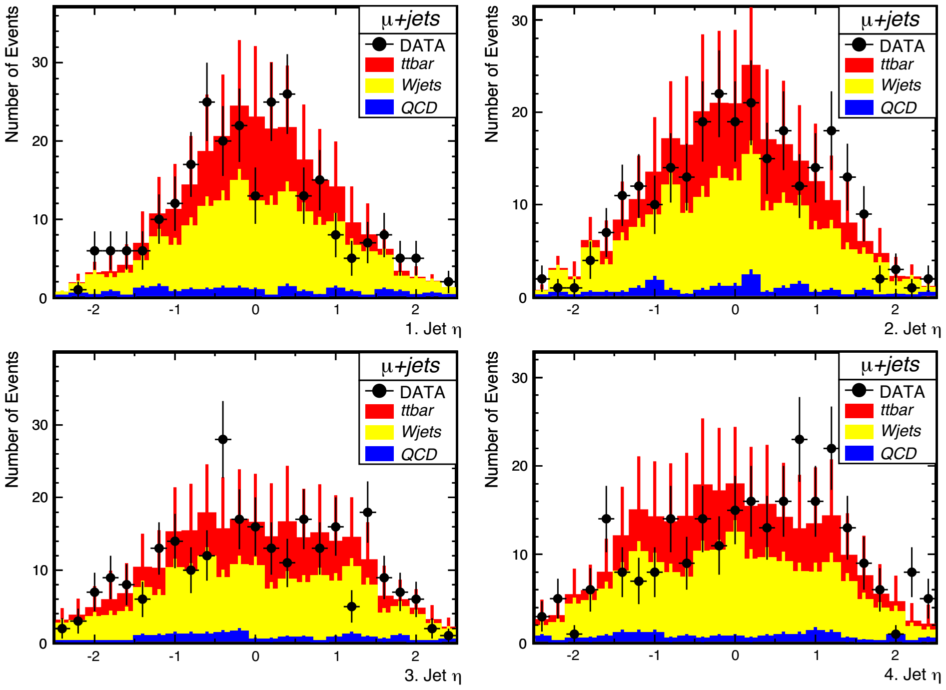

Figure G.9: Data-MC jet η comparison for the μ+jets channel.

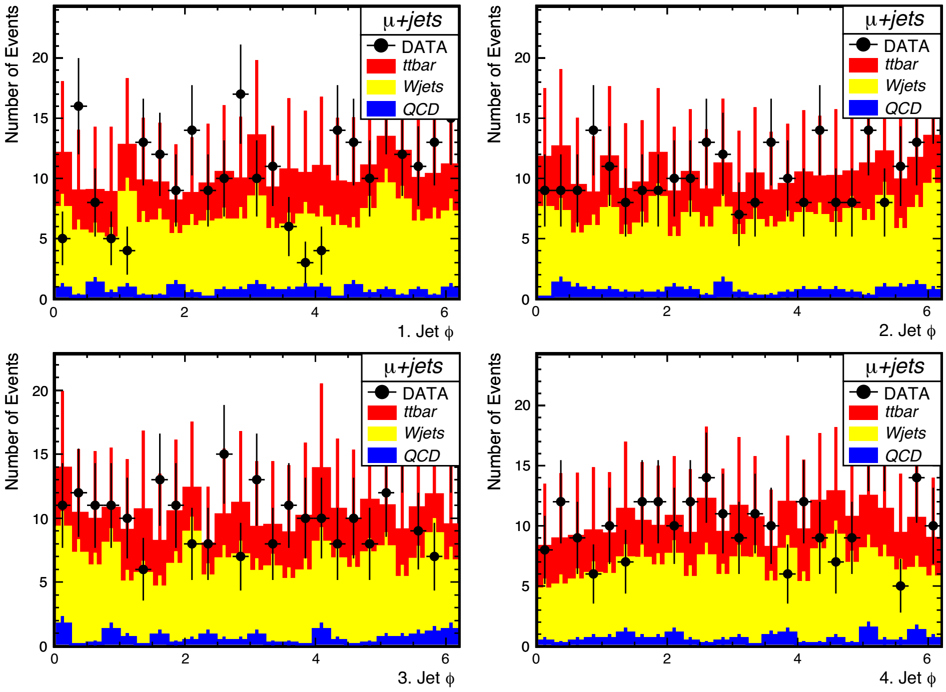

Figure G.10: Data-MC jet ϕ comparison for the μ+jets channel.

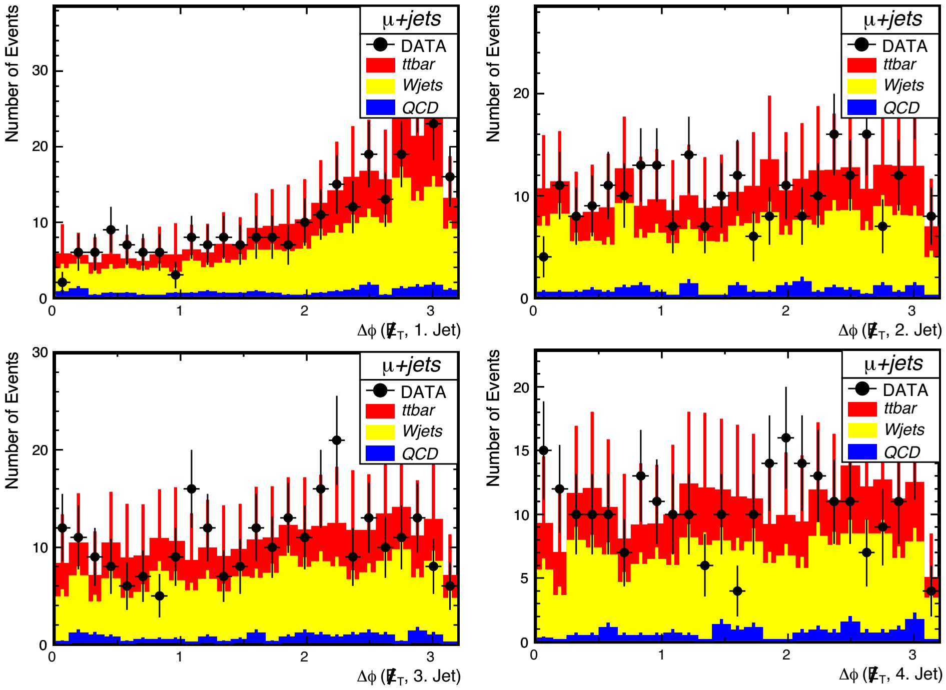

Figure G.11: Data-MC Δϕ(jet, $\not{E}_t$) comparison for the μ+jets channel.

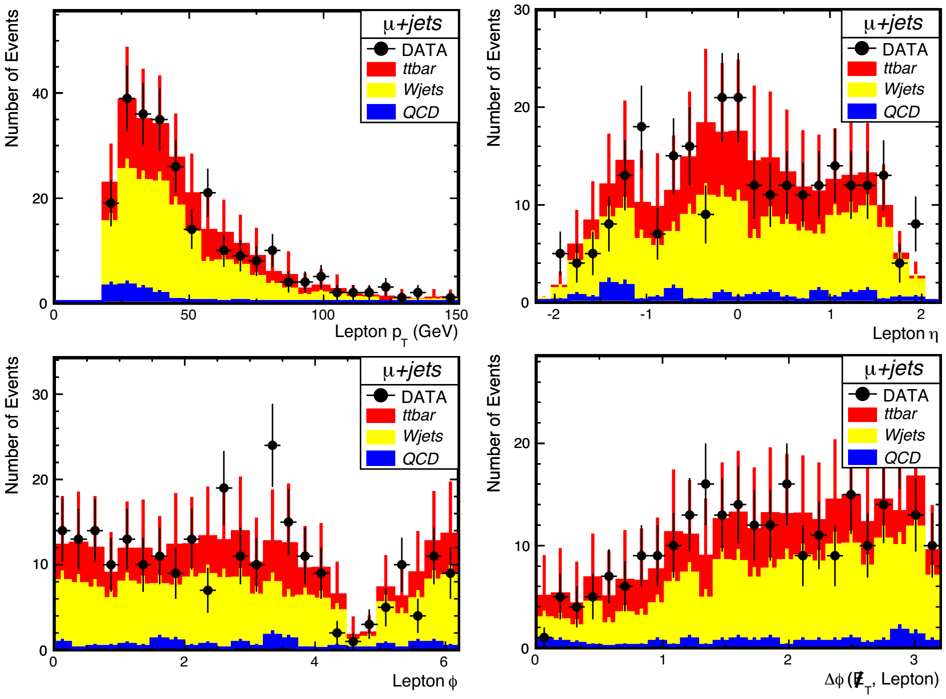

Figure G.12: Data-MC lepton comparisons for the μ+jets channel.

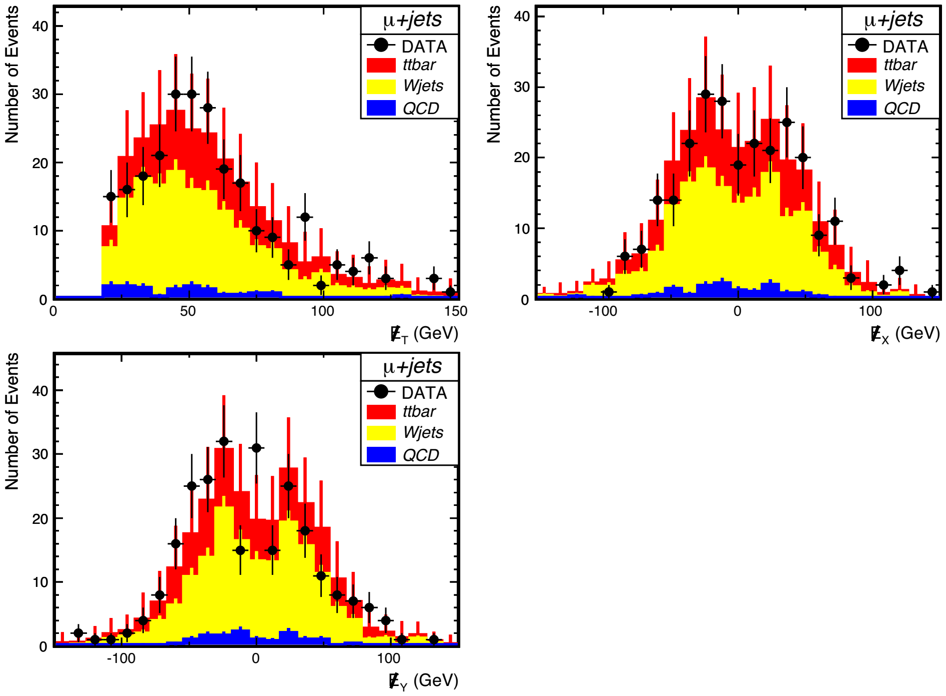

Figure G.13: Data-MC $\not\!\!E_t$ comparisons for the μ+jets channel.

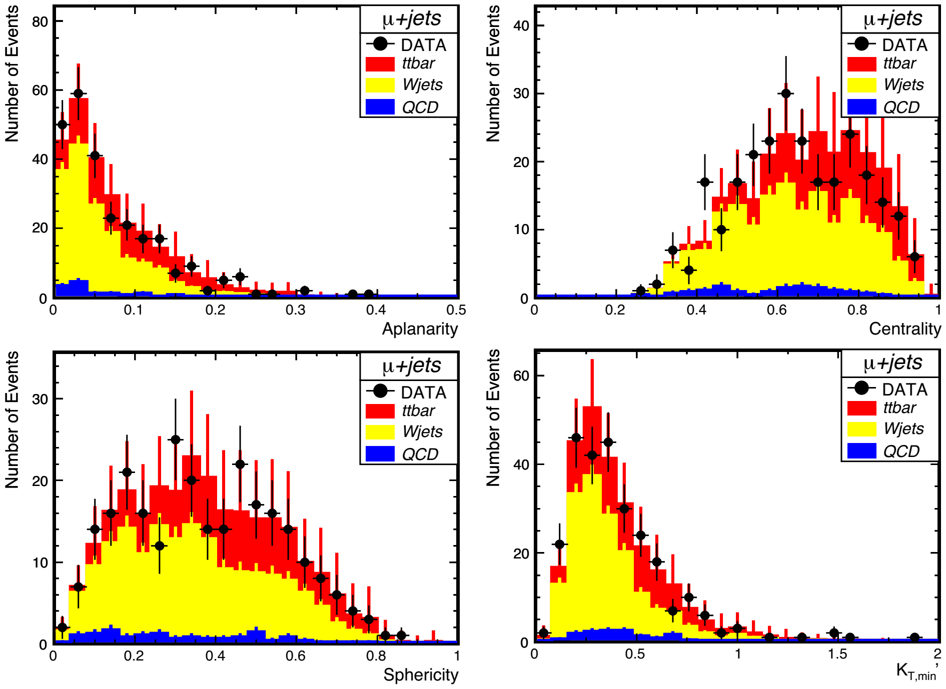

Figure G.14: Data-MC topological variable comparisons for the μ+jets channel.

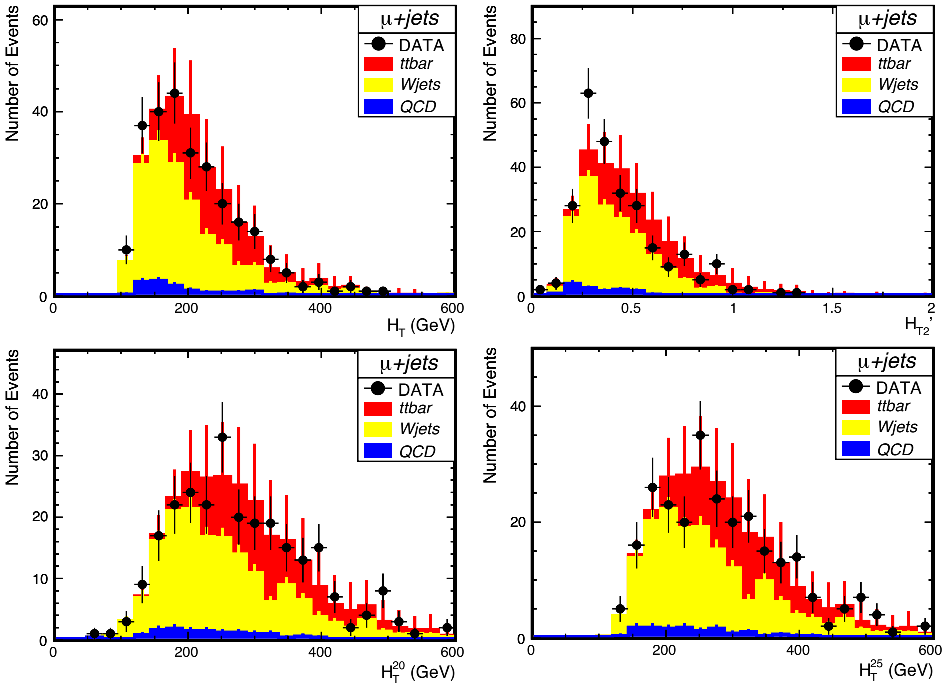

Figure G.15: Data-MC H_T variable comparisons for the μ+jets channel.

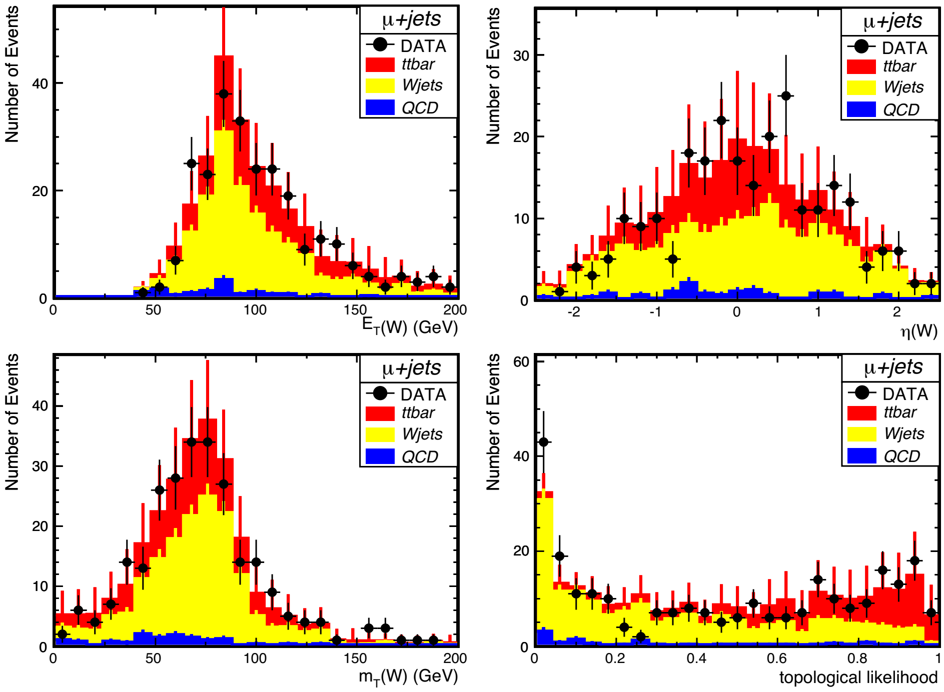

Figure G.16: Data-MC W variable comparisons for the μ+jets channel.

Appendix H

Additional Monte Carlo Studies

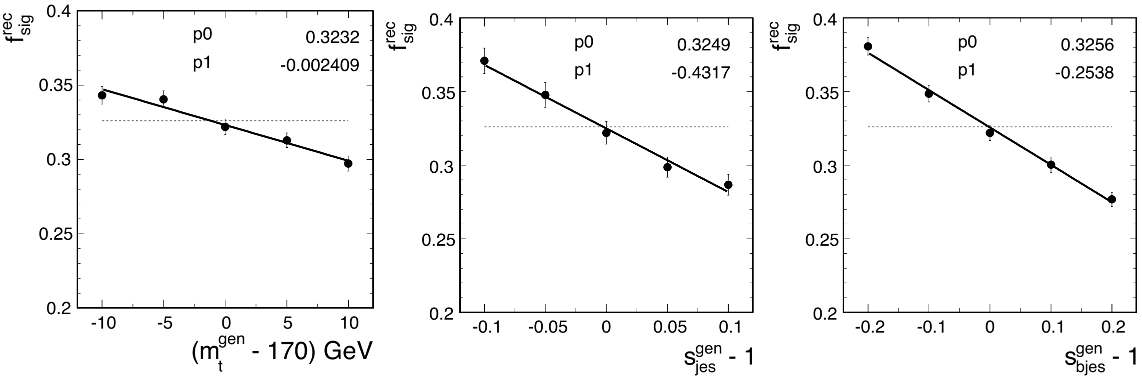

Figure H.1: Signal fraction vs. m_t, s_{jes} and s_{bjes} for fully simulated events.

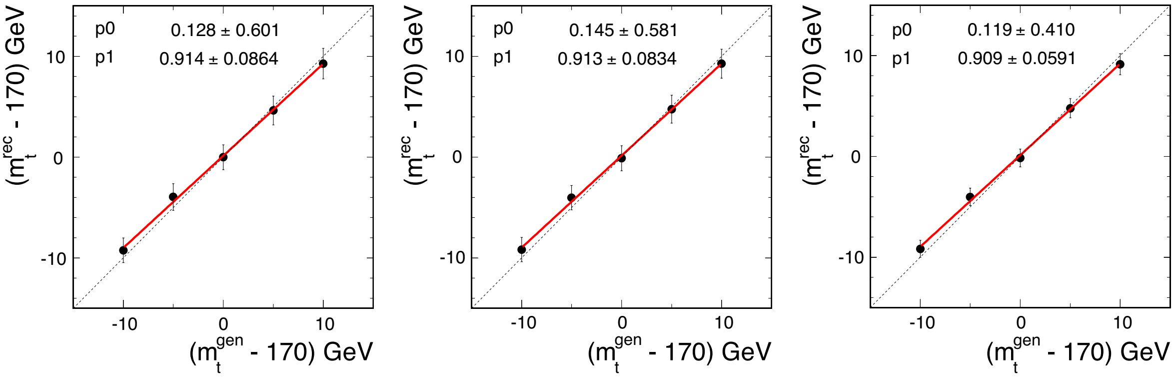

Figure H.2: Top mass calibration curves for fit ranges (2N+1) with *left:* N=3, *middle*: N=5, *right* N=7.

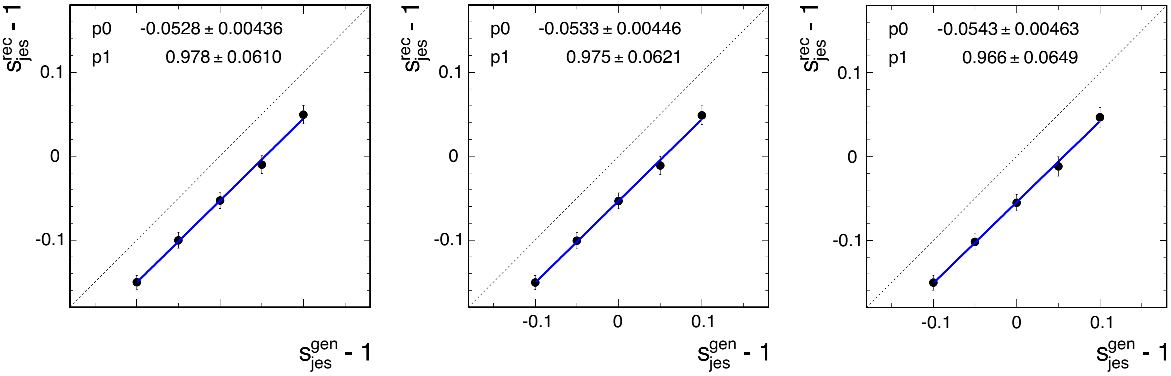

Figure H.3: s_{jes} calibration curves for fit ranges (2N+1) with *left:* N=3, *middle*: N=5, *right* N=7.

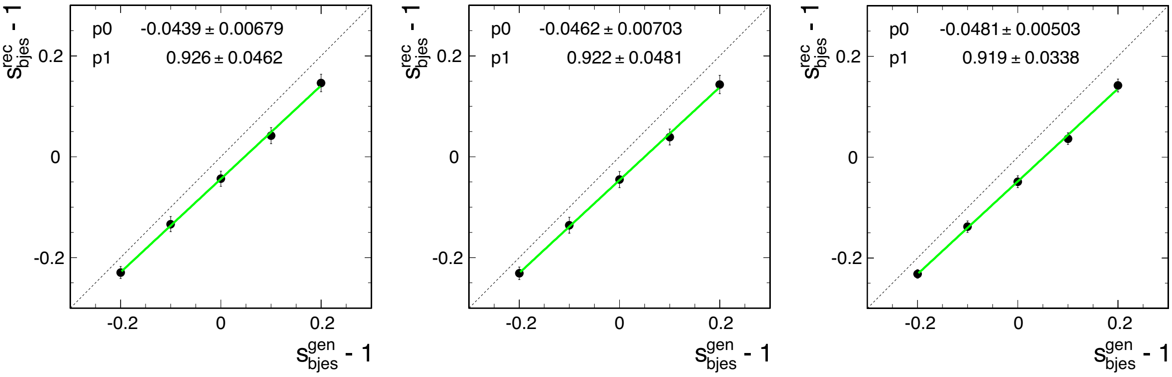

Figure H.4: s_{bjes} calibration curves for fit ranges (2N+1) with *left:* N=3, *middle*: N=5, *right* N=7.

Appendix I

Data Measurement requiring *b* tags

In the following, the measurement described in Chap. 6 is repeated with the additional requirement of 2 *b* tags. This means, two of the four jets must have the loosest possible tag (L6) or tighter. This is expected to increase the signal purity substantially while decreasing the number of selected events. The rest of the analysis is kept fixed (e.g. normalization, fit range). The fit is shown in Fig. I.1. The selection is fulfilled by 164 events compared to 543 events in the default selection. The fitted purity indeed increases from 32.6% to 78.8%. As the calibration curves were not rederived for this study, the result is calibrated with the signal fraction calibration in Fig. 6.25 and Fig. 6.29 at the corresponding reconstructed signal fraction (i.e m_t-0.2 GeV, s_{jes} + 0.01, s_{bjes} + 0.02, $f_{sig} \longrightarrow$ 94.7%). For the statistical error calibration the same pull widths as in the default data measurement are applied (cf. Sec. 6.4).

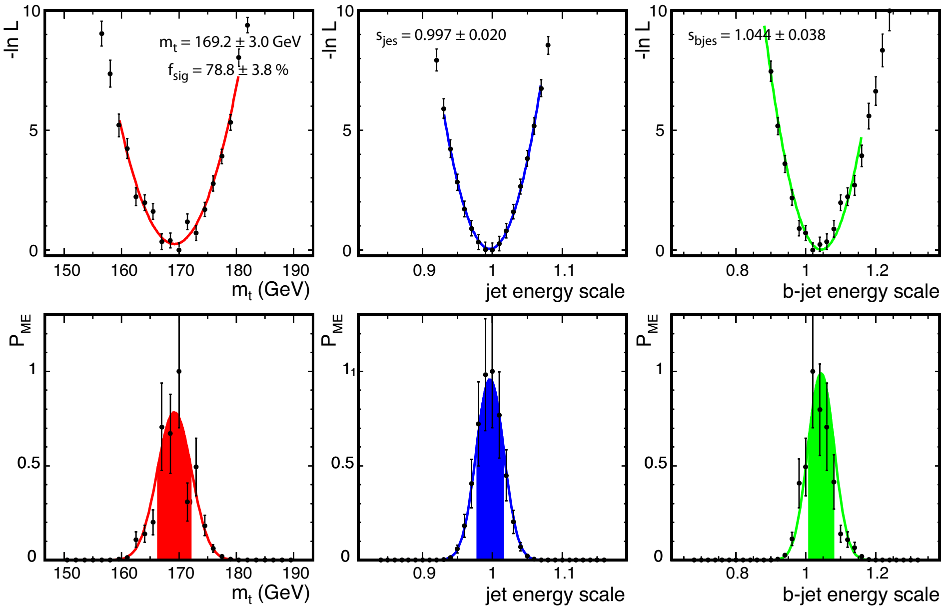

Figure I.1: Likelihood fits of m_t, s_{jes} and s_{bjes} for the data measurement with the requirement of two *b* tags (uncalibrated). *Top*: negative log likelihoods. *Bottom*: Probability distributions..

List of Figures

1.1 Overview of the content of the Standard Model of particle physics and the particle masses. 2

1.2 Evolution of the indirect prediction and direct measurement of the top quark mass with time [21]. 3

1.3 Contour curves of 68% probability in the (m_t, m_W) plane. 4

2.1 D0 detector side view 8

2.2 The Silicon Microstrip Tracker in a 3D visualization. 10

2.3 Overview of the full tracking system. 11

2.4 Schematic view of a quarter of the D0 calorimeter showing the transverse and longitudinal segmentation pattern. 12

2.5 Calorimeter unit cell. 13

3.1 Distribution of the neural network output for light, *c*- and *b* jets. The cut values of the 12 certified operating points are indicated by the solid lines. 22

4.1 Schematic illustration of the factorization approach [81]. 26

4.2 The `CTEQ6L` parametrization [82] of the parton distribution functions. 26

4.3 Leading order Feynman diagrams for $t\bar{t}$ production at hadron colliders. 27

4.4 Overview of top pair decay channels and branching fractions. 28

5.1 Schematic overview of the signal probability evaluation. 33

5.2 Top mass resolution with *top:* electron reconstructed, *middle:* muon reconstructed, *bottom: b* jet reconstructed. 34

5.3 Top mass resolution for several energy intervals with *left:* electron reconstructed, *middle:* muon reconstructed, *right: b* jet reconstructed. 35

5.4 Di-jet invariant mass distributions for the two quarks of the *W* decay for jet-parton matched events. 38

5.5 Jet transfer functions for the three jet flavors in four η_{det} regions. 40

5.6 Muon resolution fitted by a gaussian for $1.0 \leq |\eta_{evt}| \leq 1.2$ and $0.025 \leq (1/p_t)_{evt} \leq 0.030$ GeV^{-1}. 42

5.7 Muon resolution dependence on η_{evt} and $(1/p_t)_{evt}$ for muons including SMT hits in the post-shutdown period. 43

5.8 Schematic of muon transfer function described by the quadratic sum of a constant and a straight line. 43

5.9 Dependence of the σ_0 and c parameters on $(1/p_t)_{evt}$ for the post-shutdown period. *Left*: Muons without SMT hits. *Right*: Muons with SMT hits. 44

5.10 Muon resolution vs. $1/p_t$ (a, b) and η (c, d) with and without SMT hits (smear = MC smearing, pvtx = primary vertex constraint). 45

5.11 Comparison of the muon resolution for pre- and post-shutdown data, separated by run number 200 000. 46

5.12 Schematic representation of the s_{jes} and s_{bjes} constraints in the topological signal likelihood evaluation. 49

5.13 Schematic comparison between 3D and 1D normalization. 54

5.14 Distribution of the neural network output for a $t\bar{t}$ MC sample ($m_t = 170$ GeV). The red lines indicate the position of the cut values for the 12 operating points. 57

5.15 Distribution of the highest operating point giving a tag for MC samples with and without b jets. *Left:* $t\bar{t}$ sample ($m_t = 170$ GeV). *Right*: W+jets sample. 57

5.16 Tag Rate Function (TRF) output for three example operating points: *Top*: L6, *Middle*: Loose, *Bottom*: MegaTight; for the three possible parton flavors: *Left*: fake, *Middle*: c quark, *Right*: b quark. 58

5.17 b-tagging probabilities vs. NN output of all operating points for the three jet flavors fake, c, b. The first bin contains non-tagged jets. 59

5.18 Possible 24 jet-parton assignments in the semileptonic $t\bar{t}$ decay channel. 60

5.19 Descrimination power of signal vs. background likelihoods between $t\bar{t}$ signal (red), W+4lp background (blue) and W+bb+jj background (green). 61

5.20 Number of permutations needed to obtain 95% of the full event probability in a $t\bar{t}$ parton level test. 62

5.21 Overview of the fitting procedure for the example of the top mass. 64

6.1 Overview of the ensemble testing procedure for the example of the top mass. 69

6.2 Normalization of the signal likelihood for the parton level studies. 71

6.3 Normalization of the background likelihood for the parton level studies. 72

6.4 Ensemble fit for an arbitrary ensemble with generated values of m_t = 170 GeV, s_{jes} = 1.0 and s_{bjes} = 1.0. *Top*: negative signal log-likelihood. *Bottom*: signal probability, with the filled area indicating the integral of 68% probability. 73

6.5 Ensemble test for the m_t = 170 GeV calibration point. For each of the observables m_t, s_{jes} and s_{bjes} the distributions of the reconstructed value, its error and the pull are shown. 74

6.6 Mass calibration for pure e+jets signal events without b identification probabilities included. 75

6.7 Mass calibration for pure e+jets signal events including b identification probabilities. 76

6.8 Mass calibration curves. *Left*: e+jets, without use of b identification probabilities. *Right*: e+jets, with use of b identification probabilities. 77

6.9 s_{jes} calibration for pure e+jets signal events. 79

6.10 s_{bjes} calibration for pure e+jets signal events. 80

6.11 s_{bjes} calibration for pure e+jets signal events. s_{jes} and s_{bjes} are varied simultaneously according to Table 6.3. 81

6.12 Calibration curves for pure e+jets signal events. *Left*: s_{jes} variation. *Middle*: s_{bjes} variation. *Right*: s_{jes} and s_{bjes} variation. 82

6.13 Mass calibration for pure μ+jets signal events. 83

6.14 Mass calibration curves. *Left*: e+jets decay. *Right*: μ+jets decay. 84

6.15 Background fraction calibration for pure e+jets events. No background likelihoods are included. 85

6.16 Background fraction calibration including background likelihoods. 86

6.17 Calibration for the $W+bb$+jj fraction. 87

6.18 Calibration including events with an extra parton in the final state (ttljj). Background likelihoods are included. 88

6.19 Signal fraction calibration curves for the different types of background. 89

6.20 Signal fraction calibration curves for the three fit observables. The ensembles include 50% W+4lp background. 90

6.21 Templates for the topological likelihood fits in the e+jets and μ+jets decay channels. 95

6.22 Topological likelihood fits or the e+jets and μ+jets decay channels. 95

6.23 Normalization of the signal likelihood for the calibration. 96

6.24 Normalization of the background likelihood for the calibration. 97

6.25 Background calibration for fully simulated events. 99

6.26 Top mass calibration for fully simulated events. 100

6.27 s_{jes} calibration for fully simulated events. 101

6.28 s_{bjes} calibration for fully simulated events. 103

6.29 Calibration curves for the four fit observables for fully simulated events. 104

6.30 Likelihood fits of m_t, s_{jes} and s_{bjes} for the data measurement (uncalibrated). *Top*: negative log likelihoods. *Bottom*: Probability distributions. 106

6.31 Fitted statistical uncertainties for m_t, s_{jes} and s_{bjes} (arrows) compared to the error distributions in MC ensembles (histograms). All uncertainties are inflated by the average pull widths obtained in the calibration. 106

6.32 Parameterized distributions of the relative JES error for the four η_{det} regions used in the jet transfer functions. 111

6.33 Uncertainty on m_t caused by a slope in bJES vs. p_t^{jet}. The shift in m_t is parameterized by a second-order polynomial. 112

7.1 World average of the top quark mass as of March 2008 [115]. Preliminary results are indicated by a star. The result of this analysis is plotted for comparison. 119

B.1 Parton level calibration curves including background likelihoods. 125

B.2 s_{bjes} calibration including background likelihoods. The ensembles contain 25% $W+$4lp and 25% $W+bb+$jj events. Due to the more signal-like background the signal fraction is about 15% higher than in the case of pure $W+$4lp background. 126

B.3 Mass calibration including $W+$4lp events. 127

B.4 Mass calibration for the $\mu+$jets channel including $W+$4lp events. 128

B.5 s_{jes} calibration including $W+$4lp events. 129

B.6 s_{bjes} calibration including $W+$4lp events. 130

B.7 s_{bjes} calibration including 25% $W+$4lp and 25% $W+bb+$jj events. 131

F.1 Aplanarity. 139

F.2 Sphericity. 140

F.3 Centrality. 140

F.4 H_T. 141

F.5 $k_{T,min}$. 141

F.6 $\Delta\phi$(l, $\not{E}_t$). 142

G.1 Data-MC jet ϕ comparison for the $e+$jets channel. 144

G.2 Data-MC $\Delta\phi$(jet, $\not{E}_t$) comparison for the $e+$jets channel. 145

G.3 Data-MC lepton comparisons for the $e+$jets channel. 145

G.4 Data-MC $\not\!\!E_t$ comparisons for the e+jets channel. 146

G.5 Data-MC topological variable comparisons for the e+jets channel. 146

G.6 Data-MC H_T variable comparisons for the e+jets channel. 147

G.7 Data-MC W variable comparisons for the e+jets channel. 147

G.8 Data-MC jet p_t comparison for the μ+jets channel. 148

G.9 Data-MC jet η comparison for the μ+jets channel. 148

G.10 Data-MC jet ϕ comparison for the μ+jets channel. 149

G.11 Data-MC Δϕ(jet, $\not\!\!E_t$) comparison for the μ+jets channel. 149

G.12 Data-MC lepton comparisons for the μ+jets channel. 150

G.13 Data-MC $\not\!\!E_t$ comparisons for the μ+jets channel. 150

G.14 Data-MC topological variable comparisons for the μ+jets channel. 151

G.15 Data-MC H_T variable comparisons for the μ+jets channel. 151

G.16 Data-MC W variable comparisons for the μ+jets channel. 152

H.1 Signal fraction vs. m_t, s_{jes} and s_{bjes} for fully simulated events. 153

H.2 Top mass calibration curves for fit ranges (2N+1) with *left:* N=3, *middle*: N=5, *right* N=7. 154

H.3 s_{jes} calibration curves for fit ranges (2N+1) with *left:* N=3, *middle*: N=5, *right* N=7. . 154

H.4 s_{bjes} calibration curves for fit ranges (2N+1) with *left:* N=3, *middle*: N=5, *right* N=7. 154

I.1 Likelihood fits of m_t, s_{jes} and s_{bjes} for the data measurement with the requirement of two b tags (uncalibrated). *Top*: negative log likelihoods. *Bottom*: Probability distributions.. 155

List of Tables

5.1 Jet transfer function parameters derived for the three jet types considered in four η_{det} ranges. 39

5.2 Muon transfer function parameters for muons with and without SMT hits in the pre -and post shutdown run periods. 46

5.3 Operating points and cut values certified for the NN b-tagger. 56

6.1 Parameters for the three-dimensional grid of hypotheses. The default values (i.e. origin), range, step size and number of hypotheses in each dimension are given. 68

6.2 Event pool sizes available for the parton level studies. 70

6.3 Calibration points for the simultaneous variation of s_{jes} and s_{bjes}. 78

6.4 Event pool sizes of the $t\bar{t}$ signal available for the MC calibration. 92

6.5 Overview of the W+jets background available for the MC calibration. Cross sections, heavy flavor (HF) scale factors, sample composition and pool sizes are listed. 93

6.6 Fitted fractions of $t\bar{t}$ signal, W+jets and QCD multijet background. 96

6.7 Event numbers for the eight event pools used to compose the calibration ensembles. . 98

6.8 Integrated luminosities in pb^{-1}. 103

6.9 Selected event numbers for the e+jets and μ+jets decay signatures in the pre- and post-shutdown run periods. 104

6.10 Measurement results vs. fit range. The range always consists of $(2N_{pt}+1)$ points to be fitted and is symmetric around the absolute likelihood minimum. 105

6.11 Reconstructed and calibrated data measurement results and external measurements for comparison. The $\Delta\sigma$ values between this analysis and the external results are obtained by adding both uncertainties in quadrature. 105

6.12 Systematic variation of the calibration curve parameters. *up* and *down* denote a variation in positive or negative direction. 108

6.13 Overview of the systematic uncertainties of the top mass measurement presented in this analysis and their combination with the statistical uncertainty. Systematic uncertainties listed in brackets are not considered in the total as they are statistically insignificant. 115

7.1 Comparison of the measurement presented in this analysis to the result one would obtain by requiring two *b*-tags and the 2D measurement of m_t and s_{jes} on the same data set [92]. (*) For the *b*-tagging result no calibration curves and systematics are rederived (cf. App. I). 118

A.1 Example of b-tagging probabilities for 4 fictitious jets. 123

C.1 List of all `CAF` packages used in this analysis. 133

D.1 List of D0 Monte Carlo request IDs for the $t\bar{t}$ sample. 135

D.2 List of D0 SAM-Definitions and the corresponding Monte Carlo request IDs for the W+jets sample. 136

E.1 Trigger Lists and the corresponding integrated luminosities for the e+jets and μ+jets channel of the data sample used in this analysis. 137

G.1 Efficiencies for signal and QCD background to pass the tight lepton isolation cut for $e+$jets and $\mu+$jets. 144

Bibliography

[1] GELL-MANN, M.: *A Schematic Model of Baryons and Mesons*. *Phys. Lett.* 8 (1964), pp. 214–215

[2] AUGUSTIN, J. E.; ET AL. (SLAC-SP-017): *Discovery of a Narrow Resonance in e+ e- Annihilation*. *Phys. Rev. Lett.* 33 (1974), pp. 1406–1408

[3] AUBERT, J. J.; ET AL. (E598): *Experimental Observation of a Heavy Particle J*. *Phys. Rev. Lett.* 33 (1974), pp. 1404–1406

[4] PERL, M. L.; ET AL.: *Evidence for anomalous lepton production in e+ e- annihilation*. *Phys. Rev. Lett.* 35 (1975), pp. 1489–1492

[5] HERB, S. W.; ET AL.: *Observation of a dimuon resonance at 9.5-GeV in 400-GeV proton - nucleus collisions*. *Phys. Rev. Lett.* 39 (1977), pp. 252–255

[6] INNES, W. R.; ET AL.: *Observation of structure in the* Υ *region*. *Phys. Rev. Lett.* 39 (1977), p. 1240

[7] ARNISON, G.; ET AL. (UA1): *Experimental observation of isolated large transverse energy electrons with associated missing energy at s**(1/2) = 540-GeV*. *Phys. Lett.* B122 (1983), pp. 103–116

[8] BANNER, M.; ET AL. (UA2): *Observation of single isolated electrons of high transverse momentum in events with missing transverse energy at the CERN anti-p p collider*. *Phys. Lett.* B122 (1983), pp. 476–485

[9] ARNISON, G.; ET AL. (UA1): *Experimental observation of lepton pairs of invariant mass around 95-GeV/c**2 at the CERN SPS collider*. *Phys. Lett.* B126 (1983), pp. 398–410

[10] BAGNAIA, P.; ET AL. (UA2): *Evidence for Z0 –¿ e+ e- at the CERN anti-p p collider*. *Phys. Lett.* B129 (1983), pp. 130–140

[11] ALBAJAR, C.; ET AL. (UA1): *Search for New Heavy Quarks at the CERN Proton - anti-Proton Collider*. *Z. Phys.* C37 (1988), pp. 505–525

[12] ALTARELLI, G.; ET AL.: *Total Cross-Sections for Heavy Flavor Production in Hadronic Collisions and QCD*. *Nucl. Phys.* B308 (1988), p. 724

[13] ABE, F.; ET AL. (CDF): *A search for the top quark in the reaction* $\bar{p}p \rightarrow e + \text{jets}$ *at* $\sqrt{s} = 1.8$ *TeV*. *Phys. Rev. Lett.* 64 (1990), p. 142

[14] ABE, F.; ET AL. (CDF): *Top quark search in the electron + jet channel in* $p\bar{p}$ *collisions at* $\sqrt{s} = 1.8$ *TeV*. *Phys. Rev.* D43 (1991), pp. 664–686

[15] ABE, F.; ET AL. (CDF): *A Lower limit on the top quark mass from events with two leptons in* $p\bar{p}$ *collisions at* $\sqrt{s} = 1.8$ *TeV*. *Phys. Rev. Lett.* 68 (1992), pp. 447–451

[16] ABE, F.; ET AL. (CDF): *A Limit on the top quark mass from* $p\bar{p}$ *collisions at* $\sqrt{s} = 1.8$ *TeV*. *Phys. Rev.* D45 (1992), pp. 3921–3948

[17] HALZEN, F.; KIM, C. S.; MARTIN, A. D.: *Top quark signatures at the TEVATRON collider*. *Mod. Phys. Lett.* A4 (1989), p. 1531

[18] ABE, F.; ET AL. (CDF): *Observation of top quark production in* $\bar{p}p$ *collisions*. *Phys. Rev. Lett.* 74 (1995), pp. 2626–2631. `hep-ex/9503002`

[19] ABACHI, S.; ET AL. (D0): *Observation of the top quark*. *Phys. Rev. Lett.* 74 (1995), pp. 2632–2637. `hep-ex/9503003`

[20] *Combined preliminary data on Z parameters from the LEP experiments and constraints on the Standard Model* (1994). Contributed to the 27th International Conference on High- Energy Physics - ICHEP 94, Glasgow, Scotland, UK, 20 - 27 Jul 1994

[21] WILLENBROCK, S.: *Hadron colliders, the standard model, and beyond* (2002). `hep-ph/0212032`

[22] THE ALEPH, DELPHI, L3, OPAL, SLD COLLABORATIONS, THE LEP ELECTROWEAK WORKING GROUP, THE SLD ELECTROWEAK AND HEAVY FLAVOUR GROUPS: *Precision Electroweak Measurements on the Z Resonance*. *Phys. Rept.* 427 (2006), p. 257. `hep-ex/0509008`

[23] ABACHI, S.; ET AL. (D0): *The D0 Detector*. *Nucl. Instrum. Meth.* A338 (1994), pp. 185–253

[24] ABAZOV, V. M.; ET AL. (D0): *The upgraded D0 detector*. *Nucl. Instrum. Meth.* A565 (2006), pp. 463–537. `physics/0507191`

[25] VOUTILAINEN, M.: *Jet* p_t *resolution for run iia final jes (v7.2) with dijet j4s jet corrections*. D0 Note 5499, 2007

[26] BORISSOV, G.: *Ordering a chaos or... technical details of aa tracking*. All D0 Meeting, 2003. `http://www-d0.fnal.gov/atwork/adm/d0_private/2003-02-28/adm_talk.ps`

[27] KHANOV, A.: *Htf: histogramming method for finding tracks. the algorithm description*. D0 Note 3778, 2000

[28] DEMINA, R.; KHANOV, A.: *Histogramming track finding algorithm performance study*. D0 Note 3845, 2001

[29] KALMAN, R. E.: *A new approach to linear filtering and prediction problems*. *Trans. ASME* D (1960)(82), pp. 35–44

[30] KALMAN, R. E.; BUCY, R. S.: *New results in linear filtering and prediction theory*. *Trans. ASME* D (1961)(83), pp. 95–108

[31] BILLOIR, P.: *Track fitting with multiple scattering: A new method*. *Nucl. Instrum. Meth.* A (1984)(225), pp. 352–366

[32] GREENLEE, H.: *The d0 kalman fit*. D0 Note 4303, 2003

[33] SCHWARTZMAN, A.; NARIAN, M.: *Primary vertex selection*. D0 Note 3906, 2001

[34] SCHWARTZMAN, A.; NARIAN, M.: *Probabilistic primary vertex selection*. D0 Note 4042, 2001. `http://www-clued0.fnal.gov/~aran/m_4042.ps`

[35] GARCIA-BELLIDO, A.; ET AL.: *Primary vertex certification in p14*. D0 Note 4320, 2004

[36] SCHWARTZMAN, A.; TULLY, C.: *Primary vertex reconstruction by means of adaptive vertex fitting*. D0 Note 4918, 2005

[37] SCHWARTZMAN, A.; PETERS, Y.; GREENLEE, H.: *Adaptive primary vertex certification in p17*. D0 Note 5192, 2006

[38] ATRAMENTOV, O.; MARAVIN, Y.: *Utilizing cft and smt hits count for photon and electron reconstruction*. D0 Note 4444, 2004

[39] NORMAN: *Improved low et electron identification using lower dimensionalh-matrices and fisher variables*. D0 Note 2453, 1995

[40] ABDESSELAM, A.: *Comparison of h-matrices for electron identification in d0 run ii*. D0 Note 3745, 2000

[41] WHITESON, D.; PHAF, L.: *Electron likelihood*. D0 Note 4184, 2003

[42] KUMAR, A.; ET AL.: *Electron likelihood study*. D0 Note 4769, 2005

[43] WANG, L.; ET AL.: *Electron likelihood efficiency in p17*. D0 Note 5114, 2006

[44] HAYS, J.; ET AL.: *Single electron efficiencies in p17 data and monte-carlo*. D0 Note 5025, 2006

[45] HAYS, J.; ET AL.: *Single electron efficiencies in p17 data and monte-carlo using p18.05.00 d0correct*. D0 Note 5105, 2006

[46] GRIS, P.: *Electron smearing studies with runiia data*. D0 Note 5400, 2007

[47] CALFAYAN, P.; ET AL.: *Muon identification certification for p17 data*. D0 Note 5157, 2006

[48] BASSLER, U.; BERNARDI, G.: *Towards a coherent treatment of calorimetric energies: Missing transverse energy, jets, e.m. objects and the t42 algorithm*. D0 Note 4124, 2003

[49] VLIMANT, J.-R.; ET AL.: *Technical description of the t42 algorithm for the calorimeter noise suppression*. D0 Note 4146, 2003

[50] BERNARDI, G.; BUSATO, E.; VLIMANT, J.-R.: *Improvements from the t42 algorithm on calorimeter objects reconstruction*. D0 Note 4335, 2004

[51] BLAZEY, G. C.; ET AL.: *Run II jet physics* (2000). `hep-ex/0005012`

[52] HAREL, A.: *Jet id optimization*. D0 Note 4919, 2005

[53] HAREL, A.; WAGNER, R.: *Improved l1 confirmation*. D0 Note 4932, 2005

[54] HEGEMAN, J.: *Showering analysis for the final p17 jet energy scale*. D0 Note 5383, 2007. `http://www-d0.fnal.gov/phys_id/jes/d0_private/cb_material/p17_final/d0_note_5383_v1.2.ps`

[55] JES GROUP: *Jet energy scale determination at d0 run ii (final p17 version)*. D0 Note 5382, 2007. `http://www-d0.fnal.gov/phys_id/jes/d0_private/cb_material/p17_final/jes_note_v1.4.pdf`

[56] BLOCH, D.; ET AL.: *b-jet identification in the dzero detector*. D0 Note 4590, 2004

[57] B ID GROUP: *b-jet identification in the d0 experiment*. D0 Note 5062, 2006

[58] DEMINA, R.; KHANOV, A.; RIZATDINOVA, F.: *b-tagging with counting signed impact parameter method*. D0 Note 4049, 2002

[59] DEMINA, R.; KHANOV, A.; RIZATDINOVA, F.: *b-tagging with csip algorithm in p13*. D0 Note 4075, 2003

[60] DEMINA, R.; ET AL.: *Measurement of b-tagging efficiency and mis-tagging rates with csip method*. D0 Note 4133, 2003

[61] DEMINA, R.; ET AL.: *Measurement of b-tagging efficiency and mis-tagging rates with csip method*. D0 Note 4432, 2004

[62] BLOCH, D.; ET AL.: *Jet lifetime b-tagging*. D0 Note 4069, 2002

[63] BLOCH, D.; ET AL.: *Performance of the jet lifetime probability method for b-tagging in d0 data*. D0 Note 4158, 2003

[64] BLOCH, D.; ET AL.: *Performance of the jlip b-tagger in p14*. D0 Note 4348, 2004

[65] BLOCH, D.; CLEMENT, B.: *Update of the jlip b-tagger performance in p14/pass2 with jes 5.3*. D0 Note 4824, 2005

[66] FILTHAUT, F.; WIJNGAARDEN, B.: *Impact parameter b-jet tagging*. D0 Note 3850, 2001

[67] DEMINA, R.; KHANOV, A.: *Histogramming track finder: the impact parameter b-tagging performance*. D0 Note 3855, 2001

[68] SCHWARTZMAN, A.; NARAIN, M.: *Secondary vertex b-tagging using the kalman filter algorithm*. D0 Note 3909, 2001

[69] SCHWARTZMAN, A.; NARAIN, M.: *b-quark jet identification via secondary vertex reconstruction*. D0 Note 4080, 2003

[70] CLUTTER, J.: *Performance of the svt b-tagging algorithm on p17 data*. D0 Note 5385, 2007

[71] HANAGAKI, K.; KASPER, J.: *Identification of b-jet by soft muon*. D0 Note 4867, 2005

[72] SCANLON, T.: *A neural network b-tagging tool*. D0 Note 4889, 2005

[73] SCANLON, T.; ANASTASOAIE, M.: *Neural network b-tagging tool on pass 2 data*. D0 Note 4890, 2005

[74] SCANLON, T.: *Nn_cert: An all in one package for certifying b-tagging tools at d0*. D0 Note 5377, 2007

[75] ANASTASOAIE, M.; ROBINSON, S.; SCANLON, T.: *Performance of the nn b-tagging tool on p17 data*. D0 Note 5213, 2007

[76] SCANLON, T.: *Improvements to the b-tagging performance measurement in p17 data*. D0 Note 5402, 2007

[77] GERBER, C.; SHABALINA, E.; Y GARZON, G. O.: *Taggability in pass2 p14 data*. D0 Note 4995, 2006

[78] ANGHEL, I.; ET AL.: *Studies of taggability vs. npv for p17*. D0 Note 5240, 2006

[79] SAWYER, L.; STONE, A.: *Missing et reconstruction: variables and methods*. D0 Note 3957, 2003

[80] TRINCAZ-DUVOID, S.; VERDIER, P.: *Missing et reconstruction in p17*. D0 Note 4474, 2004

[81] FIEDLER, F.: *Precision Measurements of the Top Quark Mass*. Habil., Ludwig-Maximilians-Universität München, 2007

[82] PUMPLIN, J.; ET AL.: *New generation of parton distributions with uncertainties from global QCD analysis*. *JHEP* 07 (2002), p. 012. `hep-ph/0201195`

[83] ABAZOV, V. M.; ET AL. (D0): *Evidence for production of single top quarks and first direct measurement of —V(tb)—*. *Phys. Rev. Lett.* 98 (2007), p. 181802. `hep-ex/0612052`

[84] ABAZOV, V. M.; ET AL. (D0 Collaboration): *Evidence for production of single top quarks*. *Phys. Rev. D* 78 (2008)(1), p. 012005. `0803.0739`

[85] QUADT, A.: *Top quark physics at hadron colliders*. *Eur. Phys. J.* C48 (2006), pp. 835–1000

[86] JEZABEK, M.; KUHN, J. H.: *QCD Corrections to Semileptonic Decays of Heavy Quarks*. *Nucl. Phys.* B314 (1989), p. 1

[87] CDF TOP GROUP: `http://www-cdf.fnal.gov/physics/new/top/top.html`

[88] D0 Top Group: `http://www-d0.fnal.gov/Run2Physics/top/top_public_web_pages/top_public.html`

[89] Abazov, V. M.; et al. (D0): *A precision measurement of the mass of the top quark*. *Nature* 429 (2004), pp. 638–642. `hep-ex/0406031`

[90] Abazov, V. M.; et al. (D0): *Measurement of the top quark mass in the lepton + jets final state with the matrix element method*. *Phys. Rev.* D74 (2006), p. 092005. `hep-ex/0609053`

[91] Abazov, V. M.; et al. (D0): *Precise measurement of the top quark mass from lepton+jets events at D0*. *Phys. Rev. Lett.* (2008). Submitted, `0807.2141`

[92] Wang, M.; et al.: *Measurement of the mass of the top quark in the lepton+jets channel using the matrix element method on 1* fb^{-1} *of run iia data (p17)*. D0 Note 5495, 2008

[93] Haefner, P.; Fiedler, F.: *Determination of the muon transfer function for top mass measurements*. D0 Note 4818, 2005

[94] Sjostrand, T.; Lonnblad, L.; Mrenna, S.: *PYTHIA 6.2: Physics and manual* (2001). `hep-ph/0108264`

[95] Mangano, M. L.; et al.: *ALPGEN, a generator for hard multiparton processes in hadronic collisions*. *JHEP* 07 (2003), p. 001. `hep-ph/0206293`

[96] Wang, M.: 2007. `http://www-d0.hef.kun.nl//askArchive.php?base=agenda&categ=a071376&id=a071376s1t3/transparencies/mestat_jetmass_16aug07.pdf`

[97] Mahlon, G.; Parke, S. J.: *Maximizing spin correlations in top quark pair production at the Tevatron*. *Phys. Lett.* B411 (1997), pp. 173–179. `hep-ph/9706304`

[98] Schieferdecker, P.: *Measurement of the Top Quark Mass at D0 Run II with the Matrix Element Method in the Lepton+Jets Final State*. Diss., Ludwig-Maximilians-Universität München, 2005

[99] Skands, P.; Wicke, D.: *Non-perturbative QCD effects and the top mass at the Tevatron*. *Eur. Phys. J.* C52 (2007), pp. 133–140. `hep-ph/0703081`

[100] Lepage, G. P.: *A New Algorithm for Adaptive Multidimensional Integration*. *J. Comput. Phys.* 27 (1978), p. 192

[101] Lepage, G. P.: *VEGAS: AN ADAPTIVE MULTIDIMENSIONAL INTEGRATION PROGRAM* (1980). CLNS-80/447

[102] Galassi, M.; et al.: *GNU Scientific Library: Reference Manual*. Second revised edn., 2005, ISBN 0-9541617-3-4. `http://www.network-theory.co.uk/gsl/manual/`

[103] Berends, F. A.; et al.: *On the production of a W and jets at hadron colliders*. *Nucl. Phys.* B357 (1991), pp. 32–64

[104] Abazov, V. M.; et al. (D0): *Measurement of the $p\bar{p} \rightarrow t\bar{t}$ production cross section at $\sqrt{s}$ = 1.96-TeV in the fully hadronic decay channel*. *Phys. Rev.* D76 (2007), p. 072007. `hep-ex/0612040`

[105] Maltoni, F.; Stelzer, T.: *MadEvent: Automatic event generation with MadGraph*. *JHEP* 02 (2003), p. 027. `hep-ph/0208156`

[106] Mulders, M.: *Ensemble testing for the top mass measurement*. D0 Note 4460, 2004

[107] Barlow, R.: *Application of the bootstrap resampling technique to particle physics experiments*. 2000. `http://www.hep.man.ac.uk/preprints/manhep99-4.ps`

[108] Lai, H. L.; et al.: *Global QCD analysis of parton structure of the nucleon: CTEQ5 parton distributions*. *Eur. Phys. J.* C12 (2000), pp. 375–392. `hep-ph/9903282`

[109] Hoche, S.; et al.: *Matching parton showers and matrix elements* (2006). `hep-ph/0602031`

[110] CERN Application Software Group: *Geant: Detector description and simulation tool*. CERN Program Library Long Writeup, 1993

[111] Fisyak, Y.; Womersley, J.: *D0gstar d0 geant simulation o fthe total apparatus response*. D0 Note 3191, 1997

[112] Peters, Y.; et al.: *Study of the w+jets heavy flavor scale factor in p17*. D0 Note 5406, 2007

[113] Shabalina, E.: *private communication*. 2007

[114] Haefner, P.: *Data to monte-carlo comparisons for the l+jets top mass measurement in p17*. D0 Note 5716, 2008

[115] *A Combination of CDF and D0 Results on the Mass of the Top Quark* (2008). `0803.1683`

[116] Harel, A.: *An estimate of the data over mc, b over light jet response uncertainty for runiia jes*. D0 Note 5654, 2008

[117] Hegeman, J.: *Luminosity determination and reweighting of monte carlo overlay luminosity for p17 hadronic top analyses*. D0 Note 5561, 2008

[118] Cammin, J.: *private communication*. 2008

[119] Bowler, M. G.: *e^+e^- Production of Heavy Quarks in the String Model*. *Zeit. Phys.* C11 (1981), p. 169

[120] *Precision electroweak measurements on the Z resonance*. *Phys. Rept.* 427 (2006), p. 257. `hep-ex/0509008`

[121] Peters, Y.; et al.: *Reweighting of the fragmentation function for the d0 monte carlo*. D0 Note 5325, 2007

[122] Barberis, E.; et al.: *The matrix method and its error calculation*. D0 Note 4564, 2007

[123] PETERS, Y.; SHABALINA, E.: *Simultaneous measurement of b(t→wb)/b(t→wq) and* $\sigma(p\bar{p} \rightarrow t\bar{t})*b(t\rightarrow wq)^2$ *with p17 data*. D0 Note 5422, 2007

[124] PLEIER, M.-A.: *Measurement of the electron and muon fake rates in lepton+jets datasets*. D0 Note 5469, 2007

Danksagung

Als erstes möchte ich der Person danken, die mich von allen Menschen am längsten kannte. Sie hat einmal neun Monate auf mich gewartet - und dann noch einmal, als es ihre Tochter in die weite Welt hinauszog, um zu forschen. Sie wollte so gerne meinen Doktorhut sehen. Es war ihr nicht vergönnt. Ich hoffe, Mama, Du siehst ihn doch von irgendwo dort oben. Danke für alles.

Der Mensch, der diese Doktorarbeit erst ermoeglicht hat und an ihrem Gelingen massgeblich beteiligt war, ist mein Doktorvater Prof. Dr. Otmar Biebel. Ohne ihn würde das Graduiertenkolleg nicht existieren, das mich nach München geholt hat. Danke für die Einführung in die Hochenergiephysik, für die unzähligen ”physikalischen” Kaffeepausen und die Chance meine Arbeit so weit voranzutreiben. Ohne die finanzielle und ideelle Unterstützung durch das Graduiertenkolleg ”Particle Physics at the Energy Frontier of New Phenomena” wäre dies nicht möglich gewesen.

Auch Prof. Dr. Dorothee Schaile möchte ich für die Unterstützung meiner Arbeit, die konstruktiven Fragen und die Finanzierung meines Aufenthalts am Fermilab in Chicago danken.

Mein Dank gilt zudem Frank Fiedler und Raimund Ströhmer, die meine Analyse begleitet und unterstützt haben und sie in vielen angeregten Diskussionen vorangebracht haben. Auch Alexander Grohsjean und Philipp Schieferdecker möchte ich für ihre Unterstützung rund um die Analyse danken.

I would like to thank the members of the D0 collaboration, especially the Top Group conveners Regina Demina, Michele Weber, Gaston Gutierrez and my service work supervisor Ariel Schwartzman who sparked my interest in energy flow algorithms. My thank also goes to Carlos Garcia, Michael Wang and Rob Harrington who worked with me on the top mass measurement analysis.

Thanks, to Andrea Bangert who thoroughly read my thesis concerning my usage of the English language and made many useful suggestions.

Ich möchte die Gelegenheit nutzen, auch den Mitarbeitern des Grid Computing Centre Karlsruhe (GridKa) für die Bereitstellung und Wartung der Rechenfarm zu danken, ohne die diese Analyse nicht möglich gewesen wäre.

Last but not least, danke ich Heinz-Hermann Adam, der mir zwar in physikalischen Fragen nicht immer weiterhelfen konnte, dafür aber bei allen Computerproblemen umso mehr und der mich auch im Stress der letzten Wochen ertragen hat. Danke, dass Du mir die Freiheit gegeben hast, meinen Weg zu gehen.

”Daß ich erkenne, was die Welt
im Innersten zusammenhält,
schau’ alle Wirkenskraft und Samen,
und tu’ nicht mehr in Worten kramen.”

Johann Wolfgang von Goethe
dt. Schriftsteller
(1749 - 1832)